HYDROMECHANICS AND OPTIMIZATION OF FAST AND EFFICIENT SWIMMING

DANIEL FLORYAN

A DISSERTATION
PRESENTED TO THE FACULTY
OF PRINCETON UNIVERSITY
IN CANDIDACY FOR THE DEGREE
OF DOCTOR OF PHILOSOPHY

RECOMMENDED FOR ACCEPTANCE
BY THE DEPARTMENT OF
MECHANICAL AND AEROSPACE ENGINEERING
ADVISERS: CLARENCE W. ROWLEY AND ALEXANDER J. SMITS

JUNE 2019

ProQuest Number: 13882597

All rights reserved

INFORMATION TO ALL USERS
The quality of this reproduction is dependent upon the quality of the copy submitted.

In the unlikely event that the author did not send a complete manuscript
and there are missing pages, these will be noted. Also, if material had to be removed,
a note will indicate the deletion.

ProQuest 13882597

Published by ProQuest LLC (2019). Copyright of the Dissertation is held by the Author.

All rights reserved.
This work is protected against unauthorized copying under Title 17, United States Code
Microform Edition © ProQuest LLC.

ProQuest LLC.
789 East Eisenhower Parkway
P.O. Box 1346
Ann Arbor, MI 48106 – 1346

© Copyright by Daniel Floryan, 2019.

All rights reserved.

Abstract

This dissertation focuses on the mechanics of locomotion through a fluid medium characterized by propulsors (fins and wings) with a large aspect ratio and a large Reynolds number. The subject so delimited is of particular interest because on the order of 100 million years of animal evolution have led to fast and efficient animals converging upon such features. Idealized models of propulsors are studied in order to distill the essential physics responsible for fast and efficient locomotion, rather than the idiosyncrasies of any particular animal.

The first half considers a rigid propulsor, where the kinematics are known *a priori*. We derive a set of scaling laws for the thrust, power, and efficiency of a propulsor sinusoidally heaving or pitching while translating in a uniform stream. The validity of the scaling laws is borne out by their success in collapsing a wide array of experimental data. Moreover, physical phenomena are easily attributed to different terms in the scaling laws, revealing an important but previously unappreciated interplay between added mass and lift-based forces. The scaling laws are extended to non-sinusoidal kinematics, intermittent kinematics, and combined heaving and pitching kinematics, at each step collapsing experimental data and revealing important physics.

The second half considers a flexible propulsor, where the kinematics are unknown *a priori*. We start with the simplest case of a propulsor with homogeneous stiffness. To understand the role of fluid-structure resonance, we calculate the spectrum of the governing equations. The results demonstrate that resonance induces local maxima in thrust and power, in agreement with the literature, but does not by itself induce local maxima in efficiency, as assumed in the literature. Flutter eigenfunctions emerge as the system's stiffness is decreased, increasing locomotory efficiency. The results are then extended to propulsors with heterogeneous stiffness, and we calculate optimal distributions of stiffness over a wide range of conditions.

Throughout, the importance of fluid drag is discussed. For rigid propulsors, drag induces a global maximum in efficiency, plausibly explaining the narrow operating conditions observed in dolphins, sharks, bony fish, birds, bats, and insects. For flexible propulsors, drag induces local maxima in efficiency at resonance.

Acknowledgements

First, I would like to thank my advisors, Clancy Rowley and Lex Smits, for their advice and support over my years at Princeton. They struck the right balance between guiding me in the right direction and encouraging me to move in my own direction, from which I benefitted tremendously.

Next, I would like to thank my Ph.D. committee members, Marcus Hultmark and Howard Stone, and my dissertation readers, Luc Deike and George Lauder, who have respectively provided guidance during the course of my Ph.D. and the writing of this dissertation. Howard has been especially engaging and encouraging in matters related and unrelated to this dissertation.

Having been part of two research groups and a tight-knit community at Princeton, there are far too many people with whom I have crossed paths to list here without inevitably omitting a name, but I will say that they made my decision to come to Princeton the right one. All the experimental work was conducted with Tyler Van Buren, so he gets a special mention.

Finally, I would like to thank my parents, my brothers, my sister, and Kaamya. In some sense, this dissertation marks the end of a long educational process in which my family played a major role. This dissertation is for them, those who have passed, and those who will come.

The work presented in this dissertation was supported by the Office of Naval Research grant N00014-14-1-0533 (program manager Robert Brizzolara). I am additionally grateful for the support of the Charles W. Lummis Scholarship, the Daniel and Florence Guggenheim Foundation Fellowship, the Brit and Eli Harari Fellowship, and the Porter Ogden Jacobus Fellowship.

This dissertation carries T#3372 in the records of the Department of Mechanical and Aerospace Engineering.

To the memory of Anthony “Shambles” Boiano.

Preface

This dissertation contains two parts. The first part provides an overview of foils oscillating in a fluid, with the overview split between rigid and flexible foils. The first part reviews the relevant theoretical, experimental, and computational results, and also briefly describes some of the new results from this dissertation. The second part consists of published and submitted papers, which are also split between rigid and flexible foils. These papers contain the detailed results of this dissertation. The papers have been reformatted from their published forms, and the content of the submitted papers may change after peer-review; the reader should consult the published papers for finalized results. Author contributions are listed in Chapter 5, and the bibliography for the entire dissertation is listed at the end of this dissertation.

Contents

Abstract . . . iii

Acknowledgements . . . v

Preface . . . vii

List of Tables . . . xiii

List of Figures . . . xiv

I Introduction 1

1 Motivation and goals 2

1.1 The classical theory and its limitations . . . 4

2 Rigid propulsors 8

2.1 Theoretical background . . . 9

2.2 Experiments and computations . . . 17

2.3 New results . . . 22

2.A Prefactors in Garrick's work . . . 27

3 Flexible propulsors 28

3.1 Theoretical background . . . 29

3.2 Experiments and computations . . . 32

3.3 New results . . . 36

4 Conclusion 41

4.1 Summary 41

4.2 Outlook 43

II Papers 45

5 Overview 46

5.1 Author contributions 47

6 Scaling the propulsive performance of heaving and pitching foils 49

6.1 Introduction 50

6.2 Scaling laws 51

6.2.1 Lift-based forces 52

6.2.2 Added mass forces 54

6.2.3 Summary 56

6.3 Experimental setup 57

6.4 Heave results 58

6.5 Pitch results 60

6.6 Rescaling thrust 63

6.6.1 Biological data 64

6.7 Conclusions 66

7 Forces and energetics of intermittent swimming 68

7.1 Introduction 69

7.2 Experimental setup 70

7.3 Forces and power 72

7.4 Free swimming performance 75

7.4.1 Results on mean speed 77

7.4.2 Results on energetics 79

7.5 Conclusions 84

8 **Large-amplitude oscillations of foils for efficient propulsion** **86**

8.1 Introduction 86

8.2 Problem description and motivating analysis 89

8.3 Experimental setup 92

8.4 Propulsive performance 94

8.4.1 Thrust 94

8.4.2 Power 96

8.4.3 Efficiency 98

8.4.4 Thrust/efficiency tradeoff 101

8.5 Conclusions 103

9 **Efficient cruising for swimming and flying animals is dictated by fluid drag** **106**

9.A Supplementary information 114

9.A.1 Thrust and power 114

9.A.2 Motion composition 116

9.A.3 Materials and methods 116

10 **Clarifying the relationship between efficiency and resonance for flexible inertial swimmers** **118**

10.1 Introduction 119

10.2 Problem description 123

10.3 A note on parameters 126

10.4 Inviscid results 129

10.4.1 Propulsive characteristics of rigid swimmers 130

10.4.2 Propulsive characteristics of flexible swimmers 132

10.4.3 Fluid-structure eigenvalues and their relationship with efficiency 139

10.5 Finite Reynolds number effects 147
10.6 Conclusions 149
10.A Method of solution 151
    10.A.1 Numerical method 154
10.B Eigenvalues of the system 155
    10.B.1 Nonlinear eigenvalue problem 157
    10.B.2 Quiescent fluid 159
10.C Some useful formulas 162

11 Distributed flexibility in inertial swimmers 164

11.1 Introduction 165
11.2 Problem description 169
11.3 Parameters and scope 172
11.4 Inviscid results 174
    11.4.1 Propulsive characteristics of flapping plates with uniform flexibility 176
    11.4.2 Propulsive characteristics of flapping plates with distributed flexibility 179
11.5 Optimal stiffness distributions 182
    11.5.1 Linear stiffness distributions 184
    11.5.2 Quadratic stiffness distributions 197
    11.5.3 Finite Reynolds number effects 206
11.6 Conclusions 208
11.A Method of solution 209
    11.A.1 Numerical method 212
11.B Eigenvalues of the system 213
    11.B.1 Nonlinear eigenvalue problem 215
    11.B.2 Quiescent fluid 217

11.C Green's function of the system 220

11.D Some useful formulas 222

Bibliography **224**

List of Tables

8.1 Ranges of efficiency η reported in different works under nominally identical conditions and in the same facility. Kinematic parameters are $h_0/c = 0.75$, $\alpha_{\max} = 20^\circ$, $\phi = 270^\circ$, and $St_h = 2fh_0/U_\infty \in [0.25, 0.4]$ (definitions given in Section 8.2). 88
8.2 Motion parameters (start: step: end). 93

10.1 Summary of parameters used in the literature. † denotes studies where the swimmer swam freely (in which case Re, S, and f^* are dependent variables), and ‡ denotes studies where the free-stream velocity was zero. In some cases, parameter values were estimated, and in other cases, parameter values could not be estimated from the information provided (marked as —). 121
10.2 Parameter values used in this work. 127

11.1 Parameter values used in this work. 173

List of Figures

1.1 A body in the complex plane and the force acting on an element. . . 4

2.1 A rigid heaving and pitching foil. 8

2.2 The Knoller-Betz effect. 11

2.3 Magnitude and phase of the Theodorsen function. 15

2.4 Typical (a) thrust curve, (b) power curve, (c) efficiency curve, and (d) wake for a rigid oscillating foil. The sketch of the wake is adapted from Eloy (2012). 18

2.5 Time-averaged thrust coefficient C_T as a function of Strouhal number St for a heaving foil, for various heave amplitude to chord ratios, h^*. Experimental results from the current study. The parameters C_T and St are defined in Section 6.2. Repeated from figure 6.1. 23

2.6 Efficiency as a function of thrust coefficient, with the drag-free scaling shown. colour indicates $C_T/1.2A^*_\theta$. Repeated from figure 8.10. 26

3.1 A flexible plate actuated at its leading edge. 28

3.2 Typical (a) thrust curve, (b) power curve, (c) efficiency curve, and (d) wake and deflection for a flexible oscillating foil. 33

3.3 Trailing edge amplitude as a function of reduced frequency f^* and stiffness ratio S for a (a) heaving and (b) pitching plate with $R = 0.01$ relative to that of an equivalent rigid plate. Dashed white lines indicate where the flexible plate has the same trailing edge amplitude as the equivalent rigid plate. Under-resolved areas have been whited out. Repeated from figure 10.6. 37
3.4 Efficiency as a function of reduced frequency f^* and stiffness ratio S for a (a) heaving and (b) pitching plate with $R = 0.01$ relative to that of an equivalent rigid plate. Dashed white lines indicate where the flexible plate has the same efficiency as the equivalent rigid plate. Under-resolved areas and areas with negative efficiency have been whited out. Repeated from figure 10.14. 38

6.1 Time-averaged thrust coefficient C_T as a function of Strouhal number St for a heaving foil, for various heave amplitude to chord ratios, h^*. Experimental results from the current study. The parameters C_T and St are defined in Section 6.2. 51
6.2 Experimental setup and sketch of motions. 57
6.3 Heaving motions. Time-averaged (a) thrust and (b) power coefficients as functions of the scaling parameters (see (6.11)) for various $h^* = h_0/c$. 59
6.4 Heaving motions. Efficiency as a function of (a) St, and (b) and f^*. Solid lines indicate the scaling given by (6.11); dashed line indicates the scaling with $C_{Dh} = 0$. 60
6.5 Pitching motions. Time-averaged (a) thrust and (b) power coefficients as functions of the scaling parameters (see (6.12)), with $c_7 = 0$. . . . 61
6.6 Pitching motions. Efficiency as a function of (a) St, and (b) f^*. Solid lines indicate the scaling given by (6.12); dashed line indicates the scaling with $C_{Dp} = 0$. 62

6.7 Newly non-dimensionalized thrust as a function of reduced frequency for (a) heaving and (b) pitching. (6.15)–(6.16) are shown by the dashed lines. Colours are the same as in figures 6.3 and 6.5. 64

6.8 Dimensional thrust as a function of frequency at various free-stream velocities for (a) pitching at $\theta_0 = 7^\circ$ and (b) heaving at various $h^* = h_0/c$. 65

6.9 (a) Fluke-beat frequency and (b) non-dimensional fluke-beat amplitude as functions of length-specific swimming speed for several odontocete cetaceans. Adapted from Rohr and Fish (2004). 65

7.1 Experimental setup. 71

7.2 Time-averaged thrust (circular symbols) and power coefficients (square symbols) as they vary with smoothing parameter ξ ($\theta_0 = 10^\circ$, $f = 1$ Hz, $\Delta = 0.5$.) 73

7.3 Time-averaged (a) thrust and (b) power coefficients as functions of Strouhal number. Dark to light symbols represent increasing duty cycles, ranging from $\Delta = 0.2$ to 1 every 0.1. Symbols identify pitch amplitudes of $\theta_0 = 5^\circ$ (circle), 10° (square), and 15° (triangle). 74

7.4 Time-averaged (a) thrust and (b) power coefficients normalized by duty cycle as functions of Strouhal number. Symbols and tones as in figure 7.3. 74

7.5 Instantaneous wake vorticity with in-plane velocity arrows overlaid for (a) continuous motion, (b) duty cycle of $\Delta = 0.25$, (c) $\Delta = 0.5$, and (d) $\Delta = 0.75$ and a Strouhal number of $St = 0.4$. Small graphics in the bottom right show the pitch angle over time and the generation points of each vortex in the actuation cycle. 75

7.6 A swimmer can be simply represented as a combination of a drag-producing body and a thrust-producing propulsor. 76

7.7 Mean speed versus steady speed for all frequencies, amplitudes, and duty cycles. Mass ratios are $m^* = 0.01, 0.1, 1, 10$ (light to dark symbols), and area ratios are $A_w^* = 1$ (circles) and 10 (squares). 78

7.8 Ratio of energy expended by intermittent motions to energy expended by continuous motions as a function of duty cycle for $\theta_0 = 15°$, all frequencies, $m^* = 1$, and $A_w^* = 10$. 80

7.9 Ratio of energy expended by intermittent motions to energy expended by continuous motions, including metabolic energy losses, as a function of duty cycle for $\theta_0 = 15°$, all frequencies, $m^* = 1$, and $A_w^* = 10$. Each point is an average over all frequencies. The colour denotes the value of the metabolic power fraction c_m, 0 to 2 in intervals of 0.25 (dark to light). 81

7.10 Ratio of energy expended by intermittent motions to energy expended by continuous motions, restricted to equal mean speeds, as a function of duty cycle for $\theta_0 = 15°$. Dashed lines correspond to (7.18), with $m^* = 1$, $A_w^* = 10$. The symbol grey scale corresponds to three values of (dimensional) mean speed chosen, $U_{\text{mean}} = 0.2, 0.25, 0.3$ (dark to light). The frequency of the intermittent motion was chosen so that it would have a speed equal to the continuous motion. 83

8.1 Experimental setup and sketch of motions. 89

8.2 An illustration of two motions that produce the same thrust. Velocity profiles are shown in the frame of reference where the fluid at infinity is at rest. 91

8.3 Efficiency as a function of maximum angle of attack at the leading edge for our data. Colour indicates pitch angle (in degrees). 93

8.4 Coefficient of thrust as a function of (a) St for raw thrust, and (b) St^2 for drag-corrected thrust. Colour indicates pitch amplitude θ_0. . . . 95

8.5 Drag curve at $Re = 8{,}000$ for the foil used in all experiments. Values are reported relative to the drag at $\theta = 0$. Colour indicates each of the three trials. 96

8.6 Coefficient of power as a function of (a) St and (b) the scaling variable $f^*St^2(1 - H^*\Theta^*)$. Colour indicates θ_0. 97

8.7 Coefficient of power as a function of f^*St^2 and $1 - H^*\Theta^*$. Colour indicates C_P. The two plots are the same, but viewed from different angles. 98

8.8 Efficiency as a function of St. Colour indicates: (a) dimensionless amplitude A^*; (b) pitch amplitude θ_0. 99

8.9 (a) Raw efficiency and (b) reduced-drag efficiency as functions of St. colour indicates A^*. 101

8.10 Efficiency as a function of thrust coefficient, with the drag-free scaling shown. colour indicates $C_T/1.2A^*_\theta$. 103

9.1 A typical efficiency curve showing efficiency η as a function of St. Data are for a heaving and pitching NACA0012 foil (Quinn et al., 2015) ($A/c = 0.19$, and heaving leads pitching by 90°). 108

9.2 Swimmers and fliers can be decomposed into thrust-producing (orange) and drag-producing (blue) parts, with the propulsor aptly represented by an oscillating airfoil. 109

9.3 Efficiency η as a function of St. Data are as given in figure 9.1 for a heaving and pitching NACA0012 foil (Quinn et al., 2015). Solid lines are given by (9.6) with a fixed proportionality constant of 0.155. The drag constant, b_1, is set to 0.5, 0.35, 0.23, 0.15, 0.1, and 0.05 as the colours vary from dark to light, and we have set $g(\theta_0) = \theta_0$. The proportionality constant and the value of b_1 corresponding to the experimental data were calculated by a total least squares fit to the data. 113

9.4 Thrust and power data plotted against (9.13)–(9.14) for $\phi = 0°$ (blue) and $\phi = 270°$ (orange). The coefficients are $c_1 = 4.65$, $c_4 = 0.49$, $a_2 = 62.51$. 116

10.1 Schematic of the problem. 123
10.2 Efficiency as a function of mass ratio R and stiffness ratio S for a (a) heaving and (b) pitching plate at $f^* = 1$. Areas with negative efficiency have been whited out. 128
10.3 First four natural frequencies in a quiescent fluid as a function of mass ratio. Asymptotic behaviour overlaid. 129
10.4 (a) Mean thrust coefficient and (b) mean power coefficient as a function of reduced frequency f^* for a heaving (red) and pitching (blue) rigid plate. Asymptotic behaviour included. At low f^*, a pitching rigid plate produces drag in the mean. 131
10.5 Efficiency as a function of reduced frequency f^* for a heaving (red) and pitching (blue) rigid plate. At low f^*, a pitching rigid plate produces drag in the mean, hence its efficiency is negative. 131
10.6 Trailing edge amplitude as a function of reduced frequency f^* and stiffness ratio S for a (a) heaving and (b) pitching plate with $R = 0.01$ relative to that of an equivalent rigid plate. Dashed white lines indicate where the flexible plate has the same trailing edge amplitude as the equivalent rigid plate. Under-resolved areas have been whited out. . . 132
10.7 Same as in figure 10.6, but with quiescent natural frequencies overlaid as green lines. 133
10.8 Schematic explaining resonance. (a) Level sets on the complex plane of the magnitude of a transfer function with one pole, marked with a cross. (b) Magnitude of the same transfer function evaluated on the imaginary axis. 135

10.9 Thrust coefficient as a function of reduced frequency f^* and stiffness ratio S for a (a) heaving and (b) pitching plate with $R = 0.01$ relative to that of an equivalent rigid plate. Dashed white lines indicate where the flexible plate has the same thrust coefficient as the equivalent rigid plate. Under-resolved areas and areas which produce negative thrust have been whited out. 135

10.10 Power coefficient as a function of reduced frequency f^* and stiffness ratio S for a (a) heaving and (b) pitching plate with $R = 0.01$ relative to that of an equivalent rigid plate. Dashed white lines indicate where the flexible plate has the same power coefficient as the equivalent rigid plate. Under-resolved areas and areas which produce negative power input have been whited out. 136

10.11 Same as in figure 10.9, but with quiescent natural frequencies overlaid as green lines. 137

10.12 Same as in figure 10.10, but with quiescent natural frequencies overlaid as green lines. 137

10.13 Efficiency as a function of reduced frequency f^* and stiffness ratio S for a (a) heaving and (b) pitching plate with $R = 0.01$. Under-resolved areas and areas with negative efficiency have been whited out. 138

10.14 Efficiency as a function of reduced frequency f^* and stiffness ratio S for a (a) heaving and (b) pitching plate with $R = 0.01$ relative to that of an equivalent rigid plate. Dashed white lines indicate where the flexible plate has the same efficiency as the equivalent rigid plate. Under-resolved areas and areas with negative efficiency have been whited out. 139

10.15 Same as in figure 10.14, but with natural frequencies overlaid as cyan lines. 140

10.16 First few eigenvalues of the system as a function of stiffness ratio S: (a) real parts; and (b) imaginary parts. 141

10.17 Our simple notion of resonance becomes unclear when multiple poles are relatively close. (a) Level sets on the complex plane of the magnitude of a transfer function with four poles, marked with crosses. (b) Magnitude of the same transfer function evaluated on the imaginary axis. 144

10.18 Ten snapshots, evenly spaced in time, of (a) Euler-Bernoulli mode P2 and (b) flutter mode S1 for $S = 0.1$ comprising one period of motion. The modes have been normalized so that their second derivatives at the leading edge are real and equal to 1. 146

10.19 (a) Magnitude and (b) phase in radians of the deflection along the chord for Euler-Bernoulli mode P2 (red) and flutter mode S1 (blue), for $S = 0.1$. The modes have been normalized so that their second derivatives at the leading edge are real and equal to 1. 146

10.20 Efficiency as a function of reduced frequency f^* and stiffness ratio S for a (a) heaving and (b) pitching plate with $R = 0.01$ with additional drag. Under-resolved areas and areas with negative efficiency have been whited out. 149

10.21 Comparison between eigenvalues calculated using our method and those found in figures 4c and 4d in Alben (2008a). Note that just for this figure, we adopt the notation used in Alben (2008a). 159

11.1 Schematic of the problem. The varying colour represents the varying material properties. 169

11.2 Thrust coefficient, power coefficient, and efficiency as a function of the mass distribution for a (a) heaving and (b) pitching plate for $\langle R \rangle = 0.01$, $S \equiv 1$, and $f^* = 1$. R is linear, and values are normalized by their value when the mass is uniformly distributed. 175

11.3 Thrust coefficient, power coefficient, and efficiency as a function of the stiffness distribution for a (a) heaving and (b) pitching plate for $R \equiv 0.01$, $\langle S \rangle = 1$, and $f^* = 1$. S is linear, and values are normalized by their value when the mass is uniformly distributed. 175

11.4 Trailing edge amplitude as a function of reduced frequency f^* and stiffness ratio S for a (a) heaving and (b) pitching plate with $R \equiv 0.01$ relative to that of an equivalent rigid plate. Dashed white lines indicate where the flexible plate has the same trailing edge amplitude as the equivalent rigid plate. Under-resolved areas have been whited out. Results are for a uniformly flexible plate. The mean thrust and mean power coefficients are qualitatively the same as the trailing edge amplitude. 177

11.5 Efficiency as a function of reduced frequency f^* and stiffness ratio S for a (a) heaving and (b) pitching plate with $R \equiv 0.01$ relative to that of an equivalent rigid plate. Dashed white lines indicate where the flexible plate has the same efficiency as the equivalent rigid plate. Under-resolved areas and areas that produce negative efficiency have been whited out. Results are for a uniformly flexible plate. 178

11.6 Trailing edge amplitude as a function of reduced frequency f^* and mean stiffness ratio $\langle S \rangle$ for a (a) heaving and (b) pitching plate with $R \equiv 0.01$ relative to that of an equivalent rigid plate. Dashed white lines indicate where the flexible plate has the same trailing edge amplitude as the equivalent rigid plate. Under-resolved areas have been whited out. Results are for a flexible plate with stiffness distribution $S^*(x) = 1 - 0.9x$ (stiff leading edge). The mean thrust and mean power coefficients are qualitatively the same as the trailing edge amplitude. 179

11.7 Trailing edge amplitude as a function of reduced frequency f^* and mean stiffness ratio $\langle S \rangle$ for a (a) heaving and (b) pitching plate with $R \equiv 0.01$ relative to that of an equivalent rigid plate. Dashed white lines indicate where the flexible plate has the same trailing edge amplitude as the equivalent rigid plate. Under-resolved areas have been whited out. Results are for a flexible plate with stiffness distribution $S^*(x) = 1 + 0.9x$ (soft leading edge). The mean thrust and mean power coefficients are qualitatively the same as the trailing edge amplitude. 180

11.8 Efficiency as a function of reduced frequency f^* and mean stiffness ratio $\langle S \rangle$ for a (a) heaving and (b) pitching plate with $R \equiv 0.01$ relative to that of an equivalent rigid plate. Dashed white lines indicate where the flexible plate has the same efficiency as the equivalent rigid plate. Under-resolved areas and areas that produce negative efficiency have been whited out. Results are for a flexible plate with stiffness distribution $S^*(x) = 1 - 0.9x$ (stiff leading edge). 181

11.9 Efficiency as a function of reduced frequency f^* and mean stiffness ratio $\langle S \rangle$ for a (a) heaving and (b) pitching plate with $R \equiv 0.01$ relative to that of an equivalent rigid plate. Dashed white lines indicate where the flexible plate has the same efficiency as the equivalent rigid plate. Under-resolved areas and areas that produce negative efficiency have been whited out. Results are for a flexible plate with stiffness distribution $S^*(x) = 1 + 0.9x$ (soft leading edge). 181

11.10(a) Feasible set of quadratic flexibility distributions. The interior region contains stiffness distributions that are positive everywhere on the plate, and the border contains stiffness distributions that are positive except at a point. The dark region contains stiffness distributions whose minima are at the leading/trailing edge, and the light region contains stiffness distributions whose minima are at an interior point of the plate. We have drawn some representative distributions in (b), corresponding to the circles in (a). 183

11.11Optimal linear stiffness distribution as a function of reduced frequency f^* and mean stiffness ratio $\langle S \rangle$ for a (a) heaving and (b) pitching plate with $R \equiv 0.01$. Under-resolved areas and areas that produce negative thrust have been whited out. Results are for a flexible plate with linear stiffness distribution optimized for thrust. 185

11.12Thrust coefficient as a function of reduced frequency f^* and mean stiffness ratio $\langle S \rangle$ for a (a) heaving and (b) pitching plate with $R \equiv 0.01$ relative to that of an equivalent rigid plate. Dashed white lines indicate where the flexible plate has the same thrust coefficient as the equivalent rigid plate. Under-resolved areas and areas that produce negative thrust have been whited out. Results are for a flexible plate with linear stiffness distribution optimized for thrust. 185

11.13 Same as in figure 11.11, but with natural frequencies overlaid as curves for $\mathrm{d}S^*/\mathrm{d}x = -0.9$ (stiff leading edge, green), $\mathrm{d}S^*/\mathrm{d}x = 0$ (uniformly stiff, white), and $\mathrm{d}S^*/\mathrm{d}x = 0.9$ (soft leading edge, purple). 186

11.14 First four quiescent natural frequencies as a function of the stiffness distribution. The natural frequencies have been normalized by the natural frequencies of a uniformly stiff plate, $\mathrm{d}S^*/\mathrm{d}x = 0$. 187

11.15 Thrust coefficient as a function of reduced frequency f^* and mean stiffness ratio $\langle S \rangle$ for a (a) heaving and (b) pitching plate with $R \equiv 0.01$. The green surface corresponds to a plate with a stiff leading edge ($\mathrm{d}S^*/\mathrm{d}x = -0.9$), and the purple surface corresponds to a plate with a soft leading edge and matched third natural frequency ($\mathrm{d}S^*/\mathrm{d}x \in [0.416, 0.445]$). 188

11.16 Same as figure 11.12, but compared to a plate with uniformly distributed stiffness instead of a rigid plate. 190

11.17 Optimal linear stiffness distribution as a function of reduced frequency f^* and mean stiffness ratio $\langle S \rangle$ for a (a) heaving and (b) pitching plate with $R \equiv 0.01$. Under-resolved areas and areas that produce negative power have been whited out. Results are for a flexible plate with linear stiffness distribution optimized for power. 191

11.18 Power coefficient as a function of reduced frequency f^* and mean stiffness ratio $\langle S \rangle$ for a (a) heaving and (b) pitching plate with $R \equiv 0.01$ relative to that of an equivalent rigid plate. Dashed white lines indicate where the flexible plate has the same power coefficient as the equivalent rigid plate. Under-resolved areas and areas that produce negative power have been whited out. Results are for a flexible plate with linear stiffness distribution optimized for power. 192

11.19 Same as figure 11.18, but compared to a plate with uniformly distributed stiffness instead of a rigid plate. 193

11.20 Optimal linear stiffness distribution as a function of reduced frequency f^* and mean stiffness ratio $\langle S \rangle$ for a (a) heaving and (b) pitching plate with $R \equiv 0.01$. Under-resolved areas and areas that produce negative thrust or power have been whited out. Results are for a flexible plate with linear stiffness distribution optimized for efficiency. 194

11.21 Efficiency as a function of reduced frequency f^* and mean stiffness ratio $\langle S \rangle$ for a (a) heaving and (b) pitching plate with $R \equiv 0.01$ relative to that of an equivalent rigid plate. Dashed white lines indicate where the flexible plate has the same efficiency as the equivalent rigid plate. Under-resolved areas and areas that produce negative thrust or power have been whited out. Results are for a flexible plate with linear stiffness distribution optimized for efficiency. 194

11.22 Same as figure 11.21, but compared to a plate with uniformly distributed stiffness instead of a rigid plate. 195

11.23 Amplitude of deflection (left column) and local phase speed (right column) along the chord for heaving plates with uniform flexibility ($\mathrm{d}S^*/\mathrm{d}x = 0$), a stiff leading edge ($\mathrm{d}S^*/\mathrm{d}x = -0.99$), and a soft leading edge ($\mathrm{d}S^*/\mathrm{d}x = 0.99$). Optimal constant phase speeds are shown as thin horizontal lines in the right column. 198

11.24 Amplitude of deflection (left column) and local phase speed (right column) along the chord for pitching plates with uniform flexibility ($\mathrm{d}S^*/\mathrm{d}x = 0$), a stiff leading edge ($\mathrm{d}S^*/\mathrm{d}x = -0.99$), and a soft leading edge ($\mathrm{d}S^*/\mathrm{d}x = 0.99$). Optimal constant phase speeds are shown as thin horizontal lines in the right column except in (b), where no phase speed produces net thrust. 199

11.25 Colour coding for quadratic stiffness distributions. 200

11.26 Optimal quadratic stiffness distribution as a function of reduced frequency f^* and mean stiffness ratio $\langle S \rangle$ for a (a) heaving and (b) pitching plate with $R \equiv 0.01$. Under-resolved areas and areas that produce negative thrust have been whited out. Results are for a flexible plate with quadratic stiffness distribution optimized for thrust. 201

11.27 Thrust coefficient as a function of reduced frequency f^* and mean stiffness ratio $\langle S \rangle$ for a (a) heaving and (b) pitching plate with $R \equiv 0.01$ relative to that of an equivalent rigid plate. Dashed white lines indicate where the flexible plate has the same thrust coefficient as the equivalent rigid plate. Under-resolved areas and areas that produce negative thrust have been whited out. Results are for a flexible plate with quadratic stiffness distribution optimized for thrust. 201

11.28 Optimal quadratic stiffness distribution as a function of reduced frequency f^* and mean stiffness ratio $\langle S \rangle$ for a (a) heaving and (b) pitching plate with $R \equiv 0.01$. Under-resolved areas and areas that produce negative power have been whited out. Results are for a flexible plate with quadratic stiffness distribution optimized for power. 203

11.29 Power coefficient as a function of reduced frequency f^* and mean stiffness ratio $\langle S \rangle$ for a (a) heaving and (b) pitching plate with $R \equiv 0.01$ relative to that of an equivalent rigid plate. Dashed white lines indicate where the flexible plate has the same power coefficient as the equivalent rigid plate. Under-resolved areas and areas that produce negative power have been whited out. Results are for a flexible plate with quadratic stiffness distribution optimized for power. 203

11.30 Optimal quadratic stiffness distribution as a function of reduced frequency f^* and mean stiffness ratio $\langle S \rangle$ for a (a) heaving and (b) pitching plate with $R \equiv 0.01$. Under-resolved areas and areas that produce negative thrust or power have been whited out. Results are for a flexible plate with quadratic stiffness distribution optimized for efficiency. 204

11.31 Efficiency as a function of reduced frequency f^* and mean stiffness ratio $\langle S \rangle$ for a (a) heaving and (b) pitching plate with $R \equiv 0.01$ relative to that of an equivalent rigid plate. Dashed white lines indicate where the flexible plate has the same efficiency as the equivalent rigid plate. Under-resolved areas and areas that produce negative thrust or power have been whited out. Results are for a flexible plate with quadratic stiffness distribution optimized for efficiency. 205

11.32 Same as figure 11.31, but compared to a plate with uniformly distributed stiffness instead of a rigid plate. 206

Part I

Introduction

Chapter 1

Motivation and goals

The primary goals in designing the next generation of underwater vehicles are that they be fast, efficient, maneuverable, and stealthy. Traditional propeller-based underwater vehicles may be fast, but generally lag in the other three measures of performance. To achieve all of the performance goals simultaneously, next-generation designs require a new paradigm.

In this respect, biology offers a rich source of inspiration. Aquatic animals have benefited from on the order of 100 million years of evolution, surely leading them to develop features that make them good swimmers in the sense of the previous paragraph. Although not all of the evolved features may have a hydrodynamic purpose (or may have a hydrodynamic purpose other than the four previously outlined), it is reasonable to expect that many of them will. After all, many aquatic animals are indeed fast, efficient, maneuverable, and stealthy (though not necessarily all at once).

The capabilities of aquatic animals have led engineers to construct robotic systems imitating biological systems. Perhaps the best-known example is the RoboTuna, an eight-link tendon- and pulley-driven robot emulating the physical form and kinematics of a bluefin tuna (Triantafyllou and Triantafyllou, 1995). More recent examples include the GhostSwimmer (Rufo and Smithers, 2011), another robot fashioned after tuna, and the MantaBot (Fish et al., 2011), a partially soft robot fashioned after cow-nosed rays. These systems exemplify biomimicry (also called biomimetics), the design of human-made systems modelled directly on biological systems, and are mostly limited to the performance of the biological systems on which they are modelled.

In order to surpass the performance of biological systems, we turn to the bioinspired design paradigm. Bioinspiration is the design of human-made systems based on fundamental principles of biological systems, contrasting the direct imitation of biomimicry; it requires a deep understanding of the physical principles at play. To design underwater vehicles capable of great speed, efficiency, maneuverability, and stealth, we must gain a deeper understanding of the physics of underwater locomotion based on principles derived from biology.

The goal of this dissertation is to uncover the underlying physics of the fluid-structure interaction responsible for propelling large-scale (high Reynolds number) aquatic animals forward. The focus is on the first two goals outlined in the beginning—speed and efficiency—with maneuverability and stealth being left for future study. Fast and efficient swimmers, epitomized by animals such as tuna, are interesting in that nearly all of the propulsive force is generated by their tails, which are well-separated from the rest of the body which essentially amounts to a source of balancing drag (Webb, 1984). Furthermore, the tails characteristically have large aspect ratio and move in an oscillatory fashion. The essential features of the propulsion of these swimmers can therefore be understood via an abstracted problem: the propulsion of an oscillating two-dimensional foil. The foil represents the propulsive surface of the animals, henceforth referred to as the propulsor. This is the problem studied in this dissertation, with the hope that the principles uncovered here may guide the design of the next generation of underwater vehicles.

Since biological propulsors are at times rigid and at other times flexible, half of the dissertation is devoted to each topic. Accordingly, the rest of Part I is split between

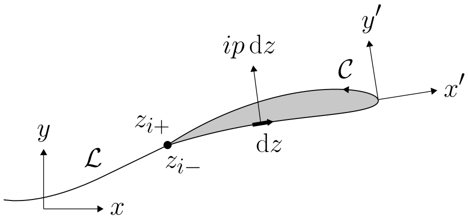

Figure 1.1: A body in the complex plane and the force acting on an element.

rigid and flexible propulsors. Each chapter begins with a review of the relevant theoretical background, followed by experimental and computational results from the literature, and ends with a summary of the results from this dissertation (the details of which are in Part II of the dissertation).

1.1 The classical theory and its limitations

To begin with, consider unsteady two-dimensional flow of a perfect fluid of constant density ρ around an object. The object is allowed to move and change shape, the flow is assumed to be continuous, and the fluid is at rest at infinity. For convenience, we work in the complex plane. The object is described by a closed contour $\mathcal{C}$, and we wish to determine the force and moment about the origin acting on the object due to the pressure p acting on the exterior surface of $\mathcal{C}$. The setup is sketched in figure 1.1 in a fixed coordinate system (x, y) and a moving coordinate system (x', y'), with $\mathcal{L}$ being a curve along which the tangential velocity and velocity potential ϕ may be discontinuous if there is circulation Γ about $\mathcal{C}$, and z_i being the point where $\mathcal{C}$ and $\mathcal{L}$ intersect. The analysis follows Sedov (1965), although we note that the results first appeared in Sedov (1935).

The force and moment about the origin acting on an element $\mathrm{d}z$ of $\mathcal{C}$ (per unit span) are

$$\mathrm{d}F_x + i\,\mathrm{d}F_y = ip\,\mathrm{d}z, \tag{1.1}$$

$$\mathrm{d}M = x\,\mathrm{d}F_y - y\,\mathrm{d}F_x = -\operatorname{Re}\{i\bar{z}(\mathrm{d}F_x + i\,\mathrm{d}F_y)\}, \tag{1.2}$$

where i is the imaginary unit and the overbar denotes complex conjugation. The pressure can be determined from the unsteady form of Bernoulli's principle,

$$p = -\rho\frac{\partial\phi}{\partial t} - \frac{\rho}{2}(u^2 + v^2) + f, \tag{1.3}$$

where t is time, $u + iv$ is the complex velocity of the fluid, and f is some function of only time. Letting $\mathrm{d}/\mathrm{d}t$ denote the material derivative, we have

$$\frac{\mathrm{d}\phi}{\mathrm{d}t} = \frac{\partial\phi}{\partial t} + u^2 + v^2, \tag{1.4}$$

where we have used the definition of the velocity potential. The force on the element $\mathrm{d}z$ is then

$$\mathrm{d}F_x + i\,\mathrm{d}F_y = if\,\mathrm{d}z - i\rho\frac{\mathrm{d}\phi}{\mathrm{d}t}\mathrm{d}z + \frac{i\rho}{2}(u + iv)(u - iv)\mathrm{d}z. \tag{1.5}$$

By the definition of the complex potential $w = \phi + i\psi$, where ψ is the stream function, and the fact that $\mathrm{d}w/\mathrm{d}z = u - iv$, we have

$$(u - iv)\mathrm{d}z = \mathrm{d}\phi + i\,\mathrm{d}\psi. \tag{1.6}$$

Additionally, using the fact that

$$-i\frac{\mathrm{d}\phi}{\mathrm{d}t}\mathrm{d}z = -i\,\mathrm{d}\left(z\frac{\mathrm{d}\phi}{\mathrm{d}t}\right) + i\frac{\mathrm{d}}{\mathrm{d}t}(z\,\mathrm{d}\phi) - i(u + iv)\mathrm{d}\phi \tag{1.7}$$

and that on $\mathcal{C}$

$$\mathrm{d}\frac{\mathrm{d}\phi}{\mathrm{d}t} = \frac{\mathrm{d}}{\mathrm{d}t}\mathrm{d}\phi, \qquad \frac{\mathrm{d}z}{\mathrm{d}t} = u + iv, \tag{1.8}$$

we may rewrite the force on the element $\mathrm{d}z$ as

$$\mathrm{d}F_x + i\,\mathrm{d}F_y = if\,\mathrm{d}z - i\rho\,\mathrm{d}\left(z\frac{\mathrm{d}\phi}{\mathrm{d}t}\right) + \overline{\frac{i\rho}{2}\frac{\mathrm{d}w}{\mathrm{d}z}}\mathrm{d}w + \rho\frac{\mathrm{d}}{\mathrm{d}t}(z\,\mathrm{d}\psi) + i\rho\frac{\mathrm{d}}{\mathrm{d}t}(z\,\mathrm{d}w). \tag{1.9}$$

To obtain the force on the entire body, we integrate (1.9) around the closed curve $\mathcal{C}$, yielding

$$F_x + iF_y = -i\rho z_i\frac{\mathrm{d}\Gamma}{\mathrm{d}t} + \overline{\frac{i\rho}{2}\oint_{\mathcal{C}}\left(\frac{\mathrm{d}w}{\mathrm{d}z}\right)^2\mathrm{d}z} + \frac{\mathrm{d}}{\mathrm{d}t}\left(\rho\frac{\mathrm{d}\,Sz^*}{\mathrm{d}t} + i\rho\oint_{\mathcal{C}} z\frac{\mathrm{d}w}{\mathrm{d}z}\mathrm{d}z\right), \tag{1.10}$$

where S is the area bounded by $\mathcal{C}$ and z^* is the centroid of this area. In a similar way, we may obtain an expression for the moment about the origin on the body; see Sedov (1965) for details. We obtain

$$M = -\frac{\rho}{2}z_i\overline{z_i}\frac{\mathrm{d}\Gamma}{\mathrm{d}t} + \mathrm{Re}\left[-\frac{\rho}{2}\oint_{\mathcal{C}} z\left(\frac{\mathrm{d}w}{\mathrm{d}z}\right)^2\mathrm{d}z + \frac{\rho}{2}\frac{\mathrm{d}}{\mathrm{d}t}\oint_{\mathcal{C}} z\overline{z}\frac{\mathrm{d}w}{\mathrm{d}z}\,\mathrm{d}z\right]. \tag{1.11}$$

We may generalize the formulas to a moving coordinate system. Let $q = U + iV$ denote the velocity of the origin of the moving coordinate system, and let Ω denote its angular velocity. The coordinates in the moving system are denoted with a prime, and let $\delta/\delta t$ denote differentiation with respect to the fixed coordinate system. Then we have

$$\frac{\mathrm{d}z}{\mathrm{d}t} = \frac{\delta z'}{\delta t} + i\Omega z' + q. \tag{1.12}$$

The force on the body in the moving coordinate system is then

$$F_x + iF_y = i\rho q\Gamma - i\rho z_i\frac{\mathrm{d}\Gamma}{\mathrm{d}t} + \overline{\frac{i\rho}{2}\oint_{\mathcal{C}}\left(\frac{\mathrm{d}w}{\mathrm{d}z}\right)^2\mathrm{d}z} + \frac{\mathrm{d}}{\mathrm{d}t}\left(\rho\frac{\mathrm{d}\,Sz^*}{\mathrm{d}t} + \rho Sq + i\rho\oint_{\mathcal{C}} z\frac{\mathrm{d}w}{\mathrm{d}z}\,\mathrm{d}z\right), \tag{1.13}$$

and the moment about the origin of the moving coordinate system is

$$\begin{aligned} M = -\frac{\rho}{2} z_i \overline{z_i} \frac{\mathrm{d}\Gamma}{\mathrm{d}t} + \mathrm{Re} \Bigg[-i\rho\overline{q} \left(\frac{\mathrm{d}\, S z^*}{\mathrm{d}t} + i \oint_{\mathcal{C}} z \frac{\mathrm{d}w}{\mathrm{d}z}\, \mathrm{d}z \right) - \frac{\rho}{2} \oint_{\mathcal{C}} z \left(\frac{\mathrm{d}w}{\mathrm{d}z} \right)^2 \mathrm{d}z \\ + \frac{\delta}{\delta t} \frac{1}{2} \oint_{\mathcal{C}} z\overline{z} \frac{\mathrm{d}w}{\mathrm{d}z}\, \mathrm{d}z \Bigg]. \end{aligned} \tag{1.14}$$

where we have omitted the prime on z. The paths of integration of the integrals may be changed, and the integrals may be evaluated as sums of residues at the poles of the integrands.

The steady force on a rigid body moving with constant velocity follows immediately from (1.13), giving Joukowski's theorem: $F_x + iF_y = i\rho q\Gamma$. The force on a body with unsteady motion shedding vorticity into its wake, i.e. the flapping foil we use to model the propulsors of fast and efficient swimmers, cannot be readily evaluated with the above formulas due to the difficulty in evaluating the full flow field. This motivates the approximate models developed in the literature and in this dissertation.

Chapter 2

Rigid propulsors

This chapter considers rigid propulsors, where the kinematics are known *a priori.* The model problem is a two-dimensional foil of chord c and span s heaving and pitching in a uniform incoming flow of speed U_∞, as sketched in figure 2.1 (span is the distance into the page). The sketched coordinate system is used to facilitate comparison to experiments later. Both motions are sinusoidal, with the heave motion described by $h(t) = h_0 \sin(2\pi f t)$ and the pitch motion described by $\theta(t) = \theta_0 \sin(2\pi f t + \phi)$, where h_0 is the heave amplitude, f is the frequency of motion, t is time, θ_0 is the pitch amplitude, and ϕ is the phase difference between the heave and pitch motions.

The primary quantities of interest are the time-averaged thrust $\overline{T}$ produced by the oscillating foil, the time-averaged power $\overline{P}$ consumed by the foil, and the efficiency η

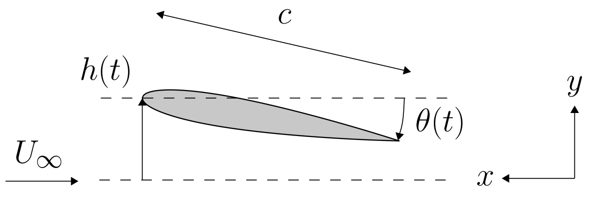

Figure 2.1: A rigid heaving and pitching foil.

of thrust production. These quantities are given by

$$\overline{T} = \overline{F_x}, \quad \overline{P} = \overline{F_y \dot{h} + M\dot{\theta}}, \quad \eta = \frac{\overline{T}U_\infty}{\overline{P}}, \tag{2.1}$$

respectively, where the dot denotes differentiation with respect to time, and the overbar denotes time-averaging (the distinction between when an overbar denotes time-averaging and when it denotes complex conjugation should be clear from context). The measure of efficiency we use is called the Froude efficiency. The corresponding dimensionless quantities are the time-averaged thrust and power coefficients

$$\overline{C_T} = \frac{\overline{T}}{\frac{1}{2}\rho U_\infty^2 sc}, \quad \overline{C_P} = \frac{\overline{P}}{\frac{1}{2}\rho U_\infty^3 sc}, \tag{2.2}$$

with the Froude efficiency already being dimensionless. Note that the Froude efficiency is equal to $\overline{C_T}/\overline{C_P}$.

2.1 Theoretical background

In the absence of circulation in the flow, the complex potential is holomorphic and single-valued outside of the foil, simplifying the expressions for the force and moment developed in Chapter 1. Starting with (1.13), the expression for the force, the first three terms are zero since there is no circulation and the expansion of the complex potential near infinity begins with a term of the order $1/z$ (hence the expansion of $(\mathrm{d}w/\mathrm{d}z)^2$ begins with a term of the order $1/z^4$). The force simplifies to

$$F_x + iF_y = \frac{\mathrm{d}I}{\mathrm{d}t}, \tag{2.3}$$

where

$$I = \rho S q^* + i\rho \oint_{\mathcal{C}} z \frac{\mathrm{d}w}{\mathrm{d}z}\,\mathrm{d}z = i\rho \oint_{\mathcal{C}} z\,\mathrm{d}\phi, \tag{2.4}$$

and $q^* = q + i\Omega z^*$ is the velocity of the centroid of the foil. Integrating by parts, we may write

$$I = -i\rho \oint_{\mathcal{C}} \phi \, \mathrm{d}z, \tag{2.5}$$

which shows that $-I$ is the total momentum of the fluid.

If the velocity and angular velocity with respect to the moving coordinate system are the same at two times, then the momentum of the fluid is the same at those two times. Furthermore, if the orientation of the moving coordinate system relative to the fixed coordinate system is the same at those two times, then the absolute momentum of the fluid is the same at those two times. This implies that the mean force with respect to the fixed coordinate system produced by a foil moving periodically is zero. In other words, a lone, rigid, periodically oscillating foil cannot produce a mean propulsive force purely through non-circulatory forces.

Although the inability to produce net propulsion may make the non-circulatory framework seem worthless in the context of this dissertation, the non-circulatory forces will find use later on, so we continue on. Ultimately, the forces and moment may be written as

$$F_x = -\lambda_x \frac{\mathrm{d}U}{\mathrm{d}t} - \lambda_{xy} \frac{\mathrm{d}V}{\mathrm{d}t} - \lambda_{x\omega} \frac{\mathrm{d}\Omega}{\mathrm{d}t} + \Omega(\lambda_{xy} U + \lambda_y V + \lambda_{y\omega}\Omega), \tag{2.6}$$

$$F_y = -\lambda_{xy} \frac{\mathrm{d}U}{\mathrm{d}t} - \lambda_y \frac{\mathrm{d}V}{\mathrm{d}t} - \lambda_{y\omega} \frac{\mathrm{d}\Omega}{\mathrm{d}t} - \Omega(\lambda_x U + \lambda_{xy} V + \lambda_{x\omega}\Omega), \tag{2.7}$$

$$M = -\lambda_{x\omega} \frac{\mathrm{d}U}{\mathrm{d}t} - \lambda_{y\omega} \frac{\mathrm{d}V}{\mathrm{d}t} - \lambda_{\omega} \frac{\mathrm{d}\Omega}{\mathrm{d}t} - \lambda_{xy}(U^2 - V^2) - (\lambda_y - \lambda_x)UV - (\lambda_{y\omega}U - \lambda_{x\omega}V)\Omega. \tag{2.8}$$

In the above, the forces and velocities are in the moving coordinate system of figure 1.1 and will need to be transformed into the coordinate system of figure 2.1. The λ_{ij} are called the coefficients of added or virtual mass due to the analogous role of mass they play in the above expressions; we refer to the non-circulatory forces as added mass forces. Formulas to calculate λ_{ij} given the geometry of a two-dimensional body can

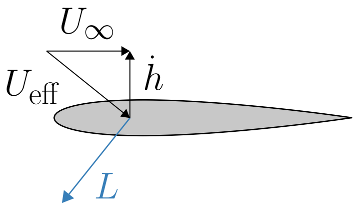

Figure 2.2: The Knoller-Betz effect.

be found in Sedov (1965), as well as values for several shapes. Later, we will make use of the values for a flat plate with chord c:

$$\lambda_x = 0, \quad \lambda_y = \frac{\pi}{4}\rho c^2, \quad \lambda_{xy} = 0, \quad \lambda_{x\omega} = 0, \quad \lambda_{y\omega} = \frac{\pi}{8}\rho c^3, \quad \lambda_\omega = \frac{9\pi}{128}\rho c^4. \tag{2.9}$$

In order to produce net propulsion, we must somehow allow for circulation in the flow. Although there does not presently exist a general solution for the unsteady motion of a two-dimensional foil with a line of discontinuity emanating from its trailing edge, approximations allowing for circulation in the flow can be made that make the problem amenable to analysis. Even quasi-steady circulation can produce thrust. For example, suppose a foil heaves periodically while translating forward with a constant speed as sketched in figure 2.2. Instantaneously, the fluid moves uniformly and obliquely to the foil with a speed $U_{\text{eff}} = \sqrt{U_\infty^2 + \dot{h}^2}$ and angle $\arctan(\dot{h}/U_\infty)$ relative to the foil's centerline. Considering only the instantaneous circulation around the foil, Joukowski's theorem provides that the force on the foil is perpendicular to the effective velocity vector. Hence, there is a component of the force in the streamwise direction, as sketched in figure 2.2. This thrust-producing effect is called the Knoller-Betz or Katzmayr effect (Knoller, 1909; Betz, 1912; Katzmayr, 1922).

To incorporate unsteady effects, an approximation must be made. In particular, consider a *flat* foil oscillating with *small* amplitudes (small heave and pitch motions). For such motions, the force and moment on the foil were solved for by Glauert (1930). The proceeding exposition follows Theodorsen (1935), first developing the non-circulatory velocity potential that satisfies the no-penetration boundary condition at the surface of the foil, and then the circulatory potential that satisfies the Kutta condition without disturbing the no-penetration boundary condition.

Consider a flat foil in the (x, y) plane normalized by its half-chord $c/2$ so that its leading edge is located at $(-1, 0)$ and its trailing edge is located at $(1, 0)$. The flat foil corresponds to the surface of the unit circle in the (X, Y) plane through the Joukowski transformation. In the (X, Y) plane, the velocity potential associated with a source of strength 2ϵ located at (X_1, Y_1) and a source of strength -2ϵ at $(X_1, -Y_1)$ is

$$\phi = \frac{\epsilon}{2\pi} \ln \frac{(X - X_1)^2 + (Y - Y_1)^2}{(X - X_1)^2 + (Y + Y_1)^2}. \tag{2.10}$$

On the upper surface of the circle, $Y = \sqrt{1 - X^2}$ and $Y_1 = \sqrt{1 - X_1^2}$. Making this substitution, allowing for a distribution of sources and sinks on the surface of the circle, and applying the Joukowski transformation gives the velocity potential on the surface of the flat plate:

$$\phi(x, t) = \frac{c}{4\pi} \int_{-1}^{1} \epsilon(x_1, t) \ln \frac{(x - x_1)^2 + (\sqrt{1 - x^2} - \sqrt{1 - x_1^2})^2}{(x - x_1)^2 + (\sqrt{1 - x^2} + \sqrt{1 - x_1^2})^2} \, \mathrm{d}x_1. \tag{2.11}$$

Here, $\epsilon(x, t)$ is the strength of the source/sink distribution and depends on space and time.

To uphold the no-penetration boundary condition at the surface of the plate, the velocity generated by the source/sink distribution and the component of the free-stream velocity normal to the plate must equal the normal velocity of the plate, giving

$$\epsilon = U_\infty \frac{\partial y_p}{\partial x} + \frac{c}{2} \frac{\partial y_p}{\partial t} \quad \text{on } x \in [-1, 1], \tag{2.12}$$

where y_p is the local height of the plate. Relating the local height of the plate to the heave and pitch motions gives

$$\phi_{\text{nc}} = \frac{1}{2} U_\infty c \theta \sqrt{1-x^2} + \frac{c}{2} \dot{h} \sqrt{1-x^2} + \frac{c^2}{4} \dot{\theta} \left(1 + \frac{x}{2}\right) \sqrt{1-x^2} \tag{2.13}$$

for the non-circulatory potential on the surface of the plate.

For the circulatory potential, we allow a continuous sheet of point vortices to be shed from the trailing edge. Since the amplitudes of motion are assumed small, the sheet remains on the x-axis and advects downstream with the free-stream velocity. Consider first a pair of point vortices in the (X, Y) plane, one outside the unit circle located at $(X_0, 0)$ with strength $-\Delta\Gamma$ and an image vortex of opposite strength at $(1/X_0, 0)$. The vortices are positioned such that the no-penetration boundary condition is maintained. The resulting velocity potential is

$$\phi = \frac{\Delta\Gamma}{2\pi} \left(\arctan \frac{Y}{X - X_0} - \arctan \frac{Y}{X - 1/X_0} \right). \tag{2.14}$$

In the (x, y) plane, the velocity potential is

$$\phi = -\frac{\Delta\Gamma}{2\pi} \arctan \frac{\sqrt{1-x^2}\sqrt{x_0^2 - 1}}{1 - x x_0}. \tag{2.15}$$

The circulatory potential for a sheet of vorticity extending to infinity is then

$$\phi_{\text{c}} = -\frac{c}{4\pi} \int_1^\infty \arctan \frac{\sqrt{1-x^2}\sqrt{x_0^2 - 1}}{1 - x x_0} \gamma(x_0, t) \, \mathrm{d}x_0, \tag{2.16}$$

where $\gamma(x, t)$ is the strength of the vorticity distribution and depends on space and time. The strength γ is determined by the Kutta condition, which requires that no infinite velocities exist at the trailing edge. To evaluate the velocity at the trailing edge, we use the full velocity potential (the sum of the circulatory and non-circulatory potentials).

With the full velocity potential in hand, we may evaluate the pressure difference across the plate via

$$p = -2\rho \left(U_\infty \frac{\partial \phi}{\partial x} + \frac{\partial \phi}{\partial t} \right), \tag{2.17}$$

and integrate it to get the forces and moment about the leading edge. Assuming complex exponential heave and pitch motions, the force and moment per unit span on the plate in the coordinate system of figure 2.1 are

$$F_y = \frac{\rho}{4} c^2 \left(\pi U_\infty \dot{\theta} - \pi \ddot{h} + \frac{\pi}{2} c \ddot{\theta} \right) + \pi \rho U_\infty c C \left(U_\infty \theta - \dot{h} + \frac{3c}{4} \dot{\theta} \right), \tag{2.18}$$

$$M = -\frac{\rho}{4} c^2 \left(\frac{3\pi}{4} U_\infty c \dot{\theta} + \frac{9\pi}{32} c^2 \ddot{\theta} - \frac{\pi}{2} c \ddot{h} \right) - \frac{\pi}{4} \rho U_\infty c^2 C \left(U_\infty \theta - \dot{h} + \frac{3c}{4} \dot{\theta} \right), \tag{2.19}$$

where C is a complex function defined by

$$C(\cdot) = \frac{H_1^{(2)}(\cdot)}{H_1^{(2)}(\cdot) + i H_0^{(2)}(\cdot)}, \tag{2.20}$$

and $H_\nu^{(2)}$ are Hankel functions. C is often called the Theodorsen function. In (2.18) and (2.19), C is evaluated at $\pi f c / U_\infty$; see Theodorsen (1935) for details. Note that F_y and M above are complex since the heave and pitch motions were described by complex exponentials. The real parts correspond to the real parts of the motions, and the imaginary parts correspond to the imaginary parts of the motions. The Theodorsen function changes both the magnitude and phase of the circulatory force at certain values of the reduced frequency $f^* = fc/U_\infty$, as shown in figure 2.3.

The thrust force has two components: one due to the component of the lift force projected in the streamwise direction, and another due to the suction force on the leading edge. We leave the details to Garrick (1936), but quote the final result for the time-averaged thrust and time-averaged power per unit span that we originally

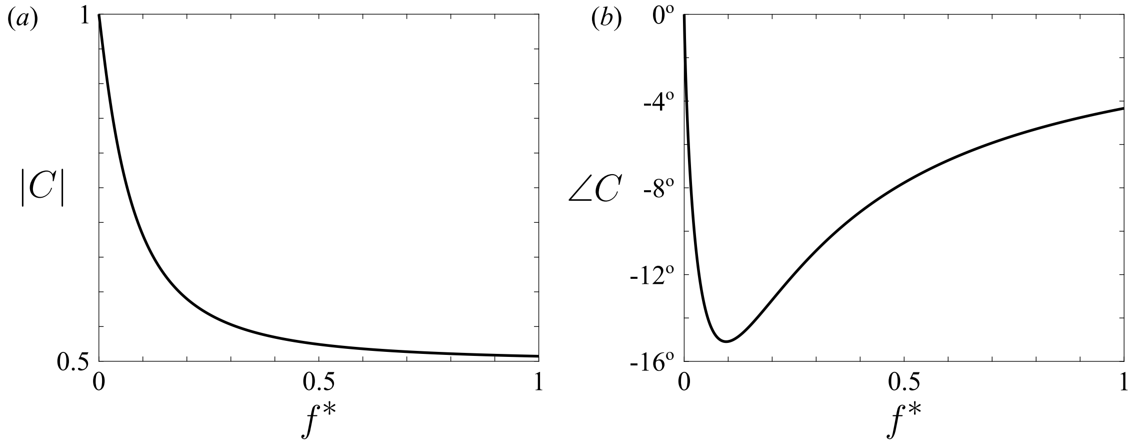

Figure 2.3: Magnitude and phase of the Theodorsen function.

sought:

$$\overline{F_x} = 2\pi^3 \rho c f^2 (a_1 h_0^2 + a_2 \theta_0^2 + 2a_3 \theta_0 h_0), \tag{2.21}$$

$$\overline{P} = 2\pi^3 \rho U_\infty c f^2 (b_1 h_0^2 + b_2 \theta_0^2 + 2b_3 \theta_0 h_0). \tag{2.22}$$

The expressions for the prefactors a_i and b_i are in Appendix 2.A.

The small-amplitude theory fares well in some respects. Experimental measurements of the amplitude and phase of streamwise and cross-stream forces match the predictions from the small-amplitude theory reasonably well (Mackowski and Williamson, 2015). Unfortunately, the small-amplitude theory overpredicts the thrust and efficiency produced by an oscillating foil (in some cases it overpredicts the power and in other cases it underpredicts the power) (Young and Lai, 2007; Mackowski and Williamson, 2015). The small-amplitude theory falls short in three ways: the flow is assumed inviscid (the importance of a finite Reynolds number is shown in Chapter 9); the vortex wake is assumed planar, which significantly impacts the thrust and power predictions (Young and Lai, 2007); and the vortex wake is not allowed to deform under its own induced velocity, although this effect has very minor consequences (Young and Lai, 2007).

Chopra (1976) was able to extend the two-dimensional inviscid theory to large-amplitude motions. Although he did not explicitly restrict the amplitudes of motion, they are implicitly restricted by the assumption of a small effective angle of attack. The main difficulty lay in modelling the vortex wake. Chopra modelled the wake as an infinitesimally thin sheet of vorticity shed at the trailing edge of the foil and advected downstream at the rate of the free-stream velocity; in the reference frame of the fluid, the vortex wake appears as a standing wave. Although his non-planar vortex wake is not allowed to deform according to the induced velocity field, this makes little difference for modest reduced frequencies (Katz and Weihs, 1978; Young and Lai, 2007). The principal drawback of Chopra's theory is how complicated it is; as far as we are aware, no subsequent authors made use of his theory other than quoting results computed by Chopra himself. Furthermore, it does not account for finite Reynolds number effects.

The available theory does not represent experimental and computational measurements very well, and the best theory is complicated to the point of not having been used. Consequently, the theoretical results are not shown here. We turn to experimental and computational results to show the main propulsive features of oscillating foils. The main features are governed by the dimensionless parameters

$$Re = \frac{\rho U_\infty c}{\mu}, \quad f^* = \frac{fc}{U_\infty}, \quad \frac{h_0}{c}, \quad \sin\theta_0, \quad \phi, \tag{2.23}$$

where Re is the Reynolds number, μ is the dynamic viscosity of the fluid, f^* is the reduced frequency, and the others are the dimensionless amplitudes and phase. The effects of the Reynolds number are oftentimes ignored. There are other dimensionless parameters that are often used, but they can be obtained from the preceding ones.

Popular examples include the Strouhal number,

$$St = \frac{2fA}{U_\infty}, \tag{2.24}$$

where A is the amplitude of the trailing edge, which can be calculated from the reduced frequency, amplitudes, and phase; the angle of attack is another commonly used dimensionless parameter. The shape of the foil will also affect the performance, but it is hardly ever considered (which is not to say that shape effects are insignificant). The effects of these dimensionless parameters are explored in the next section.

2.2 Experiments and computations

In the context of using oscillating foils as a means of propulsion, there are four principal questions studies try to answer:

1. How does the thrust production depend on the motion?
2. How does the power consumption depend on the motion?
3. How does the efficiency depend on the motion?
4. How does the fluid move?

Experiments and computations reveal some robust features, and the typical behaviours of the thrust, power, efficiency, and fluid are sketched in figure 2.4. Most of the cited work discusses at least one of the above questions.

First, consider the thrust. The thrust coefficient tends to increase with the Strouhal number at an increasing rate. The Strouhal number can be thought of as a measure of the intensity of the motion (increasing the frequency or amplitude of motion increases the Strouhal number). At low values of the Strouhal number, the thrust tends to be negative; we will refer to this as the 'offset drag' C_D. Beyond

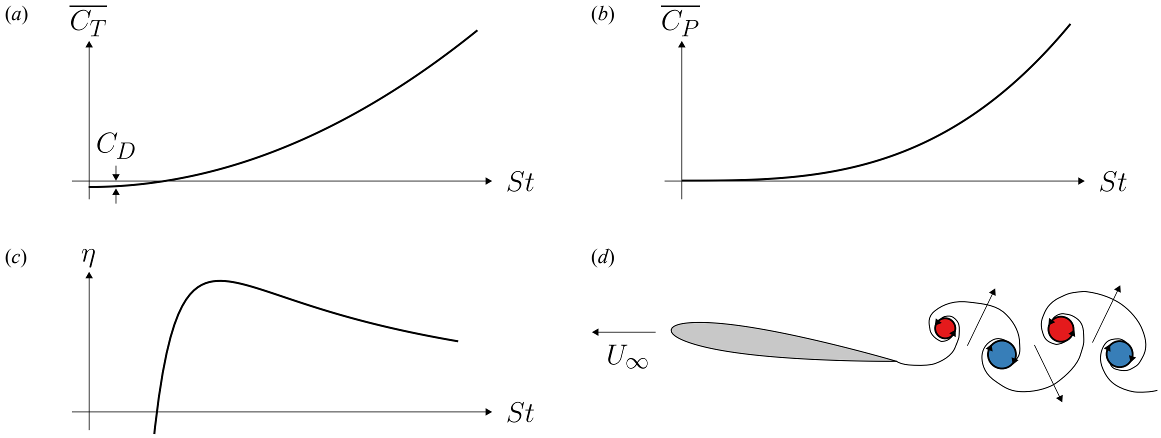

Figure 2.4: Typical (a) thrust curve, (b) power curve, (c) efficiency curve, and (d) wake for a rigid oscillating foil. The sketch of the wake is adapted from Eloy (2012).

observational studies, the understanding of thrust production is mostly limited to the linear theory, arguments based on the wake (discussed later), and a simplified argument based on added mass (Gazzola et al., 2014). The results of this dissertation advance the understanding of thrust production.

Second, the power. The power coefficient also tends to increase with the Strouhal number at an increasing rate. The power coefficient tends to increase at a faster rate than the thrust coefficient does. As the motion weakens, the power coefficient approaches zero. The power is rarely analyzed, with most studies focusing instead on thrust and efficiency, and studies that do show measurements of power are observational in nature. The results of this dissertation provide an understanding of the power consumption.

Third, the efficiency. The efficiency is the ratio of the thrust coefficient to the power coefficient, and its behaviour can be deduced from the behaviours of the thrust and power. By definition, the zero-crossing point of the efficiency coincides with that of the thrust. Near the zero-crossing point, the efficiency changes rapidly with the Strouhal number. Since the power coefficient increases at a faster rate than the thrust coefficient does, the efficiency decreases with the Strouhal number for large values of the Strouhal number. Consequently, there is an intermediate value of the Strouhal number where a peak in efficiency exists, typically in the range $0.2 < St < 0.4$ (Triantafyllou et al., 1991). The rapid increase after the zero-crossing point, followed by the peak and gradual decay with Strouhal number, is quite typical. Much of the literature focuses on the efficiency, so this section will as well.

Fourth, the wake. Oscillating foils tend to leave a distinctive pattern of vortices in their wake. Some nice smoke visualization is shown in Bratt (1953), and the patterns there are reflected in the sketch in figure 2.4d. During each cycle of the motion, the foil leaves a counter-rotating pair of vortices in its wake. Different patterns are possible (see Koochesfahani (1989) for some examples), but the sketched pattern is the one most frequently observed and reported.

The wake is often used to make conclusions about what is happening to the foil; Andersen et al. (2017) went so far as to create phase maps of the different vortex patterns and relate them to thrust production. In the configuration shown in the sketch, where the red counterclockwise rotating vortices lie above the blue clockwise rotating vortices, the velocity field induced by the vortices creates a meandering jet that increases the streamwise momentum of the fluid opposite to the direction of travel, indicating that the fluid likely imparts a streamwise force on the foil in the direction of travel. This vortex configuration is called a 'reverse von Kármán' vortex street, dubbed so since it has the opposite configuration of the classic von Kármán vortex street, a staggered array of counter-rotating vortex pairs where the counterclockwise rotating vortices lie *below* the clockwise rotating vortices. A von Kármán vortex street is usually thought of as being indicative of net drag due to the induced velocity field, and the reverse von Kármán vortex street is usually thought of as being indicative of net thrust, but this is not quite true (Andersen et al., 2017). (The incongruity should be obvious, since the wake argument only considers the momentum flux but ignores the pressure on the foil.)

In praising Andersen et al.'s phase maps of the vortex patterns in the wake, Zhang (2017) makes an analogy between the vortex patterns in the wake of an oscillating foil (or swimming/flying animals, for that matter) and the footprints of animals walking on muddy ground. Just as scientists can learn much from the footprints of animals, scientists can also learn much from the vortex patterns observed in the wake of an oscillating foil. The view developed during the progress of this dissertation is that the wake is indeed like the trail of an animal's footprints: some estimates can be made from it, but much more can be learned by analyzing the foil itself (the 'animal'). The wake is a consequence of the motion of the foil, and the situation should not be confused with the chicken-or-egg dilemma. The rest of the dissertation will make no mention the wake, unless needed when reviewing existing literature.

Now back to the efficiency. To achieve high levels of efficiency, heave and pitch motions need to be combined (see Van Buren et al. (2018a), for example). The phase difference between the motions greatly impacts the efficiency. The linear theory predicts that a 90° phase difference maximizes efficiency (Lighthill, 1970; Wu, 1971), and this has also been observed in computations (Isogai et al., 1999; Tuncer and Kaya, 2005) and experiments (Read et al., 2003; Schouveiler et al., 2005). Nonoptimal phase differences are associated with flow separation at the leading edge, leading to decreases in efficiency (Wang, 2000; Lewin and Haj-Hariri, 2003). Although Anderson et al. (1998) stated that favourable leading edge vortex dynamics contributed positively to their highest efficiency case, it is important to note that this conclusion was reached through flow visualization at Re = 1,100, whereas the efficiency measurement was carried out at Re = 40,000. Indeed, a careful set of computations has shown that leading edge vorticity is generally detrimental to efficiency (Tuncer and Kaya, 2005; Young et al., 2006; Young and Lai, 2007).

The amplitudes of motion also affect the efficiency. Generally speaking, large amplitudes give high efficiencies (Anderson et al., 1998). It is difficult to understand why this is so, since the small-amplitude theory is far from applicable. Alexander (2003) provides a very simplified but nice analysis that suggests that large amplitudes should be highly efficient; his analysis is recounted in detail in Chapter 8.

Perhaps the parameter with the most significant (and best known) effect on the efficiency is the Strouhal number. As previously mentioned, oscillating foils tend to peak in efficiency in a fairly tight range of Strouhal numbers, $0.2 < St < 0.4$, and this range is quite robust. Probably for this reason, the Strouhal number has been called "the governing parameter of the overall problem" (Triantafyllou et al., 1993). Furthermore, this range of Strouhal numbers coincides with the range observed in swimming and flying animals (Triantafyllou et al., 1991; Taylor et al., 2003). Naturally, the community was quite curious why a peak in efficiency is consistently observed in a tight range of Strouhal numbers. Three theories have been put forth. In the first theory, conceived by Triantafyllou et al. (1991), the authors argue that peak efficiency occurs when the kinematics of the foil result in the maximum amplification of the shed vortices in the wake, yielding maximum thrust per unit of input energy. The Strouhal number of maximum spatial amplification always lies in the range $St \in [0.25, 0.35]$ for their data. The phenomenon of maximum spatial amplification of shed vortices has been called 'wake resonance' (Moored et al., 2012). The second theory argues that the preferred Strouhal number is connected with maximizing the angle of attack allowed while avoiding the shedding of leading edge vortices (Wang, 2000). In other words, the motion should be made strong, but not so strong so as to cause flow separation at the leading edge. The third theory is directed towards swimming animals, but states that the ratio of tail beat amplitude to the body length essentially dictates the Strouhal number for steadily cruising animals, since it requires a balance between thrust and drag. This is similar to the explanation provided by Gazzola et al. (2014), who stated that the range of Strouhal numbers observed in nature is due to a thrust-drag balance, that is, the range of Strouhal numbers observed in nature is a consequence of a statement about momentum, not a statement about energy. A new theory is the subject of Chapter 9.

2.3 New results

Here, new results from this dissertation are summarized. The details are contained in Chapters 6–9.

Since the available theory does not accurately represent the available experimental data, we set out to develop scaling relations that accurately represent the mean propulsive performance of oscillating rigid propulsors in Chapter 6. Since the Strouhal number is considered “the governing parameter of the overall problem” (Triantafyllou et al., 1993), the hope was that experimental data could be scaled by the Strouhal number alone. In conducting many experiments on heaving and pitching foils, however, we found that propulsive performance cannot be represented solely by the Strouhal number. For instance, figure 2.5 shows that for a heaving foil, motions with different amplitudes but the same Strouhal number can produce significantly different levels of thrust.

Using the theory of Theodorsen (1935), Garrick (1936), and Sedov (1965) reviewed in Section 2.1, we developed scaling relations for the time-averaged thrust, power, and efficiency of heaving or pitching foils; the details are in Chapter 6. The scaling relations also allow for an offset drag to the thrust to capture finite Reynolds number effects. The work of Liu et al. (2014) is important to the scaling relations because there the authors showed that finite amplitudes alter the phases of the forces compared to what the linear theory predicts. This observation suggests that forces that are zero when time-averaged in the small-amplitude setting may have a non-zero mean in the finite amplitude setting. Since the magnitude of the time-varying forces is generally large compared to time-averaged values, the phase shift due to finite amplitudes may

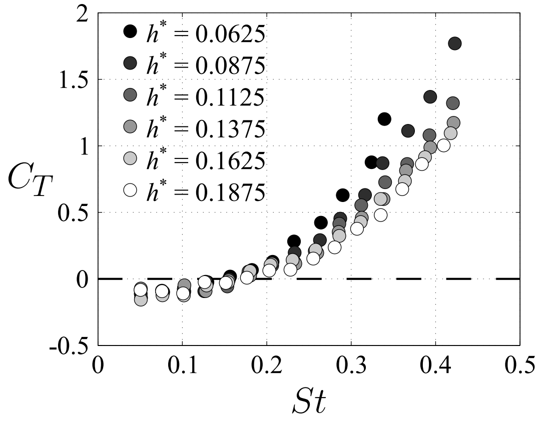

Figure 2.5: Time-averaged thrust coefficient C_T as a function of Strouhal number St for a heaving foil, for various heave amplitude to chord ratios, h^*. Experimental results from the current study. The parameters C_T and St are defined in Section 6.2. Repeated from figure 6.1.

create new time-averaged forces that have important contributions to the total time-averaged propulsive performance. Our scaling relations allow for such contributions, and experimental data dictates whether these contributions are important through empirical pre-factors.

When tested against experimental data for heaving or pitching foils, the scaling relations successfully collapse the thrust and power data. The efficiency data collapse when drag can be ignored, and diverge in a way predicted by the scaling relations when drag becomes important. Drag is seen to be responsible for the precipitous drop in efficiency when motions become weak.

The scaling laws also suggest a new definition for the thrust coefficient, where the thrust is normalized by the velocity of the trailing edge of the foil instead of by the dynamic pressure. For heaving foils, the new thrust coefficient depends only on the reduced frequency, whereas for pitching foils, the new thrust coefficient is a constant. Consequently, the dimensional thrust of a pitching foil is independent of the free-stream velocity, which is confirmed through additional experiments.

In Chapter 7, we experimentally explore the energetic benefits of intermittent pitching motions. Fish have been observed to intermittently flap their fins in many contexts (Fish et al., 1991; Gleiss et al., 2011), leading us to ask if there are any associated energetic benefits. The experiments were conducted in a water tunnel with a constant free-stream velocity, whereas intermittently flapping fish accelerate and decelerate. Based on the scaling relations, however, pitching motions are independent of the free-stream velocity, so experiments conducted under a constant velocity can be used to make conclusions about the behaviour of accelerating bodies.

The first conclusion is that propulsive performance scales directly with the duty cycle, which describes the fraction of time that the foil is moving during intermittent motions. By averaging the thrust and power over only the active portion of the motion, the data taken at different duty cycles collapse. Together with the particle image velocimetry results, which show that the main vortical structures do not change between intermittent and continuous motions, the results suggest that each cycle of active motion is independent of the others. In other words, the whole is the sum of its parts.

The second conclusion concerns the energetics of intermittent swimming. We compare the energy expended by intermittent and continuous motions in three scenarios: (1) energy expended in traversing a given distance; (2) energy expended in traversing a given distance, including metabolic energy losses; and (3) energy expended in traversing a given distance in a given amount of time. Intermittent motions were generally energetically favourable as no energy is spent during the inactive portion of the motion where the swimmer still coasts forward. When metabolic energy losses were added, they could be high enough to make continuous swimming energetically advantageous.

The original scaling relations were extended to describe intermittent motions and to provide insights into the energetics of intermittent swimming. The scaling relations have also been extended to non-sinusoidal motions and combined heaving and pitching motions in subsequent work (Van Buren et al., 2017, 2018a). In Van Buren et al. (2018a), many free constants are needed in order for the scaling relations to successfully collapse experimental thrust and power data. In Chapter 8, we specialize to combined heaving and pitching motions where the heave leads the pitch by a 90° phase difference, since such motions are most efficient. In narrowing the scope to the most efficient motions, we develop scaling relations that have *no free constants* (see Appendix 9.A.1 for details). Even though there are no empirical constants, the scaling relations successfully collapse experimental data from motions with peak-to-peak trailing edge amplitudes of nearly two chord lengths.

The new scaling relations reveal that large-amplitude motions should produce high efficiency, as observed in past experiments (Anderson et al., 1998). What is new is that the scaling relations give a reason as to why large-amplitude motions are more efficient than small-amplitude motions. Moreover, low-frequency motions are also predicted to be more efficient, and this is validated by the experimental data. At a certain point, however, the predictions break down, and large-amplitude, low-frequency motions become inefficient. The reason is that the offset drag also increases with the pitch amplitude (recall that drag leads to a precipitous drop in efficiency once motions become weak enough). In other words, big and slow (large-amplitude, low-frequency) motions are more efficient until they become so big and so slow that drag overwhelms the thrust production and the efficiency decreases. Modest decreases in drag, for example through increases in the Reynolds number, will lead to greater efficiencies everywhere.

Although at a given thrust coefficient we may increase efficiency by increasing the amplitude (unless drag is important), there is a fundamental tradeoff between thrust coefficient and efficiency: an increase in one requires a decrease in the other. We developed a scaling relation that captures this tradeoff in the limit of no drag and

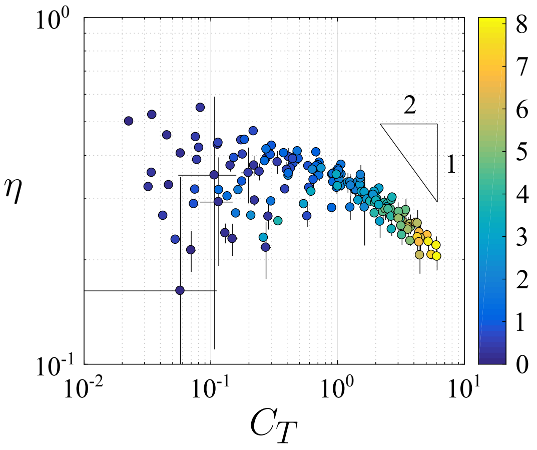

Figure 2.6: Efficiency as a function of thrust coefficient, with the drag-free scaling shown. colour indicates $C_T/1.2A_\theta^*$. Repeated from figure 8.10.

reflects the experimental measurements, as shown in figure 2.6. The presence of drag lowers the gains in efficiency that can be achieved through sacrifices in thrust.

The scaling relations are then used to make conclusions about the biology in Chapter 9. As previously mentioned, many swimming and flying animals are observed to cruise in a narrow range of Strouhal numbers $0.2 < St < 0.4$, which is where efficiency consistently peaks for oscillating foils. We show that this peak in efficiency is due to the drag experienced by the foil. Furthermore, the drag is also responsible for the precipitous drop in efficiency at low Strouhal numbers, and our scaling relations also predict the gradual decay of the efficiency past the peak with increasing Strouhal number. The observations of the constancy of the Strouhal number in nature are due to the drag experienced by these animals' propulsive surfaces. Since drag is expected to weaken with increasing Reynolds number, our scaling relations predict the Strouhal number of animals should decrease with increasing Reynolds number, which is indeed observed in nature (Gazzola et al., 2014). Our theory is strong because not only does it predict the peak in efficiency and variation with Reynolds number seen in nature, it also predicts all of the off-peak behaviour. This work puts to rest why animals swim and fly the way they do.

2.A Prefactors in Garrick's work

Following are the prefactors used in (2.21) and (2.22).

$$
\begin{aligned}
a_1 &= F^2 + G^2, && (2.25)\\
a_2 &= \frac{c^2}{4}\left[(F^2+G^2)\left(\frac{1}{\pi^2 f^{*2}} + \frac{9}{4}\right) + \frac{3}{4} - \left(\frac{3}{2} + \frac{1}{\pi^2 f^{*2}}\right)F + \frac{G}{2\pi f^*}\right], && (2.26)\\
a_3 &= \frac{c}{2}\left[(F^2+G^2)\left(\frac{3}{2}\cos\phi + \frac{1}{\pi f^*}\sin\phi\right) + \left(-\frac{F}{2} + \frac{1}{4} + \frac{G}{2\pi f^*}\right)\cos\phi \right.\\
&\qquad \left. - \left(\frac{G}{2} + \frac{F}{2\pi f^*}\right)\sin\phi\right], && (2.27)\\
b_1 &= F, && (2.28)\\
b_2 &= \frac{c^2}{4}\left[\frac{3}{4} + \frac{1}{2}\left(\frac{3F}{2} + \frac{G}{\pi f^*}\right)\right], && (2.29)\\
b_3 &= \frac{c}{4}\left[\left(\frac{1}{2} + 2F + \frac{G}{\pi f^*}\right)\cos\phi + \left(\frac{F}{\pi f^*} - G\right)\sin\phi\right]. && (2.30)
\end{aligned}
$$

Above, F and G are respectively the real and imaginary parts of the complex function C defined in (2.20), that is $C = F + iG$, and $f^* = fc/U_\infty$ is the reduced frequency.

Chapter 3

Flexible propulsors

This chapter considers passively flexible propulsors, where the kinematics are unknown *a priori*. The model problem is a two-dimensional flexible, inextensible plate of chord c and span s heaving and pitching at its leading edge in a uniform incoming flow of speed U_∞, as sketched in figure 3.1. Both motions are sinusoidal, with the heave motion described by $h(t) = h_0 \sin(2\pi f t)$ and the pitch motion described by $\theta(t) = \theta_0 \sin(2\pi f t + \phi)$, where h_0 is the heave amplitude, f is the frequency, t is time, θ_0 is the pitch amplitude, and ϕ is the phase difference between the heave and pitch motions. The unknown deflection is denoted Y, and depends on the fluid properties (speed U_∞ and density ρ_f) and the material properties (density ρ_s, Young's modulus E, and second moment of area I).

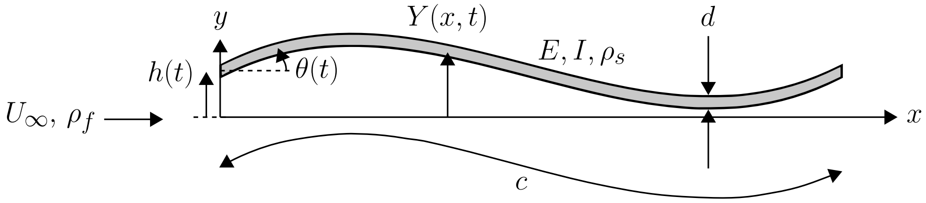

Figure 3.1: A flexible plate actuated at its leading edge.

The quantities of interest are the time-averaged thrust produced by the oscillating plate, the time-averaged power, and the efficiency. These are defined the same way as in (2.1), with the corresponding dimensionless quantities defined in (2.2).

3.1 Theoretical background

The best available theory is that of Wu (1961). In his theory, Wu considers the two-dimensional flow of an inviscid fluid generated by the motion of a thin deformable plate. The deflection and slope are assumed to be small everywhere, allowing for linearization of the governing equations. Let $q = (U_\infty + u, v)$ denote the flow velocity, where (u, v) is the perturbation velocity due to the motion of the plate. The perturbation velocity satisfies the continuity equation,

$$\frac{\partial u}{\partial x} + \frac{\partial v}{\partial y} = 0. \tag{3.1}$$

Since the motion of the plate is assumed small, u and v are small compared to U_∞, allowing for linearization of the Euler equations:

$$\left(\frac{\partial}{\partial t} + U_\infty \frac{\partial}{\partial x}\right) q = -\frac{1}{\rho_f}\nabla p, \tag{3.2}$$

where p is the pressure of the fluid.

The fluid additionally satisfies the no-penetration and Kutta conditions, which may be written as

$$v|_{x\in[0,c],y=0} = \frac{\partial Y}{\partial t} + U_\infty \frac{\partial Y}{\partial x}, \tag{3.3}$$

$$|v||_{(x,y)=(c,0)} < \infty. \tag{3.4}$$

In the linear setting, the heave and pitch motions are imposed as boundary conditions at the leading edge in the form

$$Y(0,t) = h(t), \tag{3.5}$$

$$\frac{\partial Y}{\partial x}(0,t) = \theta(t). \tag{3.6}$$

Given the deflection Y of the plate, Wu's theory allows us to calculate all of the forces on the plate, the power consumption, and the efficiency; the details are given in Chapter 10. Wu's theory generalizes the linear theory of Chapter 2 to deformable plates. For a passively flexible plate, however, the deflection is unknown *a priori*. Additional information is needed to simultaneously solve for the deflection of the plate and the flow.

Under the assumptions of Wu's linear theory for the flow, the plate deforms according to Euler-Bernoulli beam theory. That is, the transverse deflection of the plate satisfies

$$\rho_s d s \frac{\partial^2 Y}{\partial t^2} + \frac{\partial^2}{\partial x^2}\left(B \frac{\partial^2 Y}{\partial x^2}\right) = s \Delta p, \tag{3.7}$$

where d is the thickness of the plate, $B = EI$ is the flexural rigidity, and the second moment of area is given by $I = sd^3/12$. The left-hand side of the equation describes the solid mechanics, and the right-hand side couples the solid and fluid mechanics through the pressure difference across the plate due to the fluid. (The solid mechanics affect the fluid mechanics through the no-penetration condition (3.3).) Since (3.7) is fourth-order in space, it requires four boundary conditions; two are given by the heave and pitch motions as in (3.5) and (3.6), and two more boundary conditions appropriate for the oscillating plate problem are the 'free-end' boundary conditions,

$$\frac{\partial^2 Y}{\partial x^2}(c,t) = 0, \tag{3.8}$$

$$\frac{\partial^3 Y}{\partial x^3}(c,t) = 0. \tag{3.9}$$

Altogether, we have a coupled system of equations for the linearized fluid-structure interaction problem. This represents the best analytically tractable theory for passively flexible plates oscillating in a fluid. Details of the solution for the general case of a plate with spatially distributed properties are given in Moore (2017) and Chapter 11. Although the assumptions of the theory are restrictive, we will later use the theory to provide some new results.

The theory cannot capture finite-amplitude and viscous effects, however. To get the full picture, we turn to the experimental and computational results. In addition to the dimensionless parameters in (2.23) identified for rigid foils, flexible foils will depend on

$$R = \frac{\rho_s d}{\rho_f c}, \quad S = \frac{E d^3}{\rho_f U_\infty^2 c^3}, \quad \frac{d}{c}, \tag{3.10}$$

where R is the ratio of characteristic solid mass to characteristic fluid mass, S is a ratio of elastic forces to fluid forces, and the other dimensionless parameter is the dimensionless thickness. The dimensionless thickness is usually quite small and can be ignored. In the context of swimming, the mass ratio is small (since the dimensionless thickness is small and swimmers are neutrally buoyant), but it is important in the context of flight. The effects of these dimensionless parameters are explored in the next section.

3.2 Experiments and computations

The same four questions that guided the review of rigid oscillating foils guide this review of flexible foils. The overarching question is how passive flexibility *modifies* the thrust production, power consumption, efficiency, and wake of rigid oscillating foils.

The wake of flexible foils is qualitatively the same as the wake of rigid foils. The foil creates patterns of vortices in its wake whose induced velocities create meandering jets. Since there are no serious differences and the wake is considered a mere footprint in this dissertation, no more will be said about it.

The presence of passive flexibility can qualitatively alter the thrust, power, and efficiency, however. The passive flexibility introduces natural frequencies into the system. When the system is actuated near a natural frequency (when the system is 'in resonance'), the response to the actuation will be large. The deflection sketched in figure 3.2d reflects the type of behaviour seen when the first natural frequency of the system is excited; as higher natural frequencies are excited, the wavelength of the deflection decreases. The enhanced deflection around a natural frequency causes the thrust, power, and efficiency to change as well. The typical view is sketched in figure 3.2, with local maxima arising near natural frequencies.

Thrust has generally been found to benefit from passive flexibility. Increases in thrust have been noted across a wide range of frequencies, from far below the first natural frequency of the system to deep into the region of higher-order natural frequencies (Alben, 2008b; Ferreira de Sousa and Allen, 2011; Dewey et al., 2013; Katz and Weihs, 1978, 1979; Quinn et al., 2014). When the frequency of actuation is near a natural frequency of the system, thrust generally exhibits a local maximum (Alben, 2008b; Dewey et al., 2013; Quinn et al., 2014). The explanation is that when the system is in resonance, the deflection becomes substantial, which leads to greater

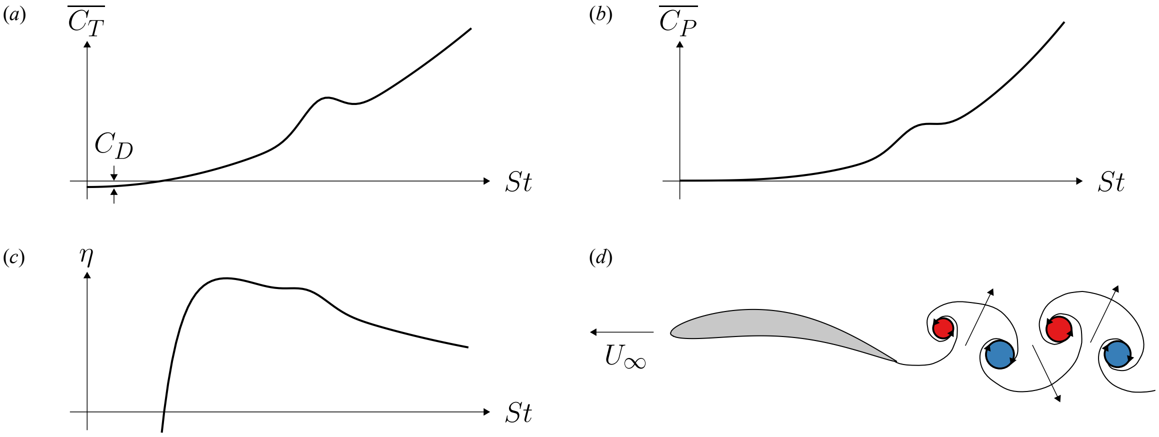

Figure 3.2: Typical (a) thrust curve, (b) power curve, (c) efficiency curve, and (d) wake and deflection for a flexible oscillating foil.

thrust production. Here, a tacit equivalence is made between rigid and flexible foils (recall that rigid foils produce greater thrust when oscillating with larger amplitudes).

The power is similarly affected by the introduction of passive flexibility, at least qualitatively. Although detailed analyses of the power are lacking, the power mostly follows the behaviour of the thrust near and away from natural frequencies, with resonance tending to increase the power consumption, leading to local maxima in power (Alben, 2008b; Ferreira de Sousa and Allen, 2011; Dewey et al., 2013; Kang et al., 2011; Michelin and Llewellyn Smith, 2009).

The behaviour of efficiency is a much trickier issue. On one hand, passive flexibility can increase thrust and therefore efficiency; on the other hand, passive flexibility can increase power and therefore decrease efficiency. Since the boosts in thrust and power occur near each other, it is not immediately clear whether to expect increases or decreases in efficiency.

Studies tend to report that flexibility leads to increases in efficiency. Just as for thrust, increases in efficiency have been observed everywhere from far below the first natural frequency to deep into the region of higher-order natural frequencies (Alben, 2008b; Ferreira de Sousa and Allen, 2011; Dewey et al., 2013; Katz and Weihs, 1978, 1979; Quinn et al., 2014). Unlike the thrust, local maxima in efficiency have been observed below, near, and above natural frequencies (Dewey et al., 2013; Moored et al., 2014; Quinn et al., 2014, 2015; Paraz et al., 2016), as well as at frequencies far from any natural frequency (Ramananarivo et al., 2011; Kang et al., 2011; Vanella et al., 2009; Zhu et al., 2014; Michelin and Llewellyn Smith, 2009). What is the reason for the variety of behaviour reported, and the seeming confusion?

Part of the confusion can be explained by ill-defined natural frequencies. Some studies calculated natural frequencies based on a beam in a vacuum, disregarding the effect of the fluid (Hua et al., 2013; Kang et al., 2011; Vanella et al., 2009). Even in a system without dissipation, the added mass of the fluid alone may significantly alter the natural frequencies, as is nicely shown in Michelin and Llewellyn Smith (2009). In the context of swimming, where the characteristic fluid mass is much greater than the characteristic foil mass, the fluid's effect on the natural frequencies will be significant. In other studies, the added mass of the fluid was mistaken for drag, leading to an incorrect definition of the total mass of the system (Vanella et al., 2009; Combes and Daniel, 2003b). When efficiency and resonance were unrelated, large-amplitude motions were considered, and the nonlinear dynamics at play likely make the linear notion of resonance an inappropriate frame through which to analyze the system.

Nonetheless, the general sentiment in the community is that resonance *should* lead to local maxima in efficiency, because resonance is 'good.' Perhaps the tacit argument made is that resonance takes a given amount of input energy and locally boosts the output. Although intuitive in some way (or at least consistent with observations), this idea is not quite right. After all, resonance also leads to increases in power consumption. This dissertation makes headway in clarifying how resonance and efficiency are related.

In cases where non-resonant boosts in efficiency were observed, physical mechanisms unrelated to fluid-structure resonance were offered. One is the idea of 'wake resonance,' where the fluid itself has some preferred frequency of actuation (this was briefly discussed in Chapter 2) (Moored et al., 2014). Other ideas are offered by Quinn et al. (2015), who argued that peaks in efficiency occur when the Strouhal number is high enough that the flow does not separate but low enough that the shed vortices remain tightly packed, the trailing edge amplitude is maximized while flow remains attached along the body, and the effective angle of attack is minimized. (Note that in these two works, fluid-structure resonance coincided with maxima in efficiency.) Ramananarivo et al. (2011) argued that, in their study, efficiency was maximized by making use of the nonlinear nature of a drag transverse to the direction of travel and when the trailing edge is approximately parallel to the local velocity. In their case, the characteristic fluid and foil masses were of the same order, appropriate for flight but not for swimming.

Modifying how the flexibility is distributed can also modify the propulsive performance. Experiments relevant to the context of swimming have generally shown that concentrating stiffness towards the leading edge enhances thrust and efficiency (Riggs et al., 2010; Lucas et al., 2015; Kancharala and Philen, 2016). It is important to note, however, that these studies did not control for the mean stiffness when changing the distribution, so it is unclear whether the observed effects are due to a changing mean stiffness or a changing distribution of stiffness.

The stiffness distribution is also of interest when the characteristic fluid mass is of the same order as the characteristic foil mass, relevant to flying insects that have veined wings (Combes and Daniel, 2003a). Both Shoele and Zhu (2013) and Yeh et al. (2017) found that a stiffer leading edge lowers and broadens local maxima in thrust, and broadly increases efficiency. Moore (2015) used the linear theory and optimized the stiffness (mean and distribution) for thrust at a fixed frequency, finding that a rigid foil with a torsional spring at its leading edge was optimal. Again, these studies did not control for mean stiffness, so it is unclear how the distribution itself affects the propulsive performance. Chapter 11 addresses this issue.

3.3 New results

Here, new results from this dissertation are summarized. The details are contained in Chapters 10–11.

Since there is apparent confusion about how fluid-structure resonance affects the propulsion of oscillating flexible foils, particularly propulsive efficiency, we study the propulsion of flexible foils in a context where the linear notion of resonance is clear. Namely, we study the linear inviscid model of a passively flexible swimmer from Section 3.1, valid for small-amplitude motions. The frequencies of actuation and stiffness ratios considered span many orders of magnitude, while the mass ratio is fixed to a low value representative of swimmers.

In Chapter 10, we begin by considering foils with uniform flexibility, where the local stiffness along the chord is the same everywhere. The trailing edge deflection shows sharp ridges of resonant behaviour for reduced frequencies $f^* > 1$ and stiffness ratios $S > 1$, as shown in figure 3.3. For $f^* < 1$ and $S < 1$, however, the resonant peaks smear together. Calculating the eigenvalues of the fluid-structure system shows that the sharp ridges of resonant behaviour align with the imaginary parts of the eigenvalues, more commonly referred to as the natural frequencies. We call the Euler-Bernoulli eigenvalues since their behaviour is reminiscent of an Euler-Bernoulli beam in a vacuum. The sharp ridges smear as the eigenvalues dampen. When the ridges are sharp, their locations are predicted quite well by the quiescent eigenvalues, that is, the eigenvalues calculated in the limit where the bending velocity is large compared to the fluid velocity. The thrust coefficient and power coefficient behave the same as the trailing edge deflection, showing sharp resonant ridges at natural frequencies

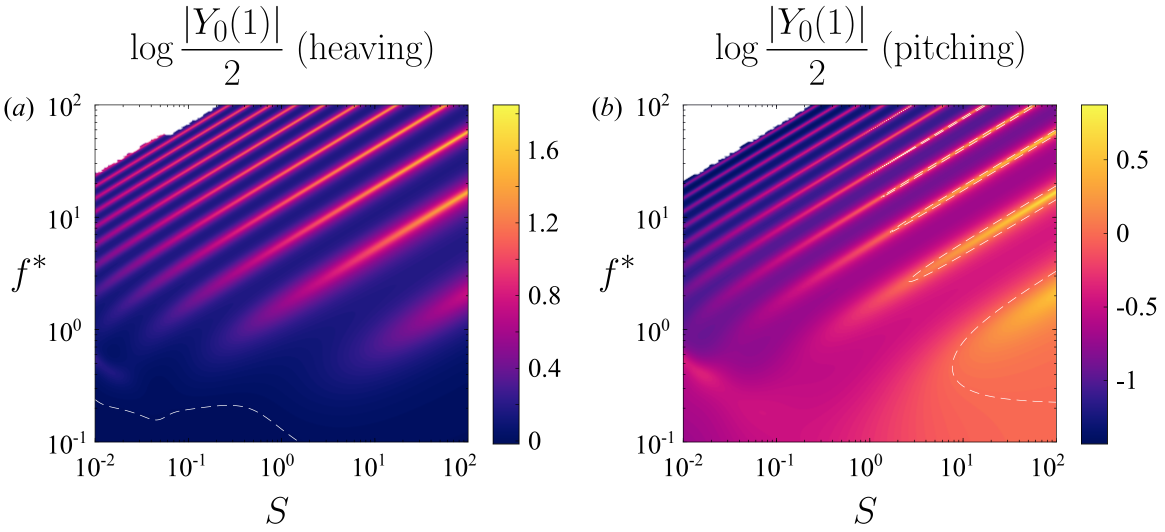

Figure 3.3: Trailing edge amplitude as a function of reduced frequency f^* and stiffness ratio S for a (a) heaving and (b) pitching plate with $R = 0.01$ relative to that of an equivalent rigid plate. Dashed white lines indicate where the flexible plate has the same trailing edge amplitude as the equivalent rigid plate. Under-resolved areas have been whited out. Repeated from figure 10.6.

which smear together at low values of the reduced frequency and stiffness ratio. This behaviour is consistent with the literature.

The efficiency, on the other hand, does not show any resonant behaviour. Rather, the efficiency is broadly high when the reduced frequency and stiffness ratio are low, shown in figure 3.4. This behaviour is not seen in the literature. In the linear inviscid setting, the thrust and power increase by the same factor when the foil is actuated at a natural frequency, the peaks in each nullifying each other, making the efficiency flat across natural frequencies. The region of broadly high efficiency is quite interesting, and it coincides with a different type of eigenvalue. When the stiffness ratio is low enough, the Euler-Bernoulli eigenvalues essentially disappear and are replaced by flutter eigenvalues. The flutter eigenvalues have imaginary parts that increase as the stiffness ratio decreases, and eventually move into the right-half plane where they induce unstable flag flapping behaviour (which is why we call the flutter eigenvalues). Inspecting the associated flutter eigenfunctions, they take on a form

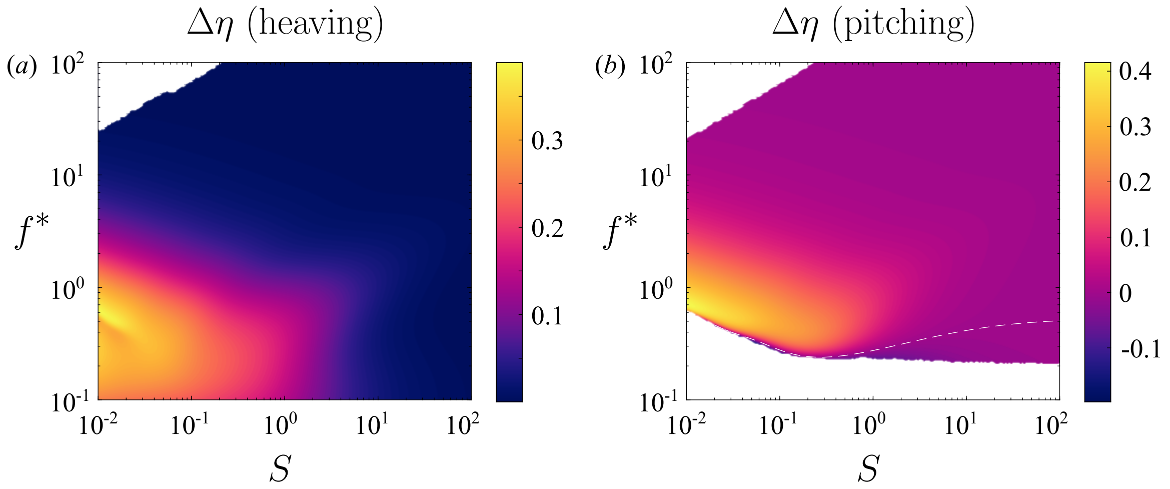

Figure 3.4: Efficiency as a function of reduced frequency f^* and stiffness ratio S for a (a) heaving and (b) pitching plate with $R = 0.01$ relative to that of an equivalent rigid plate. Dashed white lines indicate where the flexible plate has the same efficiency as the equivalent rigid plate. Under-resolved areas and areas with negative efficiency have been whited out. Repeated from figure 10.14.

close to a travelling wave, whereas the Euler-Bernoulli eigenfunctions do not. In the actuated system, cases with high efficiency take on near travelling wave forms, and the degradation of efficiency coincides with the degradation of the travelling wave. Since travelling waves are known to be an efficient set of kinematics (Wu, 1961), we conclude that the emergence of flutter behaviour as the stiffness ratio decreases induces efficient kinematics.

Once we add finite Reynolds number effects into the system in the form of a streamwise drag, resonant peaks in the efficiency emerge that are not present in the inviscid system. In moving from a non-resonant to a resonant condition in a system without drag, the mean thrust and power coefficients effectively scale up by some factor $a > 1$. Since the efficiency is the ratio of the two, the factor a appears in the numerator and denominator, cancels, and there is no resonant peak. When drag is present, it reduces the baseline non-resonant efficiency compared to the system without drag. In moving to a resonant condition, the thrust and power scale up by the factor a, but the drag does not. The net thrust therefore scales up by a factor greater than a, so the efficiency increases at resonance. This effect creates local maxima in efficiency at resonance. Since drag affects the system at first order, this effect of streamwise drag inducing resonant peaks in efficiency should be robust to nonlinearities present at finite amplitudes. Since any real system will have some streamwise drag, resonant peaks should be present, explaining why peaks in efficiency are observed in experiments.

In Chapter 11, we consider the effects of distributed flexibility, where the local stiffness varies along the chord. In order to separate the effects of mean stiffness and stiffness distribution, we use a set of orthogonal polynomials to describe the stiffness distribution. Doing so allows us to independently control the mean stiffness and stiffness distribution, which has not been done before. This ability is important because it allows us to distinguish effects due to distribution from effects due to the mean stiffness. Allowing the stiffness to vary spatially produces no qualitative differences from uniformly flexible foils.

Important quantitative differences do arise, however. Although the mean stiffness is kept constant, varying the spatial distribution of stiffness changes the eigenvalues of the system. To elucidate these differences, we find stiffness distributions that maximize the thrust, minimize the power, and maximize the efficiency. We find that: (1) to maximize thrust, stiffness should be distributed so as to create a natural frequency at the frequency of actuation, or concentrated toward the leading edge if a natural frequency cannot be placed at the frequency of actuation; (2) to minimize power, stiffness should be distributed so as to avoid natural frequencies, or concentrated away from the leading edge; and (3) meaningful gains in efficiency can be made when the stiffness is distributed so as to elicit flutter behaviour, which induces efficient travelling wave kinematics.

Just as a finite Reynolds number produced qualitative changes for uniformly flexible foils, it also does so for foils with distributed flexibility. The thrust-maximizing and power-minimizing stiffness distributions are unchanged, but the presence of streamwise drag will change the efficiency-maximizing distribution to resemble the thrust-maximizing distribution and be dictated by the eigenvalues of the system.

Chapter 4

Conclusion

4.1 Summary

Modelling remains central to understanding the behaviour of natural and artificial swimmers. This dissertation was motivated by wanting to understand the free swimming of full-bodied, three-dimensional swimmers found in nature. Several simplifications were made. First, we distinguished between thrust-producing and drag-producing parts of animals' bodies, focusing on the thrust-producing part (the 'propulsor') in isolation. Such a simplification seems reasonable for the fast and efficient animals of interest here (e.g. tuna), where the propulsor and forebody tend to be distinct, but cannot be made for animals like eels. Second, we ignored all three-dimensional effects, focusing on the two-dimensional problem. Again, such a simplification seems reasonable for the fast and efficient animals of interest here since their propulsors tend to be nearly two-dimensional, and we have already ignored the three-dimensional forebodies in the first simplification. Third, we greatly simplified the fluid mechanics, studying the problem through the lens of scaling laws and linear models. Fourth, we considered propulsors in a 'tethered' configuration, where they are not free to according to the instantaneous forces they feel. In particular, they experience a net streamwise force in the mean.

Have we oversimplified the problem? In some ways, yes, but in the most important ways, probably not (as far as speed and efficiency of propulsion are concerned, that is). The ideas developed in this thesis have been tested and held up against a flurry of experimental data. Furthermore, the behaviour of swimmers in nature seems consistent with our ideas. The third simplification outlined above is therefore acceptable.

The most important ideas to take away from this dissertation are twofold. First, all of the scaling relations and experimental data strongly indicate that the characteristic lateral velocity of the foil, and not the free-stream velocity, is the relevant velocity scale in the problem. This is a departure from the standard thinking; indeed, anonymous reviewers of our papers have expressed great surprise and even incredulity that the forces do not scale with the dynamic pressure. The primacy of the characteristic lateral velocity over the free-stream velocity largely erases any differences between tethered and free swimming, implying that tethered swimming studies can be used to make conclusions about free swimming (so long as the other simplifications outlined above are acceptable). Unsteady streamwise motions of the propulsor will be highly damped when the propulsor is attached to a body (see Chapter 7), so we need not consider their effects. Even if unsteady streamwise motions are present, their effects on mean propulsive performance are miniscule (Van Buren et al., 2018b) (although instantaneous forces will likely be affected). Although not shown in this dissertation, ongoing work suggests that forces on flexible foils also scale with the characteristic lateral velocity of the foil.

The second important takeaway is the importance of drag. For the most part, drag negatively offsets the thrust curve by a modest amount, so it has been dismissed as relatively unimportant in the past. When considering the efficiency, however, the offset in the thrust curve is critically important. The presence of drag creates a peak in efficiency at intermediate Strouhal numbers, a peak that has been hypothesized as being responsible for the constancy of Strouhal numbers observed in steadily cruising swimmers and fliers in nature. The presence of drag is therefore responsible for these biological observations, bringing to a close a 30 years old mystery. When flexible propulsors are considered, the same effect of drag on efficiency is present. Additionally, drag is responsible for creating the resonant peaks in efficiency observed in experiments. In an inviscid setting, no resonant peaks in efficiency are present, but the addition of drag induces such peaks.

4.2 Outlook

In the beginning of this dissertation, we noted four aspects of swimming at which natural swimmers excel: speed, efficiency, maneuverability, and stealth. This dissertation thoroughly covers the first two, but some related questions remain. The most obvious question is whether the scaling analysis can be extended to flexible foils. Early work suggests this is possible. Another question is, what is the role of nonlinearity in the propulsion of flexible foils? The linear analysis in this dissertation reproduces the main qualitative features observed in experiments (once drag is accounted for), but not quantiative features. How do finite amplitudes affect the results? Studies aimed at addressing this question are underway. A related question is, if nonlinearity is important, is it important in the fluid mechanics, the solid mechanics, or both?

The other two aspects of swimming at which natural swimmers excel—maneuverability and stealth—leave many opportunities for future studies. The sounds of swimming fish are non-harmonic with frequencies ranging from 100 Hz to below 10 Hz (Moulton, 1960; Kasumyan, 2008). These sounds are primarily due to near-field displacements and can only be detected over a short range when produced at high intensity (Tavolga, 1971). When studying maneuverability, the whole system will need to be taken into account, that is, the propulsor should not be studied in isolation as it has previously been (Read et al., 2003). The reason is that although the propulsor may be able to generate a large moment if it is sufficiently far from the center of mass of the forebody, simply bending the body will likely produce a moment about the center of mass much more effectively. Once maneuverability of these whole-body swimmers is understood, the tools of model-based control can be effectively used to navigate these swimmers; see Kelly (1998), Kanso and Marsden (2005), and Free and Paley (2018) for some examples. Single-body control will naturally lead to the control of many-body systems.

Part II

Papers

Chapter 5

Overview

Part II of this dissertation contains papers that have either been published or submitted to journals. Some minor differences in format may be present between published papers and the chapters here. The papers are organized into chapters as follows:

- Chapter 6 presents scaling laws for the thrust production, power consumption, and efficiency of rigid foils sinusoidally heaving or pitching while translating in a uniform stream. The scaling laws are validated by experiments and are also shown to be consistent with biological data on swimming aquatic animals.
- Chapter 7 presents experiments on rigid foils intermittently pitching while translating in a uniform stream. The individual bursts of motion are shown to be essentially independent of each other. Furthermore, intermittent motions are shown to be energetically advantageous in certain free-swimming situations, and the scaling laws from Chapter 6 are used to explain the advantages.
- Chapter 8 extends the scaling laws from Chapter 6 to efficient, large-amplitude, simultaneously heaving and pitching motions. The scaling laws are validated by experiments, and implications are drawn for the efficiency in particular.

- Chapter 9 uses the scaling laws from Chapter 8 to explain the observations that many swimming and flying animals cruise with a Strouhal number $0.2 < St < 0.4$.

- Chapter 10 analyzes the deformation, thrust production, power consumption, and efficiency of passively (and uniformly) flexible thin foils sinusoidally heaving or pitching while translating in a uniform stream. The eigenvalues of the coupled fluid-structure system are used to clarify misconceptions about the role of resonance, and some new effects are discovered.

- Chapter 11 extends the analysis from Chapter 10 to foils with distributed flexibility. Optimal distributions of flexibility are sought and understood through the eigenvalues of the coupled fluid-structure system.

5.1 Author contributions

In the following chapters, I designed and performed the research, analyzed the data, and wrote the content. The listed co-authors advised me on aspects of the research, and revised and edited these papers. I outline specific contributions from co-authors below, with unlisted contributions being from myself.

- In Chapter 6, Van Buren helped perform the experiments.

- In Chapter 7, Smits conceived the experiments, and Van Buren wrote part of the introduction, helped perform the experiments, and scaled the forces and power by duty cycle.

- In Chapter 8, Smits suggested investigating the relationship between thrust and efficiency, and Van Buren helped perform the experiments.

- In Chapter 9, Van Buren helped perform the experiments.

- In Chapter 10, Rowley suggested calculating eigenvalues of the coupled fluid-structure system.
- In Chapter 11, Rowley suggested describing the stiffness distributions by Legendre polynomials.

Chapter 6

Scaling the propulsive performance of heaving and pitching foils

Daniel Floryan, Tyler Van Buren, Clarence W. Rowley, and Alexander J. Smits

Appears as Floryan et al. (2017a).

Scaling laws for the propulsive performance of rigid foils undergoing oscillatory heaving and pitching motions are presented. Water tunnel experiments on a nominally two-dimensional flow validate the scaling laws, with the scaled data for thrust, power, and efficiency all showing excellent collapse. The analysis indicates that the behaviour of the foils depends on both Strouhal number and reduced frequency, but for motions where the viscous drag is small the thrust closely follows a linear dependence on reduced frequency. The scaling laws are also shown to be consistent with biological data on swimming aquatic animals.

6.1 Introduction

The flow around moving foils serves as an abstraction of many interesting swimming and flight problems observed in nature. Our principal interest here is in exploiting the motion of foils for the purpose of propulsion, and so we focus on the thrust they produce, and their efficiency.

Analytical treatments of pitching and heaving (sometimes called plunging) foils date back to the early–mid 20th century. In particular, Garrick (1936) used the linear, inviscid, and unsteady theory of Theodorsen (1935) to provide expressions for the mean thrust produced by an oscillating foil, and the mean power input and output. Lighthill (1970) extended the theory to undulatory motion in what is called elongated-body theory. More recently, data-driven reduced-order modelling by, for example, Brunton et al. (2013), Brunton et al. (2014), and Dawson et al. (2015), has extended the range of validity and accuracy of similar models. A drawback of these treatments, however, is that it is often difficult to extract physical insights from them in regard to mean propulsive parameters such as thrust and efficiency.

In this respect, scaling laws can often prove valuable (Triantafyllou et al., 2005). In a particularly influential paper, Triantafyllou et al. (1993) established the importance of the Strouhal number in describing fish-like swimming flows, calling it the "dominant new parameter for fish propulsion" and "the governing parameter of the overall problem." The Strouhal number has since been adopted in nearly all subsequent works as the main parameter of interest (see, for instance, Quinn et al. (2014)), although the reduced frequency is sometimes preferred for foils with significant flexibility (Dewey et al., 2013).

Nevertheless, in conducting extensive experiments on pitching and heaving foils we find that such flows cannot be adequately described using only the Strouhal number or the reduced frequency. For instance, figure 6.1 shows the time-averaged thrust coefficient as a function of Strouhal number for a heaving foil. We see that the ratio

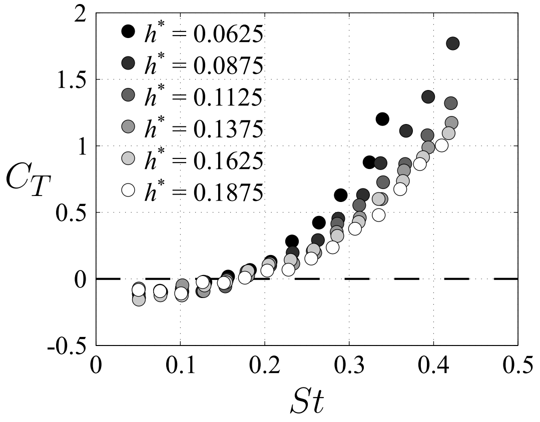

Figure 6.1: Time-averaged thrust coefficient C_T as a function of Strouhal number St for a heaving foil, for various heave amplitude to chord ratios, h^*. Experimental results from the current study. The parameters C_T and St are defined in Section 6.2.

of the heave amplitude to chord, $h^* = h_0/c$, has a significant impact on the thrust generated at a fixed Strouhal number. Here we report these findings, together with a new scaling analysis that helps to explain the experimental propulsive performance of rigid foils undergoing either heaving or pitching motions.

6.2 Scaling laws

Consider a rigid two-dimensional foil moving at a constant speed U_∞ while heaving and pitching about its leading edge. These motions are described by $h(t) = h_0 \sin(2\pi f t)$ and $\theta(t) = \theta_0 \sin(2\pi f t)$, respectively, where h_0 is the heave amplitude, θ_0 is the pitch amplitude, and f is the frequency; see figure 6.2. We are chiefly concerned with the time-averaged thrust in the streamwise direction produced by the foil motion, F_x, and the corresponding Froude efficiency

$$\eta = \frac{F_x U_\infty}{F_y \dot{h} + M\dot{\theta}}, \tag{6.1}$$

where F_y is the force perpendicular to the free-stream and M is the moment taken about the leading edge. This efficiency is the ratio of power output to the fluid to power input to the foil. The relevant dimensionless parameters are

$$St = \frac{2fA}{U_\infty}, \qquad f^* = \frac{fc}{U_\infty}, \qquad A^* = \frac{A}{c}, \tag{6.2}$$

where St is the Strouhal number, f^* is the reduced frequency, A is the trailing edge amplitude of the motion (h_0 for heave, $c \sin\theta_0$ for pitch), and c is the chord length of the foil. Although $St = 2f^*A^*$, we use all three parameters as a matter of convenience. Force and power coefficients are defined by

$$C_T = \frac{F_x}{\frac{1}{2}\rho U_\infty^2 sc}, \qquad C_y = \frac{F_y}{\frac{1}{2}\rho U_\infty^2 sc}, \qquad C_P = \frac{F_y \dot{h} + M\dot{\theta}}{\frac{1}{2}\rho U_\infty^3 sc}, \tag{6.3}$$

where ρ is the density of the surrounding fluid, and s is the span of the foil.

We start with the notion that the forces acting on the foil are due to lift-based mechanisms, added mass effects, and viscous drag. We will assume that over our range of Reynolds numbers the drag coefficient C_D is constant, independent of the amplitude or frequency of the actuation of the foil. This assumption will be justified by reference to the experimental data.

6.2.1 Lift-based forces

The only lift-based forces we consider are those that arise when the foil is at an instantaneous angle of attack to the free-stream given by $\alpha = \theta - \arctan(\dot{h}/U_\infty)$. The effective flow velocity seen by the foil has a magnitude $U_{\text{eff}} = \sqrt{U_\infty^2 + \dot{h}^2}$, and an angle relative to the free-stream velocity of $\arctan(\dot{h}/U_\infty)$. Hence,

$$\left.\begin{aligned} F_x &= -L\sin(\theta-\alpha) = -L\dot{h}/U_{\text{eff}}, \\ F_y &= L\cos(\theta-\alpha) = LU_\infty/U_{\text{eff}}, \end{aligned}\right\} \tag{6.4}$$

where L is the lift on the foil given by $L = \frac{1}{2}\rho U_{\text{eff}}^2 scC_L$, and the lift coefficient $C_L = 2\pi\sin\alpha + \frac{3}{2}\pi\dot{\alpha}c/U_\infty$ (Theodorsen, 1935). The moment about the leading edge is $M = -cL/4$. Note that for a purely pitching foil, quasi-steady lift forces do not produce any thrust. High-frequency and large-amplitude motions will strengthen the nonlinearities in the response; the work of Liu et al. (2014) suggests that this will alter the phase differences between forces and motions. As such, terms that are expected to be 90° out of phase (for example, displacement and velocity, or velocity and acceleration) may develop in-phase components. These phase shifts are assumed to be constant for simplicity.

For heaving motions, neglecting viscous drag, we find

$$\left.\begin{aligned} &C_T \sim 2\pi^3 St^2 + 3\pi^4 St^2\, f^*\, U^*, \\ &C_y \sim 2\pi^2 St + 3\pi^3 St\, f^*\, U^*, \\ &C_P \sim 2\pi^3 St^2 + 3\pi^4 St^2\, f^*\, U^*, \\ &\eta \sim 1, \end{aligned}\right\} \tag{6.5}$$

where $U^* = U_\infty/U_{\text{eff}} = 1/\sqrt{1+\pi^2 St^2}$. Similarly, for small pitching motions,

$$\left.\begin{aligned} &C_T \sim 0, \\ &C_y \sim 2\pi A^* + \tfrac{3}{2}\pi^2 St, \\ &C_P \sim \tfrac{1}{2}\pi^2 St\, A^* + \tfrac{3}{8}\pi^3 St^2, \\ &\eta \sim 0. \end{aligned}\right\} \tag{6.6}$$

In these scaling relations the first term is due to the angle of attack, and the second is due to the rate of change of the angle of attack. The $\sim$ sign indicates a proportionality, and although we expect the relative magnitudes of the first and second terms to be given by the analysis, the absolute magnitudes will need to be found by experiment.

6.2.2 Added mass forces

From Sedov (1965), the added mass forces per unit span on a flat plate are

$$\left.\begin{aligned} &F_t/s = \rho\pi c'^2 V\dot{\theta} - \rho\pi c'^3\dot{\theta}^2, \\ &F_n/s = -\rho\pi c'^2\dot{V} + \rho\pi c'^3\ddot{\theta}, \\ &M/s = \rho\pi c'^3\dot{V} - \tfrac{9}{8}\rho\pi c'^4\ddot{\theta} - \rho\pi c'^2 UV + \rho\pi c'^3 U\dot{\theta}, \end{aligned}\right\} \tag{6.7}$$

where $c' = c/2$, U and V are the instantaneous velocities in the directions tangential and normal to the plate, and subscripts t and n denote the instantaneous forces in the same directions. In our laboratory reference frame

$$\left.\begin{aligned}
F_x/s \;&= \rho\pi c'^2\left(\dot{h}\dot{\theta}\cos\theta - U_\infty\dot{\theta}\sin\theta - c'\dot{\theta}^2\right)\cos\theta\\
&\quad+\rho\pi c'^2\left(\ddot{h}\cos\theta - \dot{h}\dot{\theta}\sin\theta - U_\infty\dot{\theta}\cos\theta + c'\ddot{\theta}\right)\sin\theta,\\
F_y/s \;&= \rho\pi c'^2\left(-\ddot{h}\cos\theta + \dot{h}\dot{\theta}\sin\theta + U_\infty\dot{\theta}\cos\theta + c'\ddot{\theta}\right)\cos\theta\\
&\quad+\rho\pi c'^2\left(\dot{h}\dot{\theta}\cos\theta - U_\infty\dot{\theta}\sin\theta - c'\dot{\theta}^2\right)\sin\theta,\\
M/s \;&= \rho\pi c'^2\Big[c'\left(\ddot{h}\cos\theta - \dot{h}\dot{\theta}\sin\theta - U_\infty\dot{\theta}\cos\theta\right) - \tfrac{9}{8}c'^2\ddot{\theta}\\
&\qquad -\left(U_\infty\cos\theta + \dot{h}\sin\theta\right)\left(\dot{h}\cos\theta - U_\infty\sin\theta\right)\\
&\qquad +c'\left(U_\infty\cos\theta + \dot{h}\sin\theta\right)\dot{\theta}\Big].
\end{aligned}\right\}\tag{6.8}$$

Note that for a purely heaving foil, added mass does not produce any thrust.

For heaving motions, neglecting viscous drag, we find

$$\left.\begin{aligned}
&C_T \sim 0,\\
&C_y \sim \pi^3 St\, f^*,\\
&C_P \sim \pi^4 St^2\, f^*,\\
&\eta \sim 0.
\end{aligned}\right\}\tag{6.9}$$

Similarly, for small pitching motions,

$$\left.\begin{aligned}
&C_T \sim \tfrac{1}{2}\pi^3 St^2 + \pi^2 St\, A^*,\\
&C_y \sim \tfrac{1}{2}\pi^3 St\, f^* + \tfrac{1}{2}\pi^2 St,\\
&C_P \sim \tfrac{9}{32}\pi^4 St^2\, f^* + \tfrac{1}{2}\pi^2 St\, A^*,\\
&\eta \sim \frac{16 + 16\pi f^*}{8 + 9\pi^2 f^{*2}}.
\end{aligned}\right\}\tag{6.10}$$

In these scaling relations, the first term is the absolute added mass term, while the second term is due to being in a rotating frame of reference.

6.2.3 Summary

Combining lift-based and added mass forces, for purely heaving motions we have

$$\left.\begin{aligned} C_T &= c_1 St^2 + c_2 St^2\, f^*\, U^* - C_{Dh}, \\ C_P &= c_3 St^2 + c_4 St^2\, f^* + c_5 St^2\, f^*\, U^*, \\ \eta &= \frac{c_1 + c_2 f^* U^*}{c_3 + c_4 f^* + c_5 f^* U^*}, \end{aligned}\right\} \tag{6.11}$$

where we have included the drag force for heaving motions (C_{Dh}) in the thrust scaling. The expression for the efficiency given here neglects the drag force, and so it should be interpreted as an inviscid scaling result. We will show the effects of viscous drag on the efficiency later in the text.

For purely pitching motions

$$\left.\begin{aligned} C_T &= c_6 St^2 + c_7 St\, A^* - C_{Dp}, \\ C_P &= c_8 St^2 + c_9 St^2\, f^*, \\ \eta &= \frac{1}{f^*}\frac{c_6 f^* + c_7/2}{c_9 f^* + c_8}, \end{aligned}\right\} \tag{6.12}$$

where C_{Dp} is the drag coefficient for pitching motions. The constants c_1 to c_9 will need to be found by experiment. Note that the expressions for efficiency only hold in the limit of negligible drag, so that they represent inviscid estimates.

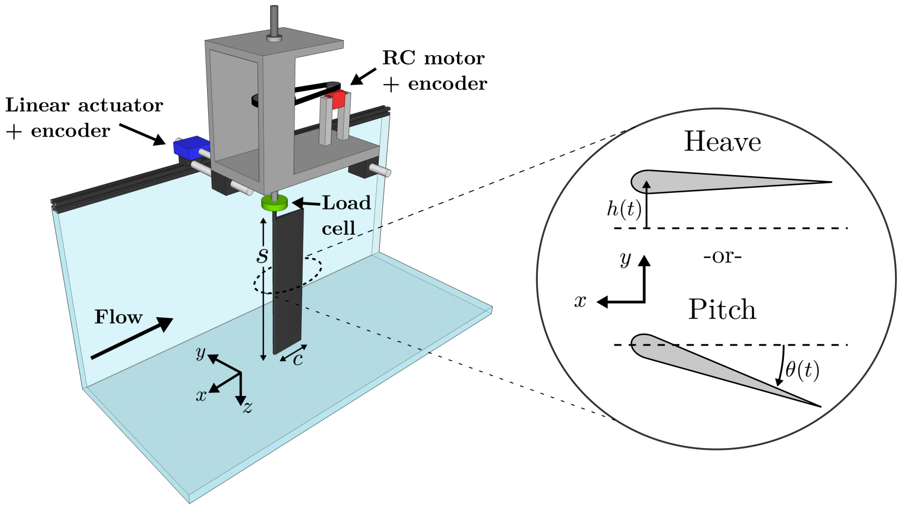

Figure 6.2: Experimental setup and sketch of motions.

6.3 Experimental setup

Experiments on a pitching or heaving foil were performed in a water tunnel. The foil was suspended in a free-surface recirculating water tunnel with a 0.46 m wide, 0.3 m deep, and 2.44 m long test section. The tunnel velocity was varied from 60 to 120 mm/s, with a typical turbulence intensity of 0.8%. A free-surface plate was used to minimize the generation of surface waves. The experimental setup is shown in figure 6.2.

A teardrop foil was used for the experiments, with a chord of $c = 80$ mm, maximum thickness 8 mm, and span $s = 279$ mm, yielding an aspect ratio of $AR = 3.5$ and chord-based Reynolds number of $Re = 4{,}780$ at 60 mm/s. To ensure that the flow was effectively two-dimensional, the gaps between the foil edges and the top and bottom surfaces of the water channel were less than 5 mm. Either pitching or heaving motions were used. A servo motor (Hitec HS-8370TH) was used to pitch the foil about its leading edge, and a linear actuator (Linmot PS01-23x80F-HP-R) was used to heave it on nearly frictionless air bearings (NewWay S301901). The pitch amplitude was varied from $\theta_0 = 3°$ to $15°$ in intervals of $2°$, the heave amplitude was varied from

$h_0 = 5$ mm to 15 mm in intervals of 2 mm, and the frequency of actuation f was chosen so that the Strouhal number varied from $St = 0.05$ to 0.4 in intervals of 0.025 (while maintaining $f < 2$ Hz). Pitch and heave motions were sampled continuously via encoders.

The foil thrust and efficiency were measured using a six-component force and torque sensor (ATI Mini40), which has force and torque resolutions of 5×10^{-3} N and 1.25×10^{-4} N·m in the x- and y-directions respectively, and 10^{-3} N and 1.25×10^{-4} N · m in the z-direction. The force and torque data were acquired at a sampling rate of 100 Hz. During each experimental trial, the motion ran for 30 total cycles: the first five cycles were warm-up cycles, the following 20 cycles were for data acquisition, and the last five cycles were cool-down cycles. Each trial was run at least six times to ensure the repeatability of the data. Altogether, data were acquired for more than 1000 individual experiments.

6.4 Heave results

Time-averaged thrust and power coefficients for the foil in heave are shown in figure 6.3. The data were taken at a fixed velocity of 60 mm/s. Performing a least-squares linear regression, the scaling constants were determined to be $c_1 = 3.52$, $c_2 = 3.69$, $c_3 = 27.47$, $c_4 = 13.81$, $c_5 = 5.06$, and a drag coefficient of 0.15 (see (6.11)). The values of the constants should not be taken to be universal; they are simply the values that work best for our data. The collapse of the data is relatively insensitive to the exact values of some of the constants, but the analysis indicates that each term in the model is of $O(1)$ importance, indicating that the physical mechanisms identified here are significant in explaining the data.

The thrust data collapse well onto a single curve, suggesting that the simplified physics used in our model is sufficient to explain the behaviour of the thrust. As

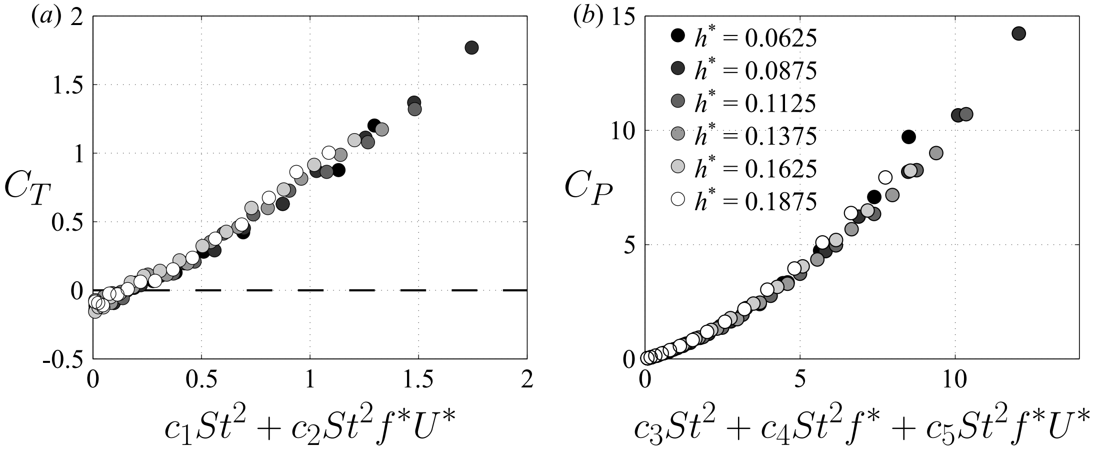

Figure 6.3: Heaving motions. Time-averaged (a) thrust and (b) power coefficients as functions of the scaling parameters (see (6.11)) for various $h^* = h_0/c$.

shown in section 6.2, the St^2 term corresponds to the angle of attack and the $St^2f^*U^*$ term corresponds to the rate of change of angle of attack. We see therefore that the thrust for heaving motions is entirely due to lift-based forces and that the effects of unsteadiness on the mean thrust are well captured by the rate of change of angle of attack.

Likewise, the power data collapse well onto a single curve, although there is some spread in the data for the stronger motions. The angle of attack, the rate of change of angle of attack, and added mass contribute to the power scaling. Power for heaving motions is thus affected by both lift-based and added mass forces, and the essential effects of unsteadiness on the mean power are well captured by the rate of change of angle of attack and added mass. It should be noted that the collapse of the mean power data is relatively insensitive to the values of the constants. The mean power is a weakly nonlinear function of the scaling parameter, suggesting the limits of our model; this is likely caused by the modification of the added mass (Liu et al., 2014).

The efficiency data are given in figure 6.4, presented as a function of Strouhal number (a), and as a function of the reduced frequency (b). For heaving motions, the scaling arguments indicate that the efficiency in the absence of drag should be

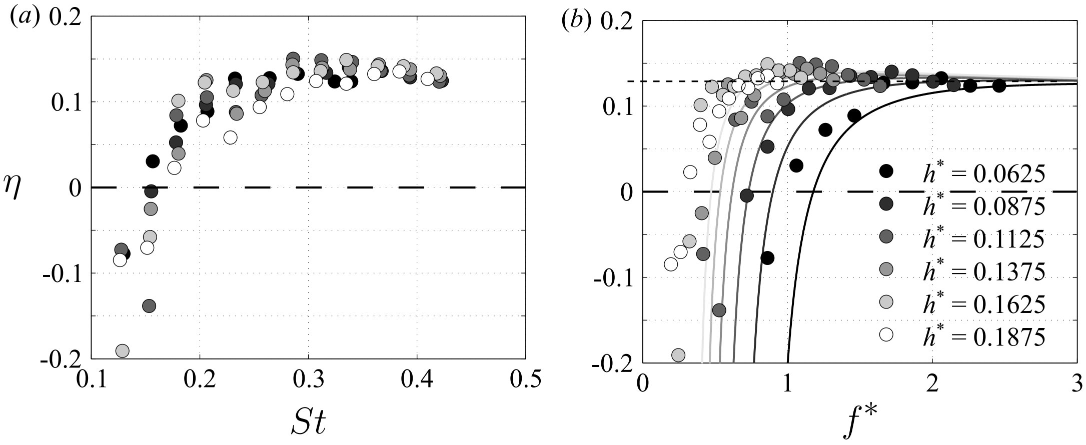

Figure 6.4: Heaving motions. Efficiency as a function of (a) St, and (b) and f^*. Solid lines indicate the scaling given by (6.11); dashed line indicates the scaling with $C_{Dh} = 0$.

approximately constant (for our constants and range of parameters). For higher values of the reduced frequency we observe that the efficiency data approach a constant, marked by a dashed line. The efficiency deviates from this trend for lower values of the reduced frequency and for smaller heave amplitudes due to the viscous drag on the foil. As motions become weaker, they produce less thrust. The drag, however, remains essentially constant. Thus as the motions become weaker, the drag will constitute a larger portion of the net streamwise force, eventually overtaking any thrust produced and leading to a negative efficiency.

6.5 Pitch results

Time-averaged thrust and power coefficients for pitching foils are shown in figure 6.5. The data were taken at a fixed velocity of 60 mm/s. Performing a least-squares linear regression, the scaling constants were determined to be $c_6 = 2.55$, $c_7 = 0$, $c_8 = 7.78$, $c_9 = 4.89$, and a drag coefficient of 0.08 (see (6.12)). Note that the thrust is affected by only the Strouhal number, as seen in previous work (Koochesfahani, 1989). The values of the constants should be interpreted the same was as noted at the beginning

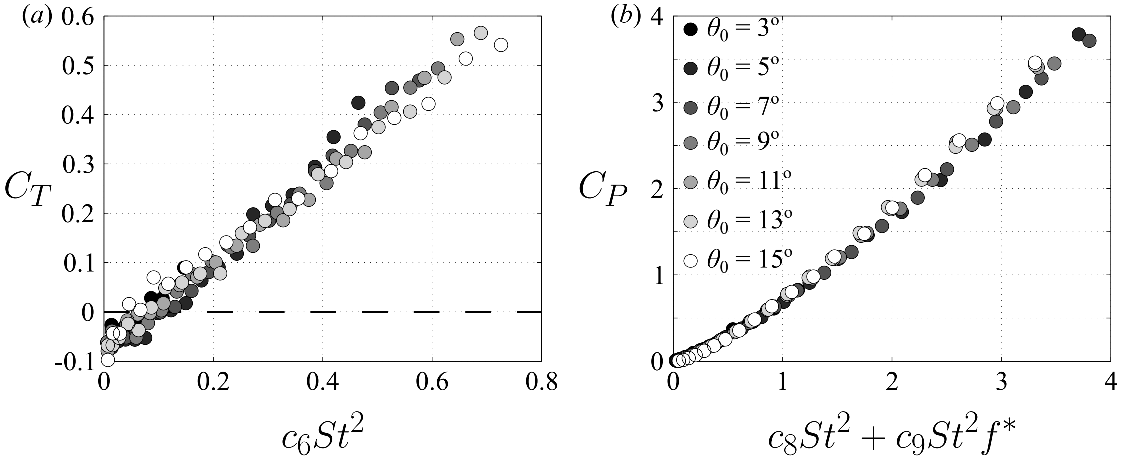

Figure 6.5: Pitching motions. Time-averaged (a) thrust and (b) power coefficients as functions of the scaling parameters (see (6.12)), with $c_7 = 0$.

of Section 6.4. The term multiplied by c_7 is negligible, indicating that it expresses the product of two terms (in this case displacement and velocity) that are 90° out of phase.

The thrust data follow our scaling model well. Although the pitch data are a bit more scattered than the heave data, the collapse is still evident and the thrust coefficient varies linearly with the scaling parameter as expected. As shown in section 6.2, the St^2 term corresponds to added mass, and so the thrust for pitching motions is entirely due to added mass forces, which capture all of the effects of unsteadiness.

The power data also follow our scaling model well. Power in pitch is governed by the rate of change of angle of attack (the St^2 term), and by added mass forces (the $St^2 f^*$ term). These two terms alone capture the essential effects of unsteadiness on the mean power. As found for heaving motions, the mean power for pitch is a weakly nonlinear function of the scaling parameter, indicating the limits of our model.

In figure 6.6 we present the efficiency data as a function of Strouhal number (a), and as a function of the reduced frequency (b). The scaling result in the absence of drag is given by $c_6/(c_8 + c_9 f^*)$ (see (6.12)), shown in the figure by the dashed line. Clearly, the reduced frequency collapses the data for faster motions, whereas the

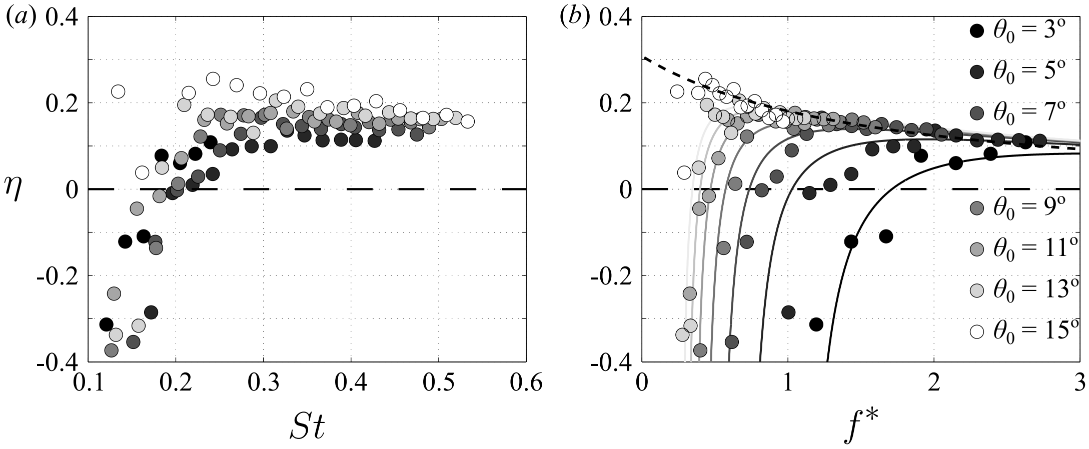

Figure 6.6: Pitching motions. Efficiency as a function of (a) St, and (b) f^*. Solid lines indicate the scaling given by (6.12); dashed line indicates the scaling with $C_{Dp} = 0$.

Strouhal number does not. As found for heaving motions, the pitching data deviate from the scaling for slower motions where viscous drag becomes a significant portion of the net streamwise force. The solid lines show the curve fits after taking the drag into account. The inviscid scaling suggests that in order to maximize efficiency, the reduced frequency should be minimized, but viscous drag begins to be important at some point, and so for maximum efficiency an intermediate reduced frequency is best.

The inviscid scaling for the efficiency can be rewritten as $(c_6/c_9)/(c_8/c_9 + f^*)$. The efficiency curve thus behaves as f^{*-1}, but translated to the left by an amount c_8/c_9. The amount of leftward translation thus depends on the relative strengths of the terms corresponding to the coefficients c_8 (rate of change of angle of attack) and c_9 (added mass). From the perspective of maximizing efficiency, a smaller translation is better (e.g. f^{*-1} without any translation approaches infinity as f^* approaches zero). It is clear that we may alter the amount of translation, and thus the efficiency, by changing the relative strengths of lift-based and added mass forces. This could be achieved, possibly, by adding higher harmonics to the motion. This approach is currently under investigation.

6.6 Rescaling thrust

If we consider motions where the viscous drag term is small, the thrust coefficients for heaving and pitching motions in (6.11)–(6.12) reduce to

$$\begin{aligned} C_{Th} &= c_1 St^2 + c_2 St^2 f^* U^*, & (6.13) \\ C_{Tp} &= c_6 St^2, & (6.14) \end{aligned}$$

respectively, where we have taken $c_7 = 0$ as shown by the data. It is apparent that we may eliminate St from both expressions by rescaling the thrust, reducing the number of necessary scaling parameters. We rewrite the thrust laws as

$$\begin{aligned} C^*_{Th} &= 4c_1 + 4c_2 f^* U^*, & (6.15) \\ C^*_{Tp} &= 4c_6, & (6.16) \end{aligned}$$

where we define a new thrust coefficient

$$C^*_T = \frac{F_x}{\frac{1}{2}\rho f^2 A^2 sc} \qquad (6.17)$$

based on a characteristic velocity scale fA. Since C^*_T does not contain the free-stream velocity U_∞, (6.16) indicates that for pitching motions the dimensional thrust should be independent of the free-stream velocity.

The results, scaled as suggested by (6.15)–(6.16), are shown in figure 6.7. They show that the non-dimensional thrust coefficient C^*_T is indeed a linear function of reduced frequency for heaving motions for large values of f^* (U^* varies only approximately 10% for our data, effectively constant), and a constant for pitching motions.

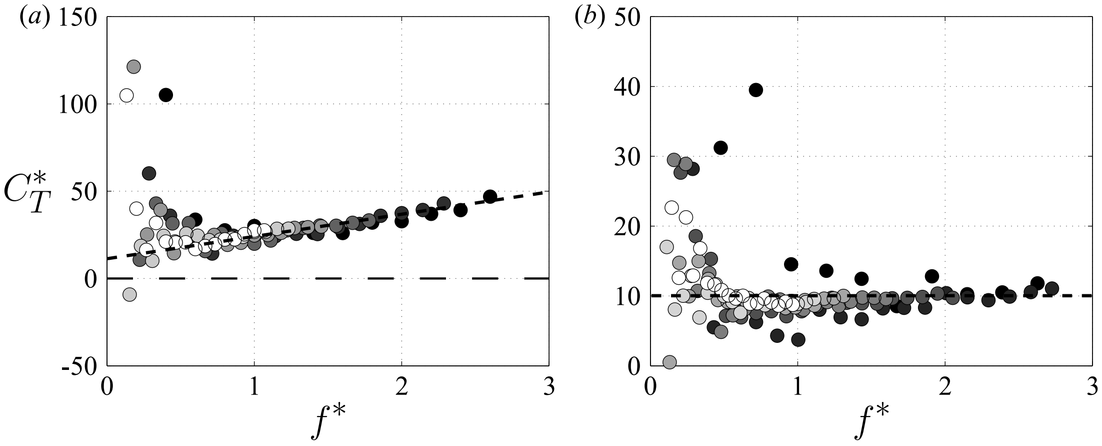

Figure 6.7: Newly non-dimensionalized thrust as a function of reduced frequency for (a) heaving and (b) pitching. (6.15)–(6.16) are shown by the dashed lines. Colours are the same as in figures 6.3 and 6.5.

The experimental results presented thus far have all been taken at a single free-stream velocity. To verify that the thrust results are truly independent of velocity, the velocity was varied from 60 to 120 mm/s. Figure 6.8 shows that the dimensional thrust is independent of free-stream velocity for pitching motions, and only weakly depends on free-stream velocity for heaving motions, confirming our scaling arguments. Although not shown here, we note that the data taken at different velocities follow the scaling laws given by (6.11)–(6.12), with the same values for the coefficients as found in Sections 6.4 and 6.5.

6.6.1 Biological data

It is instructive to test our scaling arguments against biological observations. Figure 6.9 shows fluke-beat frequency and non-dimensional fluke-beat amplitude as functions of length-specific swimming speed for several odontocete cetaceans (Rohr and Fish, 2004). The data indicate that in order to increase their swimming speeds, these cetaceans increase their fluke-beat frequency while maintaining constant fluke-beat

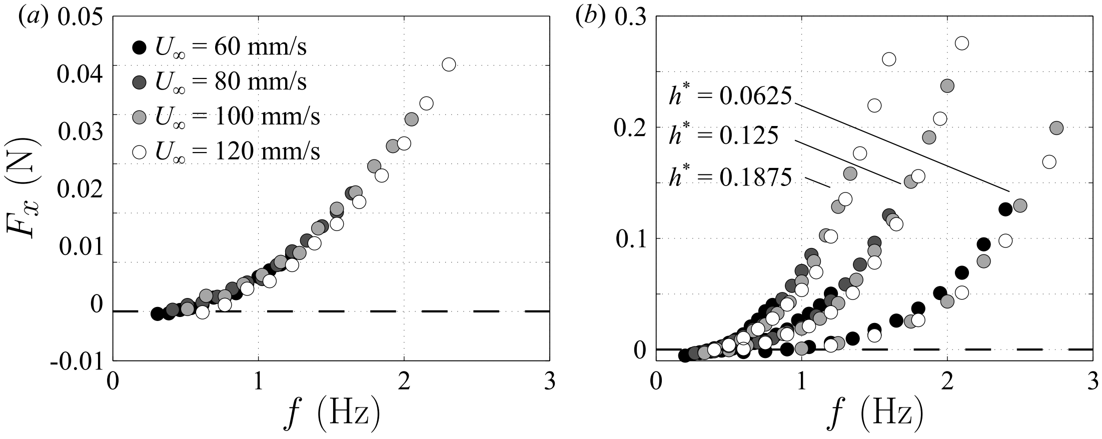

Figure 6.8: Dimensional thrust as a function of frequency at various free-stream velocities for (a) pitching at $\theta_0 = 7°$ and (b) heaving at various $h^* = h_0/c$.

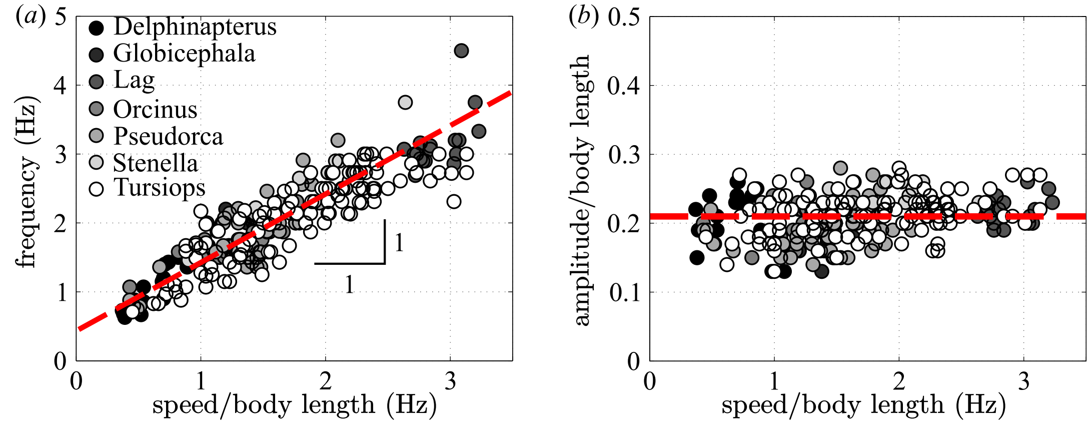

Figure 6.9: (a) Fluke-beat frequency and (b) non-dimensional fluke-beat amplitude as functions of length-specific swimming speed for several odontocete cetaceans. Adapted from Rohr and Fish (2004).

amplitude. In fact, their speeds increase at the same rate as their frequencies. In terms of non-dimensional variables, they are maintaining a constant reduced frequency.

Recall from section 6.2 that our scaling arguments indicate that the efficiency scales with f^{*-1}. Suppose that a swimmer wants to always swim as efficiently as possible. According to our scaling arguments, this corresponds to swimming at the value of reduced frequency which gives the greatest efficiency. Thus as a swimmer changes its speed, it must change its frequency accordingly in order to maintain the same reduced frequency. This is precisely what the biological data show.

6.7 Conclusions

Using only quasi-steady lift-based and added mass forces, new scaling laws for thrust coefficients, side force coefficients, power coefficients, and efficiencies were obtained for a rigid foil undergoing oscillatory heaving and pitching motions. The analysis indicates that the foil performance depends on both Strouhal number and reduced frequency. Water tunnel experiments on a nominally two-dimensional rigid foil showed that the scaling laws give an excellent collapse of the data. Viscous drag was seen to add an approximately constant negative offset to the thrust coefficient, but it causes the rapid decrease in efficiency seen for slower motions (low Strouhal number or small reduced frequency), and our scaling laws captured this behaviour well. For both heaving and pitching motions, the scaling indicates that slower motions lead to greater efficiency, as long as the motions are not so slow that viscous drag becomes a substantial component of the net streamwise force.

Biological observations of the swimming behaviour of odontocete cetaceans were shown to be consistent with our scaling arguments. When these aquatic creatures swim, they change their fluke-beat frequency in order to change their swimming speed while maintaining a constant fluke-beat amplitude. Under the premise of swimming as efficiently as possible, this behaviour of maintaining a constant reduced frequency is consistent with the scaling arguments presented.

Finally, observations of the weak dependence (or even independence) of dimensional thrust on free-stream velocity led to the introduction of a new non-dimensionalization for thrust. The new non-dimensionalization reduces the thrust to only a linear function of reduced frequency for heaving motions, and to a constant value for pitching motions. The experimental data were shown to validate the new scaling, which is independent of Strouhal number.

This work was supported by ONR Grant N00014-14-1-0533 (Program Manager Robert Brizzolara). We would also like to thank Dr. Frank Fish for providing the biological data used in figure 6.9, and Dr. Keith Moored for many useful discussions.

Chapter 7

Forces and energetics of intermittent swimming

Daniel Floryan, Tyler Van Buren, and Alexander J. Smits

Appears as Floryan et al. (2017b).

Experiments are reported on intermittent swimming motions. Water tunnel experiments on a nominally two-dimensional pitching foil show that the mean thrust and power scale linearly with the duty cycle, from a value of 0.2 all the way up to continuous motions, indicating that individual bursts of activity in intermittent motions are independent of each other. This conclusion is corroborated by particle image velocimetry flow visualizations, which show that the main vortical structures in the wake do not change with duty cycle. The experimental data also demonstrate that intermittent motions are generally energetically advantageous over continuous motions. When metabolic energy losses are taken into account, this conclusion is maintained for metabolic power fractions less than one.

7.1 Introduction

Many aquatic animals, such as large sharks and seals (Gleiss et al., 2011) to small schooling fish (Fish et al., 1991), exhibit an intermittent swimming behaviour, sometimes called burst-and-coast swimming. Fish practice intermittent swimming while hunting, fleeing a predator, pursuing a mate, or while starving, and exhibit a wide range of ratios of burst to coast times (Kramer and McLaughlin, 2001). Our primary interest here is to examine the potential energy benefit of intermittent swimming in cruising conditions.

In this respect, Weihs (1974) developed a simple theoretical model and showed that fish could achieve up to 50% savings in energy through intermittent swimming, which was supported by observations on the swimming range of salmon. Videler and Weihs (1982) then found that cod and saithe choose minimum and maximum swimming velocities that match predicted theoretical optima.

The key parameter that differentiates intermittent from continuous swimming in Weihs' model is α, the ratio of drag during active swimming to drag during coasting. The model showed that intermittent swimming is potentially energetically advantageous only for values of $\alpha > 1$. Lighthill (1971) and Webb (1975) noted that the total drag on fish is 3–5 times higher when they are actively swimming than when they do not actuate their bodies, which corresponds to a range of α where intermittent swimming is expected to be energetically advantageous. Lighthill suggested that the drag increases during active swimming due to the thinning of the boundary layer, and so boundary layer thinning may be hypothesized as the mechanism responsible for the energetic benefits of intermittent swimming; we emphasize that this is a viscous mechanism. As the author himself noted, however, this hypothesis was tentative and untested, and more recent work suggests that boundary layer thinning during unsteady swimming motions could lead to only about a 90% increase in drag (Anderson et al., 2001).

Similar simplified hydromechanic approaches were followed by Blake (1983) and Chung (2009), but the main focus of their work was on the impact of the shape of the body of the fish and how to minimize drag, factors that directly impact the energy expenditure of intermittent motions. Numerical simulations by Wu et al. (2007) show similar energetic benefits as the theory.

To understand the consequences of intermittent swimming, we have conducted an experimental investigation of intermittent propulsion by a rigid pitching foil. The performance of pitching and heaving foils in continuous motion is relatively well understood, and Floryan et al. (2017a) recently presented a comprehensive scaling argument that collapses the available data on thrust and power well. In that context, our aim is to understand how intermittent swimming motions affect the forces produced, and the energy expended, and to develop a scaling analysis to describe these changes. We seek to answer three specific questions: (1) do intermittent motions reduce the energy needed to traverse a given distance if metabolic losses are ignored; (2) how does this conclusion change when metabolic energy losses are taken into account; and (3) do intermittent motions reduce the energy needed to traverse a given distance when the average speed is fixed?

7.2 Experimental setup

Experiments were conducted using a rigid pitching foil in a recirculating free-surface water channel, as shown in figure 7.1. The water channel test section is 0.46 m wide, 0.3 m deep, and 2.44 m long. Baffles upstream and downstream of the foil minimized surface waves. The free-stream velocity, U_∞, was fixed at 100 mm/s for performance testing and 60 mm/s for wake measurements.

The propulsor was a two-dimensional teardrop foil with a chord of $c = 80$ mm, maximum thickness of 8 mm, and span of $s = 279$ mm. The performance was

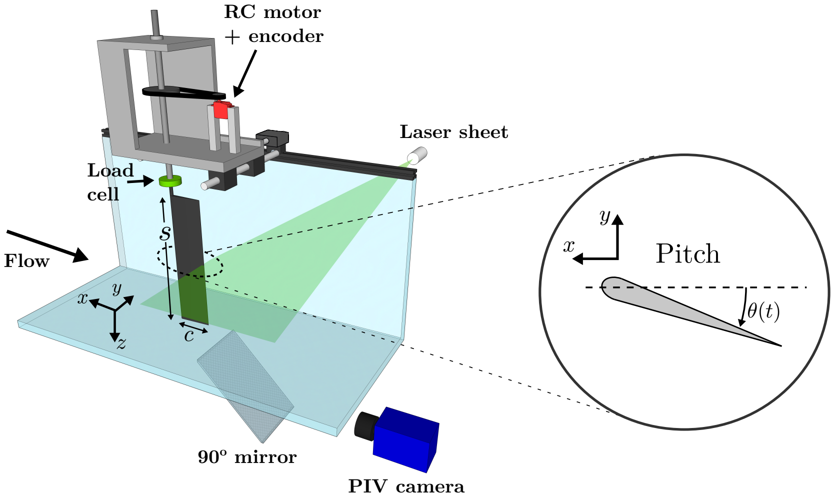

Figure 7.1: Experimental setup.

measured by a six component force/torque sensor (ATI Mini40), with force and torque resolutions of 5×10^{-3} N and 1.25×10^{-4} N·m, respectively. The pitching motions were generated by a servo motor (Hitec HS-8370TH) monitored via a separate encoder. Pitching motions were sinusoidal, and the amplitudes were varied from $\theta_0 = 5°$ to $15°$ every $5°$. For intermittent motions, duty cycles of $\Delta = 0.2$ to 0.9 every 0.1 were explored and compared to continuous motion ($\Delta = 1$). A duty cycle of 0.2, for example, means that the foil completes one full period of pitching, and then stops moving with $\theta = 0$ for a time equal to four periods. The actuation frequency, that is, the frequency of the active portion of the cycle, varied from $f = 0.2$ to 1.5 Hz every 0.1 Hz. This yielded a Strouhal number, $St = 2fc\sin(\theta_0)/U_\infty$, range from 0.05 to 0.4. Each trial consisted of 30 cycles, and the data were averaged over the middle 20 cycles. Each trial was repeated a minimum of three times to ensure repeatability and reduce uncertainty.

The wake velocity measurements were taken at the center-span of the foil with particle image velocimetry (PIV). Silver coated hollow ceramic spheres (Potter Industries Inc. Conduct-O-Fil AGSL150 TRD) were used to seed the flow, illuminated by a CW argon-ion laser (Spectra Physics 2020). An 8-bit monochrome CCD camera (MotionXtra HG-LE) with 1128×752 resolution was used to acquire images at 25 Hz. Images were processed sequentially with commercial DaVis software using spatial correlation interrogation window sizes of 64×64 and twice at 32×32 with 50% overlap. The (cropped) measurement region covered 86 mm in the streamwise direction and 84 mm across, with a resolution of 7 vectors per 10 mm. Average and instantaneous velocity errors are estimated to be 2.7% and 1–5%, respectively (Sciacchitano et al., 2013).

7.3 Forces and power

We begin by considering experiments in which the foil is fixed in the streamwise direction and pitched sinusoidally either continuously or intermittently. The propulsive performance is described using the conventional definitions of thrust and power coefficients, where

$$C_T = \frac{F_x}{\frac{1}{2}\rho U_\infty^2 sc}, \qquad C_P = \frac{M\dot{\theta}}{\frac{1}{2}\rho U_\infty^3 sc}. \tag{7.1}$$

Here, F_x is the streamwise force, M is the spanwise torque, $\dot{\theta}$ is the angular velocity of pitching, and ρ is the fluid density.

In switching from swimming to non-swimming, the form of the transition is important since it has an impact on both the thrust and power, as shown in figure 7.2. We therefore define a smoothing parameter ξ, where $\xi = 0$ is unsmoothed (see inlay of figure 7.2). The waveforms are smoothed via a Gaussian filter, where ξ is the width of the Gaussian kernel relative to the width of the active portion of the wave. As the waveform becomes smoother, the thrust and power decrease because the starting and stopping accelerations decrease. To make comparisons meaningful, we apply a smoothing parameter of $\xi = 0.1$ for all experiments.

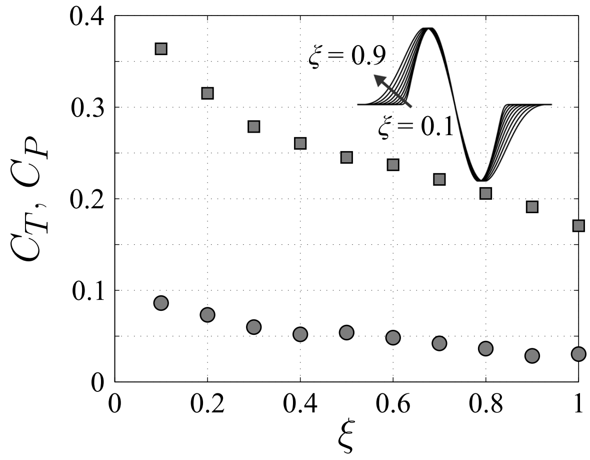

Figure 7.2: Time-averaged thrust (circular symbols) and power coefficients (square symbols) as they vary with smoothing parameter ξ ($\theta_0 = 10°$, $f = 1$ Hz, $\Delta = 0.5$.)

The thrust and power coefficients are shown in figure 7.3 for a range of duty cycles and pitch amplitudes. Both the thrust and power increase nonlinearly with Strouhal number and duty cycle in all cases. In figure 7.4 we show the same results scaled with the duty cycle, which collapses all of the data points onto a single curve. For intermittent motions, it appears to be sufficient to correct the time-averaged force such that the averaging is only done on the active portion of the cycle. This procedure is similar to that used by Akoz and Moored (2017), who scale the thrust for intermittent motions with the frequency of motion, which effectively accounts for duty cycle. This result has the important implication that the thrust and power generated in each actuation cycle can be treated independently. The whole is, indeed, the sum of its parts.

Figure 7.5 shows the instantaneous wake vortex structure at the point in the generation cycle where the primary positive vortex is generated (labeled 1 in each figure). The continuous sinusoidal motion produces a typical thrust-producing “reverse von Kármán vortex street,” generating two opposite-sense vortices per actuation cycle. The intermittent motion, however, produces two primary vortices (1 and 2) and two smaller secondary vortices (1’ and 2’). These secondary vortices are due to the rapid

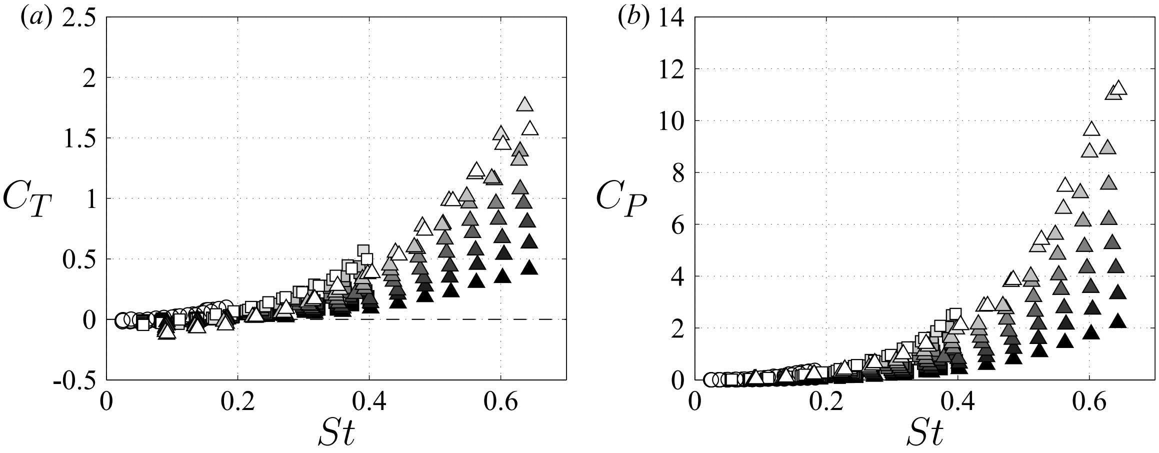

Figure 7.3: Time-averaged (a) thrust and (b) power coefficients as functions of Strouhal number. Dark to light symbols represent increasing duty cycles, ranging from $\Delta = 0.2$ to 1 every 0.1. Symbols identify pitch amplitudes of $\theta_0 = 5°$ (circle), 10° (square), and 15° (triangle).

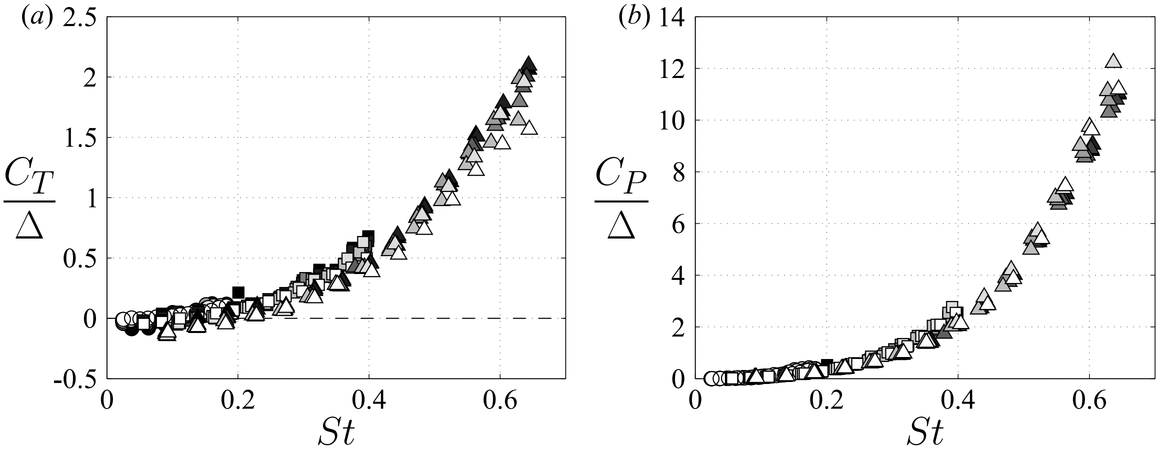

Figure 7.4: Time-averaged (a) thrust and (b) power coefficients normalized by duty cycle as functions of Strouhal number. Symbols and tones as in figure 7.3.

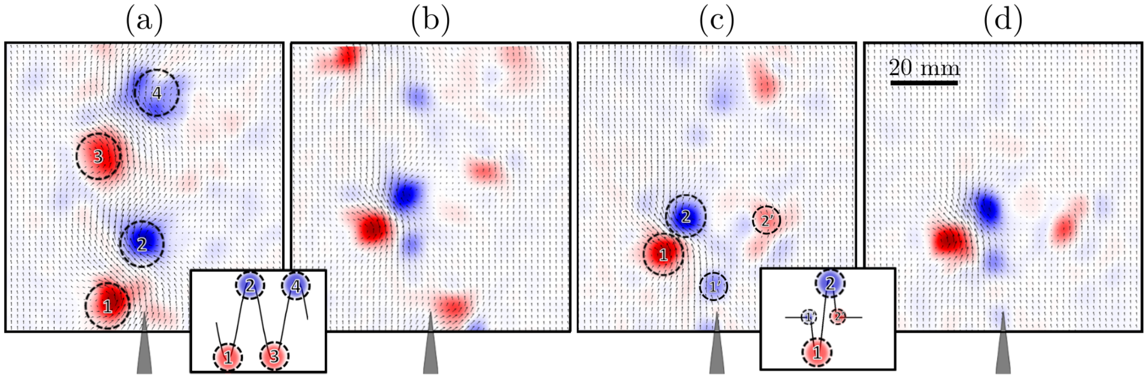

Figure 7.5: Instantaneous wake vorticity with in-plane velocity arrows overlaid for (a) continuous motion, (b) duty cycle of $\Delta = 0.25$, (c) $\Delta = 0.5$, and (d) $\Delta = 0.75$ and a Strouhal number of $St = 0.4$. Small graphics in the bottom right show the pitch angle over time and the generation points of each vortex in the actuation cycle.

start and stop of the intermittent motion. Similar vortex formations have been shown numerically for intermittent motions (Wu et al., 2007) and secondary vortices are also found in rapid starting and stopping square wave motions (Van Buren et al., 2017).

Changing the duty cycle appears to have little effect on the location and strength of the vortices produced per cycle, suggesting that there is minimal interaction between separate cycles. This finding is consistent with the observed scaling of the thrust and power coefficients with the duty cycle.

7.4 Free swimming performance

We now consider a free swimmer, no longer constrained to move at a fixed speed. Its motion is governed by Newton's Second Law

$$m\frac{\mathrm{d}u}{\mathrm{d}t} = T - D, \tag{7.2}$$

where m is the mass, u is the speed, T is the thrust, and D is the drag. We make the assumptions that the swimmer can be effectively split into a drag-producing part

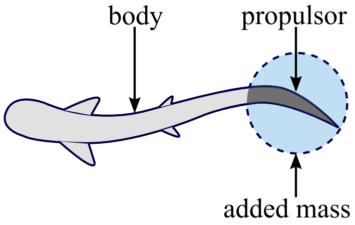

Figure 7.6: A swimmer can be simply represented as a combination of a drag-producing body and a thrust-producing propulsor.

(the body) and a thrust-producing part (the propulsor), as illustrated in figure 7.6, and that these parts are independent of each other.

We further assume a quadratic drag law (White, 2011), such that

$$D = \frac{1}{2}\rho u^2 A_w C_D, \tag{7.3}$$

where ρ is the fluid density, A_w is the wetted area of the body, and C_D is the drag coefficient. We know from Floryan et al. (2017a) that the thrust produced by a pitching foil is independent of the free-stream velocity, so we can assume that the thrust measured from the fixed velocity experiments is the same as what would be measured if the foil were allowed to move. Furthermore, the appropriate velocity scale for a pitching foil is fA, where f is the frequency of the motion, and A is the amplitude of the motion. The non-dimensionalized governing equation is then

$$2\frac{m^*}{A^*}\frac{\mathrm{d}u^*}{\mathrm{d}t^*} = C_T^* - C_D A_w^* u^{*2}, \tag{7.4}$$

where $m^* = m/\rho c^2 s$ is the ratio of the body mass to the propulsor added mass, $A^* = A/c$ is the ratio of the amplitude to the chord, $u^* = u/fA$ is the non-dimensional speed, $t^* = tf$ is the non-dimensional time, $C_T^* = T/\frac{1}{2}\rho(fA)^2 sc$ is the thrust coefficient using the new velocity scale, C_D is the drag coefficient as in (7.3), and $A_w^* = A_w/sc$ is the ratio of the body's wetted area to the propulsor's wetted area. The prefactor

m^*/A^* is the ratio of the body's mass to the mass of the fluid displaced by the propulsor.

We find the mean speed for the free swimmer by inputting the phase-averaged thrust measured in our experiments into (7.4) and solving numerically. We solve using MATLAB's built-in integrator ODE45 (Dormand and Prince, 1980; Shampine and Reichelt, 1997), evolving the system forward until it settles on the limit cycle. The drag coefficient is kept constant at 0.01 (Barrett et al., 1999), A^* varies with the data, and we vary the mass and area ratios over some orders of magnitude.

7.4.1 Results on mean speed

We first compare the calculated mean speed U^*_{mean} to the "steady-state" speed U^*_{steady}, that is, the speed found by setting $\mathrm{d}u^*/\mathrm{d}t^* = 0$ in (7.4) and equating mean thrust to mean drag. The results, plotted in figure 7.7, show that the two speeds are nearly equal. The calculated mean speed falls below the steady value only for small values of the mass ratio m^* and large values of the area ratio A^*_w, which represent unphysical realizations. Points with mean speed greater than the steady speed seem to be spurious.

The relation between the calculated mean and steady speeds can be understood by considering the problem in the frequency domain. Let

$$C^*_T = \sum_n C_n e^{i\omega n t}, \quad u^* = \sum_n u_n e^{i\omega n t} \tag{7.5}$$

be the Fourier series representing the thrust and speed, respectively. Since the thrust and speed are real, we require that $C_{-n} = \overline{C_n}$ and $u_{-n} = \overline{u_n}$, where the overbar denotes the complex conjugate. The equation for the zeroth Fourier mode of speed is then

$$u_0^2 = \frac{C_0}{C_D A^*_w} - \sum_{n \neq 0} u_n \overline{u_n}. \tag{7.6}$$

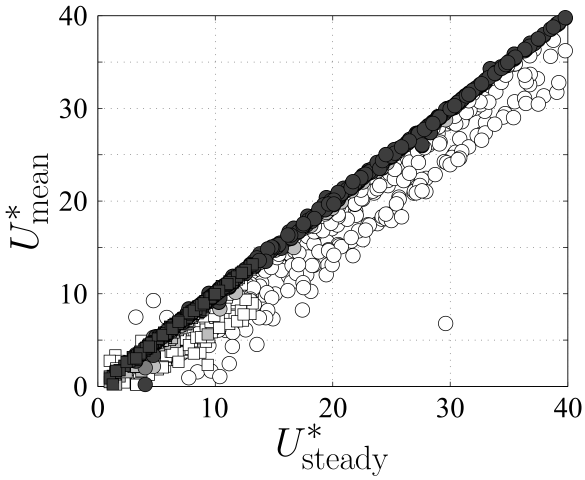

Figure 7.7: Mean speed versus steady speed for all frequencies, amplitudes, and duty cycles. Mass ratios are $m^* = 0.01, 0.1, 1, 10$ (light to dark symbols), and area ratios are $A^*_w = 1$ (circles) and 10 (squares).

We see that the higher harmonics will act to decrease the mean speed. The effects of the mean thrust, drag coefficient, and area ratio on the mean speed are as expected.

To understand the effect of the mass ratio, we linearize (7.4) about the steady speed and take the Laplace transform. The system has a single left-half-plane pole at $-bC_D A^*_w A^*/m^*$, where b is a constant arising from linearization. A greater mass ratio moves the pole closer to the origin, thus attenuating high frequencies. Intuitively, a greater mass ratio corresponds to a swimmer with greater inertia; the greater inertia will cause the speed to fluctuate less about its mean. According to (7.6), the attenuation of high frequencies with greater mass ratio brings the mean speed closer to the steady speed, explaining the observed behaviour.

The effect of the area ratio on the mean speed can be understood in the same way. A smaller area ratio moves the pole closer to the origin, attenuating high frequencies. The mean speed should thus be closer to the steady speed as the area ratio is decreased.

We end by noting that the mean speed only deviates from the steady speed for extreme values of the parameters, unlikely to be encountered in nature, and for low values of the mean speed where experimental errors in our force measurements are relatively large. For a wide range of the parameters, estimating the mean speed to be the steady speed appears to be a reasonable approximation.

7.4.2 Results on energetics

Consider now the energetics of intermittent motions. Given a set of actuation parameters (frequency and amplitude), we would like to know whether changing the duty cycle decreases the energy required to travel a certain distance. This is captured by $\phi = E/E_0$, the ratio of the energy expended by intermittent motion to the energy expended by continuous motion with the same actuation. This energy ratio can be otherwise expressed as

$$\phi = \frac{E}{E_0} = \frac{Pt}{P_0 t_0} = \frac{Pd/U}{P_0 d_0/U_0} = \frac{PU_0}{P_0 U}, \tag{7.7}$$

where P is the mean power, and t is the time taken to travel a distance d at a mean speed U. For the problem considered here, $d = d_0$. Values of $\phi < 1$ indicate that intermittent motions are energetically favourable, whereas values of $\phi > 1$ indicate that intermittent motions are unfavourable.

The results are plotted in figure 7.8. We only use data with $m^* = 1$ and $A_w^* = 10$, as trends should not vary with the mass and area ratios for reasonable values, as found earlier. We see that intermittent motions are almost always energetically favourable compared to continuous motions, with greater energy savings with decreasing duty cycle. We know from section 7.3 that $T \sim T_0 \Delta$ (Δ is the duty cycle), where T is the mean thrust, and the symbol $\sim$ means "proportional to." Similarly, $P \sim P_0 \Delta$. Furthermore, figure 7.7 shows that $U \sim \sqrt{T}$ for a wide range of parameters. The

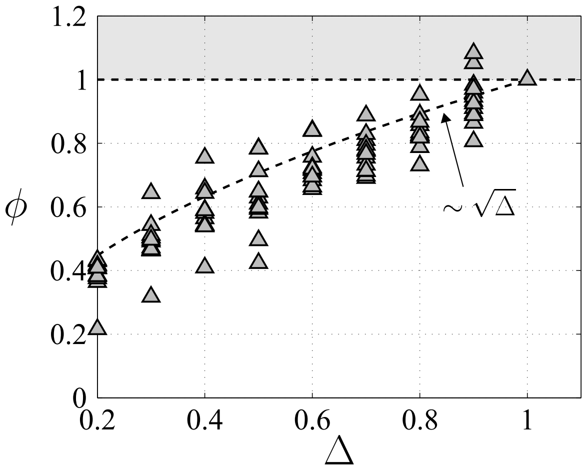

Figure 7.8: Ratio of energy expended by intermittent motions to energy expended by continuous motions as a function of duty cycle for $\theta_0 = 15°$, all frequencies, $m^* = 1$, and $A_w^* = 10$.

energy ratio should then behave according to

$$\phi = \frac{P}{P_0}\frac{U_0}{U} \sim \Delta \frac{1}{\sqrt{\Delta}} = \sqrt{\Delta}. \tag{7.8}$$

Figure 7.8 indicates that the data follow this trend, which is not unexpected: a swimmer in this scenario does not expend any energy during the inactive portion of intermittent motions, but still coasts forward, so that intermittent motions are always energetically favourable.

Apart from energy spent on swimming, aquatic animals also expend energy on metabolic processes. To capture this, we consider the metabolic energy ratio

$$\psi = \frac{E + E_m}{E_0 + E_{m0}}, \tag{7.9}$$

where E_m is the energy spent due to metabolic processes. We will assume that the mean power spent on metabolic processes is the same for continuous and intermittent motion, and that it is a constant fraction c_m of the power lost in continuous swimming,

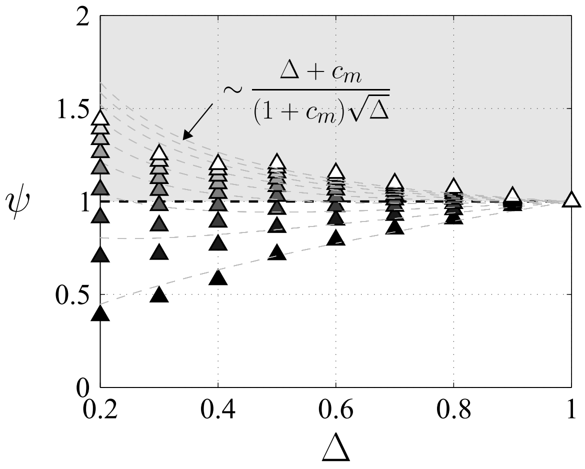

Figure 7.9: Ratio of energy expended by intermittent motions to energy expended by continuous motions, including metabolic energy losses, as a function of duty cycle for $\theta_0 = 15°$, all frequencies, $m^* = 1$, and $A^*_w = 10$. Each point is an average over all frequencies. The colour denotes the value of the metabolic power fraction c_m, 0 to 2 in intervals of 0.25 (dark to light).

P_0. Hence,

$$\psi = \frac{E + E_m}{E_0 + E_{m,0}} = \frac{Pt + c_m P_0 t}{P_0 t_0 + c_m P_0 t_0} = \frac{(P + c_m P_0) d/U}{(1 + c_m) P_0 d_0 / U_0} = \frac{P + c_m P_0}{(1 + c_m) P_0} \frac{U_0}{U}, \qquad (7.10)$$

since $d = d_0$. Values of $\psi < 1$ indicate motions that are energetically favourable. The experimental results are plotted in figure 7.9. We have varied the metabolic power fraction c_m from 0 to 2, typical in biology (Di Santo and Lauder, private communication). With $c_m = 0$ (darkest symbols), the plot is the same as in figure 7.8, indicating that intermittent motions are energetically favourable. As the metabolic power fraction is increased, however, the trend reverses. For large enough values of c_m (approximately bounded by $c_m > 1$), intermittent motions expend more energy than continuous motions, a trend that increases as the duty cycle decreases.

Based on the mean thrust, power, and speed scalings, the metabolic energy ratio should scale as

$$\psi = \frac{P + c_m P_0}{(1 + c_m) P_0} \frac{U_0}{U} \sim \frac{(\Delta + c_m) P_0}{(1 + c_m) P_0} \frac{1}{\sqrt{\Delta}} = \frac{\Delta + c_m}{(1 + c_m)\sqrt{\Delta}}. \tag{7.11}$$

From figure 7.9 we see that the data and the scaling tell the same story: even though intermittent motions expend less energy on swimming, the metabolic losses can play a significant role because intermittent motions take more time to traverse a given distance than continuous motions. The extra time to travel will increase the metabolic energy losses, and this effect may dominate the benefits gained in swimming energy losses.

Another comparison we can make is to consider the energy ratio ϕ, but restrict ourselves to motions which produce the same mean speed, that is, $\phi|_{U_{\text{mean}}}$. For example, it may be that a continuous motion produces the same mean speed as an intermittent motion with a duty cycle of 0.5 actuating at twice the frequency, but which motion expends more energy? The answer to this question will reveal which gait is best if a swimmer wants to traverse a given distance in a given amount of time. The results are plotted in figure 7.10. Interestingly, it appears that intermittent motions continue to be energetically favourable with the added time restriction. Energetically optimal duty cycles exist, and savings are greater for lower speeds, at least for the data considered here. Despite having to increase the frequency of actuation in order to match the mean speed of continuous motions, intermittent motions are nevertheless energetically favourable in this context.

We can understand this behaviour by using the scaling relations obtained here and in previous work (Floryan et al., 2017a). The thrust coefficient approximately follows

$$\frac{C_T}{\Delta} \sim c_1 St^2 - C_{D,u}, \tag{7.12}$$

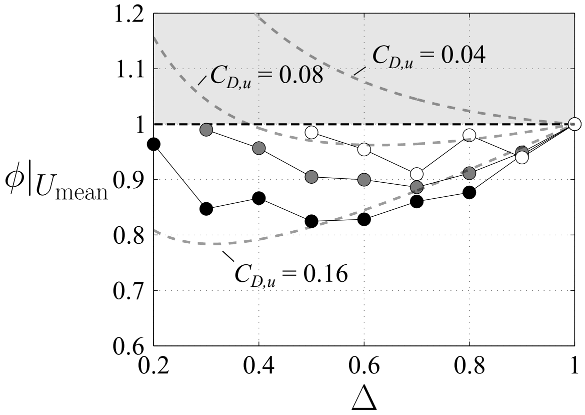

Figure 7.10: Ratio of energy expended by intermittent motions to energy expended by continuous motions, restricted to equal mean speeds, as a function of duty cycle for $\theta_0 = 15°$. Dashed lines correspond to (7.18), with $m^* = 1$, $A_w^* = 10$. The symbol grey scale corresponds to three values of (dimensional) mean speed chosen, $U_{\mathrm{mean}} = 0.2, 0.25, 0.3$ (dark to light). The frequency of the intermittent motion was chosen so that it would have a speed equal to the continuous motion.

where $C_{D,u}$ is the offset of the thrust curve. Similarly, the power coefficient approximately follows

$$\frac{C_P}{\Delta} \sim St^3. \tag{7.13}$$

Note that this relationship is different than given in Floryan et al. (2017a), but it fits our data almost as well and is more convenient for our purposes here. Solving for the power gives

$$P \sim \Delta \cdot f^3 A^3 \rho sc = \Delta \cdot \left(\frac{2T}{\Delta \cdot \rho sc} + C_{D,u} U^2 \right)^{3/2} \rho sc. \tag{7.14}$$

As shown earlier, the mean speed can be estimated well by equating the mean thrust of the propulsor to the mean drag of the body, so that

$$T = D = \frac{1}{2} \rho U^2 A_w C_D. \tag{7.15}$$

The power then becomes

$$P \sim \Delta \cdot U^3 \left(\frac{1}{\Delta} \frac{A_w}{sc} C_D + C_{D,u} \right)^{3/2} \rho sc. \tag{7.16}$$

In this case, the energy ratio between intermittent and continuous motions is

$$\phi|_{U_{\text{mean}}} = \frac{E}{E_0} = \frac{Pt}{P_0 t_0} = \frac{P}{P_0}, \tag{7.17}$$

since $t = t_0$. Hence,

$$\phi|_{U_{\text{mean}}} \sim \frac{\Delta \cdot \left(\frac{1}{\Delta} A_w^* C_D + C_{D,u}\right)^{3/2}}{\left(A_w^* C_D + C_{D,u}\right)^{3/2}}. \tag{7.18}$$

For the cases analyzed here, we chose $A_w^* = 10$ and $C_D = 0.01$. This expression is plotted in figure 7.10 for $C_{D,u} \in \{0.04, 0.08, 0.16\}$ (for our data, $C_{D,u} = 0.08$). Note that the energy ratio is quite sensitive to the value of $C_{D,u}$. The expression is in qualitative agreement with the data, having a U-shape and indicating that there may be a particular duty cycle which is optimal.

7.5 Conclusions

The forces and energetics of intermittent swimming motions, characterized by the duty cycle, were analyzed and compared to continuous swimming. Water tunnel experiments on a nominally two-dimensional rigid foil pitching about its leading edge showed that mean thrust and power increased with increasing duty cycle, all the way up to continuous motion. The mean thrust and power data for different duty cycles were collapsed by dividing the mean thrust and power by the duty cycle, indicating that thrust and power in one burst cycle are not affected by the previous burst cycle. PIV measurements of the wake showed that the dominant structures shed into the wake were always counter-rotating pairs of vortices, regardless of the duty cycle. The PIV measurements corroborated the assertion that individual cycles of activity are unaffected by previous cycles.

Free swimming speed and energetics were analyzed by numerically integrating the measured experimental data. Although the experimental data was acquired for a foil moving at a constant speed, previous work showed that the thrust produced by a pitching foil is independent of speed so we expect that the thrust measured in stationary experiments would be the same as what would be measured in free swimming experiments. For a large range of area and mass ratios, the mean speed was then found to be the same as what would be calculated by assuming a constant speed and equating mean thrust with mean drag. The mean speed was lower than this steady speed only for parameters unlikely to be encountered in nature, indicating that the constant steady speed is a good approximation to the mean speed.

The energetics of intermittent motions were then compared to continuous motions according to three criteria: (1) energy expended in traversing a given distance; (2) energy expended in traversing a given distance, including metabolic energy; and (3) energy expended in traversing a given distance in a given time. Intermittent motions were generally energetically favourable as no energy is spent during the inactive portion of the motion where the swimmer still coasts forward. When metabolic energy losses were added, they could be high enough to make continuous swimming energetically advantageous.

The assertion that forces are unaffected by speed for pitching motions, shown in a previous study, was instrumental in being able to use the stationary experiments in the free swimming analysis. Although the forces produced by general motions (for example, combinations of pitch and heave) will depend on the speed, this work nonetheless highlights the potential benefits and pitfalls of intermittent motions as a swimming protocol.

This work was supported by ONR Grant N00014-14-1-0533 (Program Manager Robert Brizzolara). We would also like to thank Dr. Keith Moored for stimulating our interests in intermittent swimming.

Chapter 8

Large-amplitude oscillations of foils for efficient propulsion

Daniel Floryan, Tyler Van Buren, and Alexander J. Smits

Appears as Floryan et al. (2019).

Large-amplitude oscillations of foils have been observed to yield greater propulsive efficiency than small-amplitude oscillations. Using scaling relations and experiments on foils with peak-to-peak trailing edge amplitudes of up to two chord lengths, we explain why this is so. In the process, we reveal the importance of drag, specifically how it can significantly reduce the efficiency, and how this effect depends on amplitude. The scaling relations and experimental data also reveal a fundamental tradeoff between high thrust and high efficiency, where the drag also plays a crucial role.

8.1 Introduction

The propulsive performance of two-dimensional heaving and pitching foils was first considered by Garrick (1936), using Theodorsen's aerodynamic analysis (Theodorsen, 1935). The theory assumes that the amplitudes of motion are small (allowing for linearization of the governing equations), and that the fluid is inviscid everywhere except in an infinitesimally thin rectilinear vortex wake shed from the trailing edge of the foil. As Garrick himself put it, the assumptions of the theory make it so that "[q]uantitative agreement with experimental values [...] can hardly be expected" (Garrick, 1936). The requirement of small amplitudes seems particularly restrictive in the context of underwater propulsion, in that Scherer surmised that "[i]n order to achieve practical levels of thrust such an oscillating foil must undergo large amplitude oscillations at relatively high frequency," rendering the classical small-amplitude theory inapplicable (Scherer, 1968). Here, we are interested in maintaining high levels of thrust and efficiency simultaneously, partly motivated by Van Buren et al. (2018a), and we explore how large-amplitude motions can be incorporated in theory and how theory compares to experiment.

In this respect, Chopra (1976) extended the two-dimensional inviscid theory to large-amplitude motions, although the amplitudes were implicitly bounded by the assumption of small effective angles of attack. Chopra found that large amplitudes accompanied by small angles of attack and small reduced frequencies produced high efficiency but low thrust, while increasing the angle of attack and the reduced frequency enhanced thrust but diminished efficiency. Efficiencies over 0.8 and even 0.9 were easily attained according to his inviscid theory, but no experimental verification was presented.

In an influential experiment, Anderson et al. (1998) measured efficiencies of up to 0.87 in their large-amplitude experiments, attributing the high efficiencies to optimal wake formation (corresponding to a relatively narrow range of Strouhal numbers) and favourable leading edge vortex dynamics. We note, however, that the flow visualization used to capture the favourable leading edge vortex dynamics was performed at a Reynolds number of 1,100, whereas the propulsive measurements were performed at

Study	Anderson et al. (1998)	Read et al. (2003)	Schouveiler et al. (2005)
η range	0.77–0.83	0.55–0.56	0.53–0.61

Table 8.1: Ranges of efficiency η reported in different works under nominally identical conditions and in the same facility. Kinematic parameters are $h_0/c = 0.75$, $\alpha_{\max} = 20°$, $\phi = 270°$, and $St_h = 2fh_0/U_\infty \in [0.25, 0.4]$ (definitions given in Section 8.2).

a Reynolds number of 40,000, casting doubt on whether the same favourable leading edge vortex dynamics persist at the higher Reynolds number where the efficiency was measured. Indeed, computational investigations of similar motions have shown that the production of leading edge vortices is detrimental to efficiency, and optimal (in terms of efficiency) motions steer clear of generating leading edge vortices (Tuncer and Kaya, 2005; Young et al., 2006; Young and Lai, 2007). Furthermore, subsequent work by the same experimental group using the same experimental setup produced significantly different efficiencies at identical motions, as shown in table 8.1 (Read et al., 2003; Schouveiler et al., 2005). Even the latter two works disagree, especially regarding the Strouhal number corresponding to peak efficiency ($St_{\eta_{\max}} = 0.16$ versus $St_{\eta_{\max}} = 0.25$).

In what follows, we aim to provide a consistent framework through which the high-efficiency propulsion of large-amplitude heaving and pitching rigid foils can be understood, including reasons for *why* large-amplitude motions should be pursued to begin with. We test our ideas against experimental measurements of (old) small-amplitude motions and (new) large-amplitude motions, and explain the measurements by a scaling theory. Finally, we use the scaling theory to provide a path forward for improving the propulsive performance of oscillating propulsors.

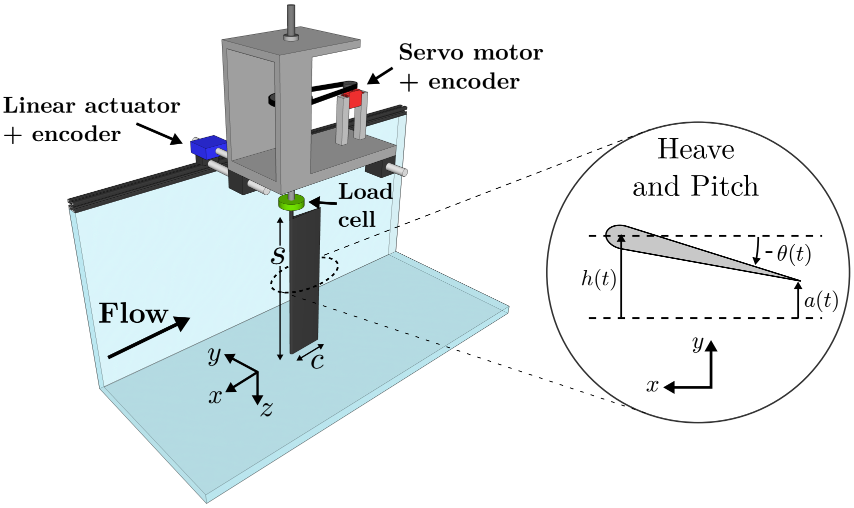

Figure 8.1: Experimental setup and sketch of motions.

8.2 Problem description and motivating analysis

Consider a rigid two-dimensional foil moving at a constant speed U_∞ while heaving and pitching about its leading edge. These motions are described by $h(t) = h_0 \sin(2\pi f t)$ and $\theta(t) = \theta_0 \sin(2\pi f t + \phi)$, where h_0 is the heave amplitude, θ_0 is the pitch amplitude, f is the frequency, t is time, and ϕ is the phase difference between the motions; see figure 8.1. We are chiefly concerned with the time-averaged thrust in the streamwise direction produced by the foil, $\overline{F_x}$, the time-averaged power consumed, $\overline{P}$, and the corresponding Froude efficiency η, defined in terms of dimensionless thrust and power coefficients as follows:

$$C_T = \frac{\overline{F_x}}{\frac{1}{2}\rho U_\infty^2 sc}, \qquad C_P = \frac{\overline{F_y \dot{h} + M\dot{\theta}}}{\frac{1}{2}\rho U_\infty^3 sc}, \qquad \eta = \frac{C_T}{C_P}, \tag{8.1}$$

where ρ is the density of the surrounding fluid, s is the span of the foil, c is its chord length, F_y is the force perpendicular to the free-stream and M is the moment about the leading edge. The efficiency measures the ratio of the power output to the fluid to the power input to the foil. We further define the dimensionless amplitude $A^* = A_0/c$, where A_0 is the amplitude of motion of the foil trailing edge, taken to be half of the peak-to-peak excursion of the trailing edge. The leading edge of the foil sees a local effective angle of attack

$$\alpha \equiv -\theta - \arctan(\dot{h}/U_\infty), \tag{8.2}$$

defined such that a positive constant value of α yields positive lift in our coordinate system. Note that different points along the foil see different local effective angles of attack due to the rotational motion. We also define the dimensionless frequencies

$$f^* = \frac{fc}{U_\infty}, \qquad St = \frac{2fA_0}{U_\infty}, \tag{8.3}$$

where f^* is the reduced frequency, and St is the Strouhal number based on trailing edge amplitude. The Strouhal number may be interpreted as the ratio of the characteristic trailing edge velocity to the free-stream velocity. Although these dimensionless parameters are not all independent ($St \equiv 2f^*A^*$, for example), they are introduced as a matter of convenience.

The results in the literature point towards using large-amplitude motions to attain high efficiency, but do not explain why they are efficient. To motivate the use of large-amplitude motions, we borrow the analysis of Alexander (2003). Suppose (in a time-averaged sense) a foil accelerates fluid in its wake to a speed u_w at a mass flow rate $\dot{m}$. By action/reaction, the thrust generated is then

$$F_x = \dot{m}u_w. \tag{8.4}$$

Notice that a given quantity of thrust can be produced in many ways; for example, accelerating a large mass of fluid to a low speed can produce the same thrust as accelerating a small mass of fluid to a high speed. We illustrate this schematically in figure 8.2.

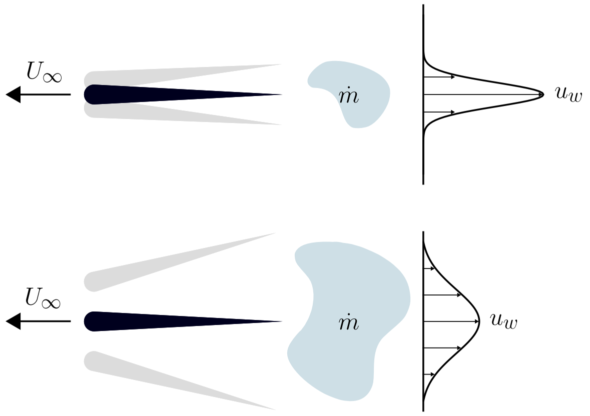

Figure 8.2: An illustration of two motions that produce the same thrust. Velocity profiles are shown in the frame of reference where the fluid at infinity is at rest.

Now consider the energetics of the process. Work is done to push the swimmer forward with thrust F_x and speed U_∞ at a rate

$$\dot{W} = F_x U_\infty = \dot{m} u_w U_\infty. \tag{8.5}$$

Energy is also expended in increasing the kinetic energy of the fluid in the wake at a rate

$$\dot{E}_w = \tfrac{1}{2} \dot{m} u_w^2. \tag{8.6}$$

The efficiency is then

$$\eta = \frac{\dot{W}}{\dot{W} + \dot{E}_w} = \frac{1}{1 + \frac{1}{2} u_w / U_\infty}. \tag{8.7}$$

According to this analysis, the greatest efficiency is attained when the wake velocity u_w is minimized. To produce a given quantity of thrust most efficiently, we must decrease u_w as much as possible while proportionately increasing $\dot{m}$. We will test this hypothesis by experiment on foils heaving and pitching over a large range of motion amplitudes.

These results can also be tested against the scaling laws proposed by Van Buren et al. (2018a). We restrict ourselves to the case of $\phi = 270°$, so that we adopt the simplified scaling relations for thrust and power given by Floryan et al. (2018), that is,

$$C_T + C_D \sim St^2, \tag{8.8}$$

$$C_P \sim f^* St^2 (1 - H^* \Theta^*), \tag{8.9}$$

where $\sim$ denotes a proportionality, and $H^* = h_0/A_0$ and $\Theta^* = c \sin\theta_0 / A_0$. Also, C_D is the drag offset determined by measuring the thrust as the Strouhal number goes to small values. Van Buren et al. (2018a) found that C_D varied linearly with the pitch amplitude, $C_D \sim A^*_\theta = \sin\theta_0$, suggesting that the drag behaves as that on a flat plate with frontal area proportional to the pitch amplitude. Hence,

$$\eta \sim \frac{A^*(St^2 - c_1 A^*_\theta)}{St^3 (1 - H^* \Theta^*)}. \tag{8.10}$$

The constant c_1 sets the level of the drag relative to the thrust. We note that these relations were derived under the assumption of small motions. In particular, they do not consider the effects of leading edge flow separation.

8.3 Experimental setup

Experiments on a heaving and pitching foil were performed in a free-surface recirculating water tunnel with a 0.46 m wide, 0.3 m deep, and 2.44 m long test section. The tunnel velocity was set to $U_\infty = 0.1$ m/s, and a free-surface plate was used to minimize the generation of surface waves. The experimental setup is shown in figure 8.1.

A teardrop-shaped foil of chord length $c = 80$ mm, maximum thickness 8 mm, and span $s = 279$ mm was used, yielding an aspect ratio of 3.5 and chord-based Reynolds number of $Re = 8{,}000$. To ensure that the flow was effectively two-dimensional, the

Set	h_0 (mm)	θ_0 (degrees)	f (Hz)	ϕ (degrees)
1	10: 10: 30	5: 5: 15	0.2: 0.1: 0.8	270
2	40: 10: 60	25: 5: 40	0.2: 0.05: 0.8	270

Table 8.2: Motion parameters (start: step: end).

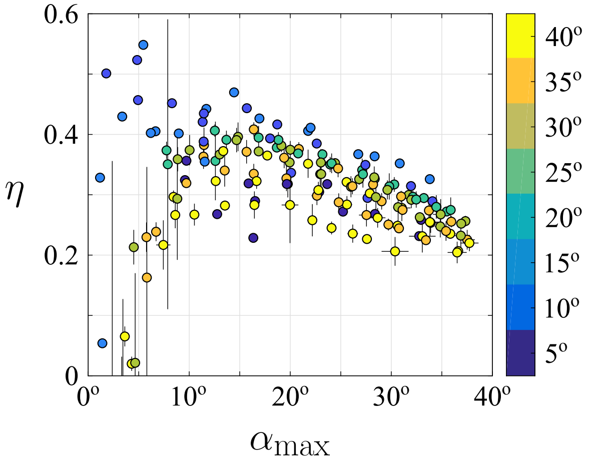

Figure 8.3: Efficiency as a function of maximum angle of attack at the leading edge for our data. Colour indicates pitch angle (in degrees).

gaps between the foil edges and the top and bottom surfaces of the water tunnel were less than 5 mm, effectively increasing the aspect ratio. Heave motions were generated by a linear actuator (Linmot PS01-23x80F-HP-R) pushing a carriage holding the foil on nearly frictionless air bearings (NewWay S301901), and pitch motions about the leading edge were generated by a servo motor (Hitec HS-8370TH). Both motions were measured via encoders. Two sets of motions were used (see table 8.2): a subset of the motions from Van Buren et al. (2018a) (set 1); and a new set of motions with larger amplitudes (set 2). We restrict ourselves to motions with $\phi = 270°$ because these have repeatedly been shown to be the most efficient (several of the references in the present work have made this observation). Motions with a nominal maximum angle of attack at the leading edge $\alpha_{\max} > 35°$ were removed from the experimental program, since large angles of attack are known to be detrimental to efficiency; see figure 8.3.

The forces and moments on the foil were measured using a six-component force and torque sensor (ATI Mini40), which has force and torque resolutions of 5×10^{-3} N and 1.25×10^{-4} N·m in the x- and y-directions, respectively, and 10^{-2} N and 1.25×10^{-4} $\mathrm{N} \cdot \mathrm{m}$ in the z-direction. The force and torque data were acquired at a sampling rate of 100 Hz. Each case ran for 30 cycles of the motion, with the first and last five cycles used for warmup and cooldown. For each case from Van Buren et al. (2018a), one trial was performed, and for the new cases, three trials were performed. Consequently, data from old cases will be plotted without error bars while data from new cases will be plotted with error bars, the error bars showing the sample standard deviation across trials. The inertia of the foil was not subtracted from the force and torque measurements since it makes exactly zero contribution to the mean forces and mean power (see Van Buren et al. (2018b) for further details).

8.4 Propulsive performance

8.4.1 Thrust

We show the time-averaged thrust coefficients for all cases in figure 8.4 as a function of Strouhal number. In figure 8.4a, we have plotted the raw thrust coefficients, coloured by the pitch amplitude. The thrust data can be separated into several different curves, each corresponding to a different pitch amplitude. The curves appear to be offset from each other by a constant amount, with curves corresponding to higher pitch amplitudes falling below curves corresponding to lower pitch amplitudes. We interpret the offset of each curve as a static drag offset C_D, that is, the mean drag produced by the motion in the limit of low frequency (slow motions).

As indicated earlier, Van Buren et al. (2018a) found that for small-amplitude motions C_D varied linearly with the pitch amplitude, $C_D \sim A_\theta^*$. To show that this is a good approximation for large-amplitude motions as well, we turn to the drag curve

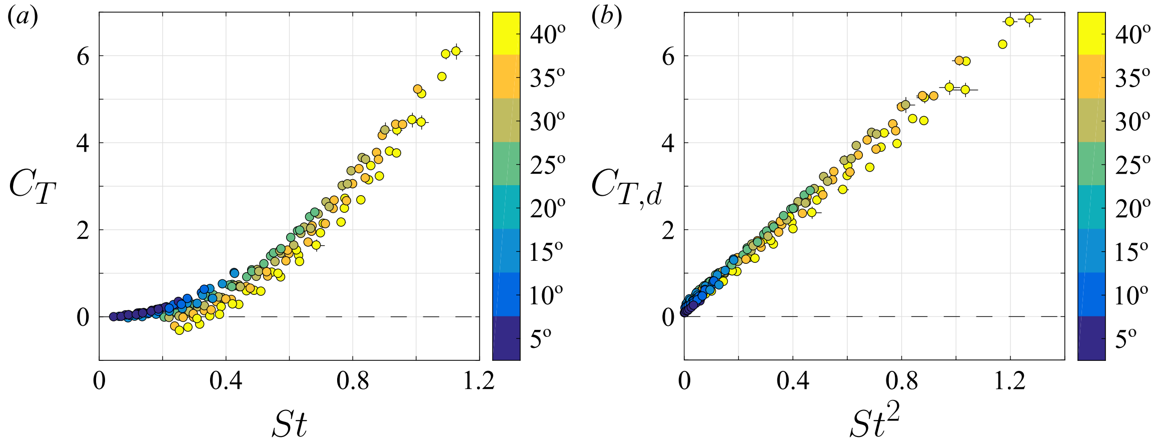

Figure 8.4: Coefficient of thrust as a function of (a) St for raw thrust, and (b) St^2 for drag-corrected thrust. Colour indicates pitch amplitude θ_0.

at constant angles of attack, as shown in figure 8.5. (The angle of attack and pitch angle are equivalent in this case.) The offset drag indeed varies linearly with the pitch amplitude, approximately as $C_D = 1.2A^*_\theta$.

When we account for the drag offset by adding it back to the thrust in the form $C_{T,d} = C_T + 1.2A^*_\theta$, then according to the scaling law in (8.8), the drag-corrected thrust should vary as

$$C_{T,d} \sim St^2. \tag{8.11}$$

We note that this scaling relation was developed for motions with small amplitudes, whereas the data in the present work contains motions with large amplitudes. Nevertheless, when we plot the drag-corrected thrust against the scaling variable in figure 8.4b, the data collapse on a straight line. The data are more scattered at larger Strouhal numbers, but the collapse is quite good overall. The simplicity of the scaling relation may obscure just how powerful it is: it collapses the low-amplitude data as well as the large-amplitude data, with trailing edge amplitudes of up to nearly one chord (two chord lengths peak-to-peak). The success of the collapse also shows the dominant role of the trailing edge velocity for thrust, even for large-amplitude motions.

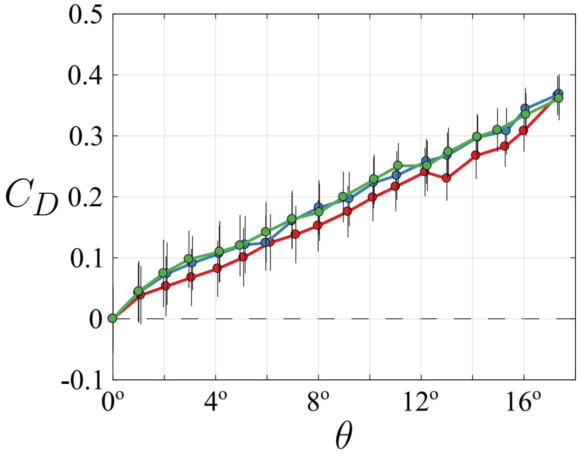

Figure 8.5: Drag curve at $Re = 8{,}000$ for the foil used in all experiments. Values are reported relative to the drag at $\theta = 0$. Colour indicates each of the three trials.

The scaling relation for thrust aligns with the heuristic analysis from Section 8.2, originally due to Alexander (2003). According to that analysis, different motions produce the same thrust as long as the amplitude and frequency are varied inversely to one another. In other words, different motions will produce the same thrust as long as their Strouhal numbers are equal, congruent to the scaling relation given by (8.11). We will show later that the presence of the drag offset has important implications for efficiency.

8.4.2 Power

The time-averaged power coefficients for all cases are presented in figure 8.6a as a function of Strouhal number, coloured by the pitch amplitude. When the time-averaged power coefficient is plotted as a function of St, the power data corresponding to higher pitch amplitudes fall below data corresponding to lower pitch amplitudes, as also found for the thrust behaviour.

According to the small-amplitude scaling analysis, the power should vary according to (8.9). When the power coefficients are plotted in this scaling form they collapse surprisingly well on a straight line for all amplitudes of motion, as shown in figure 8.6b.

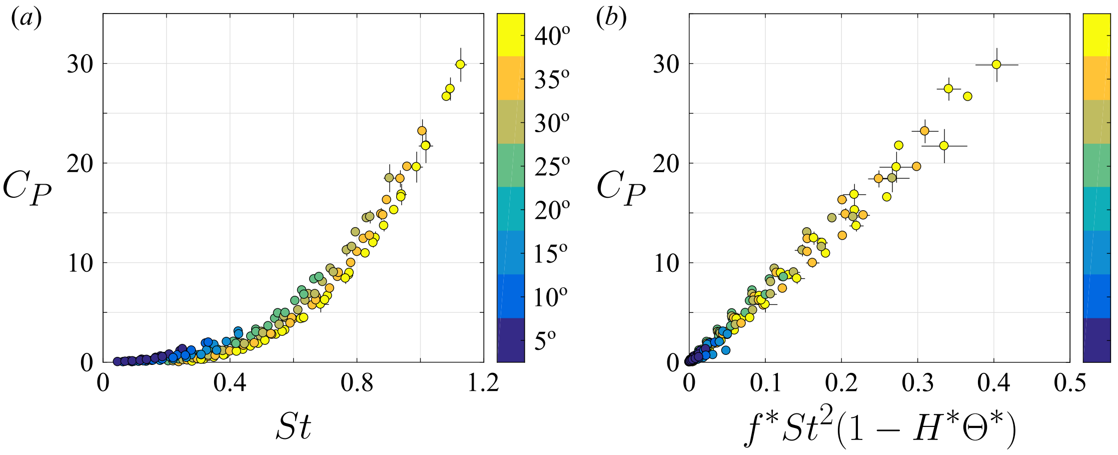

Figure 8.6: Coefficient of power as a function of (a) St and (b) the scaling variable $f^*St^2(1-H^*\Theta^*)$. Colour indicates θ_0.

As for the thrust, the data are more scattered at larger Strouhal numbers, but the collapse is quite satisfactory. We emphasize that, without any free constants, the scaling law collapses the data for motions with peak-to-peak trailing edge amplitudes of up to nearly two chord lengths.

We can gain some physical insight by considering the scaling expression for the power in more detail, that is, the variable $f^*St^2(1-H^*\Theta^*)$. The term outside of the parentheses is a product of the dimensionless frequency and the square of the Strouhal number, that is, the square of the dimensionless trailing edge velocity; it gives a measure of the intensity of the motion and sets the overall level of the power. The term inside the parentheses measures how far the product of amplitude ratios is from unity; it modulates the overall power. This term is minimized when $H^* = \Theta^*$, that is, the power is minimized when heave and pitch contribute equally to the trailing edge amplitude (Floryan et al., 2018). Because the factor $(1-H^*\Theta^*)$ does not vary as much as the factor f^*St^2 in our data, it is difficult to see their individual effects in the power curves shown. We therefore plot the time-averaged power coefficient as a function of the two terms in figure 8.7. Two different views are shown to make the variation clearer. According to (8.9), the logarithm of the power coefficient should be

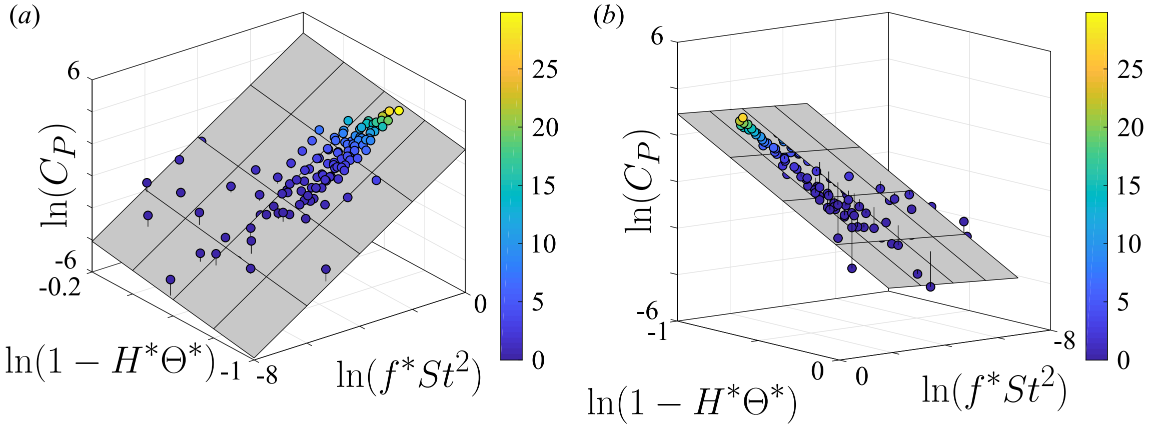

Figure 8.7: Coefficient of power as a function of f^*St^2 and $1-H^*\Theta^*$. Colour indicates C_P. The two plots are the same, but viewed from different angles.

a linear function of the logarithms of the two terms. The grey plane is the resulting least squares linear regression, and the vertical lines show the distance between the points and the plane. The slope of the grey plane shows that a decrease in the modulating term $(1 - H^*\Theta^*)$ indeed results in a decrease in the power.

8.4.3 Efficiency

The efficiency for all cases is plotted in figure 8.8a as a function of Strouhal number, with colour corresponding to the dimensionless amplitude of motion A^*. We plot the efficiency against St because increasing the amplitude while maintaining a fixed St necessarily means that we are lowering the frequency. Thus by comparing points with the same St, we directly compare low-amplitude/high-frequency data to high-amplitude/low-frequency data, allowing us to examine the hypothesis set out in Section 8.2.

For $St > 0.6$, the hypothesis holds true: larger amplitudes lead to greater efficiency. Moreover, decreasing frequency while maintaining a fixed amplitude (decreasing St while maintaining the same colour in figure 8.8a) also leads to greater efficiency. However, these trends break down at lower St, where we see that in certain regions

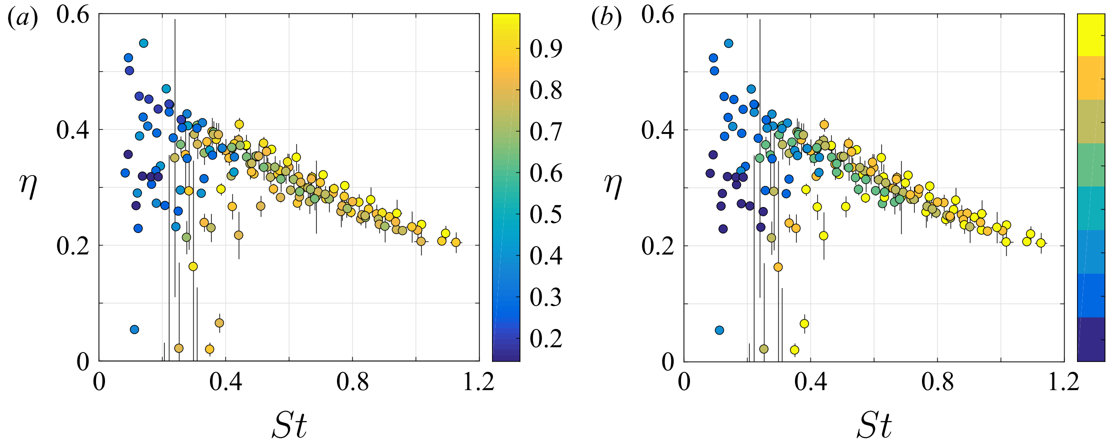

Figure 8.8: Efficiency as a function of St. Colour indicates: (a) dimensionless amplitude A^*; (b) pitch amplitude θ_0.

decreasing the amplitude actually improves the efficiency. We also see that once the frequency is low enough for a motion of fixed amplitude, decreasing the frequency decreases the efficiency.

The region where the hypothesis breaks down coincides with the region of peak efficiency. Since our original intention was to explore the use of large-amplitude motions to attain high efficiencies, understanding the breakdown—where large-amplitude motions are no longer the most efficient—is crucial. We will pursue this understanding by considering the scaling expression for the efficiency given by (8.10).

To start, consider the case $c_1 = 0$, that is, where the drag offset ignored. In that case, (8.10) reduces to $\eta \sim A^*/St(1 - H^*\Theta^*)$, suggesting that increasing the trailing edge amplitude and decreasing the Strouhal number will both increase the efficiency. The only way to accomplish both simultaneously is to increase the amplitude and decrease the reduced frequency. If we are interested in increasing efficiency while maintaining a constant level of thrust, then we must increase the amplitude while maintaining a constant Strouhal number. Again, this corresponds to increasing the amplitude while decreasing the reduced frequency. In the limit of no drag, the scaling analysis agrees with the analysis of Section 8.2, and both agree with the efficiency data for $St > 0.6$. This makes sense because for large St, the thrust term St^2 in the numerator of (8.10) dominates the drag term A^*_θ.

The analysis from Section 8.2 breaks down when the drag cannot be ignored ($St < 0.6$ here), but the scaling analysis can still shed some light on the behaviour of the efficiency. When St becomes small enough, the efficiency begins to drop precipitously. It appears that motions with large amplitudes tend to experience the drop in efficiency at larger St than those with small amplitudes, but the colouring in figure 8.8a shows that this is not quite the case (for example, the points that drop off at the largest St have a large amplitude, but not the largest). Examining (8.10) reveals the reason for the drop in efficiency. When St becomes small enough, the drag begins to dominate the thrust ($c_1 A^*_\theta$ begins to dominate St^2), consequently decreasing the efficiency. Since the drag is dominated by the pitch amplitude, we should expect motions with larger pitch amplitudes to have drops in efficiency at greater St. When we colour the data by the pitch amplitude, as in figure 8.8b, we indeed see that the drop in efficiency occurs at greater St for larger pitch amplitudes.

The results leave us at a crossroads: increasing the trailing edge amplitude increases efficiency, but in order to increase the trailing edge amplitude while avoiding large angles of attack, we need to increase the pitch amplitude, which strengthens the drag offset and increases the Strouhal number at which the precipitous drop in efficiency occurs. In other words, big and slow motions are more efficient until they become so big and so slow that drag overwhelms the thrust production. In the large-St region ($St > 0.6$ here), large-amplitude motions are the most efficient but their peak efficiency is lower. The key is to diminish the effects of drag.

To demonstrate the effect of reducing drag, we have taken our data and compensated for some of the drag by adding a fraction of it back to the thrust. If we choose

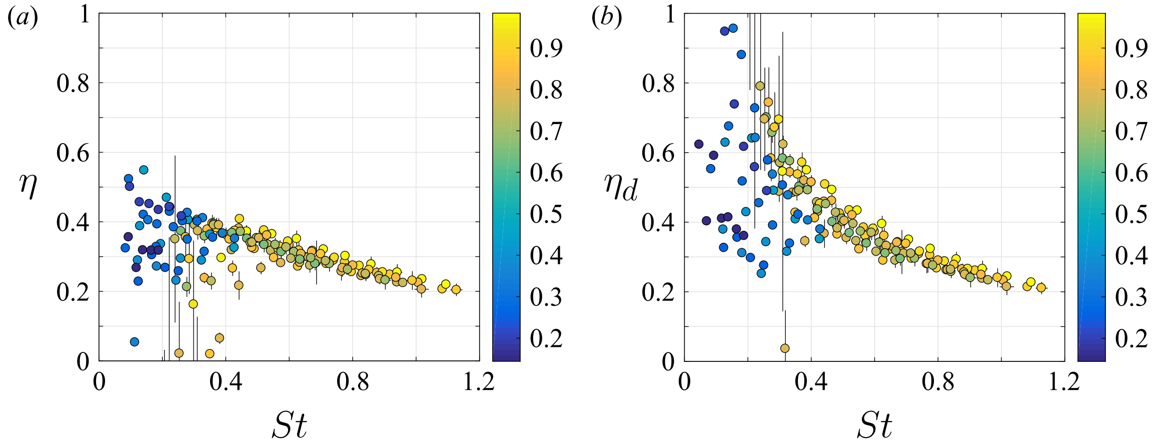

Figure 8.9: (a) Raw efficiency and (b) reduced-drag efficiency as functions of St. colour indicates A^*.

a drag reduction level of 25%, then the resulting reduced-drag efficiency is

$$\eta_d = \frac{C_T + 0.3A^*_\theta}{C_P}, \tag{8.12}$$

since we originally found that the drag was well-approximated by $C_D = 1.2A^*_\theta$. The reduced-drag efficiency is plotted in figure 8.9 next to the raw efficiency with the same scale. A relatively modest decrease in the drag of the foil leads to marked increases in efficiency, especially for large-amplitude motions, and extends the range of validity of the original analysis of large-amplitude motions. If one's goal is to produce thrust efficiently, then reducing drag should clearly be the avenue explored. Our experiments were performed at Re = 8,000, and we expect improvements in efficiency with increases in Reynolds number. Beyond increasing Re, other avenues for reducing the drag should lead to similar results.

8.4.4 Thrust/efficiency tradeoff

Perhaps the most important question is how the thrust and efficiency depend on each other. It is generally desirable for a propulsor to simultaneously have high thrust and efficiency. To produce a given amount of thrust most efficiently, we found that large-amplitude, low-frequency combinations do the best (the issue of drag aside). But is there a fundamental limit to this balance? Figure 8.8 certainly suggests so, as increasing St leads to increases in thrust but decreases in efficiency. To shed some additional light on this matter, we consider the scaling laws in the limit of negligible drag. In that case, the thrust and efficiency follow

$$C_T \sim St^2, \tag{8.13}$$

$$\eta \sim \frac{A^* St^2}{St^3(1 - H^*\Theta^*)}. \tag{8.14}$$

Combining the two, we obtain a relationship between thrust and efficiency, that is,

$$\eta \sim \frac{A^*}{1 - H^*\Theta^*} \frac{1}{\sqrt{C_T}}. \tag{8.15}$$

We do not expect this relationship to be complete; for example, we certainly do not expect unbounded efficiency as the thrust approaches zero. But the relationship gives a qualitative insight on the fundamental tradeoff between thrust and efficiency—in order to increase one, we must decrease the other.

The efficiency and thrust data are plotted against each other in figure 8.10, revealing a Pareto front nearly following the scaling in (8.15) for larger thrust coefficients. Although we do not show it here, the data closer to the edge of the Pareto front have larger amplitudes. The inviscid scaling is shown with a triangle, and we see that the Pareto front is generally flatter than the inviscid scaling. colouring the data by $C_T/1.2A^*_\theta$ (ratio of thrust to an estimate of the drag, giving an idea of 'how inviscid' any data point is) shows that 'more inviscid' data follow the inviscid scaling better, and we expect data to follow this scaling even more closely with further increases in the thrust/drag ratio. Conversely, the more important the drag is (the lower the ratio is), the greater the deviation from the inviscid scaling is. As the importance of

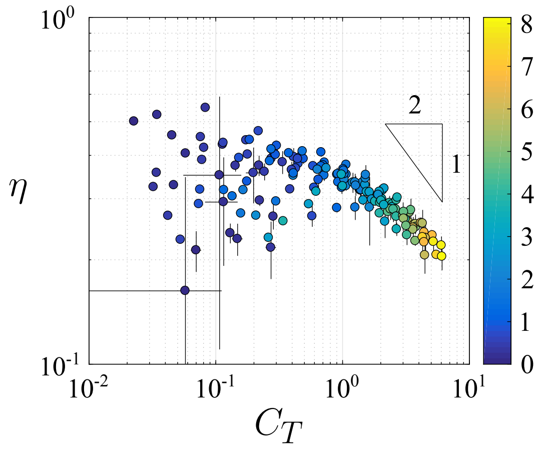

Figure 8.10: Efficiency as a function of thrust coefficient, with the drag-free scaling shown. colour indicates $C_T/1.2A^*_\theta$.

drag increases, the rate at which efficiency increases with a decrease in thrust drops. Not only is there a fundamental tradeoff between thrust and efficiency, the presence of drag worsens this tradeoff, further underlining the importance of drag and the necessity of decreasing it.

8.5 Conclusions

We examined the thrust production, power consumption, and efficiency of a two-dimensional foil in combined heave and pitch motions with peak-to-peak trailing edge amplitudes up to almost two chord lengths. The phase difference between heave and pitch motions was kept constant at 270° where high efficiency is expected. For these large-amplitude motions the classical small-amplitude theory breaks down, but the scaling relations developed by Van Buren et al. (2018a) and Floryan et al. (2018) were shown to hold across the entire range of amplitudes explored in this study, collapsing experimental data for thrust, drag, and power.

These scaling relations were then used to explain the use of large-amplitude motions in order to achieve high efficiency. In particular, when drag can be ignored, reducing frequency and increasing amplitude can increase efficiency without changing thrust, and thrust can be sacrificed for further gains in efficiency; the data reflected this conclusion when the Strouhal number was large ($St > 0.6$ for our Reynolds number), where the drag is relatively weak. When the Strouhal number is small ($St < 0.6$ for our Reynolds number), however, drag is important and increases in amplitude lead to *decreases* in efficiency. This lower Strouhal number region is important because at this Reynolds number it covers the Strouhal number corresponding to peak efficiency. This behaviour occurs because increasing the total amplitude requires increasing the pitch amplitude to maintain angles of attack below the dynamic stall limit. Since the drag is important for low St and depends primarily on the pitch amplitude, increasing the total amplitude while maintaining a reasonable angle of attack increases the drag, which can then overwhelm the thrust, causing the efficiency to decrease sharply.

In other words, big and slow (large-amplitude, low-frequency) motions are more efficient until they become so big and so slow that drag overwhelms the thrust production and the efficiency decreases. By combining the scaling relations and the experimental data, we showed that modest decreases in drag can significantly increase efficiency, especially the peak efficiency. The key to attaining high efficiency is always to decrease the drag. For a given propulsor, increasing the Reynolds number is expected to decrease the drag coefficient. Decreasing the drag also extends the range of Strouhal numbers where large-amplitude, low-frequency motions lead to high efficiencies.

Although at a given thrust coefficient we may increase efficiency by increasing the amplitude (unless drag is important), there is a fundamental tradeoff between thrust coefficient and efficiency: an increase in one requires a decrease in the other. We developed a scaling relation that captures this tradeoff in the limit of no drag and reflects the experimental measurements. The presence of drag lowers the gains in efficiency that can be achieved through sacrifices in thrust.

Our results also have implications for swimming animals. Large-Reynolds number swimmers change their speed by changing their frequency of oscillation while maintaining a constant amplitude (Rohr and Fish, 2004). That is, they maintain a constant Strouhal number and dimensionless amplitude while changing speed. According to our observations and in the limit of negligible propulsor drag, this behaviour maintains a constant level of efficiency. Moreover, we speculate that the animals use their largest possible amplitude of motion at all speeds, and by only changing their frequency to change their speed their behaviour reflects an attempt to maximize efficiency.

This work was supported by ONR Grant N00014-14-1-0533 (Program Manager Robert Brizzolara).

Chapter 9

Efficient cruising for swimming and flying animals is dictated by fluid drag

Daniel Floryan, Tyler Van Buren, and Alexander J. Smits

Appears as Floryan et al. (2018).

Many swimming and flying animals are observed to cruise in a narrow range of Strouhal numbers, where the Strouhal number $St = 2fA/U_\infty$ is a dimensionless parameter that relates stroke frequency f, amplitude A, and forward speed U_∞. Dolphins, sharks, bony fish, birds, bats, and insects typically cruise in the range $0.2 < St < 0.4$, which coincides with the Strouhal number range for maximum efficiency as found by experiments on heaving and pitching airfoils. It has therefore been postulated that natural selection has tuned animals to use this range of Strouhal numbers because it confers high efficiency, but the reason why this is so is still unclear. Here, by using simple scaling arguments, we argue that the Strouhal number for peak efficiency is largely determined by fluid drag on the fins and wings.

Swimming and flying animals across many species and scales cruise in a relatively narrow range of Strouhal numbers $0.2 < St < 0.4$ (Triantafyllou et al., 1991; Taylor et al., 2003). The Strouhal number $St = 2fA/U_\infty$ is a dimensionless parameter that relates stroke frequency f, stroke amplitude A, and forward speed U_∞. It has been hypothesized that for animals that range widely or migrate over long distances, natural selection should favor swimming and flying motions of high propulsive efficiency, and so the kinematics, described by the Strouhal number, should be tuned for high propulsive efficiency. Indeed, the cruising range of Strouhal numbers observed in nature overlaps the range of Strouhal numbers experimentally shown to result in high propulsive efficiency for simple propulsors (Triantafyllou et al., 1991; Floryan et al., 2017a; Van Buren et al., 2018a).

A typical efficiency curve for a simple propulsor is shown in figure 9.1. We see that at low Strouhal numbers, the efficiency rapidly rises with increasing Strouhal number, reaches a maximum, and then falls off relatively slowly with further increases in Strouhal number. Here, the propulsive efficiency η is defined as $\eta = TU_\infty/P$, where T is the mean net thrust that propels the animal forward, U_∞ is the mean forward cruising speed, and P is the mean mechanical power required to create the thrust.

What dictates the Strouhal number that leads to maximum efficiency? Three prevailing theories have been proposed. The first (Triantafyllou et al., 1991, 1993) argues that peak efficiency occurs when the kinematics result in the maximum amplification of the shed vortices in the wake, yielding maximum thrust per unit of input energy; this phenomenon has been termed "wake resonance" (Moored et al., 2012). The second theory (Wang, 2000) argues that the preferred Strouhal number is connected with maximizing the angle of attack allowed, while avoiding the shedding of leading edge vortices. The third (Saadat et al., 2017) holds that, for aquatic animals, the ratio of

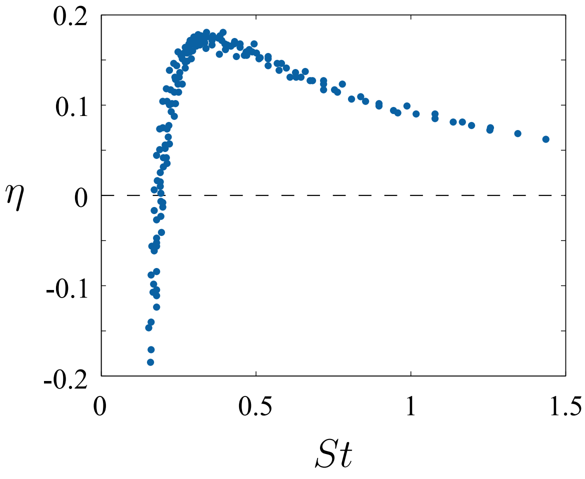

Figure 9.1: A typical efficiency curve showing efficiency η as a function of St. Data are for a heaving and pitching NACA0012 foil (Quinn et al., 2015) ($A/c = 0.19$, and heaving leads pitching by 90°).

the tail beat amplitude to the body length essentially dictates the Strouhal number for cruise, since it requires a balance between thrust and drag.

Here, we offer a simple alternative explanation for the observed peak in efficiency, and we also explain the rapid rise in efficiency at low St and the more gradual decrease at high St. Our explanation highlights the important role that fluid drag plays in determining the efficiency behaviour.

Consider a cruising animal, one that is moving at constant velocity. We make the assumption that the thrust is produced primarily by its propulsor (for example, caudal fin for a fish, fluke for a mammal, wing for a bird), and that the drag is composed of two parts: the drag due to its body (D_b, proportional to the body surface area), and an "offset" drag due to its propulsor (D_o, proportional to the propulsor frontal area projected over its range of motion). More details are given below.

This decomposition is illustrated in figure 9.2, where the thrust-producing propulsor is separated from the drag-producing body and represented by an oscillating airfoil (Wu, 2011). To be clear, fliers are distinct from swimmers in that fliers' propulsors need to produce lift to combat gravity, in addition to thrust to propel themselves for-

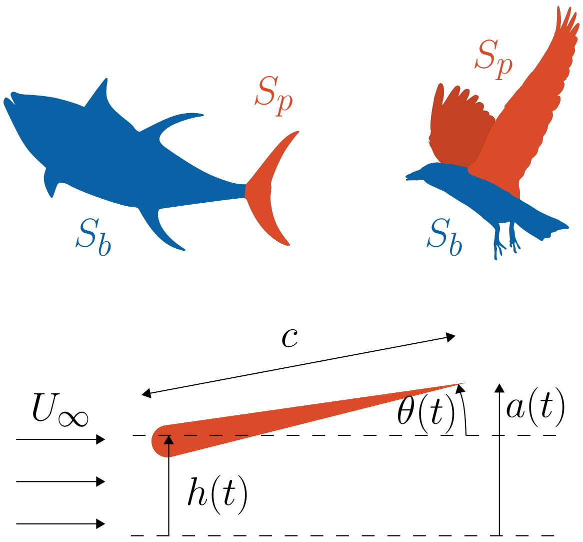

Figure 9.2: Swimmers and fliers can be decomposed into thrust-producing (orange) and drag-producing (blue) parts, with the propulsor aptly represented by an oscillating airfoil.

ward. As far as steady forward cruising is concerned, however, the physics of forward propulsion is not affected by the additional requirement of lift (Wu, 2011).

We also simplify the motion of the propulsor to model it as a combination of heaving (amplitude h_0) and pitching (amplitude θ_0). Biologically-relevant motions are ones where the heaving and pitching motions are in phase, or where the heaving motion leads the pitching motion by 90° (Van Buren et al., 2018a). In cruise, our model requires that the thrust produced by the propulsor balances the total fluid drag experienced by the body and the propulsor.

We now consider the performance (thrust, power and efficiency) of an isolated propulsor. For the net thrust T we use the scaling

$$T \sim \rho S_p V^2 - D_o, \tag{9.1}$$

where ρ is the density of the fluid, S_p is the area of the propulsor, and V ($\sim fA$) is the characteristic speed of the transverse motion of the propulsor. The V^2 scaling is derived in Section 9.A.1, where it is also shown to be representative of biologically-relevant flapping motions. In addition, the scaling is supported by theory (Garrick, 1936; Lighthill, 1971), empirical curve fits on fish performance (Bainbridge, 1958, 1963), and the performance of a large group of swimming animals (Gazzola et al., 2014). As indicated above, we will assume that for a cruising animal the net thrust of the propulsor balances the drag of the body D_b, where $D_b \sim \rho S_b U_\infty^2$, and S_b is the surface area of the body. Hence, for a negligible offset drag,

$$St^2 \sim S_b/S_p. \tag{9.2}$$

Previous work has proposed that this thrust-drag balance alone yields a constant Strouhal number (Gazzola et al., 2014). However, (9.2) shows that this conclusion implicitly assumes that $D_o = 0$, and that the area ratio S_b/S_p remains constant, which will not hold across the many different species that cruise in the preferred range $0.2 < St < 0.4$. To arrive at a more general result, we need to understand the energetics determining swimming and flying. The net thrust of the propulsor at peak efficiency then sets the cruising speed.

For the power expended, we adopt the scaling

$$P \sim \rho S_p f c \left(V^2 - V_h V_\theta\right), \tag{9.3}$$

where c is a characteristic length scale of the propulsor, and V_h and V_θ are the transverse velocity scales characteristic of the heaving and pitching motions, respectively. This scaling is derived in Section 9.A.1, where further details are given. It is based on established theory and analysis (Garrick, 1936; Theodorsen, 1935; Sedov, 1965), and it is corroborated by a large set of experiments (Van Buren et al., 2018a). It derives from the nonlinear interaction of the power produced by the propulsor velocity and its acceleration, an interaction that is critical to our understanding of the large-amplitude motions observed in nature.

We now consider the offset drag, that is, the drag of the propulsor in the limit of vanishing f, which scales as

$$D_o \sim \rho U_\infty^2 S_p g(\theta_0). \tag{9.4}$$

Here, θ_0 is the amplitude of the pitching motion, and the function $g(\theta_0)$ is positive when $\theta_0 = 0$ and increases with θ_0 (Floryan et al., 2017a; Van Buren et al., 2018a). The offset drag can be viewed as scaling with the projected frontal area of the propulsor, as in bluff body flows (White, 2011).

Hence, we arrive at

$$\eta = \frac{TU_\infty}{P} \sim \frac{V^2 U_\infty - b_1 U_\infty^3 g}{fc(V^2 - V_h V_\theta)}, \tag{9.5}$$

where the constant b_1 sets the relative importance of the drag term compared to the thrust term (in general, we expect b_1 to be a function of Reynolds number $Re = \rho c U/\mu$, where μ is the fluid viscosity). The efficiency can be recast in terms of the Strouhal number $St = 2fA/U_\infty$ and a dimensionless amplitude $A^* = A/c$, so that

$$\eta \sim \frac{A^* \left(St^2 - b_1 g\right)}{St^3 \left(1 - H^* \Theta^*\right)}. \tag{9.6}$$

The other non-dimensional terms, $H^* = h_0/A$ and $\Theta^* = c\theta_0/A$, represent, respectively, the amplitudes of the heaving and pitching motions relative to the total amplitude of motion.

We see immediately that to achieve high efficiency, the dimensionless amplitude A^* should be large. This observation is consistent with the argument put forth by R. M. Alexander, where he proposed that large-amplitude motions are more efficient than small-amplitude motions (Alexander, 2003). However, there are two potential limiting factors. First, as A^* becomes larger the instantaneous angle of attack increases, dynamic stall effects may become important, and the drag model given here for D_o will be invalidated. Second, animal morphology naturally sets a limit as to how large they can make A^*. For efficient cruising, therefore, A^* should be as large as an animal's morphology allows, while avoiding dynamic stall at all times. Our argument is consistent with the experimental observations made by Saadat et al. (2017) in what we called the third theory. Wang (2000) (the second theory) similarly argues for large-amplitude motions, although she argues that large-amplitude motions are connected to the optimal Strouhal number, whereas we argue that, all else fixed, the amplitude sets the total efficiency but it does not dictate the optimal Strouhal number.

What about the optimal Strouhal number? When there is no offset drag ($b_1 = 0$), the efficiency increases monotonically as St decreases, and the optimal efficiency is achieved in the limit $St \to 0$. However, in the presence of offset drag ($b_1 \neq 0$) the efficiency will become *negative* as $St \to 0$ because the drag dominates the thrust produced by the propulsor. In general, (9.6) gives negative efficiencies at low St, a rapid increase with St to achieve a positive peak value at $St = \sqrt{3b_1 g}$, and a subsequent slow decrease with further increase in St as the influence of drag becomes weaker. The comparison between the form given by (9.6) and the data originally shown in figure 9.1 makes this clear, as displayed in figure 9.3. The offset drag is crucial in determining the low St behaviour, and in setting the particular St at which the peak efficiency occurs. Note that the maximum value of the efficiency is directly related to the value of the drag constant b_1, which further emphasizes the critical role of the drag term in determining the efficiency behaviour. The amplification of shed vortices described in the wake resonance theory (the first theory) may simply arise as a signature of the efficient production of net thrust, but this is purely speculative.

Finally, we consider the composition of the motion, that is, the relative amounts of heaving and pitching. As shown in Section 9.A.2, for biologically-relevant flapping motions the denominator of (9.6) is minimized (and hence efficiency is maximized) when $h_0 = c\theta_0$. In other words, optimally efficient propulsors should have heaving and pitching motions that contribute equally to the total motion. When we also take the numerator of (9.6) into account, we actually expect the heaving contribution to

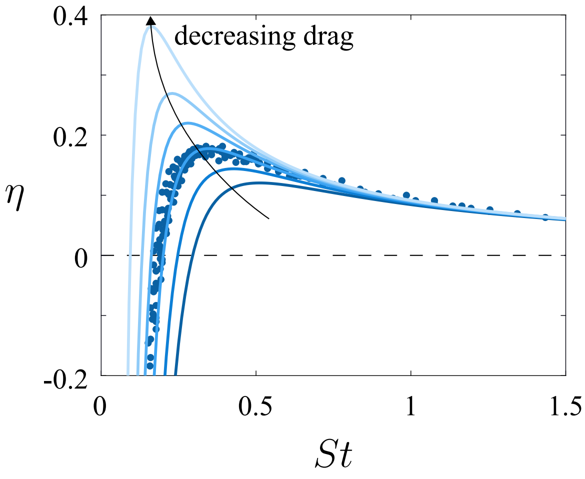

Figure 9.3: Efficiency η as a function of St. Data are as given in figure 9.1 for a heaving and pitching NACA0012 foil (Quinn et al., 2015). Solid lines are given by (9.6) with a fixed proportionality constant of 0.155. The drag constant, b_1, is set to 0.5, 0.35, 0.23, 0.15, 0.1, and 0.05 as the colours vary from dark to light, and we have set $g(\theta_0) = \theta_0$. The proportionality constant and the value of b_1 corresponding to the experimental data were calculated by a total least squares fit to the data.

be a little larger because the offset drag is dominated by pitch. We are not aware of biological measurements that would allow us to test the optimal heaving and pitching balance, so at this point it remains a hypothesis.

We leave the reader with a final thought. We expect that the relative importance of the drag, captured by b_1, will depend on the Reynolds number. Our drag model is similar to that for a bluff body, such as a sphere or cylinder, so we expect b_1 will be large at small Reynolds numbers, and decrease as the Reynolds number increases until it reaches about 1000, above which the drag will be almost constant (at least for $Re < 2 \times 10^5$, although biological measurements imply that the drag may remain constant up to $Re = 10^8$ (Schlichting, 1979; Gazzola et al., 2014)). Therefore, at low Reynolds numbers the location of the peak efficiency will change with Reynolds number: as Reynolds number increases, the optimal St will decrease, until b_1 reaches its asymptotic value at a sufficiently high Reynolds number. Our conclusion is consistent with biological measurements (at least for swimmers), where the preferred Strouhal number appears to decrease as the Reynolds number increases, until it reaches an asymptotic value (Gazzola et al., 2014). This further substantiates our claim that the presence of fluid drag on the propulsor is the crucial factor in creating an efficiency peak which dictates the cruising conditions of swimming and flying animals. In other words, energetic considerations set the kinematics of the propulsor to the most efficient one, and the net thrust of the propulsor at peak efficiency balances the drag of the body to set the cruising speed.

9.A Supplementary information

9.A.1 Thrust and power

Here we derive simple expressions for the mean thrust and power, as used in the main text, by considering sinusoidal heaving and pitching motions described by

$$h(t) = h_0 \sin(2\pi f t), \tag{9.7}$$

$$\theta(t) = \theta_0 \sin(2\pi f t + \phi), \tag{9.8}$$

where pitch leads heave by a phase angle ϕ. In our previous work (Van Buren et al., 2018a), we used aerodynamic theory to derive the following expressions for the mean thrust and power coefficients produced by a heaving and pitching foil:

$$C_T = c_1 St^2 + c_2 St_h \theta_0 \sin\phi + c_3 St_\theta \theta_0 - c_4 \theta_0, \tag{9.9}$$

$$C_P = c_5 St^2 + c_6 f^* St_h St_\theta \sin\phi + c_7 St_h \theta_0 \sin\phi + c_8 f^* St_h^2 + c_9 f^* St_\theta^2 + c_{10} St_\theta \theta_0, \tag{9.10}$$

where $St_h = 2fh_0/U_\infty$, $St_\theta = 2fc\theta_0/U_\infty$, and the reduced frequency $f^* = fc/U$. Also, $C_T = 2T/\rho S_p U_\infty^2$ is the thrust coefficient, and $C_P = 2P/\rho S_p U_\infty^3$ is the power coefficient. Note that the term $c_4\theta_0$ represents the drag coefficient for the propulsor.

These expressions were shown to collapse experimental data on a simple teardrop foil for all values of ϕ.

For the biologically-relevant phase angles $\phi \in \{0°, 270°\}$, we find that the c_2 and c_3 terms in thrust, and the c_{10} and c_7 terms in power, are small relative to the other terms and can be neglected. For power, we use $St^2 = St_h^2 + St_\theta^2 + 2St_h St_\theta \cos\phi$. As a result, we now propose, for $\phi \in \{0°, 270°\}$,

$$C_T = c_1 St^2 - c_4 \theta_0, \tag{9.11}$$

$$C_P = a_1 St^2 + a_2 f^* St^2 + a_3 f^* St_h St_\theta. \tag{9.12}$$

We have introduced new constants a_i to avoid confusion with the previous constants c_i in the power. All signs have been absorbed into the constants. Note that we now have the same thrust and power expressions for both phases. Based on the numerical values of the constants in (9.11)–(9.12), as found from the experimental data, we can propose a further reduction, where

$$C_T = c_1 St^2 - c_4 \theta_0, \tag{9.13}$$

$$C_P = a_2 f^* \left(St^2 - St_h St_\theta \right). \tag{9.14}$$

Plotting the thrust and power data against (9.13)–(9.14) yields figure 9.4. The collapse using these reduced models is as good as obtained by Van Buren et al. (2018a) using the full expressions given by (9.9) and (9.10).

(9.13) and (9.14) can be written dimensionally, so that, for $\phi \in \{0°, 270°\}$,

$$T \sim \rho S_p V^2 - D_o, \tag{9.15}$$

$$P \sim \rho S_p f c (V^2 - V_h V_\theta), \tag{9.16}$$

where D_o is the drag offset.

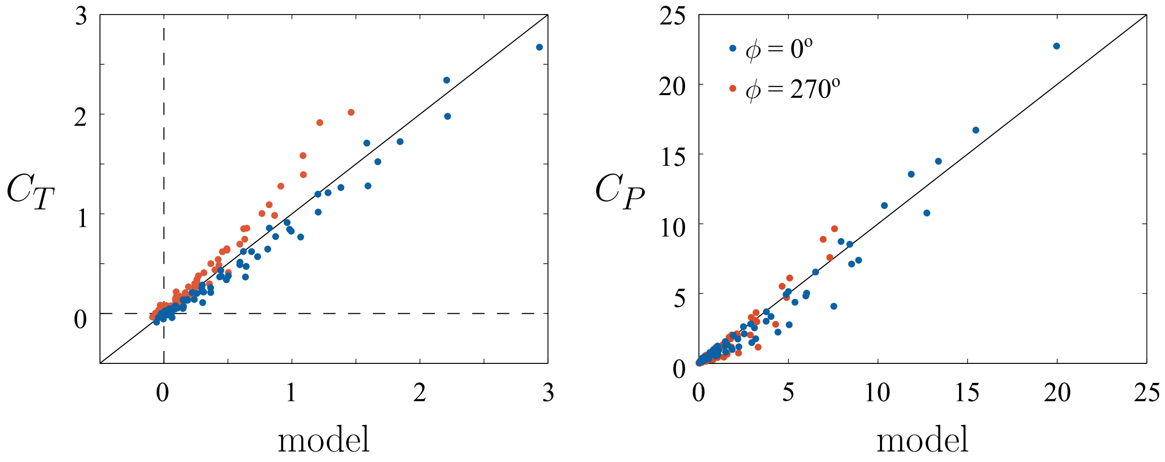

Figure 9.4: Thrust and power data plotted against (9.13)–(9.14) for $\phi = 0°$ (blue) and $\phi = 270°$ (orange). The coefficients are $c_1 = 4.65$, $c_4 = 0.49$, $a_2 = 62.51$.

9.A.2 Motion composition

The total amplitude for a motion with arbitrary phase is

$$A^2 = h_0^2 + 2h_0 c\theta_0 \cos\phi + c^2\theta_0^2. \tag{9.17}$$

For biologically-relevant phases, we then have

$$\phi = 0^{\circ} : A = h_0 + c\theta_0, \tag{9.18}$$

$$\phi = 270^{\circ} : A^2 = h_0^2 + c^2\theta_0^2. \tag{9.19}$$

For both phases, $h_0 c\theta_0 / A^2$ is maximized when $h_0 = c\theta_0$, minimized when one of them is zero, and always less than 1. (This can be shown using calculus for $\phi = 0°$, and using right triangles for $\phi = 270°$.) So for both phases, the denominator of (9.6) is positive, and is minimized when the heave and pitch amplitudes are equal.

9.A.3 Materials and methods

The experimental setup is the same as described by Van Buren et al. (2018a). Experiments on a heaving and pitching airfoil were conducted in a water tunnel with a

$0.46 \times 0.3 \times 2.44$ m test section, with the tunnel velocity set to $U_\infty = 0.1$ m/s. A teardrop airfoil of chord $c = 0.08$ m, thickness 0.008 m, and span 0.279 m was used, yielding a chord-based Reynolds number of $Re = 8{,}000$.

Heaving motions were generated by a linear actuator (Linmot PS01-23 × 80F-HP-R), pitching motions about the leading edge were generated by a servo motor (Hitec HS-8370TH), and both were measured by encoders. The heaving and pitching motions were sinusoidal, as described in (9.7)–(9.8), with frequencies $f = 0.2$ to 0.8 Hz every 0.1 Hz, heaving amplitudes $h_0 = 0.01, 0.02, 0.03$ m, pitching amplitudes $\theta_0 = 5^\circ, 10^\circ, 15^\circ$, and phase angles $\phi = 0^\circ$ and 90°, with experiments performed on all combinations of the kinematic parameters.

The forces and moments imparted by the water on the airfoil were measured by a six-component sensor (ATI Mini40) at a sampling rate of 100 Hz. The force and torque resolutions were 5×10^{-3} N and 1.25×10^{-4} N·m, respectively, in the streamwise and cross-stream directions, and 10^{-2} N and 1.25×10^{-4} N·m, respectively, in the spanwise direction. Each case was run for 30 cycles, with the first and last five cycles used for warmup and cooldown. All sensors were zeroed before every case.

Chapter 10

Clarifying the relationship between efficiency and resonance for flexible inertial swimmers

Daniel Floryan and Clarence W. Rowley

Appears as Floryan and Rowley (2018).

We study a linear inviscid model of a passively flexible swimmer, calculating its propulsive performance, eigenvalues, and eigenfunctions with an eye towards clarifying the relationship between efficiency and resonance. The frequencies of actuation and stiffness ratios we consider span a large range, while the mass ratio is mostly fixed to a low value representative of swimmers. We present results showing how the trailing edge deflection, thrust coefficient, power coefficient, and efficiency vary in the stiffness-frequency plane. The trailing edge deflection, thrust coefficient, and power coefficient show sharp ridges of resonant behaviour for mid-to-high frequencies and stiffnesses, whereas the efficiency does not show resonant behaviour anywhere. For low frequencies and stiffnesses, the resonant peaks smear together and the efficiency is high. In this region, flutter modes emerge, inducing travelling wave kinematics which make the swimmer more efficient. We also consider the effects of a finite Reynolds number in the form of streamwise drag. The drag adds an offset to the net thrust produced by the swimmer, causing resonant peaks to appear in the efficiency (as observed in experiments in the literature).

10.1 Introduction

A distinguishing feature of nature's swimmers and fliers is the flexibility of their tails and wings, prevailing across a wide range of length scales, time scales, and media. A natural question to ask is whether or not flexibility equips swimmers and fliers with any propulsive advantages over their rigid counterparts, and if so, what characterizes such advantages? The prevailing thinking is that flexibility is indeed a desirable property of a propulsor, but the characterization of its effects, particularly on the efficiency of propulsion, is tenuous.

To be clear, our own interests lie mainly in inertial swimmers characterized by high Reynolds numbers, a large ratio of characteristic fluid mass to body mass, and uniformly distributed passive flexibility. This is in contrast to fliers, for example, where the mass ratio is of order unity and higher, and where the flexibility may be localized. Nevertheless, we will draw upon some of the literature on flight to motivate and guide our analysis.

Passive flexibility has generally been found to lead to thrust and efficiency gains across a range of actuation frequencies, from far below the first natural frequency of the system, to deep into the region of higher-order natural frequencies (Alben, 2008b; Ferreira de Sousa and Allen, 2011; Dewey et al., 2013; Katz and Weihs, 1978, 1979; Quinn et al., 2014). In the context of swimming, the efficiency is a measure of how much of the power used to generate the kinematics of a swimmer is converted to useful thrust power. (Although exact definitions vary from one work to the other, they are all in the same spirit.) While thrust generally exhibits local maxima when actuating near natural frequencies (when the system is in resonance), efficiency has been observed to exhibit local maxima below natural frequencies, near natural frequencies, and above natural frequencies (Dewey et al., 2013; Moored et al., 2014; Quinn et al., 2014, 2015; Paraz et al., 2016), as well as at frequencies relatively far from a natural frequency (Ramananarivo et al., 2011; Kang et al., 2011; Vanella et al., 2009; Zhu et al., 2014; Michelin and Llewellyn Smith, 2009). This muddled relationship between efficiency and resonance can be partly explained by an ill-conceived notion of natural frequencies. In some cases (Hua et al., 2013; Kang et al., 2011; Vanella et al., 2009), natural frequencies were based off of an Euler-Bernoulli beam in a vacuum, whereas Michelin and Llewellyn Smith (2009) has shown that the presence of a fluid critically affects the natural frequencies of the system. Some of these studies mistook the added mass of the fluid for drag, leading to an incorrect definition of the total system mass (Vanella et al., 2009; Combes and Daniel, 2003b). In other cases where efficiency and resonance were unrelated, large-amplitude motions were considered, leading to a regime of highly nonlinear dynamics where the linear notion of resonance may be inappropriate. We summarize the parameters used in the literature in table 10.1, translated to correspond with the definitions employed in this work, as defined in Section 10.2. Note that some parameters had to be estimated.

The tacit argument in studies where local maxima in efficiency were observed somewhere near a resonant frequency seems to be that resonance is a condition that improves the efficiency of a system. Although appealing, it is not immediately clear that resonance should unconditionally improve the efficiency of a system. Indeed, most of the works we cite demonstrate local maxima in the input power when the system is actuated at a resonant frequency, not just the thrust, which degrades the

Study	$AR = \frac{w}{L}$	$Re = \frac{\rho_f U L}{\mu}$	$R = \frac{\rho_s d}{\rho_f L}$	$S = \frac{E d^3}{\rho_f U^2 L^3}$	$f^* = \frac{fL}{U}$	h_0	θ_0
Alben (2008b)	∞	inviscid	0	10^{-6}–10^{8}	$\{1, 2, 6, 25\}/\pi$	0	$\frac{\pi}{720}$ (linear)
Dewey et al. (2013)	2.4	7,200	$(1.4–34.5) \times 10^{-3}$	3.0–78.6	0.37–2.99	0	0.125
Ferreira de Sousa and Allen (2011)	∞	851	—	—	—	0	4°–8°
† Hua et al. (2013)	∞	200–1,800	0.5–4	2.3–1,951	0.05–0.5	0.25–2	0
Kang et al. (2011)	∞	9,000	$(4.4–33) \times 10^{-3}$	3.6, 12.5, 1,548	0.45–1.55	0.388	0
Katz and Weihs (1978)	∞	inviscid	0	—	0.025–0.075	6	5°
Katz and Weihs (1979)	$\ll 1$	inviscid	0	—	0.025–0.05	6	5°
Michelin and Llewellyn Smith (2009)	∞	inviscid	0.2	10^{-2}–10^{4}	$\{1, 2.5\}/\pi$	0.2, 0.4, 1	0
Moored et al. (2014)	2.4	7,200	$(1.4–34.5) \times 10^{-3}$	3.0–78.6	0.37–2.99	0	0.125
‡ Paraz et al. (2016)	1	0	low	∞	∞	0.07–0.24	0
Quinn et al. (2014)	0.77	7,800–46,800	low	0.01–1,987	0–17.1	0.1	0
Quinn et al. (2015)	0.77	5,000–70,000	low	0.005–1.09	0.26–21.74	0.06–0.18	0°–30°
† Ramananarivo et al. (2011)	1.57	88.5–6,375	1.2–13	6.4–44,220	0.3–26.4	0.25, 0.4	0
‡ Vanella et al. (2009)	∞	0	—	∞	∞	2.8	$\pi/4$
† Zhu et al. (2014)	∞	46–454	0.1–2	6.3–618,000	0.1–0.85	0.4–1.6	0
Present study	∞	inviscid	0.01	10^{-2}–10^{2}	10^{-1}–10^{2}	2 (linear)	1 (linear)

Table 10.1: Summary of parameters used in the literature. † denotes studies where the swimmer swam freely (in which case Re, S, and f^* are dependent variables), and ‡ denotes studies where the free-stream velocity was zero. In some cases, parameter values were estimated, and in other cases, parameter values could not be estimated from the information provided (marked as —).

efficiency. How resonance affects efficiency is subtle, and should be understood beyond a black-box understanding.

Physical mechanisms unrelated to a fluid-structure resonance have also been offered to explain maxima in efficiency. According to Moored et al. (2014), peaks in efficiency occur when the actuation frequency is tuned to a “wake resonant frequency,” which is unrelated to any structural frequency. Quinn et al. (2015) argued that peaks in efficiency occur when the Strouhal number is high enough that the flow does not separate but low enough that the shed vortices remain tightly packed, the trailing edge amplitude is maximized while flow remains attached along the body, and the effective angle of attack is minimized. In these two works, fluid-structure resonance did coincide with maxima in efficiency. In Ramananarivo et al. (2011), peak efficiency was not related to resonance; instead, it was achieved by making use of the nonlinear nature of a drag transverse to the direction of locomotion. The authors argued that efficiency is maximized when the trailing edge is approximately parallel to the total velocity.

In this work, we attempt to clarify the relationship between efficiency and resonance. Resonance is a condition where some property of the system exhibits a maximum; for a passively flexible swimmer, the deflection of its body is one such property. The relation between efficiency and deflection is complicated, making it unclear whether or not resonance of the deflection should result in maximal efficiency. To clarify the matter, we study a passively flexible swimmer using a linear model, valid for small-amplitude motions. Doing so allows us to formally calculate natural frequencies of the coupled fluid-structure system, and to stay in a dynamical regime where the notion of resonance is clear. The linear model cannot account for large-amplitude effects such as separation (especially of the leading edge vortex), but accurately models attached flows (Saffman, 1992). Systematically examining the effects of nonlinearity — perhaps separately in the fluid and solid mechanics, and

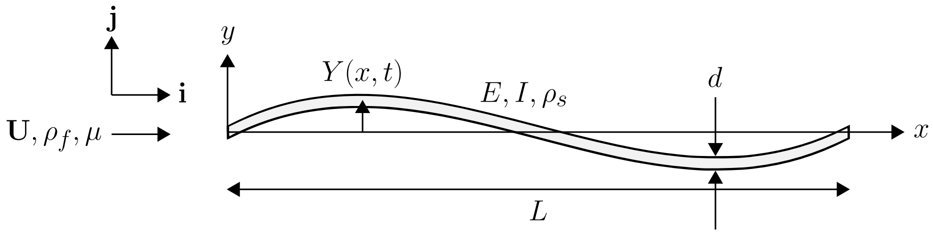

Figure 10.1: Schematic of the problem.

then together — in the context of our linear results would be a useful step forward in delineating exactly what the role of nonlinearity is in swimmers.

10.2 Problem description

Here, the setup and assumptions are the same as in Moore (2017). Consider a two-dimensional, inextensible elastic plate of length L and thickness d. The plate is thin ($d \ll L$), and is transversely deflected a small amount Y from its neutral position, with its slope $Y_x \ll 1$. Under these assumptions, the dynamics of the plate is governed by Euler-Bernoulli beam theory. The plate has uniformly distributed density ρ_s and flexural rigidity $B = EI$, where E is the Young's modulus, $I = wd^3/12$ is the second moment of area of the plate, and w is the width of the plate. The plate is immersed in an incompressible, inviscid Newtonian fluid of density ρ_f. There is no flow along the width of the plate, and far from the plate the flow is unidirectional and constant: $\mathbf{U} = U\mathbf{i}$. The setup is altogether illustrated in figure 10.1.

The motion of the plate alters the velocity field of the fluid, whose forces in turn modify the motion of the plate. The transverse position of the plate satisfies the Euler-Bernoulli beam equation

$$\rho_s d w Y_{tt} + B Y_{xxxx} = w \Delta p, \tag{10.1}$$

where Δp is the pressure difference across the plate due to the fluid flow, subscript t denotes differentiation with respect to time, and subscript x denotes differentiation with respect to streamwise position. The fluid motion satisfies the linearized incompressible Euler equations

$$\left.\begin{aligned} &\nabla \cdot \mathbf{u} = 0, \\ &\rho_f(\mathbf{u}_t + U\mathbf{u}_x) = -\nabla p, \end{aligned}\right\} \tag{10.2}$$

where $\mathbf{u} = u\mathbf{i} + v\mathbf{j}$. The above linearization is valid when the perturbation velocity $\mathbf{u}$ is much smaller than U. Since the perturbation velocity depends on the plate's vertical velocity, its slope, and the rate of change of its slope, the linear assumption holds for small-amplitude motions of the plate.

We non-dimensionalize the above equations using $L/2$ as the length scale, U as the velocity scale, and $L/(2U)$ as the time scale, yielding

$$\left.\begin{aligned} &2RY_{tt} + \frac{2}{3}SY_{xxxx} = \Delta p, \\ &\nabla \cdot \mathbf{u} = 0, \\ &\mathbf{u}_t + \mathbf{u}_x = \nabla \phi, \end{aligned}\right\} \tag{10.3}$$

where

$$R = \frac{\rho_s d}{\rho_f L}, \quad S = \frac{Ed^3}{\rho_f U^2 L^3}, \quad \phi = p_\infty - p. \tag{10.4}$$

In the above, x, t, Y, $\mathbf{u}$, and p are now dimensionless, with the pressure non-dimensionalized by $\rho_f U^2$. The coordinates are aligned such that $x = -1$ corresponds to the leading edge and $x = 1$ corresponds to the trailing edge. R is a ratio of solid-to-fluid mass, and S is a ratio of bending-to-fluid forces. Note that $\Delta\phi = -\Delta p$.

The fluid additionally satisfies the no-penetration and Kutta conditions, which can be stated as

$$\left.\begin{aligned} v|_{x\in[-1,1],y=0} &= Y_t + Y_x, \\ |v||_{(x,y)=(1,0)} &< \infty. \end{aligned}\right\} \tag{10.5}$$

We impose heaving and pitching motions h and θ, respectively, on the leading edge of the plate, while the trailing edge is free, resulting in boundary conditions

$$Y(-1,t) = h(t), \quad Y_x(-1,t) = \theta(t), \quad Y_{xx}(1,t) = 0, \quad Y_{xxx}(1,t) = 0. \tag{10.6}$$

The fluid motion resulting from the actuation of the leading edge of the plate imparts a net horizontal force onto the plate. In other words, energy input into the system by the actuation of the leading edge is used to generate a propulsive force. The net horizontal force (thrust) on the plate is

$$C_T = \int_{-1}^{1} \Delta p Y_x \,\mathrm{d}x + C_{TS}, \tag{10.7}$$

where C_{TS} is the leading edge suction force (formula given in Moore, 2017), and the power input is

$$C_P = -\int_{-1}^{1} \Delta p Y_t \,\mathrm{d}x. \tag{10.8}$$

The leading edge suction force used in Moore (2017) is the limit of the suction force on a leading edge of small but finite radius of curvature, in the limit that the radius tends to zero. The leading edge suction force is a reasonable model of the actual flow when it is attached (Saffman, 1992), so we have chosen to include it. In terms of dimensional variables, $C_T = T/(\frac{1}{2}\rho_f U^2 L w)$ and $C_P = P/(\frac{1}{2}\rho_f U^3 L w)$, where T and P are the dimensional net thrust and power input, respectively. Finally, the Froude efficiency is defined as

$$\eta = \frac{\overline{T}U}{\overline{P}} = \frac{\overline{C_T}}{\overline{C_P}}, \tag{10.9}$$

where the overbar denotes a time-averaged quantity.

In this work, we restrict ourselves to actuation at the leading edge that is sinusoidal in time, that is,

$$\left.\begin{aligned} h(t) &= h_0 \mathrm{e}^{\mathrm{j}\sigma t}, \\ \theta(t) &= \theta_0 \mathrm{e}^{\mathrm{j}\sigma t}, \end{aligned}\right\} \tag{10.10}$$

where $\sigma = \pi L f / U$ is the dimensionless angular frequency, f is the dimensional frequency in Hz, $\mathrm{j} = \sqrt{-1}$, and the real part in j should be taken when evaluating the deflection. Since the system is linear in Y, the resulting deflection of the plate and fluid flow will also be sinusoidal in time. We leave the details of the method of solution to Appendix 10.A, noting that all calculations in this work used 64 collocation points. The method to calculate the eigenvalues of the system is detailed in Appendix 10.B, and some useful formulas for the numerical method used are given in Appendix 10.C.

10.3 A note on parameters

It is important to acknowledge that the system parameters we use will critically affect the phenomena we observe. The dissensus in the literature on the relationship between efficiency and resonance may be partly attributed to results being overextended from one dynamical regime to another. We thus take the opportunity here to explicitly state the parameters we employ in this work, as well as to show some resulting qualitative features.

To be clear, the system is parameterized by its Reynolds number Re, mass, stiffness, and frequency and amplitude of actuation. Our flow is inviscid, but we will consider some of the effects of a finite Reynolds number later on. As revealed by the non-dimensional quantities in (10.4), the mass and stiffness of the system depend on both the solid *and* the fluid. For underwater swimmers, the mass ratio is generally quite low since swimmers are neutrally buoyant but thin; this is in contrast

Re	$R = \dfrac{\rho_s d}{\rho_f L}$	$S = \dfrac{E d^3}{\rho_f U^2 L^3}$	$f^* = \dfrac{fL}{U}$	h_0	θ_0
inviscid	0.01	10^{-2}–10^{2}	10^{-1}–10^{2}	2 (linear)	1 (linear)

Table 10.2: Parameter values used in this work.

to fliers, for example, where the mass ratio is of order unity and higher. Since our interests lie in swimming flows, we take the mass ratio to be $R = 0.01$ throughout. We vary the stiffness of the system from very flexible ($S \ll 1$) to very stiff ($S \gg 1$), characterized by the stiffness ratio S. We vary the frequency of actuation so that it covers multiple natural frequencies of the system. Our system is linear, so scaling the amplitude by some factor will simply scale the flow and deflection fields by the same factor. In this sense, amplitude does not matter in our problem, so we set the heaving and pitching amplitudes so that the maximum deflection of the trailing edge of a rigid plate is equal to the length of the plate. The amplitude affects both thrust and power quadratically, and does not affect efficiency in this linear setting. We do not consider nonlinear effects caused by large amplitudes. The parameters we use in the proceeding sections are summarized in table 11.1.

As a final note, we point out the effect of the mass of the system. Although we fix the mass ratio to be $R = 0.01$ in the proceeding sections in this work, we take the opportunity here to vary R in order to show how swimmers and fliers may differ, at least qualitatively. In figure 10.2, we show the efficiency as a function of mass and stiffness ratios for plates heaving and pitching at a reduced frequency $f^* = 1$ (the results are similar to those in figure 11 of Moore (2017), but for slightly different parameter values). The white areas demarcate where the plate produces a net drag (and hence negative efficiency). The relationship between efficiency and stiffness is qualitatively different for low and high mass ratios. At high mass ratios (where the plate is much more massive than a characteristic mass of fluid), the plate does not produce thrust unless the stiffness ratio is high. At $O(1)$ mass ratios, efficiency

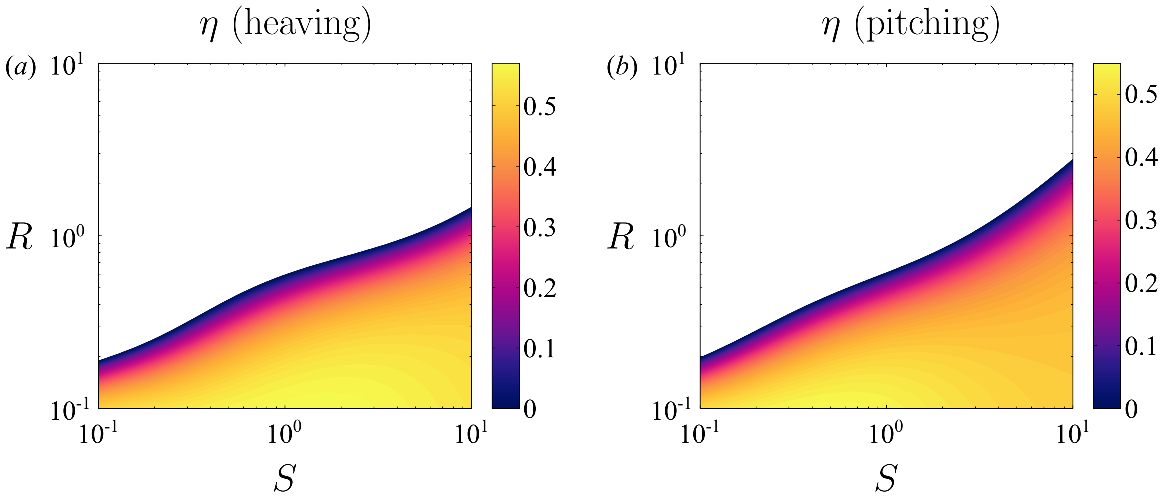

Figure 10.2: Efficiency as a function of mass ratio R and stiffness ratio S for a (a) heaving and (b) pitching plate at $f^* = 1$. Areas with negative efficiency have been whited out.

increases monotonically as the plate becomes stiffer. At low mass ratios, efficiency does not change monotonically with stiffness.

In figure 10.3, we show the first four natural frequencies of the coupled fluid-structure system as a function of the mass ratio for the limit of large bending velocity compared to flow velocity; we will refer to such frequencies (and, more generally, eigenvalues and eigenfunctions) as quiescent natural frequencies, and refer the reader to Appendix 10.B.2 for more details. To be clear, when we write "natural frequencies" we mean the imaginary parts of the eigenvalues of the system, calculated as in Appendix 10.B. For just the results in this plot, we have changed the time scale such that a flat line indicates that only the mass of the plate (but not the fluid) matters. The non-dimensional angular frequency here is $\omega^* = \omega\sqrt{3\rho_s L^4/(4Ed^2)}$, where $\omega = 2\pi f$ is the dimensional angular frequency. For high values of the mass ratio, the natural frequencies scale with the mass of the plate ($\omega^* \sim R^0$). For low values of the mass ratio, however, the natural frequencies scale with the mass of the surrounding fluid ($\omega^* \sim R^{1/2}$). There is also a region where both the characteristic plate and

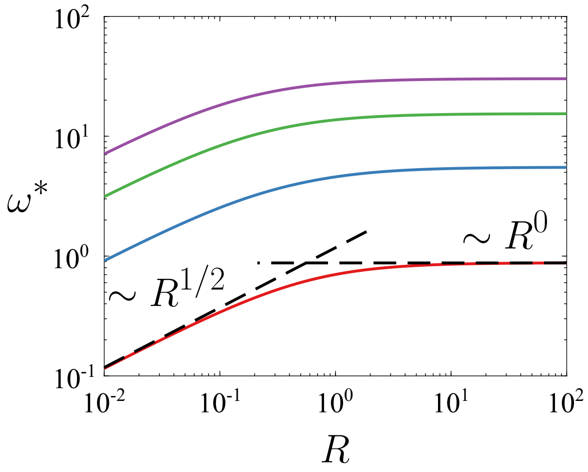

Figure 10.3: First four natural frequencies in a quiescent fluid as a function of mass ratio. Asymptotic behaviour overlaid.

fluid masses must be considered. We also note that for a non-zero incoming flow, the natural frequencies may change (we will show this later).

Together, the results briefly shown here underline the importance of specifying the dynamical regime of the system, in particular the mass ratio R. All of our results will be for $R = 0.01$, and we expect our conclusions to hold for low mass ratios ($R \lesssim 0.1$).

10.4 Inviscid results

Here, we present our results on the kinematics and propulsive characteristics of uniformly flexible swimmers. Since our interests lie in clarifying the role of resonance, we limit ourselves to purely heaving and purely pitching plates; allowing simultaneous heaving and pitching would add two parameters, and would potentially dilute our results on the role of resonance. Given our interests, it also makes sense to present results for flexible plates relative to rigid plates. For example, we will present the mean thrust that a flexible plate produces relative to the mean thrust that an otherwise identical rigid plate produces. We therefore begin by briefly reviewing the results for rigid plates.

10.4.1 Propulsive characteristics of rigid swimmers

The linear inviscid theory for sinusoidally heaving and pitching rigid plates was developed in Theodorsen (1935), and extended in Garrick (1936) to provide results on the propulsive characteristics of such plates. The mean thrust produced, as well as the mean power needed to produce the mean thrust, are shown in figure 10.4 as a function of the reduced frequency for the amplitudes in table 10.2. At high reduced frequencies, the mean thrust coefficient varies as f^{*2} for both heaving and pitching plates. At low reduced frequencies, the mean thrust coefficient varies sub-quadratically for a heaving plate, and super-quadratically for a pitching plate, for the reduced frequencies shown here. Note that a heaving plate always produces net thrust in the mean, whereas a pitching plate produces net drag in the mean for $f^* < 0.202$. The story is much the same for the mean power coefficient. At high reduced frequencies, the mean power coefficient varies as f^{*2} for both heaving and pitching plates. At low reduced frequencies, the mean power coefficient varies sub-quadratically for a heaving plate, and super-quadratically for a pitching plate, for the reduced frequencies shown here. The power input for a heaving plate is always positive in the mean, whereas the power input for a pitching plate is negative in the mean for $f^* < 0.013$. As $f^* \to 0$, $\overline{C_T} \to 0$ and $\overline{C_P} \to 0$ for both heaving and pitching plates.

Given the mean thrust and power, we may calculate the efficiency, shown in figure 10.5 as a function of the reduced frequency. At high reduced frequencies, $\eta \to 0.5$ for both heaving and pitching plates. At low reduced frequencies, the efficiencies for heaving and pitching plates diverge. For a heaving plate, the efficiency increases as the reduced frequency decreases, with $\eta \to 1$ as $f^* \to 0$. For a pitching plate, the efficiency becomes negative since a pitching plate produces net drag at low reduced frequencies. Note that because of how the efficiency is defined, there is a vertical asymptote where the mean power coefficient is zero, at $f^* \approx 0.013$. To the left of this asymptote the efficiency is positive since both the mean thrust and

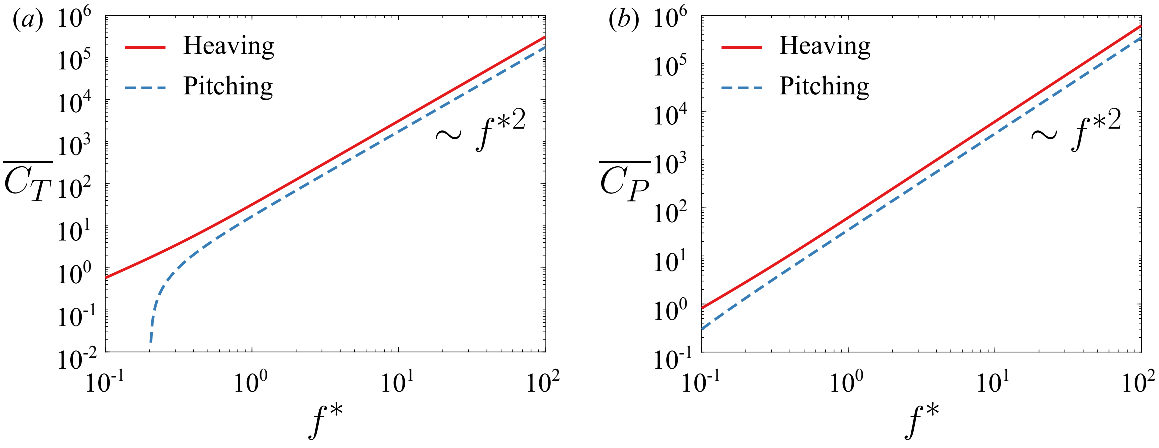

Figure 10.4: (a) Mean thrust coefficient and (b) mean power coefficient as a function of reduced frequency f^* for a heaving (red) and pitching (blue) rigid plate. Asymptotic behaviour included. At low f^*, a pitching rigid plate produces drag in the mean.

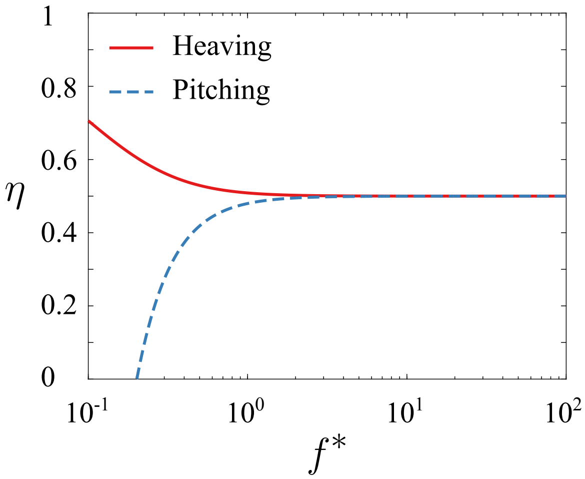

Figure 10.5: Efficiency as a function of reduced frequency f^* for a heaving (red) and pitching (blue) rigid plate. At low f^*, a pitching rigid plate produces drag in the mean, hence its efficiency is negative.

power coefficients are negative, but we shall ignore any such cases since we are only interested in thrust-producing plates.

Having briefly reviewed the propulsive characteristics of rigid plates in the linear inviscid regime, we now move on to uniformly flexible plates. It is worth bearing in mind how the thrust, power, and efficiency vary with reduced frequency for rigid

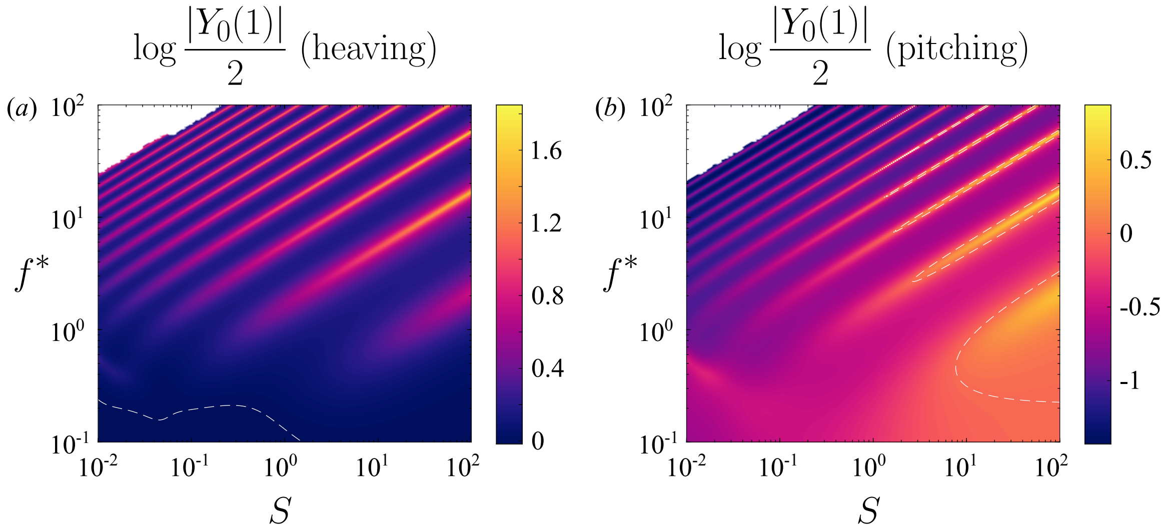

Figure 10.6: Trailing edge amplitude as a function of reduced frequency f^* and stiffness ratio S for a (a) heaving and (b) pitching plate with $R = 0.01$ relative to that of an equivalent rigid plate. Dashed white lines indicate where the flexible plate has the same trailing edge amplitude as the equivalent rigid plate. Under-resolved areas have been whited out.

heaving and pitching plates when we present the results for flexible heaving and pitching plates.

10.4.2 Propulsive characteristics of flexible swimmers

We begin by considering the kinematics of the flexible plate actuated sinusoidally at its leading edge. For our purposes, it is sufficient to look at the deflection at a single point along the length of the plate, which we choose to be the trailing edge. The amplitude of the trailing edge deflection is shown in figure 10.6. More specifically, we have plotted the logarithm of the ratio of the trailing edge amplitude of a flexible plate to the trailing edge amplitude of an otherwise identical rigid plate. The dashed white lines indicate where the flexible plate has the same trailing edge amplitude as the rigid plate. For both heaving and pitching plates, we see ridges of local maxima in trailing edge amplitude in the stiffness-frequency plane. For a given ridge, its reduced frequency increases with the non-dimensional stiffness.

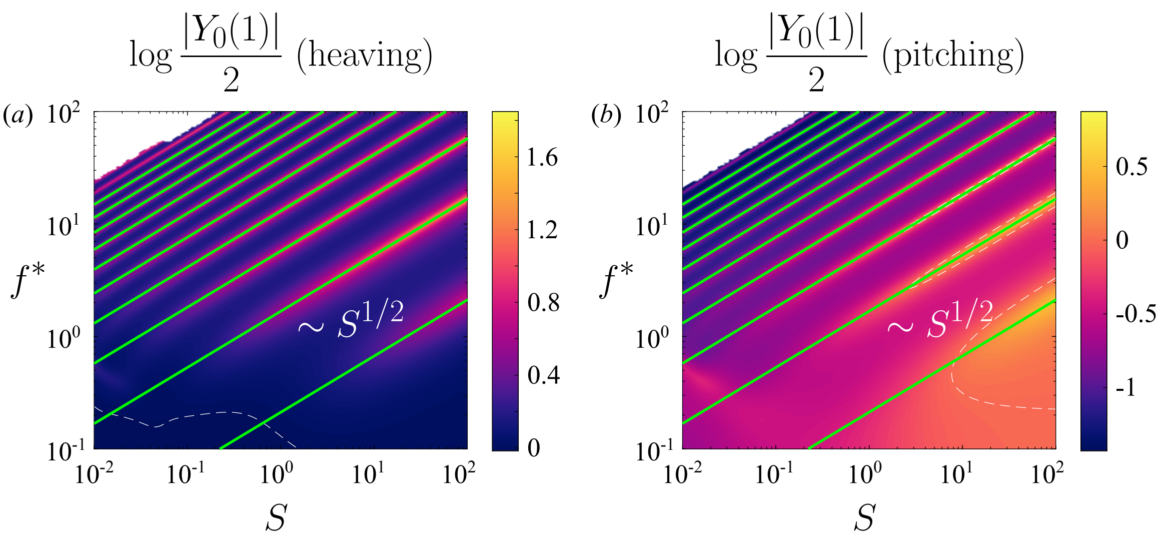

Figure 10.7: Same as in figure 10.6, but with quiescent natural frequencies overlaid as green lines.

We suspect that the locations of the local maxima of trailing edge amplitude correspond to resonances in the system. To verify our suspicion, we formally calculate the first ten pairs of quiescent eigenvalues of the coupled fluid-structure system, that is, the eigenvalues of a clamped plate in an otherwise quiescent fluid. (Formally, by quiescent we mean in the limit where the bending velocity is large compared to the fluid velocity.) We have re-plotted the trailing edge amplitudes from figure 10.6 in figure 10.7, with the imaginary parts of the eigenvalues overlaid (and re-scaled to match the non-dimensionalization employed in the plots). Indeed, the local maxima in trailing edge amplitude align with the quiescent natural frequencies of the system. The alignment is not as good when both the reduced frequency and non-dimensional stiffness are low; we leave this point aside now but will revisit it later. It can be easily shown that the quiescent natural frequencies scale as $f^* \sim S^{1/2}$.

To explain why the local maxima in trailing edge amplitude occur when the system is actuated at its natural frequencies, we turn to the transfer function from actuation to trailing edge deflection. Recall that the transfer function of a linear input-output system is a function $G(s)$, where s is a complex number, such that the response to an input of the form e^{st} is given by $G(s)e^{st}$. Since the trailing edge deflection is just a sample of the entire deflection field, the poles of the transfer function will be the eigenvalues of the system. Generally, the eigenvalues are in the left half-plane. In figure 10.8, we schematically illustrate the magnitude of a simple transfer function in the complex plane. In figure 10.8a, a single pole of the transfer function is marked as a cross, and the contour lines show level sets of the magnitude of the transfer function in the complex plane. For a single pole λ, the transfer function is $G = 1/(s - \lambda)$, where $s = \sigma + \mathrm{i}\omega$ is the complex variable. The magnitude of the transfer function decreases with distance from the pole in the complex plane, resulting in the circular level sets centered about the pole. Since our actuation is sinusoidal (i.e., $e^{\mathrm{i}\omega t}$), we are specifically interested in the behaviour along the imaginary axis; this is shown in figure 10.8b. It is clear that maxima in the magnitude of the transfer function will occur when we actuate the system at a frequency equal to the imaginary part of an eigenvalue of the system (a "natural frequency"); in other words, maxima in the magnitude of the transfer function occur when we actuate at resonance. This will generally hold true even when the system has multiple eigenvalues, as long as they are far enough from each other.

With the swimmer's kinematics understood more or less in terms of the system's eigenvalues, we move on to its propulsive characteristics. The mean thrust and power coefficients are shown in figures 10.9 and 10.10, respectively. We have plotted the logarithm of the ratio of the mean thrust/power coefficient of a flexible plate to the mean thrust/power coefficient of an otherwise identical rigid plate to show how flexibility modifies the propulsive characteristics. The dashed white lines indicate where the flexible values match the rigid values. Regions of low reduced frequency that have negative mean thrust/power have been whited out. Just as for the trailing edge amplitude, we see ridges of local maxima in the mean thrust and power coefficients.

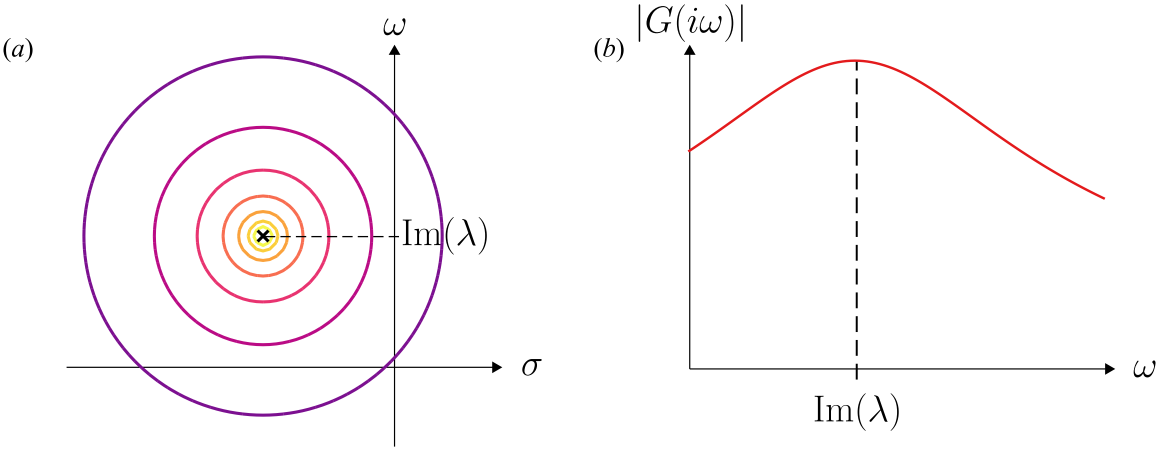

Figure 10.8: Schematic explaining resonance. (a) Level sets on the complex plane of the magnitude of a transfer function with one pole, marked with a cross. (b) Magnitude of the same transfer function evaluated on the imaginary axis.

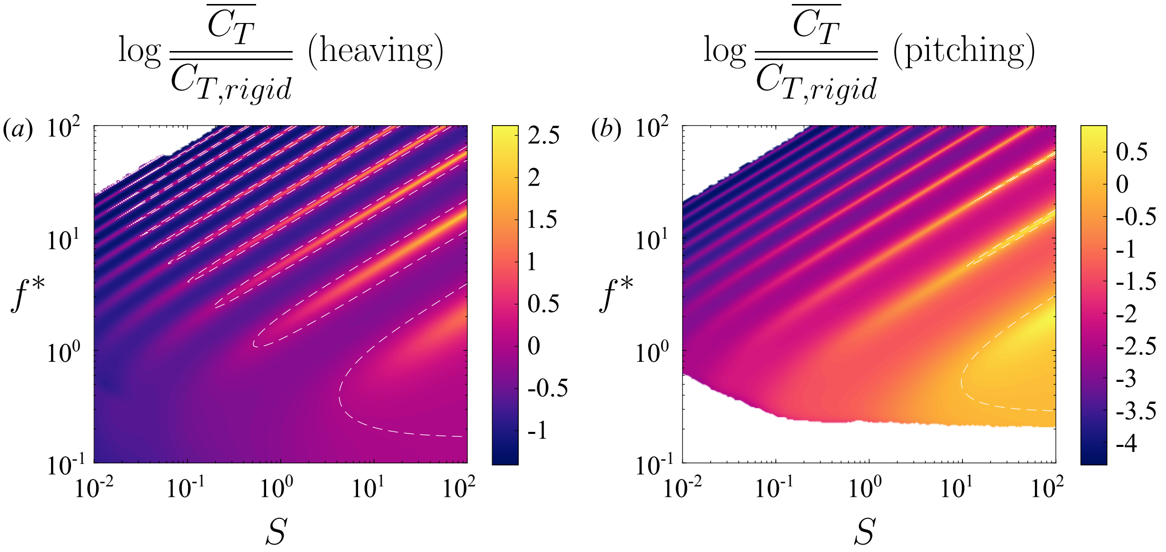

Figure 10.9: Thrust coefficient as a function of reduced frequency f^* and stiffness ratio S for a (a) heaving and (b) pitching plate with $R = 0.01$ relative to that of an equivalent rigid plate. Dashed white lines indicate where the flexible plate has the same thrust coefficient as the equivalent rigid plate. Under-resolved areas and areas which produce negative thrust have been whited out.

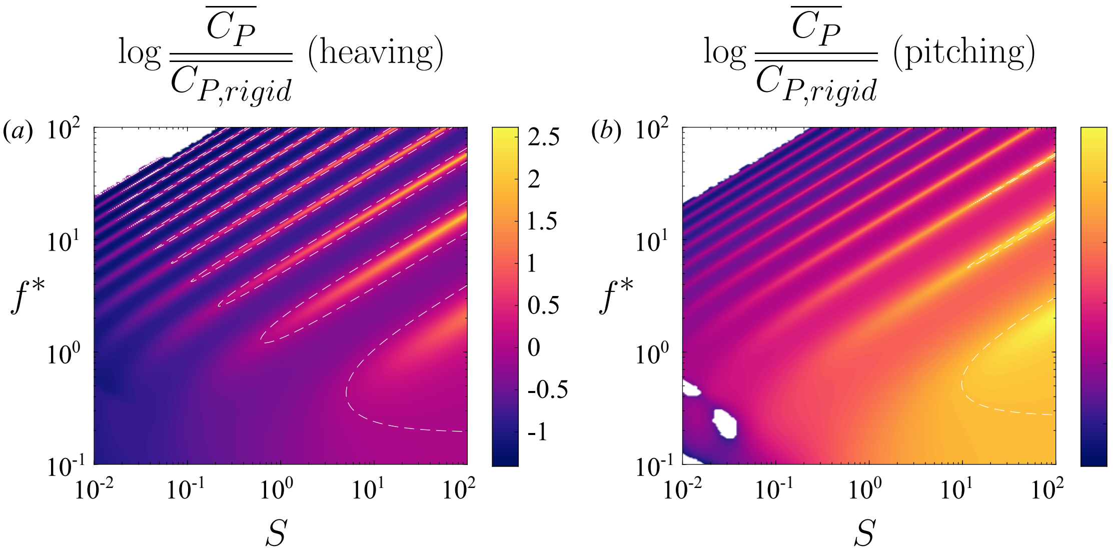

Figure 10.10: Power coefficient as a function of reduced frequency f^* and stiffness ratio S for a (a) heaving and (b) pitching plate with $R = 0.01$ relative to that of an equivalent rigid plate. Dashed white lines indicate where the flexible plate has the same power coefficient as the equivalent rigid plate. Under-resolved areas and areas which produce negative power input have been whited out.

In figures 10.11 and 10.12, we have re-plotted the mean thrust and power coefficients, with the quiescent natural frequencies overlaid. Just as for the trailing edge amplitude, the ridges of local maxima in both mean thrust and mean power align with the quiescent natural frequencies of the system (the alignment is not as good when the reduced frequency and non-dimensional stiffness are low, but we will revisit this issue later). Since the thrust and power are quadratic functions of the deflection (see (10.7) and (10.8)), we expect them to exhibit local maxima when the system is actuated at natural frequencies.

With the behaviour of the deflection, mean thrust, and mean power understood, we are left to understand the behaviour of the efficiency. The efficiency is shown in figure 10.13. For a heaving plate, the efficiency generally decreases with reduced frequency, just like for the rigid plate (cf. figure 10.5). For a pitching plate, the behaviour of the efficiency differs from the rigid case in that it increases with reduced frequency, reaches a peak, and then decreases with reduced frequency. Recall

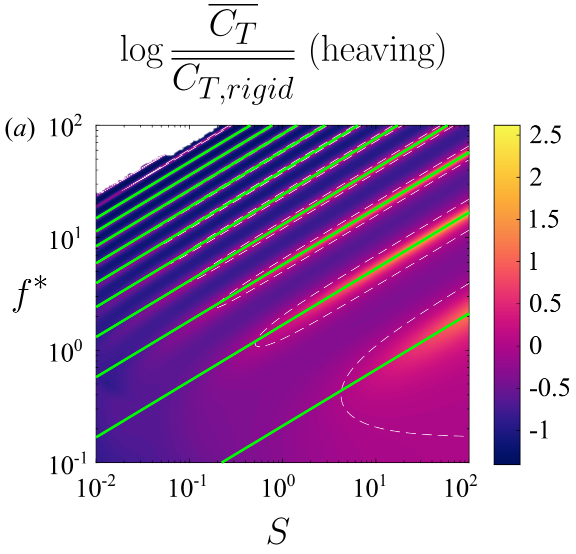

Figure 10.11: Same as in figure 10.9, but with quiescent natural frequencies overlaid as green lines.

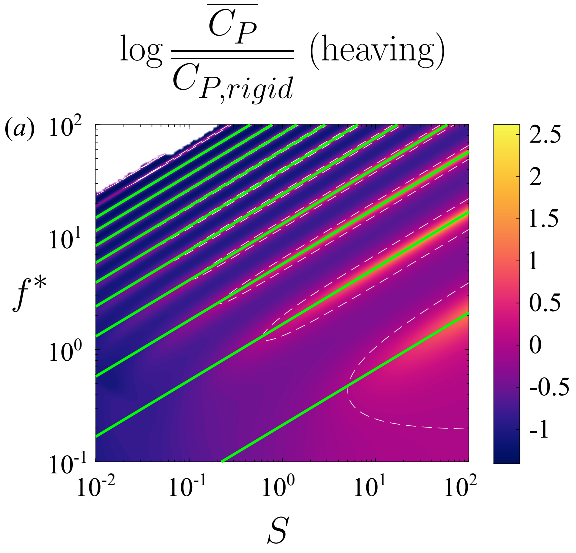

Figure 10.12: Same as in figure 10.10, but with quiescent natural frequencies overlaid as green lines.

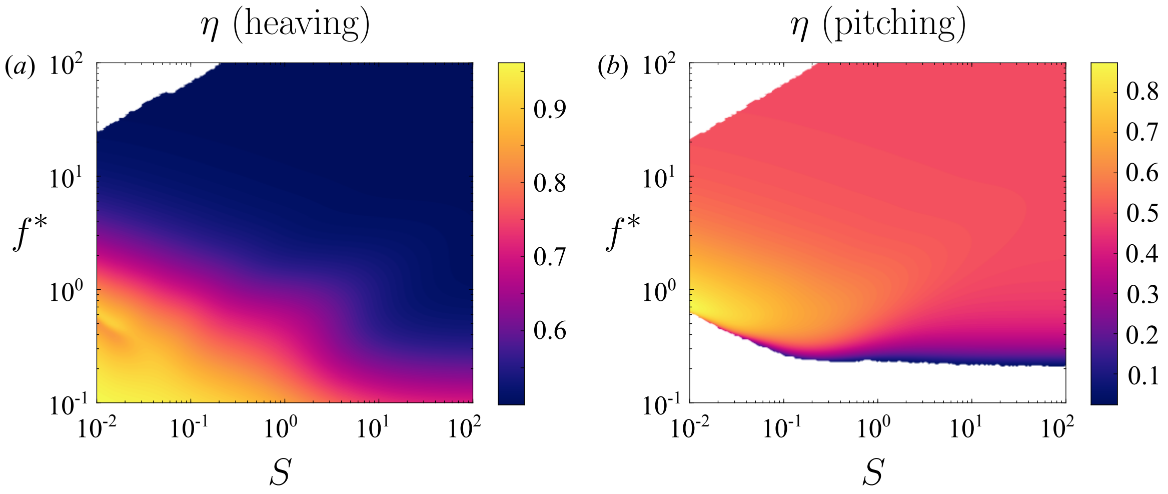

Figure 10.13: Efficiency as a function of reduced frequency f^* and stiffness ratio S for a (a) heaving and (b) pitching plate with $R = 0.01$. Under-resolved areas and areas with negative efficiency have been whited out.

that for a rigid pitching plate, the efficiency monotonically increases with reduced frequency, not displaying any local maximum. For both heaving and pitching plates, the efficiency generally increases as the non-dimensional stiffness decreases.

To isolate the effects of flexibility, we have plotted the difference in efficiency between the flexible and rigid swimmers in figure 10.14, with a dashed white line indicating where flexible and rigid swimmers attain the same efficiencies. We see that the flexible swimmer is broadly more efficient than the rigid swimmer (in fact, the flexible heaving plate always attains greater efficiency than the rigid heaving plate). This leads us to conclude that flexibility generally makes a swimmer more efficient, at least for low mass ratios. The mechanism for increased efficiency, however, is unclear. What about passive flexibility makes a swimmer more efficient?

It is apparent that the efficiency is not related to the quiescent natural frequencies. Whereas both mean thrust and mean power have ridges of local maxima aligned with the quiescent natural frequencies, this is not the case for the efficiency. The efficiency instead has a single broad region of high values in the stiffness-frequency plane. Elsewhere in the plane, the local maxima in thrust and power cancel each other

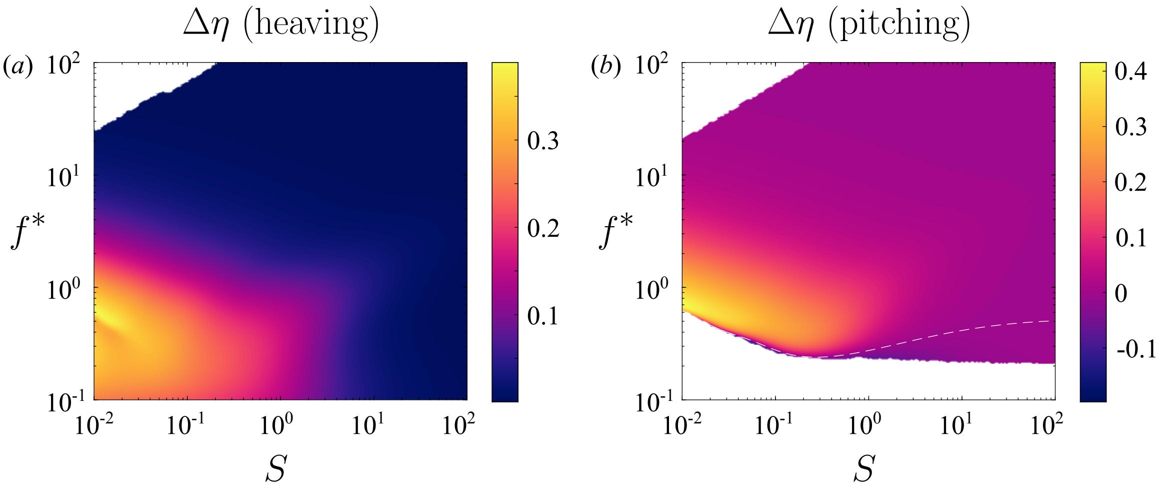

Figure 10.14: Efficiency as a function of reduced frequency f^* and stiffness ratio S for a (a) heaving and (b) pitching plate with $R = 0.01$ relative to that of an equivalent rigid plate. Dashed white lines indicate where the flexible plate has the same efficiency as the equivalent rigid plate. Under-resolved areas and areas with negative efficiency have been whited out.

exactly, resulting in flat efficiency; such behaviour has been previously observed in linear models of passively flexible swimmers (Alben, 2008b; Moore, 2014, 2017). The broad region of high efficiency is aligned with a line for which reduced frequency decreases with non-dimensional stiffness, opposite the behaviour of the quiescent natural frequencies.

10.4.3 Fluid-structure eigenvalues and their relationship with efficiency

While the efficiency appears to be unrelated to the quiescent natural frequencies, it may be possible that it is related to the full eigenvalues of the system. In the quiescent limit, the forces at play are the elastic forces from the plate and the added mass forces from the fluid, with lift forces being negligible. In the full problem, however, lift forces may be important. We expect the lift forces to be dominant when the reduced frequency and non-dimensional stiffness are low, which is where the region

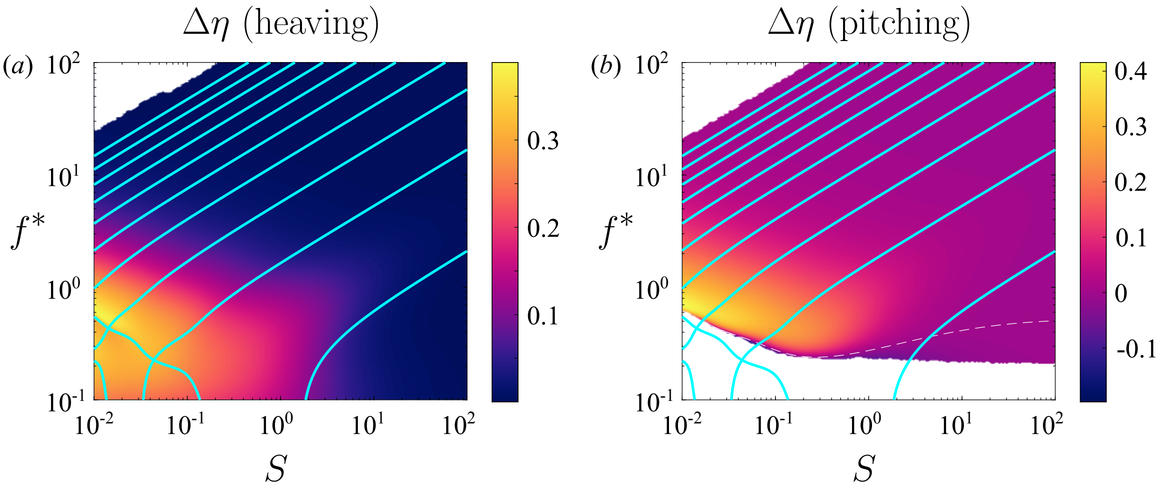

Figure 10.15: Same as in figure 10.14, but with natural frequencies overlaid as cyan lines.

of high efficiency is, and where the behaviours of the trailing edge amplitude, mean thrust, and mean power deviate from the behaviour of the quiescent eigenvalues.

In figure 10.15, we again show the difference in efficiency between flexible and rigid swimmers, but now with the full natural frequencies overlaid. When the reduced frequency and non-dimensional stiffness are high, the natural frequencies match closely with the quiescent natural frequencies, as expected. For low values of the reduced frequency and non-dimensional stiffness, lift forces become important and affect the natural frequencies, causing them to deviate from their quiescent behaviour. We even see the emergence of branches for which the reduced frequencies increase as the non-dimensional stiffness decreases, counter to our intuition for flexible plates. The region of high efficiency is aligned with the counterintuitive branch of natural frequencies, leading us to suspect that this strange branch may be responsible for high efficiency; we therefore find it paramount to understand the behaviour of the eigenvalues of the system.

In figure 10.16, we trace the first three eigenvalue pairs of the full coupled fluid-structure system as the non-dimensional stiffness decreases. Note that the eigenvalues are solutions of a nonlinear eigenvalue problem, so eigenvalues may appear and dis-

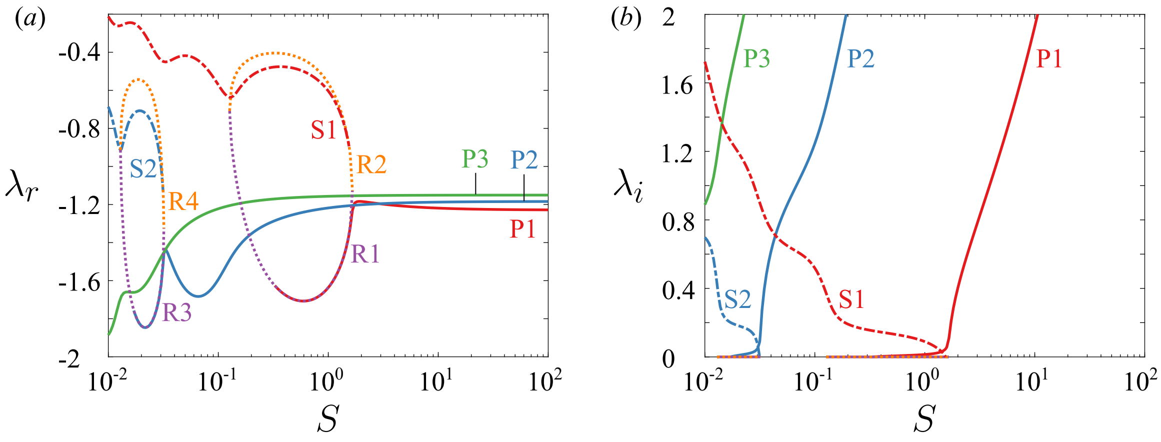

Figure 10.16: First few eigenvalues of the system as a function of stiffness ratio S: (a) real parts; and (b) imaginary parts.

appear. Also note that the imaginary parts of the eigenvalues in figure 10.16b are greater than those in figure 10.15 by a factor of π because of how we have chosen to define f^*. In the following description of the eigenvalues, we begin at large stiffness ratio S and describe how the eigenvalues change as we decrease S, since the eigenvalues essentially behave as those for an Euler-Bernoulli beam *in vacuo* for large S.

As the stiffness ratio decreases, the first three eigenvalues behave as expected: the imaginary parts decrease, and the real parts do not change. We shall refer to these as primary eigenvalues, and label them P1, P2, and P3. As S further decreases, the behaviour of P1 changes: its real part first increases a bit, then decreases dramatically, and then begins to loop up; its imaginary part first decreases more quickly, then decreases substantially more slowly, until it finally decays to zero. At this point ($S = 0.327$), P1 merges with one of the two real eigenvalues that have appeared, labelled R1 and R2. The two real eigenvalues appear when $S = 1.658$, shortly after the behaviour of P1 changes, and they merge and disappear when $S = 0.127$. Just after the two real eigenvalues appear, a new conjugate pair, labelled S1, appears when $S = 1.549$. We refer to this eigenvalue as a secondary eigenvalue because it essentially replaces the primary eigenvalue P1. We summarize the behaviour as follows: the original primary eigenvalue, P1, has decreasing imaginary part until it becomes purely real. In this time, a pair of real eigenvalues, R1 and R2, appear. P1 and R1 merge when P1 becomes real, and they eventually disappear, along with R2, when they all collide. A new conjugate pair of secondary eigenvalues, S1, appears as well, and both its real and imaginary parts increase as S decreases. The second primary eigenvalue P2 essentially demonstrates the same behaviour, and we hazard a guess that P3 shows the beginnings of the same behaviour.

What physical mechanism is at the root of the observed behaviour in the eigenvalues? It should be clear that P1 is an Euler-Bernoulli mode, since it essentially displays the behaviour of an eigenvalue of an Euler-Bernoulli beam *in vacuo*. To be more precise, the behaviour of P1 is dominated by elastic and added mass forces, leading to Euler-Bernoulli type behaviour. S1, on the other hand, is a flutter mode. S1 emerges when the stiffness ratio is low, and so its behaviour is dominated by lift and added mass forces. Both the real and imaginary parts of S1 increase as the stiffness ratio decreases, characteristic of a flutter mode. The stiffness ratio can also be thought of as the inverse of a reduced flow velocity, as in Eloy et al. (2007), whereby increasing the reduced flow velocity leads to a flutter instability. If we decreased S even further, S1 would eventually become unstable. When the non-dimensional stiffness is $O(1)$, P1, S1, R1, and R2 simultaneously exist. For such values of the non-dimensional stiffness, all three types of forces— elastic, lift, and added mass— are non-negligible. The importance of all three types of forces explains why all three modes— Euler-Bernoulli, flutter, and divergence (R1 and R2)— simultaneously exist.

The same emergence and disappearance of modes occurs for the higher-order modes as well, but at lower values of the stiffness ratio. The change in behaviour occurs at lower values of S because the higher-order modes have shorter wavelengths (see Alben, 2008a, for example), significantly increasing the Y_{xxxx} term in (10.3), thereby significantly increasing the magnitude of the elastic forces. We therefore expect the elastic forces to become dominated by lift forces at much lower values of S for the higher-order modes.

As the non-dimensional stiffness decreases, the eigenvalues of the system come closer together in the complex plane. When multiple eigenvalues are relatively close to each other, our notion of resonance, schematically illustrated in figure 10.8, becomes muddied. In figure 10.17, we schematically illustrate the magnitude of a transfer function with *multiple* poles that are relatively close to each other. In figure 10.17a, the poles of the transfer function are marked as crosses, and the contour lines show level sets of the magnitude of the transfer function in the complex plane. Because the poles are close to each other, the level sets are no longer simple circles. Since our actuation is sinusoidal, we are specifically interested in the behaviour along the imaginary axis; this is shown in figure 10.17b. Because the poles are close to each other, there are no longer local maxima when the system is actuated at one of its natural frequencies; instead, there is a broad response across the range of natural frequencies. In our example, there is a single local maximum despite there being four poles. Moreover, the local maximum does not occur at any of the natural frequencies of the system, it occurs between the imaginary parts of λ_3 and λ_4. This schematic explains why the ridges of local maxima in trailing edge amplitude, mean thrust, and mean power broaden and smear together as the reduced frequency and non-dimensional stiffness become small (see figures 10.6, 10.9, and 10.10).

With a good understanding of the eigenvalues of the system, we may now interpret the behaviour of the efficiency in light of the behaviour of the eigenvalues. Specifically, we want to understand the difference in efficiency between flexible and rigid swimmers (i.e. figures 10.14 and 10.15). Broadly speaking, we expect a flexible swimmer to be more efficient than a rigid one for a simple reason: as a flexible swimmer moves through the fluid, its body deforms in response to the forcing from the fluid, so it

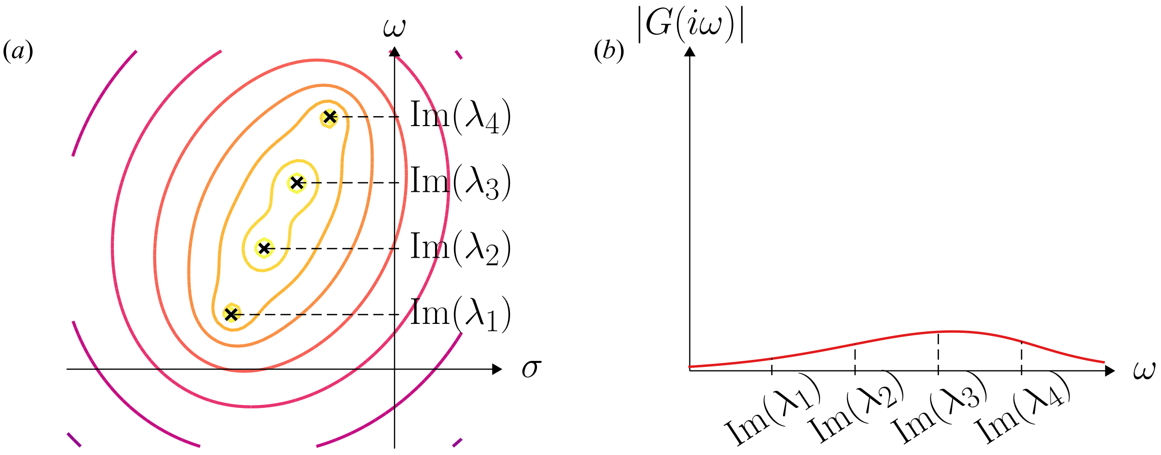

Figure 10.17: Our simple notion of resonance becomes unclear when multiple poles are relatively close. (a) Level sets on the complex plane of the magnitude of a transfer function with four poles, marked with crosses. (b) Magnitude of the same transfer function evaluated on the imaginary axis.

does not need to fight against the fluid as much as a non-deforming rigid swimmer does. A flexible swimmer therefore expends less energy in driving its motion than a rigid swimmer does. This effect becomes more pronounced as the elastic forces weaken relative to the lift forces— as the swimmer becomes flimsier. As previously discussed, the elastic forces weaken relative to the lift forces as the non-dimensional stiffness S decreases. The elastic forces also become relatively weaker when the frequency of actuation is decreased. As we can see from the eigenvalues in figure 10.15, a lower reduced frequency will excite lower-order modes. The lower-order modes have longer wavelengths, and therefore relatively weaker elastic forces. To summarize, decreasing S and f^* weakens the elastic forces in the swimmer, thereby weakening its ability to resist the fluid, lowering the power needed to drive its motion, and making it more efficient.

This is not the complete picture, however. As we can see in figure 10.15, in the lower left region there are areas where decreasing S and *increasing* f^* improves the efficiency, counter to our previous argument. This behaviour can be understood in terms of the changing behaviour of the eigenvalues of the system in that region.

When S becomes small enough, the primary eigenvalue is essentially replaced by the secondary eigenvalue. Recall that the primary eigenvalue corresponds to an Euler-Bernoulli mode, and the secondary eigenvalue corresponds to a flutter mode. Euler-Bernoulli modes are dominated by elastic forces, while flutter modes are dominated by lift forces. Based on the previous discussion, swimmers whose composition includes flutter modes should be more efficient.

A comparison between Euler-Bernoulli mode P2 and flutter mode S1 for $S = 0.1$ is shown in figure 10.18, where the modes have been normalized so that their second derivatives at the leading edge are real and equal to 1. Qualitatively, the flutter mode looks more efficient than the Euler-Bernoulli mode, with the Euler-Bernoulli mode having a rigid fore and aft. To quantify this observation, in figure 10.19 we have plotted the magnitudes of the modes as well as the phase between the leading edge and the deflection along the chord for the two modes, normalized as before. The deflection of flutter mode S1 is greater than that of Euler-Bernoulli mode P2 along the entire chord. The phase is flat for a large portion of the fore of Euler-Bernoulli mode P2, indicating that it moves rigidly. The phase also flattens out towards the aft, indicating that it too is nearly rigid. In contrast, flutter mode S2 has a nearly linearly decreasing phase. A front-to-back travelling wave would have a linearly decreasing phase, so flutter mode S1 essentially behaves as a travelling wave (with spatially varying amplitude). As shown in Wu (1961), travelling wave kinematics can be quite efficient. The emergence of the flutter modes as S decreases leads to travelling wave kinematics in the actuated system. For a value of S for which a flutter mode exists, the phase of the deflection decreases nearly linearly when the system is actuated at a low frequency, indicating that the kinematics are nearly a travelling wave. As the frequency of actuation is increased, the phase behaves less linearly, instead alternating between relatively flat and steep behaviours; the degradation of the travelling wave kinematics is more severe as the frequency of actuation is increased. The behaviour at

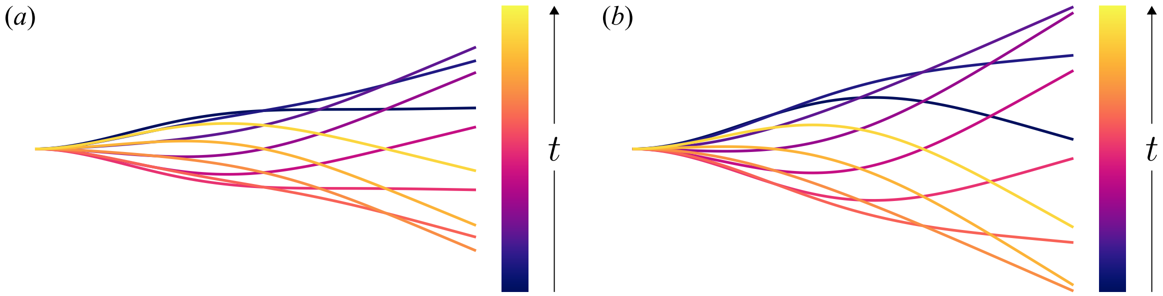

Figure 10.18: Ten snapshots, evenly spaced in time, of (a) Euler-Bernoulli mode P2 and (b) flutter mode S1 for $S = 0.1$ comprising one period of motion. The modes have been normalized so that their second derivatives at the leading edge are real and equal to 1.

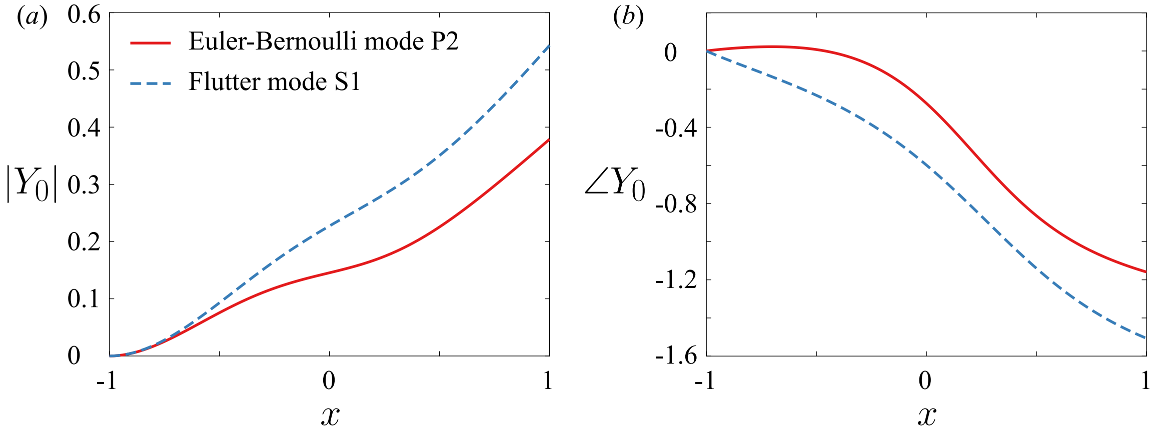

Figure 10.19: (a) Magnitude and (b) phase in radians of the deflection along the chord for Euler-Bernoulli mode P2 (red) and flutter mode S1 (blue), for $S = 0.1$. The modes have been normalized so that their second derivatives at the leading edge are real and equal to 1.

low frequencies is therefore dominated by the flutter modes, while the Euler-Bernoulli modes become dominant at higher frequencies. The frequency at which the travelling wave kinematics degrade increases as S decreases, coinciding with the frequency at which the efficiency degrades, and with the behaviour of the imaginary parts of the flutter eigenvalues. We may therefore reasonably conclude that the emergence of the flutter modes as S decreases makes the swimmer more efficient.

As a final note, we point out that increases in efficiency are often intertwined with decreases in thrust. This is apparent when comparing the plots of mean thrust with the plots of efficiency (figures 10.9 and 10.14, respectively). To generate large thrust, the swimmer needs to be able to push against the fluid. To be efficient, however, the swimmer needs to be compliant to the fluid. A limiting case of this is when the body of the swimmer takes the form of a front-to-back travelling wave. As the wave velocity approaches the free-stream velocity, the thrust vanishes, the efficiency approaches unity, and the swimmer merely travels along a sinusoidal path fixed in space (Wu, 1961). We must be mindful of regions of low thrust, especially in the presence of drag, as we shall explore in the next section.

10.5 Finite Reynolds number effects

Recently, the effects of streamwise drag on efficiency have come to be appreciated, at least for rigid swimmers (Floryan et al., 2017a). Drag can create peaks in efficiency and can make the efficiency quite sensitive to changes in the system, as also suggested in Moore (2014). Here, we consider how streamwise drag due to a finite Reynolds number affects the system.

The presence of drag in our system does not change it much. The kinematics will not change, so the trailing edge amplitude remains unchanged. The net thrust produced decreases uniformly across the stiffness-frequency plane, leaving the picture qualitatively the same. The power consumption also does not change. The efficiency, however, will change. Whereas before there were no local maxima in efficiency, the addition of an offset drag to the system will spur the emergence of ridges of local maxima in efficiency, just like the ones previously described for the trailing edge amplitude, mean thrust, and mean power.

The ridges of local maxima in efficiency caused by the addition of an offset drag can be understood in a simple way. We will consider a simplified picture of resonance in our system. Suppose we actuate the inviscid system at a non-resonant frequency, resulting in mean thrust coefficient $\overline{C_{T0}}$, mean power coefficient $\overline{C_{P0}}$, and efficiency $\eta_0 = \overline{C_{T0}}/\overline{C_{P0}}$. If we change the frequency of actuation to a resonant one, our previous results show that the mean thrust coefficient, power coefficient, and efficiency will become

$$\overline{C_{T1}} = a\overline{C_{T0}}, \quad \overline{C_{P1}} = a\overline{C_{P0}}, \quad \eta_1 = \frac{\overline{C_{T1}}}{\overline{C_{P1}}} = \frac{a\overline{C_{T0}}}{a\overline{C_{P0}}} = \frac{\overline{C_{T0}}}{\overline{C_{P0}}} = \eta_0, \tag{10.11}$$

where $a > 1$. We see that resonance does not alter the efficiency when there is no drag.

Now consider adding streamwise drag to the system. The baseline mean thrust changes by an offset, and the mean power does not change. The baseline efficiency is then

$$\eta_0 = \frac{\overline{C_{T0}} - C_D}{\overline{C_{P0}}} = \frac{\overline{C_{T0}}}{\overline{C_{P0}}} - \frac{C_D}{\overline{C_{P0}}}, \tag{10.12}$$

where C_D is the drag coefficient. When we actuate at resonance, the mean thrust and mean power increase as before, and the drag does not change. The efficiency becomes

$$\eta_1 = \frac{a\overline{C_{T0}} - C_D}{a\overline{C_{P0}}} = \eta_0 + \frac{a-1}{a}\frac{C_D}{\overline{C_{P0}}} > \eta_0. \tag{10.13}$$

We see that the addition of streamwise drag to the system causes local maxima in efficiency when the system is actuated at a natural frequency. This effect should be robust to the source of drag. Note that this effect depends on how strongly resonance affects the system (the value of a), and on how strong the drag is ($C_D/\overline{C_{P0}}$). We demonstrate this effect in figure 10.20, where we show the efficiency for $C_D = 0.1$ (Floryan et al., 2017a). Since the effect depends on the ratio $C_D/\overline{C_{P0}}$, just for this

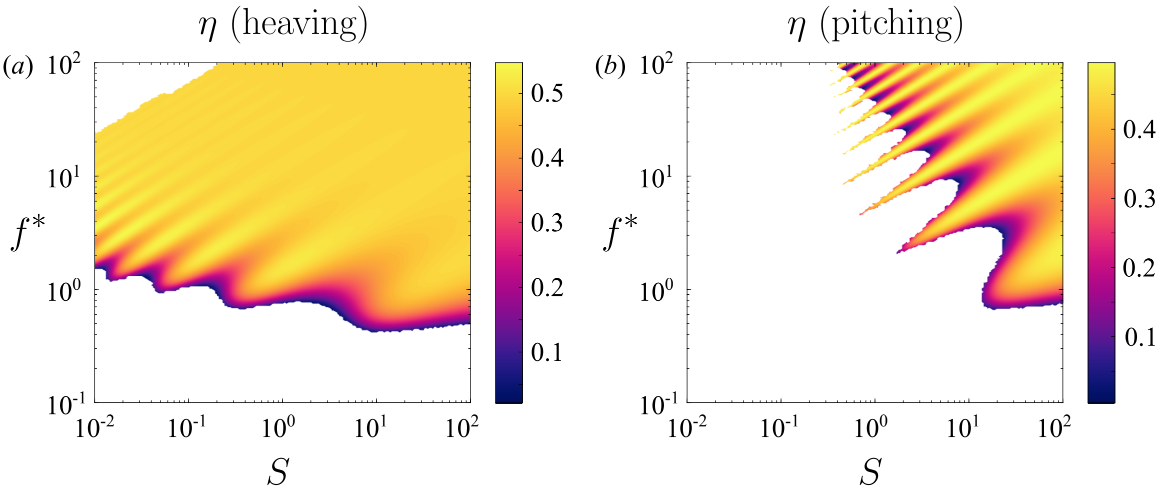

Figure 10.20: Efficiency as a function of reduced frequency f^* and stiffness ratio S for a (a) heaving and (b) pitching plate with $R = 0.01$ with additional drag. Under-resolved areas and areas with negative efficiency have been whited out.

plot we have changed the amplitudes to $h_0 = 0.2$ and $\theta_0 = 0.1$. Indeed, we see ridges of local maxima in efficiency which align with the natural frequencies. We also note that the addition of streamwise drag has pushed the thrust-drag transition to significantly higher values of the reduced frequency; this underscores the importance of streamwise drag for swimmers.

Since any real system will have some drag, resonant peaks in efficiency should be present. We offer our simple explanation as a reason for the existence of resonant peaks in efficiency observed in the literature, modulo nonlinear effects. Since our analysis is linear, the aforementioned effect of streamwise drag on the efficiency of the system is present at first order, and we therefore expect it to be robust to nonlinear effects.

10.6 Conclusions

In this work, we studied a linear inviscid model of a passively flexible swimmer, valid for small-amplitude, low-frequency motions where there is no separation. The frequencies of actuation and stiffness ratios we considered spanned a large range, while the mass ratio was mostly fixed to a low value representative of swimmers. A short set of results for which we varied the mass ratio indicates that there exist qualitative differences between flappers with low mass ratios (swimmers) and those with mass ratios of order unity and higher (fliers). The results presented in this work are therefore applicable to swimmers, and care should be taken in extending the results to fliers.

We presented results showing how the trailing edge deflection, thrust coefficient, power coefficient, and efficiency vary in the stiffness-frequency plane. The trailing edge deflection, thrust coefficient, and power coefficient showed sharp ridges of resonant behaviour for reduced frequencies $f^* > 1$ and stiffness ratios $S > 1$. In this region, the locations of the resonant peaks were well predicted by the imaginary parts of the quiescent eigenvalues of the system. For $f^* < 1$ and $S < 1$, however, the resonant peaks smeared together. The efficiency, on the other hand, did not show resonant peaks anywhere in the stiffness-frequency plane, instead showing a broad region of high values for $f^* < 1$ and $S < 1$.

Calculating the full eigenvalues and eigenfunctions of the system, we saw that the region of high efficiency coincided with the emergence of flutter modes and disappearance of Euler-Bernoulli modes. The imaginary parts of the eigenvalues of the flutter modes increase with decreasing stiffness ratio, opposite to the behaviour of the Euler-Bernoulli modes. The eigenfunctions revealed that flutter modes take on a form close to a travelling wave, whereas the Euler-Bernoulli modes have nearly rigid regions. In the actuated system, cases with high efficiency took on near travelling wave forms, and the degradation of efficiency coincided with a degradation of the travelling wave. We may therefore reasonably conclude that the emergence of the flutter modes as S decreases makes the swimmer more efficient.

Lastly, we considered the effects of a finite Reynolds number in the form of streamwise drag. Streamwise drag added an offset drag to the system, which created resonant peaks in the efficiency that are not present in the inviscid system. Since any real system will have some streamwise drag, resonant peaks should be present. We offer our simple explanation as a reason for the existence of resonant peaks in efficiency observed in the literature.

This work was supported by ONR Grant N00014-14-1-0533 (Program Manager Robert Brizzolara). We would also like to thank Dr. Andres Goza for many useful discussions.

10.A Method of solution

Consider the case where the imposed leading edge motion is sinusoidal in time with dimensionless angular frequency $\sigma = \pi L f / U$, where f is the dimensional frequency in Hz. We may then decompose the deflection into a product of temporal and spatial terms, with the temporal component being sinusoidal and the spatial component represented by a Chebyshev series:

$$\left.\begin{aligned} Y(x,t) &= \mathrm{e}^{\mathrm{j}\sigma t} Y_0(x), \\ Y_0(x) &= \frac{1}{2}\beta_0 + \sum_{k=1}^{\infty} \beta_k T_k(x), \end{aligned}\right\} \tag{10.14}$$

where $\mathrm{j} = \sqrt{-1}$, the real part in j should be taken when evaluating the deflection, and $T_k(x) = \cos(k \arccos x)$ is the Chebyshev polynomial of degree k. For a given deflection Y of this form, the solution to the flow is given in Wu (1961); we repeat the basics of that analysis in the proceeding text.

Represent two-dimensional physical space (x, y) by the complex plane $z = x + \mathrm{i}y$, where $\mathrm{i} = \sqrt{-1}$ but $\mathrm{ij} \neq -1$. There exists a complex potential $F(z,t) = \phi(z,t) +$

i$\psi(z,t)$, with ϕ and ψ harmonic conjugates, that is analytic in z and related to the complex velocity $w = u - \mathrm{i}v$ through the momentum equation by

$$\frac{\partial F}{\partial z} = \frac{\partial w}{\partial t} + \frac{\partial w}{\partial z}. \tag{10.15}$$

We use the conformal transformation

$$z = \frac{1}{2}\left(\zeta + \frac{1}{\zeta}\right) \tag{10.16}$$

to map physical space in the z-plane to the exterior of the unit circle in the ζ-plane. This transformation maps the plate onto the unit circle. The complex potential can be represented by a multipole expansion

$$F(\zeta,t) = \phi(\zeta,t) + \mathrm{i}\psi(\zeta,t) = \mathrm{i}\mathrm{e}^{\mathrm{j}\sigma t}\left(\frac{a_0}{\zeta+1} + \sum_{k=1}^{\infty}\frac{a_k}{\zeta^k}\right). \tag{10.17}$$

Evaluating on the unit circle $\zeta = \mathrm{e}^{\mathrm{i}\theta}$ gives

$$\left.\begin{aligned}\phi(\zeta = \mathrm{e}^{\mathrm{i}\theta}, t) &= \mathrm{e}^{\mathrm{j}\sigma t}\left(\frac{1}{2}a_0\tan\frac{\theta}{2} + \sum_{k=1}^{\infty} a_k \sin k\theta\right),\\ \psi(\zeta = \mathrm{e}^{\mathrm{i}\theta}, t) &= \mathrm{e}^{\mathrm{j}\sigma t}\left(\frac{1}{2}a_0 + \sum_{k=1}^{\infty} a_k \cos k\theta\right).\end{aligned}\right\} \tag{10.18}$$

In physical space, on the surface of the plate we have

$$\left.\begin{aligned}\phi(z = x \pm 0\mathrm{i}, t) &= \mathrm{e}^{\mathrm{j}\sigma t}\Phi^{\pm}(x) = \mathrm{e}^{\mathrm{j}\sigma t}\left(\pm\frac{1}{2}a_0\sqrt{\frac{1-x}{1+x}} \pm \sum_{k=1}^{\infty} a_k \sin k\theta\right),\\ \psi(z = x \pm 0\mathrm{i}, t) &= \mathrm{e}^{\mathrm{j}\sigma t}\Psi(x) = \mathrm{e}^{\mathrm{j}\sigma t}\left(\frac{1}{2}a_0 + \sum_{k=1}^{\infty} a_k T_k(x)\right),\end{aligned}\right\} \tag{10.19}$$

where we have used $x = \cos\theta$. ψ has equal values on the top and bottom since it is even in θ, whereas ϕ is odd in θ and thus has a discontinuity in physical space.

The no-penetration condition can be written as

$$\frac{\partial\psi}{\partial x}|_{y=0} = -\left(\frac{\partial}{\partial t} + \frac{\partial}{\partial x}\right)^2 Y, \tag{10.20}$$

which simplifies to

$$D\Psi = -(\mathrm{j}\sigma + D)^2 Y_0, \tag{10.21}$$

where $D = \mathrm{d}/\mathrm{d}x$. Given Y_0, this equation allows us to solve for all a_k except a_0. To solve for a_0, we begin by writing the vertical velocity on the surface of the plate as

$$v(z = x + 0\mathrm{i}, t) = \mathrm{e}^{\mathrm{j}\sigma t} V(x) = \mathrm{e}^{\mathrm{j}\sigma t}\left(\frac{1}{2}V_0 + \sum_{k=1}^{\infty} V_k T_k(x)\right). \tag{10.22}$$

The no-penetration condition can then be written as

$$V = (\mathrm{j}\sigma + D)Y_0. \tag{10.23}$$

The coefficient a_0 is given by

$$a_0 = -C(\mathrm{j}\sigma)(V_0 + V_1) + V_1, \tag{10.24}$$

where

$$C(\mathrm{j}\sigma) = \frac{K_1(\mathrm{j}\sigma)}{K_0(\mathrm{j}\sigma) + K_1(\mathrm{j}\sigma)} \tag{10.25}$$

is the Theodorsen function, and K_ν is the modified Bessel function of the second kind of order ν. The expression for a_0 is derived in Wu (1961).

With all of the a_k known, the pressure difference across the plate can be written as

$$\Delta p(x, t) = \mathrm{e}^{\mathrm{j}\sigma t} P_0(x) = \mathrm{e}^{\mathrm{j}\sigma t}\left(a_0\sqrt{\frac{1-x}{1+x}} + 2\sum_{k=1}^{\infty} a_k \sin k\theta\right). \tag{10.26}$$

We note that the pressure difference depends linearly on the deflection Y_0.

Altogether, given the deflection Y_0, we may calculate the coefficients a_k. The coefficients a_k are used to calculate the pressure difference across the plate, which alters the deflection of the plate via (10.3). The coupled fluid-structure problem must be solved numerically.

10.A.1 Numerical method

Substituting the Chebyshev series (10.14) into the Euler-Bernoulli equation (10.3) gives a fourth-order differential equation for Y_0:

$$-2\sigma^2 R Y_0 + \frac{2}{3} S D^4 Y_0 = P_0. \tag{10.27}$$

The corresponding boundary conditions (10.6) are re-written as

$$Y_0(-1) = h_0, \quad Y_{0,x}(-1) = \theta_0, \quad Y_{0,xx}(1) = 0, \quad Y_{0,xxx}(1) = 0, \tag{10.28}$$

where h_0 and θ_0 are the heaving and pitching amplitudes at the leading edge, respectively. We re-iterate that the pressure difference across the plate P_0 is a linear function of the deflection Y_0, and so (10.27)–(10.28) give a linear, homogemeous boundary value problem for Y_0. When solving for the deflection Y_0, all infinite series are truncated to the upper limit N.

The numerical method to solve the boundary value problem is given in Moore (2017). The method is a pseudo-spectral Chebyshev scheme that uses Gauss-Chebyshev points. The method is fast ($O(N \log N)$) and accurate, avoiding errors typically encountered when using Chebyshev methods to solve high-order differential equations by pre-conditioning the system with continuous operators. Quadrature formulas for the thrust and power coefficients in (10.7) and (10.8) are also given in Moore (2017).

10.B Eigenvalues of the system

Here, we seek to determine the natural response of a flexible plate whose leading edge is held clamped in an oncoming flow (Alben, 2008a; Michelin and Llewellyn Smith, 2009; Eloy et al., 2007). This amounts to finding the eigenvalues and eigenvectors of the system (10.3) with homogeneous boundary conditions ($h(t) \equiv 0$ and $\theta(t) \equiv 0$). To do so, quantities that were previously written as Fourier-Chebyshev expansions (the deflection, complex potential, and velocity) are now written as Chebyshev series with time-varying coefficients. Following the preceding analysis, we arrive at the following equations:

$$2RY_{tt} + \frac{2}{3}SY_{xxxx} = \Delta p, \tag{10.29}$$

$$Y(x,t) = \frac{1}{2}\beta_0(t) + \sum_{k=1}^{\infty} \beta_k(t) T_k(x), \tag{10.30}$$

$$\Delta p(x,t) = a_0(t)\sqrt{\frac{1-x}{1+x}} + 2\sum_{k=1}^{\infty} a_k(t) \sin k\theta, \tag{10.31}$$

$$\sum_{k=1}^{\infty} a_k T_k' = -\frac{1}{2}\ddot{\beta}_0 - \sum_{k=1}^{\infty} \left[\ddot{\beta}_k T_k + 2\dot{\beta}_k T_k' + \beta_k T_k''\right], \tag{10.32}$$

where a dot denotes differentiation with respect to t and a prime denotes differentiation with respect to x.

As before, we need an additional equation to determine a_0. For now, we use (10.24) but treat the Theodorsen function as a constant C. The coefficient a_0 is then

$$a_0 = -C(V_0 + V_1) + V_1, \tag{10.33}$$

where V_k is the kth Chebyshev coefficient of the vertical velocity on the surface of the plate. The V_k are obtained by evaluating the no-penetration condition (10.5):

$$\frac{1}{2}V_0 + \sum_{k=1}^{\infty} V_k T_k = \frac{1}{2}\dot{\beta}_0 + \sum_{k=1}^{\infty} \left[\dot{\beta}_k T_k + \beta_k T_k'\right]. \tag{10.34}$$

Treating a_0 in this manner will yield a linear eigenvalue problem. After obtaining the eigenvalues and eigenfunctions of the linear eigenvalue problem, we will use those as initial guesses for the nonlinear eigenvalue problem, which will use the full Theodorsen function. But first, we proceed with the description of the linear eigenvalue problem.

We can write the equations more compactly as follows:

$$2R\ddot{\boldsymbol{\beta}} + \frac{2}{3}SD^4\boldsymbol{\beta}) = \boldsymbol{P}, \tag{10.35}$$

$$\boldsymbol{P} = A\boldsymbol{a}, \tag{10.36}$$

$$D\boldsymbol{a} = -\ddot{\boldsymbol{\beta}} - 2D\dot{\boldsymbol{\beta}} - D^2\boldsymbol{\beta}, \tag{10.37}$$

$$\boldsymbol{V} = \dot{\boldsymbol{\beta}} + D\boldsymbol{\beta}, \tag{10.38}$$

with (10.33) for a_0. In the above, $\boldsymbol{\beta}$ is a vector of the Chebyshev coefficients of the deflection Y, and similarly for $\boldsymbol{P}$ (pressure), $\boldsymbol{a}$ (potential), and $\boldsymbol{V}$ (vertical velocity). $\boldsymbol{P} = A\boldsymbol{a}$ simply states that the Chebyshev coefficients of the pressure are linear combinations of the coefficients a_k, and D is the spectral representation of the differentiation operator.

Putting everything together, we get the following ordinary differential equation:

$$\begin{aligned} 2R\ddot{\boldsymbol{\beta}} + \frac{2}{3}SD^4\boldsymbol{\beta}) &= A[-D^-\ddot{\boldsymbol{\beta}} - 2D^-D\dot{\boldsymbol{\beta}} + \boldsymbol{e_1}(\boldsymbol{e_2} - C\boldsymbol{e_1} - C\boldsymbol{e_2})^T\dot{\boldsymbol{\beta}} \\ &\quad -D^-D^2\boldsymbol{\beta} + \boldsymbol{e_1}(\boldsymbol{e_2} - C\boldsymbol{e_1} - C\boldsymbol{e_2})^T D\boldsymbol{\beta}], \end{aligned} \tag{10.39}$$

where D^- is the spectral representation of the integration operator that makes the first Chebyshev coefficient zero, and $\boldsymbol{e_k}$ is the kth Euclidean basis vector. (10.39) can be written in state-space form as

$$\left.\begin{aligned}
&\frac{\mathrm{d}}{\mathrm{d}t}\begin{bmatrix}\boldsymbol{\beta}\\ \dot{\boldsymbol{\beta}}\end{bmatrix} = \begin{bmatrix}0 & I\\ M^{-1}A_1 & M^{-1}A_2\end{bmatrix}\begin{bmatrix}\boldsymbol{\beta}\\ \dot{\boldsymbol{\beta}}\end{bmatrix},\\
&M = 2R + AD^{-},\\
&A_1 = -\frac{2}{3}SD^4 - AD^{-}D^2 + A\boldsymbol{e_1}(\boldsymbol{e_2} - C\boldsymbol{e_1} - C\boldsymbol{e_2})^T D,\\
&A_2 = -2AD^{-}D + A\boldsymbol{e_1}(\boldsymbol{e_2} - C\boldsymbol{e_1} - C\boldsymbol{e_2})^T.
\end{aligned}\right\} \tag{10.40}$$

When numerically solving the system, the infinite series are truncated to finite series. In order to incorporate the four boundary conditions into (10.40), the last four rows of the differential equation for $\ddot{\boldsymbol{\beta}}$ are replaced by the boundary conditions. The system is then

$$\frac{\mathrm{d}}{\mathrm{d}t}\begin{bmatrix}I & 0\\ 0 & I_{-4}\end{bmatrix}\begin{bmatrix}\boldsymbol{\beta}\\ \dot{\boldsymbol{\beta}}\end{bmatrix} = \begin{bmatrix}0 & I\\ M^{-1}A_1 & M^{-1}A_2\end{bmatrix}\begin{bmatrix}\boldsymbol{\beta}\\ \dot{\boldsymbol{\beta}}\end{bmatrix}, \tag{10.41}$$

where I_{-4} is the identity matrix with the last four diagonal entries being zeros. The last four rows of the right-hand side are replaced by the boundary conditions. We now have a generalized eigenvalue problem to solve for the eigenvalues of the system.

10.B.1 Nonlinear eigenvalue problem

Having obtained the solution to the linear eigenvalue problem, we use it as an initial guess for the nonlinear eigenvalue problem. The nonlinear eigenvalue problem is obtained by making the ansatz

$$\left.\begin{aligned}
&Y(x,t) = \mathrm{e}^{\lambda t}Y_0(x),\\
&Y_0(x) = \tfrac{1}{2}\beta_0 + \textstyle\sum_{k=1}^{\infty}\beta_k T_k(x).
\end{aligned}\right\} \tag{10.42}$$

This is the same as in Appendix 10.A, except that we allow the exponent λ to be any complex number instead of just an imaginary number. Proceeding as in Appendix 10.B, we arrive at the following equations:

$$2\lambda^2 R\boldsymbol{\beta} + \frac{2}{3}SD^4\boldsymbol{\beta}) = \boldsymbol{P}, \tag{10.43}$$

$$\boldsymbol{P} = A\boldsymbol{a}, \tag{10.44}$$

$$D\boldsymbol{a} = -\lambda^2\boldsymbol{\beta} - 2\lambda D\boldsymbol{\beta} - D^2\boldsymbol{\beta}, \tag{10.45}$$

$$\boldsymbol{V} = \lambda\boldsymbol{\beta} + D\boldsymbol{\beta}, \tag{10.46}$$

$$a_0 = -C(\lambda)(V_0 + V_1) + V_1, \tag{10.47}$$

where the notation is as in Appendix 10.B.

Putting everything together, we get the following equation:

$$\begin{aligned} 2\lambda^2 R\boldsymbol{\beta} + \frac{2}{3}SD^4\boldsymbol{\beta}) \;&=\; A[-\lambda^2 D^{-}\boldsymbol{\beta} - 2\lambda D^{-}D\boldsymbol{\beta} + \lambda\boldsymbol{e_1}(\boldsymbol{e_2} - C(\lambda)\boldsymbol{e_1} - C(\lambda)\boldsymbol{e_2})^T\boldsymbol{\beta} \\ &\quad -D^{-}D^2\boldsymbol{\beta} + \boldsymbol{e_1}(\boldsymbol{e_2} - C(\lambda)\boldsymbol{e_1} - C(\lambda)\boldsymbol{e_2})^T D\boldsymbol{\beta}], \end{aligned} \tag{10.48}$$

where the notation is as in Appendix 10.B. Truncating the upper limit of the infinite series to N, (10.48) gives $N+1$ equations for $N+2$ unknowns (the $N+1$ elements of $\boldsymbol{\beta}$ and λ). We add an equation which normalizes $\boldsymbol{\beta}$ in order to make the system square. As before, the last four equations are replaced by the boundary conditions. We solve for $\boldsymbol{\beta}$ and λ using the Newton-Raphson method, using absolute and relative error tolerances 10^{-6}. For cases where the Newton-Raphson method did not converge, we calculated the solution by looking at a global picture of the determinant of the system and finding its roots.

To validate our method for calculating eigenvalues, we calculate the eigenvalues for the same set of parameters as in figure 4(c,d) in Alben (2008a). In figure 10.21, we compare the eigenvalues calculated using our method to some of the eigenvalues

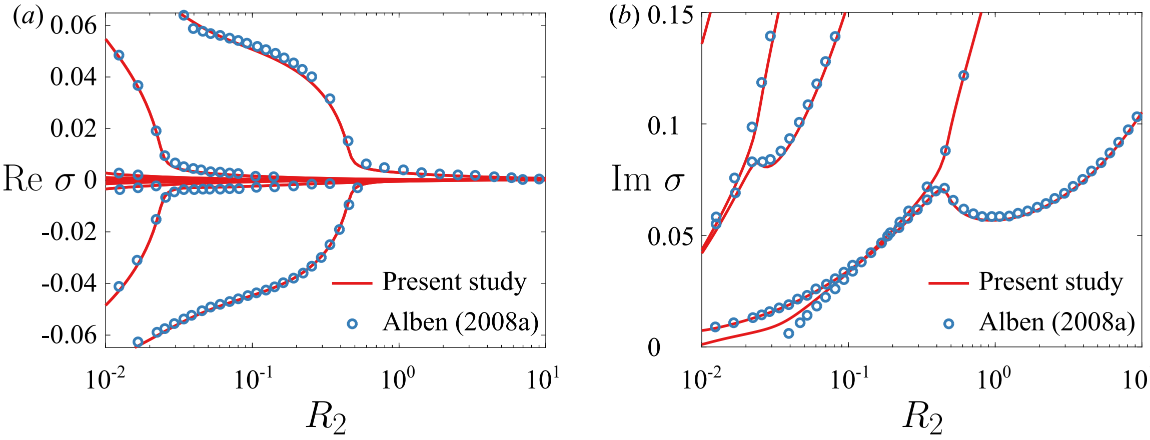

Figure 10.21: Comparison between eigenvalues calculated using our method and those found in figures 4c and 4d in Alben (2008a). Note that just for this figure, we adopt the notation used in Alben (2008a).

in Alben (2008a), adopting the notation used in that work. Our eigenvalues agree well with those from Alben (2008a), lending confidence to our method.

10.B.2 Quiescent fluid

Consider the case where the plate is immersed in a quiescent fluid, i.e. where the bending velocity is large compared to the fluid velocity. How do the eigenvalues of the system change? To answer this question, we solve the Euler-Bernoulli and Euler equations (10.1)–(10.2) in the limit of large bending velocity. In this limit, the appropriate time scale to use is the bending time scale, which we choose to be $\sqrt{3\rho_s L^4/(4Ed^2)}$. Non-dimensionalizing the solid and fluid equations using the length scale $L/2$ and the bending time scale yields

$$\left.\begin{aligned} &Y_{tt} + Y_{xxxx} = \frac{1}{2R}\Delta p, \\ &\nabla \cdot \mathbf{u} = 0, \\ &\mathbf{u}_t + \sqrt{\frac{3R}{S}}\mathbf{u}_x = \nabla\phi, \end{aligned}\right\} \tag{10.49}$$

where R and S are as in (10.4), and $\phi = p_\infty - p$. In the above, x, t, Y, $\mathbf{u}$, and p are now dimensionless, with the pressure non-dimensionalized by $\rho_f Ed^3/(3\rho_s dL^2)$. The limit of a quiescent flow corresponds to $R/S \to 0$, or equivalently $Ed^2/\rho_s L^2 \gg U^2$, which explicitly puts this limit in terms of velocity scales. For now, we keep all terms and discuss the limit later. Intuitively, large values of the solid-to-fluid mass ratio R make the fluid dynamics inconsequential to the deflection of the plate (a heavy plate will be unaffected by the surrounding fluid).

The fluid additionally satisfies the no-penetration condition, stated as

$$v|_{x\in[-1,1],y=0} = Y_t + \sqrt{\frac{3R}{S}}Y_x. \tag{10.50}$$

The boundary conditions on the plate are

$$Y(-1,t) = 0, \quad Y_x(-1,t) = 0, \quad Y_{xx}(1,t) = 0, \quad Y_{xxx}(1,t) = 0. \tag{10.51}$$

We solve for the fluid motion for a given deflection as in Appendix 10.A. Writing the deflection as

$$Y(x,t) = \frac{1}{2}\beta_0(t) + \sum_{k=1}^{\infty}\beta_k(t)T_k(x), \tag{10.52}$$

and the components of the complex potential evaluated on the surface of the plate as

$$\left.\begin{aligned} \phi(z = x \pm 0\mathrm{i}, t) &= \pm\frac{1}{2}a_0(t)\sqrt{\frac{1-x}{1+x}} \pm \sum_{k=1}^{\infty} a_k(t)\sin k\theta, \\ \psi(z = x \pm 0\mathrm{i}, t) &= \frac{1}{2}a_0(t) + \sum_{k=1}^{\infty} a_k(t)T_k(x), \end{aligned}\right\} \tag{10.53}$$

the pressure difference across the surface of the plate is

$$\Delta p(x,t) = a_0(t)\sqrt{\frac{1-x}{1+x}} + 2\sum_{k=1}^{\infty} a_k(t)\sin k\theta. \tag{10.54}$$

The coefficients a_k are obtained by applying the no-penetration condition,

$$\frac{\partial\psi}{\partial x}|_{y=0} = -\left(\frac{\partial}{\partial t} + \sqrt{\frac{3R}{S}}\frac{\partial}{\partial x}\right)^2 Y. \tag{10.55}$$

This does not yield a_0, which is instead given by the Laplace domain equation

$$a_0 = -\sqrt{\frac{3R}{S}}C(V_0 + V_1) + \sqrt{\frac{3R}{S}}V_1. \tag{10.56}$$

In the limit of a quiescent fluid ($R/S \to 0$), $a_0 \to 0$. Thus all of the coefficients a_k are determined by (10.55), which itself simplifies since the second term in the parentheses is zero in the limit $R/S \to 0$. We note that in this limit the only fluid force on the plate is the force due to added mass.

Putting everything together, we get the following ordinary differential equation:

$$\ddot{\boldsymbol{\beta}} + D^4\boldsymbol{\beta} = -\frac{1}{R}AD^-\ddot{\boldsymbol{\beta}}, \tag{10.57}$$

where $\boldsymbol{\beta}$ is the vector of coefficients β_k, D is the spectral representation of the differentiation operator, and D^- is the spectral representation of the integration operator that makes the first Chebyshev coefficient zero. The operator A maps the coefficients a_k, which are the coefficients of a *sine* series for the pressure, into the corresponding coefficients of a *cosine* series. If T_s is an operator that takes us from the x-domain to the sine domain, and T_c is an operator that takes us from the x-domain to the cosine domain, then $A = T_c T_s^{-1}$. (10.57) can be written in state-space form as

$$\frac{\mathrm{d}}{\mathrm{d}t}\begin{bmatrix}\boldsymbol{\beta}\\ \dot{\boldsymbol{\beta}}\end{bmatrix} = \begin{bmatrix} 0 & I \\ -\left(I + \frac{1}{R}AD^-\right)^{-1} D^4 & 0\end{bmatrix}\begin{bmatrix}\boldsymbol{\beta}\\ \dot{\boldsymbol{\beta}}\end{bmatrix}. \tag{10.58}$$

When numerically solving the system, the infinite series are truncated to finite series. In order to incorporate the four boundary conditions into (10.59), the last four rows of the differential equation for $\ddot{\boldsymbol{\beta}}$ are replaced by the boundary conditions. This is fine to do since the last four rows read $\ddot{\beta}_k = 0$ due to four applications of the differentiation operator D. The system is then

$$\frac{\mathrm{d}}{\mathrm{d}t}\begin{bmatrix} I & 0 \\ 0 & I_{-4} \end{bmatrix}\begin{bmatrix} \boldsymbol{\beta} \\ \dot{\boldsymbol{\beta}} \end{bmatrix} = \begin{bmatrix} 0 & I \\ -\left(I + \frac{1}{R}AD^{-}\right)^{-1} D^4 & 0 \end{bmatrix}\begin{bmatrix} \boldsymbol{\beta} \\ \dot{\boldsymbol{\beta}} \end{bmatrix}, \tag{10.59}$$

where I_{-4} is the identity matrix with the last four diagonals being zeros. The last four rows of the right-hand side are replaced by the boundary conditions. We now have a generalized eigenvalue problem to solve for the eigenvalues of the system.

10.C Some useful formulas

The following is a collection of useful definitions and formulas from Moore (2017) for the Chebyshev method employed here. The (interior) Gauss-Chebyshev points are

$$x_n = \cos\theta_n, \quad \theta_n = \frac{\pi(2n+1)}{2(N+1)}, \quad \text{for } n = 0, 1, \ldots, N. \tag{10.60}$$

Consider a function $f(x)$ interpolated at these points by the polynomial $p_N(x)$ of degree N:

$$\left.\begin{aligned} f(x_n) &= p_N(x_n), \quad \text{for } n = 0, 1, \ldots, N, \\ P_N(x_n) &= \frac{1}{2}b_0 + \sum_{k=1}^{N} b_k T_k(x). \end{aligned}\right\} \tag{10.61}$$

On the θ-grid this is

$$f(x_n) = \frac{1}{2}b_0 + \sum_{k=1}^{N} b_k \cos k\theta_n, \quad \text{for } n = 0, 1, \ldots, N. \tag{10.62}$$

Thus we may use the fast discrete cosine transform to transform between a function's values on the collocation points, $f(x_n)$, and the Chebyshev coefficients b_k.

The antiderivative of $p_N(x)$ is

$$\left.\begin{aligned} D^{-1}p_N(x) &= \frac{1}{2}B_0 + \sum_{k=1}^{N+1} B_k T_k(x), \\ B_k &= \frac{1}{2k}(b_{k-1} - b_{k+1}), \quad \text{for } n = 1, 2, \ldots, N. \end{aligned}\right\} \tag{10.63}$$

B_0 is a free constant of integration.

The derivative of $p_N(x)$ is

$$\left.\begin{aligned} & Dp_N(x) = \frac{1}{2}b'_0 + \sum_{k=1}^{N} b'_k T_k(x), \\ & b'_{N+1} = b'_N = 0, \\ & b'_k = b'_{k+2} + 2(k+1)b_{k+1}, \quad \text{for } n = N-1, N-2, \ldots, 0. \end{aligned}\right\} \tag{10.64}$$

Since the endpoints $x = \pm 1$ are not part of the collocation grid, we give a formula to evaluate the function at the endpoints:

$$p_N(\pm 1) = \frac{1}{2}b_0 + \sum_{k=1}^{N} (\pm 1)^k b_k. \tag{10.65}$$

Chapter 11

Distributed flexibility in inertial swimmers

Daniel Floryan and Clarence W. Rowley

Appears as Floryan and Rowley (2019).

Using a linear inviscid model of a passively flexible swimmer, we explore how distributed flexibility modifies the thrust production, power consumption, and propulsive efficiency compared to swimmers with uniform flexibility. The frequencies of actuation and mean stiffness ratios considered cover several orders of magnitude, while the mass ratio is fixed to a low value representative of swimmers. Distributed flexibility makes no qualitative differences, but does introduce important quantitative differences. Calculating optimal stiffness distributions, we find that: (1) to maximize thrust, stiffness should be distributed so as to create a favourable natural frequency, or concentrated toward the leading edge; (2) to minimize power, stiffness should be distributed so as to avoid natural frequencies, or concentrated away from the leading edge; and (3) meaningful gains in efficiency can be made when the stiffness is distributed so as to elicit flutter behaviour, which induces efficient travelling wave

kinematics. We also consider the effects of a finite Reynolds number in the form of streamwise drag.

11.1 Introduction

Animal swimming and flight is complex. To make headway in understanding how animals swim and fly, we often abstract the coordinated motion of entire bodies to plates flapping in a fluid; this is the “channel flow” for swimming and flying, as reflected in the vast literature (see the reviews in Triantafyllou et al. (2000); Wang (2005); Wu (2011), for example). A salient feature of the fins and wings of swimming and flying animals is flexibility. Flexibility allows fish to use fine musculature to actively control their kinematics to some degree (Fish and Lauder, 2006), and allows birds to morph their wings (Bergmann, 1839), but also passively influences kinematics through elastic restoring forces.

Simple flapping plate models of swimming and flight incorporate flexibility by modelling the plate as a uniformly elastic material, allowing it to deform according to the fluid and elastic forces it experiences. In the context of forward propulsion, we are most interested in the thrust that a flapping plate can produce, as well as how efficiently it produces the thrust. Passive flexibility changes the thrust that a flapping plate produces, as well as the efficiency of thrust production. It has generally been found that, compared to rigid plates, uniformly flexible plates produce greater thrust when actuated near a fluid-structure natural frequency, and less thrust otherwise, but the efficiency of uniformly flexible plates is greater than that of rigid plates over a broad range of frequencies and stiffnesses (Alben, 2008b; Ferreira de Sousa and Allen, 2011; Dewey et al., 2013; Katz and Weihs, 1978, 1979; Quinn et al., 2014; Floryan and Rowley, 2018). While thrust generally exhibits local maxima when actuating near natural frequencies, efficiency has been observed to exhibit local maxima below natural frequencies, near natural frequencies, and above natural frequencies (Dewey et al., 2013; Moored et al., 2014; Quinn et al., 2014, 2015; Paraz et al., 2016), as well as at frequencies relatively far from a natural frequency (Ramananarivo et al., 2011; Kang et al., 2011; Vanella et al., 2009; Zhu et al., 2014; Michelin and Llewellyn Smith, 2009). We recently clarified that resonant behaviour in efficiency — at least for swimmers, where the characteristic fluid mass is much greater than the body mass — can only arise when viscous forces are present, or if nonlinear effects are not negligible (Floryan and Rowley, 2018).

Animals' fins and wings are not uniformly flexible, however. The material properties of fins and wings may change along the chord (as the musculature, fat content, and skin changes, for example), as may the thickness. (Figure 17 in Fish and Lauder (2006) shows a beautiful example of varying material properties and thickness of the fluke of a bottlenose dolphin.) Flexibility may even be highly localized, as in the veined wings of insects Combes and Daniel (2003a). We thus ask how *distributed* (nonuniform, heterogeneous) flexibility affects thrust production and efficiency in flapping plates, in contrast to uniform flexibility.

Only recently have people begun to explore how the distribution of flexibility affects propulsion in flapping plates. Experiments tend to focus on biomimetic flexibility distributions similar to fish fins, where the leading portion of the plate is stiffer than the trailing portion. The literature includes results on distributions that are fully biomimetic with pure pitching motions (Riggs et al., 2010), stepwise constant distributions with pure heaving and zero angle of attack motions (Lucas et al., 2015), and supposedly linear distributions with pure heaving motions (Kancharala and Philen, 2016); all of these experiments were for cases where the characteristic fluid mass is much greater than the characteristic body mass, as in swimmers. The experiments generally show that plates that are stiffer towards the leading edge produce more thrust and do so more efficiently than plates that are uniformly flexible. It is very important to note, however, that in the cited works, the plates with uniform and distributed flexibilities had different mean stiffnesses, making it difficult to distinguish between the effects of changes in mean stiffness and changes in stiffness distribution. Being able to make the distinction is important because, as we will show later, changing the mean stiffness can significantly change natural frequencies, which have significant effects on thrust and efficiency, and changing the mean stiffness also changes the off-resonance behaviour in efficiency (Alben, 2008b; Floryan and Rowley, 2018).

Computational works have also analyzed how the distribution of flexibility affects propulsion. In most studies, the characteristic fluid mass is of the same order as the characteristic body mass, as in fliers (many of these studies are motivated by insect flight). Distributed flexibility has been modelled in several ways: as a uniform elastic plate with virtual linear springs at several control points (the virtual linear springs attach the elastic sheet to points with *a priori* known motions, mimicking veins in insect wings) (Shoele and Zhu, 2013); as an elastic plate with varying material properties (Moore, 2015); and as an elastic plate with homogeneous material properties but varying thickness (Yeh et al., 2017). Both Shoele and Zhu (2013) and Yeh et al. (2017) found that plates with stiff leading edges produced thrust curves that had lower, but broader, peaks than those of uniformly flexible plates, and that plates with stiff leading edges were broadly more efficient than uniformly flexible plates. Moore (2015) optimized the stiffness (mean and distribution) at fixed frequencies for thrust, and found that a plate that is rigid except at the leading edge (where it has a torsional spring) produced greater thrust than any other flexible plate (although the thrust is not much greater than that produced by a plate with linearly distributed flexibility). The only computational work directly applicable to swimmers, where the characteristic fluid mass is much greater than the characteristic body mass, is

Kancharala and Philen (2016), where the authors found that a stiffer leading edge enhances thrust and efficiency for their kinematics.

Although several studies have shown that distributed flexibility can enhance the propulsion of flexible flapping plates in some way, the mechanisms are unclear. In particular, none of the cited studies have controlled for mean stiffness, which is known to significantly affect propulsion, so it is impossible to know how the distribution of flexibility alone affects propulsion. The eigenvalues of the system can provide a basis to understand how the distribution of flexibility affects propulsion, but this approach has not yet been pursued. Furthermore, the literature has only given conditions that, if met, give rise to improvements in thrust or efficiency, but this is far from a complete characterization of the effects of the distribution of flexibility. For example, although we know that a plate with a stiff leading edge operating at a certain frequency and mean stiffness produces greater thrust than a uniformly flexible plate with a different mean stiffness, we cannot generalize this statement to other cases, or conclude that other distributions do not improve propulsion.

In this work, we attempt to completely characterize how distributed flexibility, in contrast to uniform flexibility, changes the thrust production, power consumption, and efficiency of propulsion of flapping plates. We emphasize the role of the distribution of flexibility — separate from its mean value — particularly how it alters natural frequencies and resonance. We also calculate optimal stiffness distributions, and explain them in light of the preceeding analysis. To be clear, our own interests lie mainly in inertial swimmers characterized by high Reynolds numbers and a large ratio of characteristic fluid mass to body mass. This is in contrast to fliers, for example, where the mass ratio is of order unity and higher. We employ a linear model of a passively flexible swimmer, since doing so allows us to formally calculate natural frequencies of the coupled fluid-structure system, and to stay in a dynamical regime where the notion of resonance is clear.

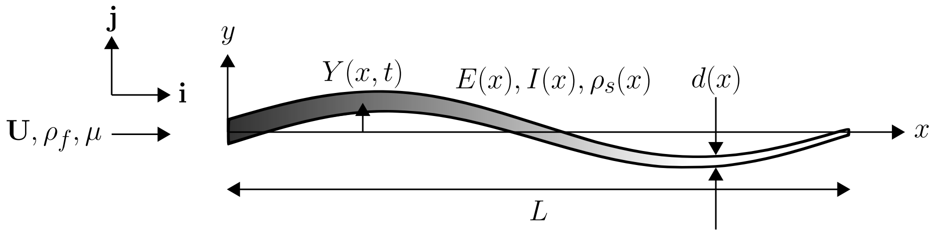

Figure 11.1: Schematic of the problem. The varying colour represents the varying material properties.

11.2 Problem description

Here, the setup and assumptions are the same as in Moore (2017). Consider a two-dimensional, inextensible elastic plate of length L and thickness d. The plate is thin ($d \ll L$), and is transversely deflected a small amount Y from its neutral position, with its slope $Y_x \ll L$. Under these assumptions, the dynamics of the plate is governed by Euler-Bernoulli beam theory. The plate has density ρ_s and flexural rigidity $B = EI$, where E is the Young's modulus, $I = wd^3/12$ is the second moment of area of the plate, and w is the width of the plate. We allow the properties of the plate to *vary spatially*, that is, ρ_s, E, and d are functions of x. The plate is immersed in an incompressible, inviscid Newtonian fluid of density ρ_f. There is no flow along the width of the plate, and far from the plate the flow is unidirectional and constant: $\mathbf{U} = U\mathbf{i}$. The setup is altogether illustrated in figure 11.1.

The motion of the plate alters the velocity field of the fluid, whose forces in turn modify the motion of the plate. The transverse position of the plate satisfies the Euler-Bernoulli beam equation

$$\rho_s d w Y_{tt} + (BY_{xx})_{xx} = w\Delta p, \tag{11.1}$$

where Δp is the pressure difference across the plate due to the fluid flow, subscript t denotes differentiation with respect to time, and subscript x denotes differentiation with respect to streamwise position. The fluid motion satisfies the linearized incompressible Euler equations

$$\left.\begin{aligned}&\nabla\cdot\mathbf{u}=0,\\[1em]&\rho_f(\mathbf{u}_t+U\mathbf{u}_x)=-\nabla p,\end{aligned}\right\}\tag{11.2}$$

where $\mathbf{u}=u\mathbf{i}+v\mathbf{j}$. The above linearization is valid when the perturbation velocity $\mathbf{u}$ is much smaller than U. Since the perturbation velocity depends on the plate's vertical velocity, its slope, and the rate of change of its slope, the linear assumption holds for small-amplitude motions of the plate.

We non-dimensionalize the above equations using $L/2$ as the length scale, U as the velocity scale, and $L/(2U)$ as the time scale, yielding

$$\left.\begin{aligned}&2RY_{tt}+\frac{2}{3}(SY_{xx})_{xx}=\Delta p,\\[1em]&\nabla\cdot\mathbf{u}=0,\\[1em]&\mathbf{u}_t+\mathbf{u}_x=\nabla\phi,\end{aligned}\right\}\tag{11.3}$$

where

$$R=\frac{\rho_s d}{\rho_f L},\quad S=\frac{Ed^3}{\rho_f U^2 L^3},\quad \phi=p_\infty-p.\tag{11.4}$$

In the above, x, t, Y, $\mathbf{u}$, and p are now dimensionless, with the pressure non-dimensionalized by $\rho_f U^2$. The coordinates are aligned such that $x=-1$ corresponds to the leading edge and $x=1$ corresponds to the trailing edge. R is a ratio of solid-to-fluid mass, and S is a ratio of bending-to-fluid forces, and both are functions of x. Note that $\Delta\phi=-\Delta p$.

The fluid additionally satisfies the no-penetration and Kutta conditions, which can be stated as

$$\left.\begin{aligned} v|_{x\in[-1,1],y=0} &= Y_t + Y_x, \\ |v||_{(x,y)=(1,0)} &< \infty. \end{aligned}\right\} \tag{11.5}$$

We impose heaving and pitching motions h and θ, respectively, on the leading edge of the plate, while the trailing edge is free, resulting in boundary conditions

$$Y(-1,t) = h(t), \quad Y_x(-1,t) = \theta(t), \quad Y_{xx}(1,t) = 0, \quad Y_{xxx}(1,t) = 0. \tag{11.6}$$

The fluid motion resulting from the actuation of the leading edge of the plate imparts a net horizontal force onto the plate. In other words, energy input into the system by the actuation of the leading edge is used to generate a propulsive force. The net horizontal force (thrust) on the plate is

$$C_T = \int_{-1}^{1} \Delta p Y_x \, \mathrm{d}x + C_{TS}, \tag{11.7}$$

where C_{TS} is the leading edge suction force (formula given in Moore (2017)), and the power input is

$$C_P = -\int_{-1}^{1} \Delta p Y_t \, \mathrm{d}x. \tag{11.8}$$

The leading edge suction force used in Moore (2017) is the limit of the suction force on a leading edge of small but finite radius of curvature, in the limit that the radius tends to zero. The leading edge suction force is a reasonable model of the actual flow when it is attached (Saffman, 1992), so we have chosen to include it. In terms of dimensional variables, $C_T = T/(\frac{1}{2}\rho_f U^2 L w)$ and $C_P = P/(\frac{1}{2}\rho_f U^3 L w)$, where T and P are the dimensional net thrust and power input, respectively. Finally, the Froude efficiency is defined as

$$\eta = \frac{\overline{T}U}{\overline{P}} = \frac{\overline{C_T}}{\overline{C_P}}, \tag{11.9}$$

where the overbar denotes a time-averaged quantity.

In this work, we restrict ourselves to actuation at the leading edge that is sinusoidal in time, that is,

$$\left.\begin{aligned} h(t) &= h_0 \mathrm{e}^{\mathrm{j}\sigma t}, \\ \theta(t) &= \theta_0 \mathrm{e}^{\mathrm{j}\sigma t}, \end{aligned}\right\} \tag{11.10}$$

where $\sigma = \pi L f / U$ is the dimensionless angular frequency, f is the dimensional frequency in Hz, $\mathrm{j} = \sqrt{-1}$, and the real part in j should be taken when evaluating the deflection. Since the system is linear in Y, the resulting deflection of the plate and fluid flow will also be sinusoidal in time. We leave the details of the method of solution to Appendix 11.A, noting that all calculations in this work used either 64 or 128 collocation points. The method to calculate the eigenvalues of the system is detailed in Appendix 11.B, and some useful formulas for the numerical method used are given in Appendix 11.D.

11.3 Parameters and scope

The system parameters we use will critically affect the phenomena we observe. We thus take the opportunity here to explicitly state the parameters we use in this work, noting some attendant qualitative features.

The system is parameterized by its Reynolds number, *Re*, mass (mean and distribution), stiffness (mean and distribution), and frequency and amplitude of actuation. Our flow is inviscid, but we will briefly remark on the effects of a finite Reynolds number later. The non-dimensional quantities in (11.4) show that the mass and stiffness of the system depend on both the solid *and* the fluid. Underwater swimmers tend to be thin and neutrally buoyant, so the mass ratio R is generally quite low; this is in contrast to fliers, for example, whose mass ratios are of order unity and higher. Since our interests lie in swimmers, we take the mean mass ratio to be $\langle R \rangle = 0.01$

Re	$\langle R\rangle = \dfrac{\langle \rho_s d\rangle}{\rho_f L}$	$\langle S\rangle = \dfrac{\langle E d^3\rangle}{\rho_f U^2 L^3}$	$f^* = \dfrac{fL}{U}$	h_0	θ_0
inviscid	0.01	10^{-2}–10^{2}	10^{-1}–10^{2}	2 (linear)	1 (linear)

Table 11.1: Parameter values used in this work.

throughout, where $\langle\cdot\rangle$ denotes the spatial mean along the length of the plate. The stiffness of the system is characterized by the stiffness ratio S; we vary the mean stiffness of the system from very flexible ($\langle S\rangle \ll 1$) to very stiff ($\langle S\rangle \gg 1$). We vary the frequency of actuation so that it covers multiple natural frequencies of the system. Since our system is linear, scaling the amplitude by some factor will simply scale the flow and deflection fields by the same factor. In this sense, amplitude does not matter in our problem, so we set the heaving and pitching amplitudes so that the maximum deflection of the trailing edge of a rigid plate is equal to the length of the plate. The amplitude affects both thrust and power quadratically, and does not affect efficiency in this linear setting. We do not consider nonlinear effects caused by large amplitudes. The parameters we use in the proceeding sections are summarized in table 11.1.

As shown in Floryan and Rowley (2018), the value of the mean mass ratio $\langle R\rangle$ qualitatively changes the propulsion of a flapping plate. At low values, however, the mass of the plate is dominated by the mass of the fluid. With $\langle R\rangle = 0.01$, we expect the mass of the plate to have little effect on propulsion, and consequently the distribution of mass should also have little effect on propulsion, at least for cases where there is not a large amount of mass concentrated in a small area. In figure 11.2, we plot the thrust coefficient, power coefficient, and efficiency as functions of the mass distribution for $\langle R\rangle = 0.01$, $S \equiv 1$, and $f^* = 1$ for heaving and pitching plates. Here, we have taken the mass to be distributed linearly, in which case it is described by a single parameter $\mathrm{d}R^*/\mathrm{d}x$, where $R = \langle R\rangle R^*$, R^* is the distribution of mass, and hence $\langle R^*\rangle = 1$. Note that $\mathrm{d}R^*/\mathrm{d}x \in [-1, 1]$ (otherwise a section of the plate would have negative mass), where $\mathrm{d}R^*/\mathrm{d}x = -1$ corresponds to a massive leading edge, $\mathrm{d}R^*/\mathrm{d}x = 0$ corresponds to uniformly distributed mass, and $\mathrm{d}R^*/\mathrm{d}x = 1$ corresponds to a massive trailing edge. The thrust coefficient, power coefficient, and efficiency in figure 11.2 have been normalized by their values when the mass is uniformly distributed. At such low $\langle R \rangle$ the distribution of mass matters little; this is in contrast to stiffness, whose distribution can greatly affect thrust, power, and efficiency, as shown in figure 11.3 for the same mean parameter values as used in figure 11.2. Accordingly, we will take $R \equiv 0.01$ in all proceeding results. We expect our results to hold for low mass ratios ($R \lesssim 0.1$). We will allow the stiffness to vary in space, with the mean value given by $\langle S \rangle$ and the distribution given by S^*. The distribution S^* can be conveniently described as a linear combination of Legendre polynomials,

$$S^* = \sum_i c_i P_i, \tag{11.11}$$

the first few of which are

$$P_0(x) = 1, \qquad P_1(x) = x, \qquad P_2(x) = \frac{1}{2}(3x^2 - 1). \tag{11.12}$$

Legendre polynomials are convenient because they are orthogonal on $x \in [-1, 1]$ with weighting function 1. Consequently, we can fix $\langle S^* \rangle = 1$ by fixing the coefficient of the first Legendre polynomial P_0 equal to 1.

11.4 Inviscid results

In the Introduction, we asked how distributed flexibility modifies propulsion in comparison to uniform flexibility. Before presenting our results on the kinematics and propulsive characteristics of flapping plates with distributed flexibility, we will briefly review the results for uniform flexibility from Floryan and Rowley (2018) in order

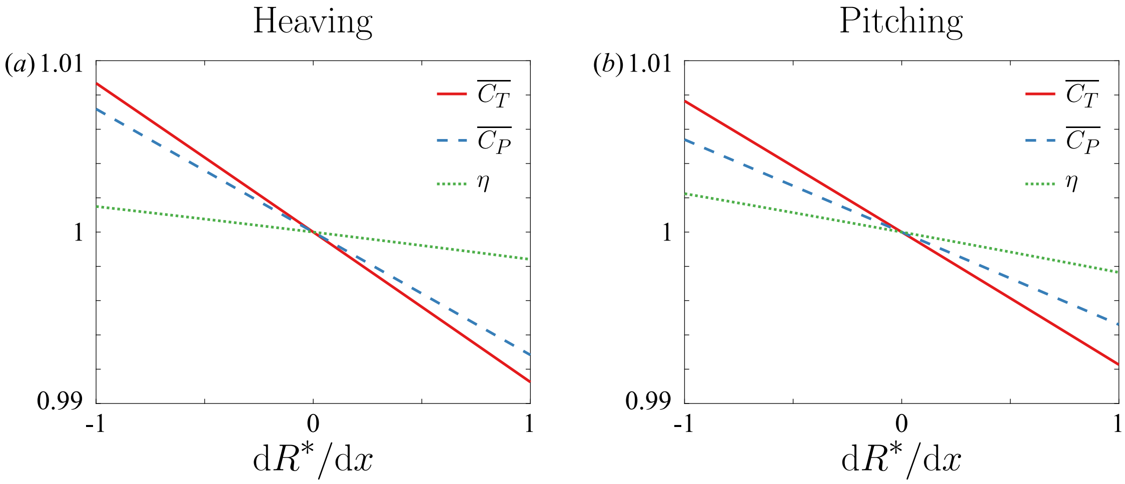

Figure 11.2: Thrust coefficient, power coefficient, and efficiency as a function of the mass distribution for a (a) heaving and (b) pitching plate for $\langle R\rangle = 0.01$, $S \equiv 1$, and $f^* = 1$. R is linear, and values are normalized by their value when the mass is uniformly distributed.

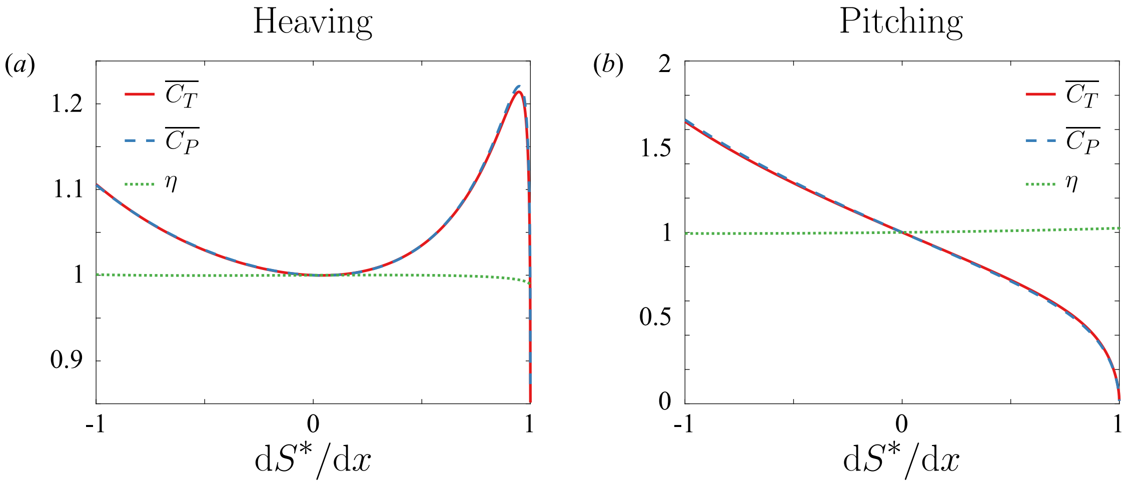

Figure 11.3: Thrust coefficient, power coefficient, and efficiency as a function of the stiffness distribution for a (a) heaving and (b) pitching plate for $R \equiv 0.01$, $\langle S\rangle = 1$, and $f^* = 1$. S is linear, and values are normalized by their value when the mass is uniformly distributed.

to contextualize our results. All of our results for uniformly flexible plates will be presented relative to rigid plates. For example, we will present the mean thrust that a uniformly flexible plate produces relative to the mean thrust that an otherwise identical rigid plate produces.

11.4.1 Propulsive characteristics of flapping plates with uniform flexibility

The amplitude of the trailing edge deflection, the mean thrust coefficient, and the mean power coefficient all exhibit the same qualitative behaviour in the frequency-stiffness plane. For reference, we have plotted the trailing edge amplitude in figure 11.4. For mid-to-high values of the reduced frequency and stiffness ratio, ridges of local maxima are apparent. These ridges coincide with the natural frequencies (imaginary parts of the eigenvalues) of the system, indicating a resonant response. In this region of the frequency-stiffness plane, the natural frequencies are well-approximated by the quiescent natural frequencies, which are calculated in the limit where the bending velocity is large compared to the fluid velocity; we provide more details in Appendix 11.B.2. The eigenvalues are lightly damped (small angle relative to the imaginary axis) and well-separated, leading to the sharp ridges observed. The natural frequencies increase as the stiffness ratio increases, conforming to our intuition based on a clamped Euler-Bernoulli beam in vacuo, and can be shown to vary as $f^* \sim S^{1/2}$ in this region of the frequency-stiffness plane. We will refer to these eigenvalues and the corresponding eigenfunctions as Euler-Bernoulli modes.

The behaviour is quite different when the reduced frequency and stiffness ratio are low, however. In this region of the frequency-stiffness plane, the resonant peaks broaden and smear together as the stiffness ratio decreases because the eigenvalues become more damped and move closer to each other. A ridge aligned in the direction opposite to the other ridges emerges, with the frequency *decreasing* with stiffness,

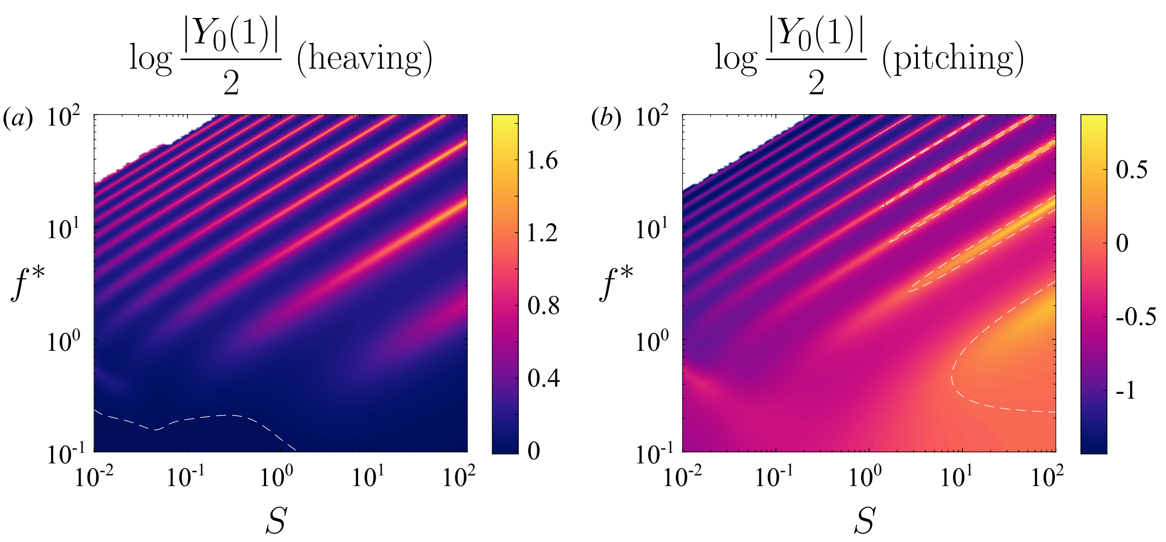
$\log \dfrac{|Y_0(1)|}{2}$ (heaving)

$\log \dfrac{|Y_0(1)|}{2}$ (pitching)

Figure 11.4: Trailing edge amplitude as a function of reduced frequency f^* and stiffness ratio S for a (a) heaving and (b) pitching plate with $R \equiv 0.01$ relative to that of an equivalent rigid plate. Dashed white lines indicate where the flexible plate has the same trailing edge amplitude as the equivalent rigid plate. Under-resolved areas have been whited out. Results are for a uniformly flexible plate. The mean thrust and mean power coefficients are qualitatively the same as the trailing edge amplitude.

although we note that the mean thrust and mean power for a pitching plate actually become negative here, in contrast to the trailing edge amplitude for a pitching plate. Whereas the previous ridges coincided with the natural frequencies of the Euler-Bernoulli modes, this ridge aligns with the natural frequencies of a flutter mode, a mode that becomes unstable for low enough stiffness ratio and induces flutter in the beam (as seen in a flag flapping in the wind, for example). With decreasing stiffness ratio, Euler-Bernoulli modes are essentially replaced by flutter modes, with the replacement occurring at lower values of the stiffness ratio for higher-order modes. The flutter modes are weakly damped compared to the Euler-Bernoulli modes, leading to ridges aligned with the flutter modes.

The efficiency behaves very differently from the trailing edge amplitude, mean thrust, and mean power. In figure 11.5, we have plotted the difference in efficiency between a uniformly flexible plate and an otherwise identical rigid plate. Whereas the

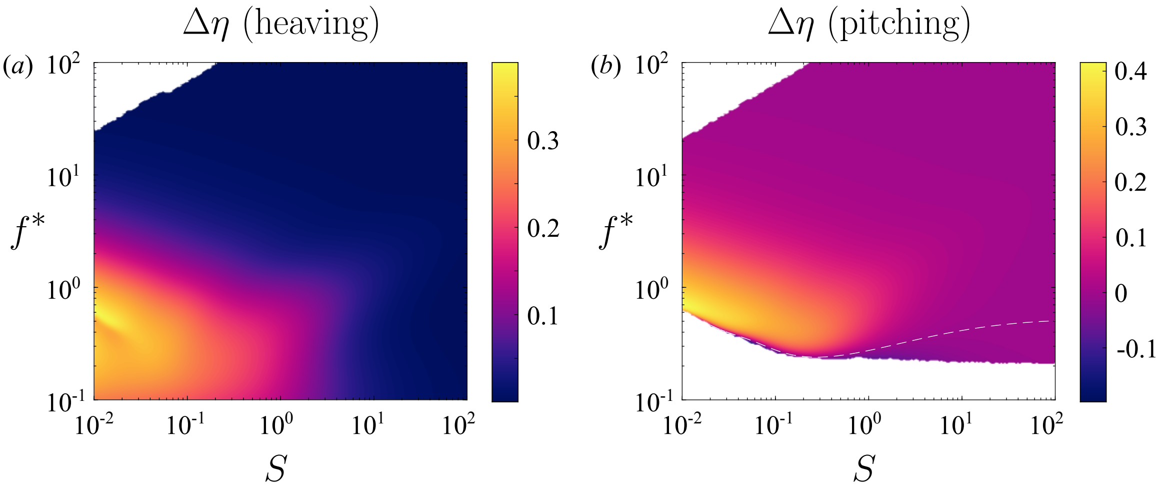

Figure 11.5: Efficiency as a function of reduced frequency f^* and stiffness ratio S for a (a) heaving and (b) pitching plate with $R \equiv 0.01$ relative to that of an equivalent rigid plate. Dashed white lines indicate where the flexible plate has the same efficiency as the equivalent rigid plate. Under-resolved areas and areas that produce negative efficiency have been whited out. Results are for a uniformly flexible plate.

trailing edge amplitude, mean thrust, and mean power have ridges of local maxima aligned with the natural frequencies, the efficiency has a single broad region of high values in the frequency-stiffness plane. Elsewhere in the plane, the local maxima in thrust and efficiency cancel each other exactly, resulting in flat efficiency. The region of high efficiency is aligned with the natural frequencies of the flutter mode. The flutter mode induces travelling wave kinematics in the plate, which is known to be highly efficient (Wu, 1961). It is worth keeping in mind that increases in efficiency are often accompanied by decreases in thrust, as is evinced by the efficiency plot for a pitching flexible plate (figure 11.5b). For the pitching plate, the cutoff where efficiency and thrust become negative is aligned with the natural frequencies of the flutter mode; although the flutter mode induces efficient kinematics, the kinematics lead to low thrust. We must be wary of low values of thrust when drag is present in the system.

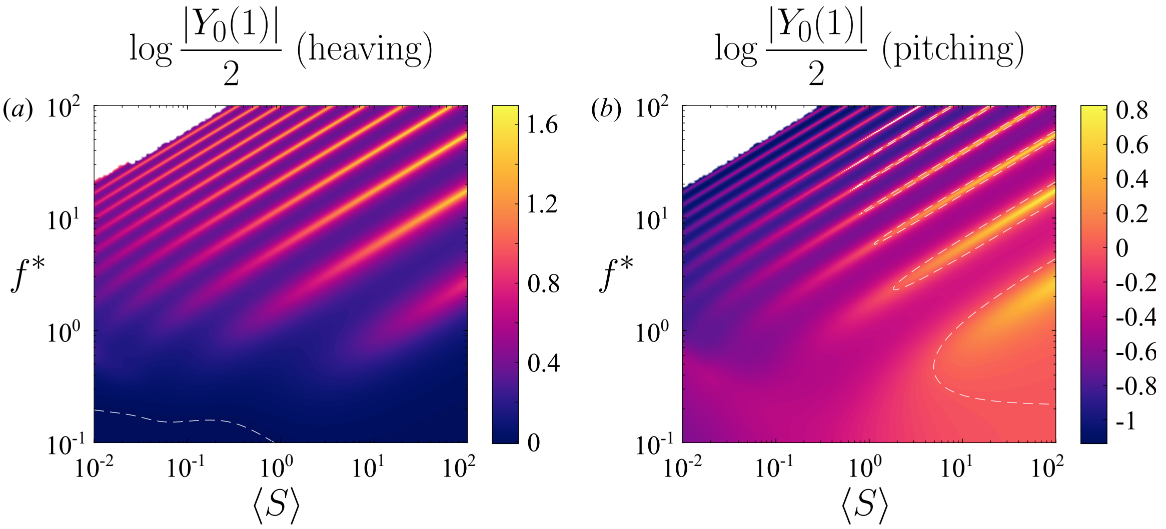

Figure 11.6: Trailing edge amplitude as a function of reduced frequency f^* and mean stiffness ratio $\langle S \rangle$ for a (a) heaving and (b) pitching plate with $R \equiv 0.01$ relative to that of an equivalent rigid plate. Dashed white lines indicate where the flexible plate has the same trailing edge amplitude as the equivalent rigid plate. Under-resolved areas have been whited out. Results are for a flexible plate with stiffness distribution $S^*(x) = 1 - 0.9x$ (stiff leading edge). The mean thrust and mean power coefficients are qualitatively the same as the trailing edge amplitude.

11.4.2 Propulsive characteristics of flapping plates with distributed flexibility

We begin by considering linear stiffness distributions, which are described by a single parameter $\mathrm{d}S^*/\mathrm{d}x$. Qualitatively, flexible plates with linearly distributed stiffness are the same as flexible plates with uniformly distributed stiffness. In figures 11.6 and 11.7, we have plotted the trailing edge amplitude of plates with a stiff leading edge ($\mathrm{d}S^*/\mathrm{d}x = -0.9$) and a soft leading edge ($\mathrm{d}S^*/\mathrm{d}x = 0.9$), respectively. As before, the trailing edge amplitude is qualitatively representative of the mean thrust and power coefficients. The plates with stiff and soft leading edges show the same trends as a uniformly flexible plate: sharp resonant ridges for high reduced frequencies and stiffness ratios; broadening and smearing of the ridges for low reduced frequencies and stiffness ratios; and emergence of flutter modes for low stiffness ratios.

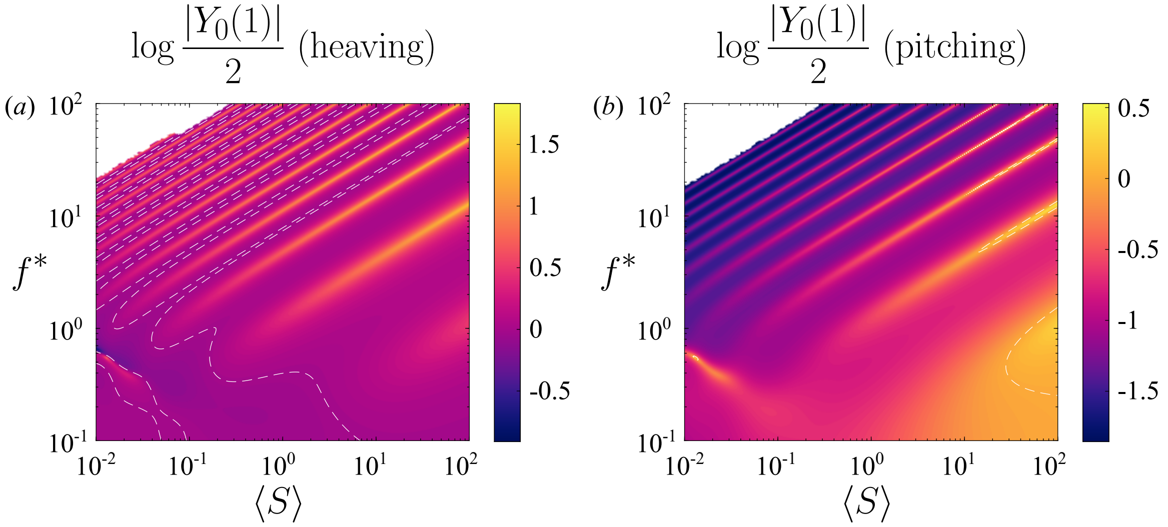

Figure 11.7: Trailing edge amplitude as a function of reduced frequency f^* and mean stiffness ratio $\langle S \rangle$ for a (a) heaving and (b) pitching plate with $R \equiv 0.01$ relative to that of an equivalent rigid plate. Dashed white lines indicate where the flexible plate has the same trailing edge amplitude as the equivalent rigid plate. Under-resolved areas have been whited out. Results are for a flexible plate with stiffness distribution $S^*(x) = 1 + 0.9x$ (soft leading edge). The mean thrust and mean power coefficients are qualitatively the same as the trailing edge amplitude.

The behaviour of the efficiency does not change either. In figures 11.8 and 11.9, we have plotted the difference in efficiency between plates with stiff and soft leading edges, respectively, and a rigid plate. In both cases, the efficiency does not have any resonant ridges, but does have a broad region of high values for low reduced frequencies and stiffness ratios. Just as for the trailing edge amplitude, mean thrust coefficient, and mean power coefficient, the efficiency of plates with distributed flexibility follows the same trends and for uniformly flexible plates.

By and large, there are no qualitative differences between plates with uniform stiffness and plates with linearly distributed stiffness. The behaviour of the measures of propulsive performance is dominated by the eigenvalues of the system, which are qualitatively the same for different distributions of stiffness: Euler-Bernoulli modes govern the performance when the stiffness ratio is high, whereas flutter modes emerge and govern the performance when the stiffness ratio is low. We posit that the behaviour

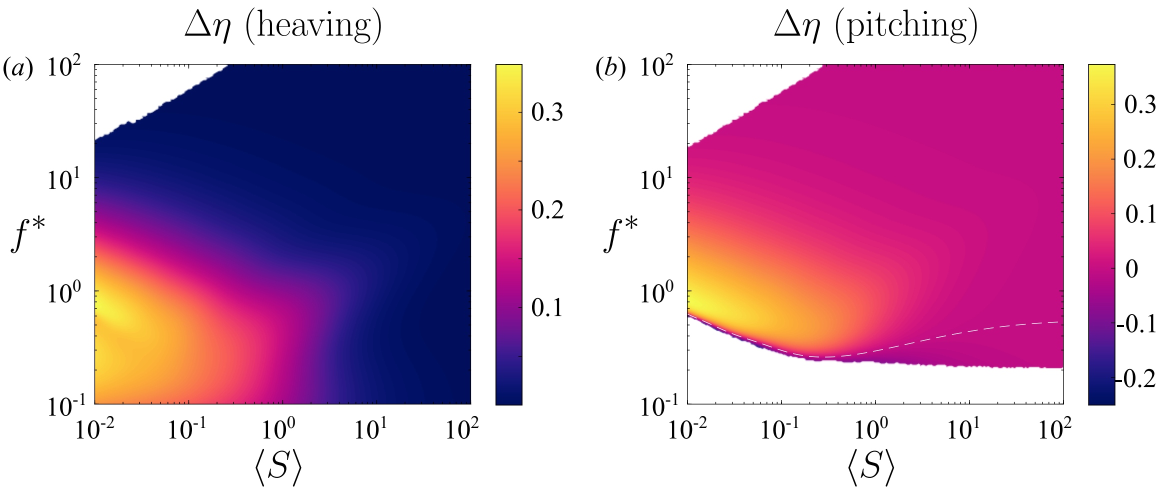

Figure 11.8: Efficiency as a function of reduced frequency f^* and mean stiffness ratio $\langle S \rangle$ for a (a) heaving and (b) pitching plate with $R \equiv 0.01$ relative to that of an equivalent rigid plate. Dashed white lines indicate where the flexible plate has the same efficiency as the equivalent rigid plate. Under-resolved areas and areas that produce negative efficiency have been whited out. Results are for a flexible plate with stiffness distribution $S^*(x) = 1 - 0.9x$ (stiff leading edge).

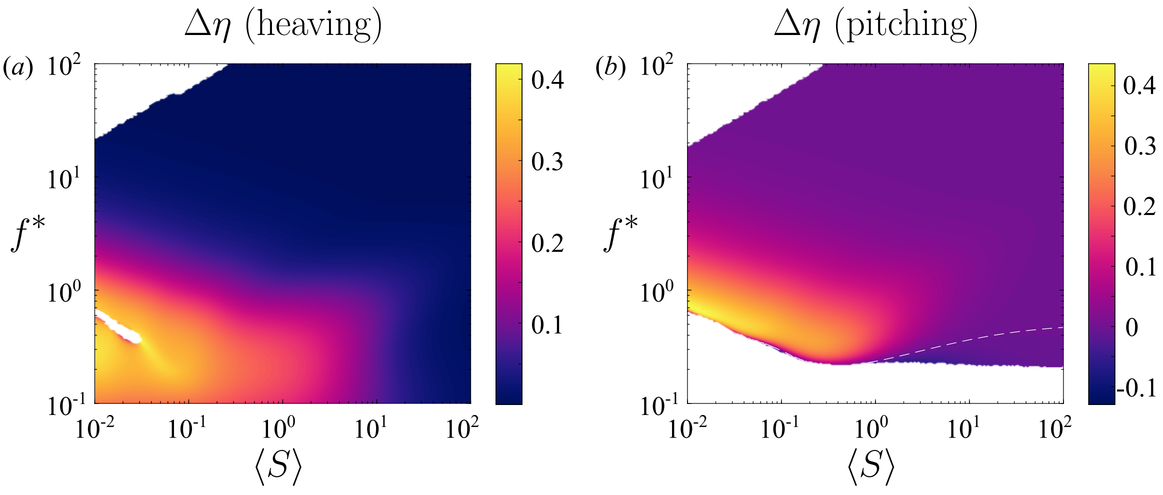

Figure 11.9: Efficiency as a function of reduced frequency f^* and mean stiffness ratio $\langle S \rangle$ for a (a) heaving and (b) pitching plate with $R \equiv 0.01$ relative to that of an equivalent rigid plate. Dashed white lines indicate where the flexible plate has the same efficiency as the equivalent rigid plate. Under-resolved areas and areas that produce negative efficiency have been whited out. Results are for a flexible plate with stiffness distribution $S^*(x) = 1 + 0.9x$ (soft leading edge).

does not change qualitatively for higher-order distributions of stiffness. Although there are no qualitative differences, there may be important quantitative differences, and we shall explore them in the next section.

11.5 Optimal stiffness distributions

As discussed in the Introduction, the literature has shown that varying the distribution of stiffness quantitatively changes the propulsive performance of flexible plates. In some cases (Moore, 2015; Kancharala and Philen, 2016), the stiffness distribution was optimized in order to achieve the greatest thrust/speed or greatest efficiency/lowest cost of transport. Optimal stiffness distributions differed qualitatively for different mass ratios. For a low mass ratio, relevant to swimmers, concentrating the stiffness towards the leading edge maximized thrust and efficiency (Kancharala and Philen, 2016), but the authors did not control for mean stiffness and only studied a few frequencies. Here, we will calculate optimal stiffness distributions at every point in the frequency-stiffness plane we have explored. Particularly, for every combination of reduced frequency and mean stiffness, we solve for the distribution of stiffness that: (a) maximizes thrust; (b) minimizes power; and (c) maximizes efficiency.

For now, we will limit ourselves to quadratic distributions of stiffness, but we will end with how we expect our results to generalize to higher-order distributions. The distribution of stiffness can be written as

$$S^* = P_0 + c_1 P_1 + c_2 P_2, \tag{11.13}$$

where P_i are the Legendre polynomials (written out in (11.12)), and c_i are the parameters we optimize over. The coefficient multiplying P_0 is fixed to 1 so that $\langle S^* \rangle = 1$. Furthermore, we must restrict c_1 and c_2 so that S^* is nonnegative on the plate. The

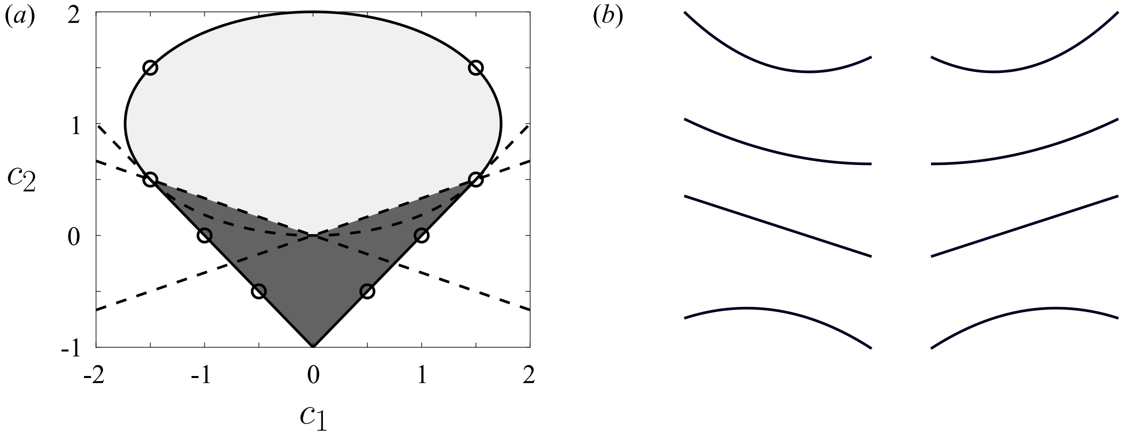

Figure 11.10: (a) Feasible set of quadratic flexibility distributions. The interior region contains stiffness distributions that are positive everywhere on the plate, and the border contains stiffness distributions that are positive except at a point. The dark region contains stiffness distributions whose minima are at the leading/trailing edge, and the light region contains stiffness distributions whose minima are at an interior point of the plate. We have drawn some representative distributions in (b), corresponding to the circles in (a).

physical constraint of nonnegativity leads to

$$\begin{cases} -3c_2^2 + 6c_2 - c_1^2 \geq 0 & \text{if } -3c_2 \leq c_1 \leq 3c_2 \\ 1 \pm c_1 + c_2 \geq 0 & \text{otherwise.} \end{cases} \tag{11.14}$$

The feasible set is drawn in figure 11.10, along with some representative stiffness distributions. The dark region contains stiffness distributions whose minima are at the leading/trailing edge, and the light region contains stiffness distributions whose minima are at an interior point of the plate.

Altogether we have a nonlinear constrained optimization problem, with both the objective function and the constraints being nonlinear in the optimization variables. Since the feasible set is the union of an ellipse and a convex polyhedron, the original optimization problem can be split into two optimization problems with linear constraints (the ellipse can be described by linear constraints in polar coordinates).

We solve the optimization problem using MATLAB's default interior-point algorithm (Mat, 2016).

11.5.1 Linear stiffness distributions

We begin by calculating optimal linear stiffness distributions, in which case the only optimization parameter is the slope of the stiffness distribution, $\mathrm{d}S^*/\mathrm{d}x$. When $\mathrm{d}S^*/\mathrm{d}x < 0$, we say that the plate has a stiff leading edge, and when $\mathrm{d}S^*/\mathrm{d}x > 0$, we say that the plate has a soft leading edge. In figure 11.11, we have plotted the optimal (thrust-maximizing) linear stiffness distribution, with the attendant optimal mean thrust coefficient plotted in figure 11.12. There is a clear distinction in behaviour between high-stiffness regions (where Euler-Bernoulli modes dominate the behaviour) and low-stiffness regions (where flutter modes dominate), so we will discuss them in turn.

When the Euler-Bernoulli modes dominate the response, the optimal stiffness distribution at a given reduced frequency and mean stiffness ratio is the one that has a natural frequency at that frequency of actuation. This is consistent with our understanding of uniformly stiff plates, where actuating at a natural frequency produces a local maximum in thrust. By tuning the stiffness distribution appropriately, we can tune the natural frequencies of the plate so that they coincide with the frequency of actuation. The ability to tune the locations of natural frequencies broadens the resonant response, thereby broadening the regions of high thrust, as evinced by figure 11.12. These results starkly contrast those for a plate with a fixed stiffness distribution, where the resonant response is quite narrow (cf. figures 11.4, 11.6, and 11.7).

A resonant response is not always possible, however. Although being able to modify the stiffness distribution greatly broadens the resonant ridges, there are still valleys of relatively low thrust in between the resonant ridges. This is because natural

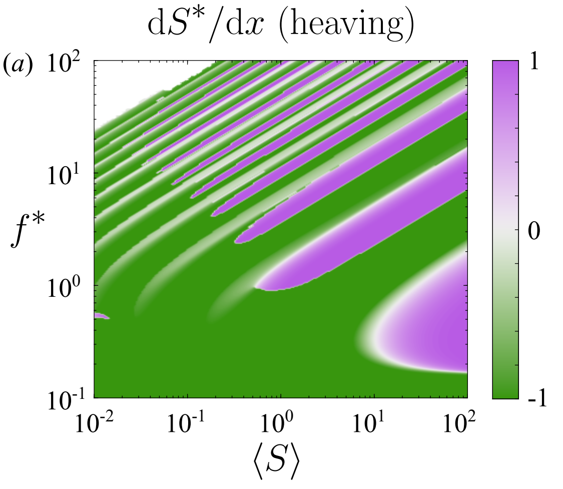

$\mathrm{d}S^*/\mathrm{d}x$ (heaving)

$\mathrm{d}S^*/\mathrm{d}x$ (pitching)

Figure 11.11: Optimal linear stiffness distribution as a function of reduced frequency f^* and mean stiffness ratio $\langle S \rangle$ for a (a) heaving and (b) pitching plate with $R \equiv 0.01$. Under-resolved areas and areas that produce negative thrust have been whited out. Results are for a flexible plate with linear stiffness distribution optimized for thrust.

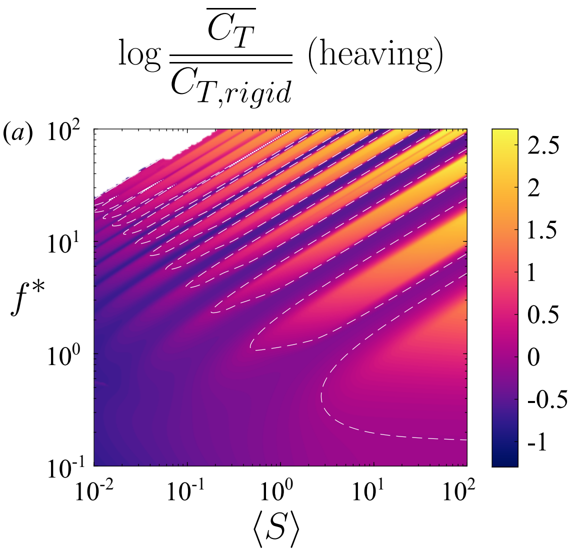

$\log \dfrac{\overline{C_T}}{\overline{C_{T,rigid}}}$ (heaving)

$\log \dfrac{\overline{C_T}}{\overline{C_{T,rigid}}}$ (pitching)

Figure 11.12: Thrust coefficient as a function of reduced frequency f^* and mean stiffness ratio $\langle S \rangle$ for a (a) heaving and (b) pitching plate with $R \equiv 0.01$ relative to that of an equivalent rigid plate. Dashed white lines indicate where the flexible plate has the same thrust coefficient as the equivalent rigid plate. Under-resolved areas and areas that produce negative thrust have been whited out. Results are for a flexible plate with linear stiffness distribution optimized for thrust.

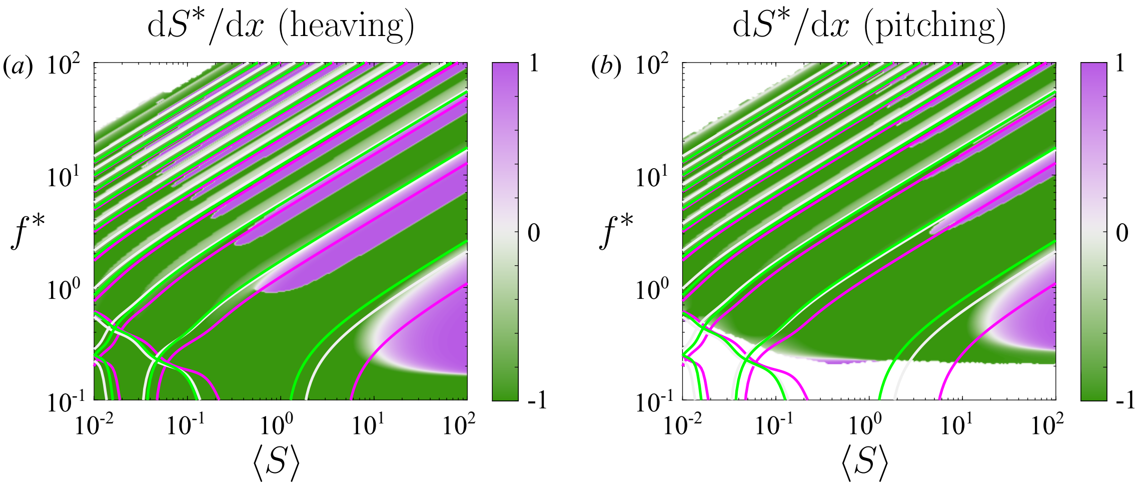

Figure 11.13: Same as in figure 11.11, but with natural frequencies overlaid as curves for $\mathrm{d}S^*/\mathrm{d}x = -0.9$ (stiff leading edge, green), $\mathrm{d}S^*/\mathrm{d}x = 0$ (uniformly stiff, white), and $\mathrm{d}S^*/\mathrm{d}x = 0.9$ (soft leading edge, purple).

frequencies of lower-order modes do not overlap with natural frequencies of higher-order modes. To make the situation clear, we have re-plotted the optimal linear stiffness distribution in figure 11.13 with the natural frequencies for stiff leading edge ($\mathrm{d}S^*/\mathrm{d}x = -0.9$, green), uniformly stiff ($\mathrm{d}S^*/\mathrm{d}x = 0$, white), and soft leading edge ($\mathrm{d}S^*/\mathrm{d}x = 0.9$, purple) plates overlaid as three sets of curves. Clearly, the natural frequency of the first Euler-Bernoulli mode for a plate with a stiff leading edge is nowhere close to the natural frequency of the second Euler-Bernoulli mode for a plate with a soft leading edge, and so on for higher-order modes. The gap between natural frequencies that are attainable with a linear stiffness distribution leads to the valleys in optimal thrust between resonant ridges.

Moreover, for high-order modes the natural frequencies do not follow the pattern we might expect. For the first mode, a plate with a soft leading edge has the lowest natural frequency, and a plate with a stiff leading edge has the highest natural frequency, as one might expect. By the third mode, however, a uniformly stiff plate has a higher natural frequency than plates with stiff or soft leading edges. This is more clearly shown in figure 11.14, where we have plotted the quiescent natural frequencies

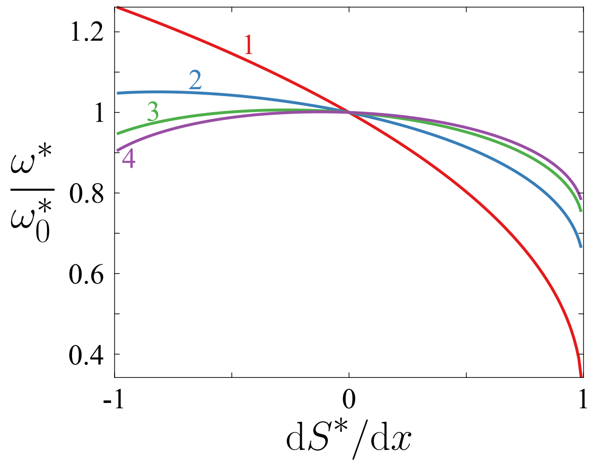

Figure 11.14: First four quiescent natural frequencies as a function of the stiffness distribution. The natural frequencies have been normalized by the natural frequencies of a uniformly stiff plate, $\mathrm{d}S^*/\mathrm{d}x = 0$.

for the first four modes as a function of the stiffness distribution. (For just this plot, we have non-dimensionalized time using the bending time scale t_{bend}, as explained in Appendix 11.B.2, yielding $\omega^* = \omega t_{bend}$, where $\omega = 2\pi f$ is the dimensional angular frequency.) We have rescaled the quiescent natural frequencies so that they are plotted relative to the values for a uniformly stiff plate. For third- and higher-order modes, uniformly stiff plates have higher natural frequencies than plates with a stiff (or soft) leading edge. Consequently, the relation between stiffness distribution and natural frequency is not injective: plates with a stiff leading edge may have the same natural frequency as plates with a soft leading edge.

When multiple stiffness distributions have the same natural frequency, which distribution is preferred? To provide insight into this question, we have calculated the thrust produced by two plates, one with a stiff leading edge and one with a soft leading edge, with both plates having the same third natural frequency. (The plate with the stiff leading edge has $\mathrm{d}S^*/\mathrm{d}x = -0.9$, while the plate with the soft leading edge has $\mathrm{d}S^*/\mathrm{d}x$ varying from 0.416 to 0.445 over the range of $\langle S \rangle$ considered so that its third natural frequency is the same as that of the plate with the stiff leading edge.)

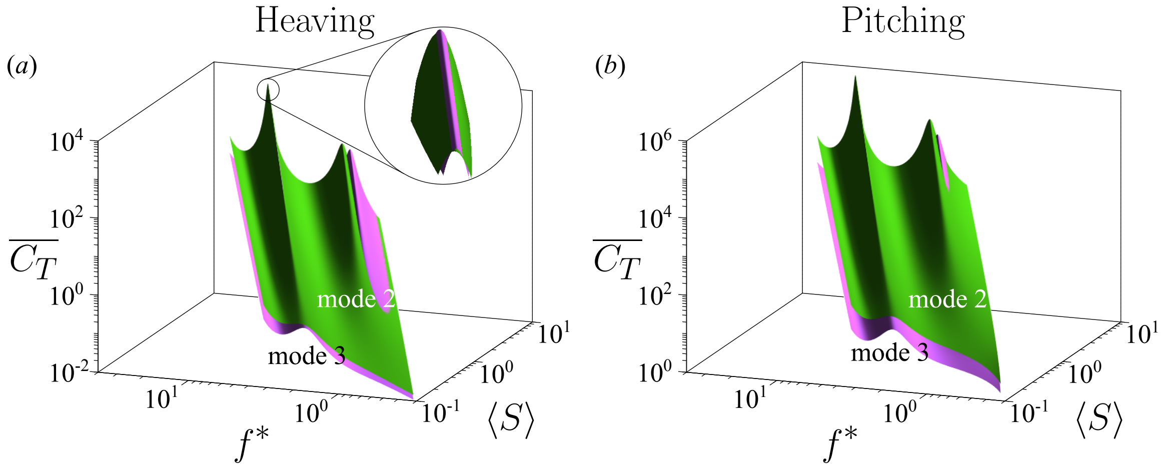

Figure 11.15: Thrust coefficient as a function of reduced frequency f^* and mean stiffness ratio $\langle S \rangle$ for a (a) heaving and (b) pitching plate with $R \equiv 0.01$. The green surface corresponds to a plate with a stiff leading edge ($\mathrm{d}S^*/\mathrm{d}x = -0.9$), and the purple surface corresponds to a plate with a soft leading edge and matched third natural frequency ($\mathrm{d}S^*/\mathrm{d}x \in [0.416, 0.445]$).

The thrusts produced by the plates are plotted as surfaces in figure 11.15, with the green surface corresponding to the plate with a stiff leading edge, and the purple surface corresponding to the plate with a soft leading edge. The surfaces are plotted on top of each other so that the surface that is visible from above has greater thrust. When heaved around the third natural frequency, the plate with a stiff leading edge produces more thrust than the plate with a soft leading edge except for a very tight range of frequencies centered about the natural frequency, as shown in the close-up view. When pitched around the third natural frequency, the plate with a stiff leading edge produces more thrust than the plate with a soft leading edge at all frequencies near the natural frequency. Except when actuated right at the natural frequency, the plate with a stiff leading edge is preferred over the plate with a soft leading edge and equal natural frequency when it comes to thrust production.

In a similar vein, which stiffness distribution is preferred when the plate is actuated away from a resonant frequency, that is, in the resonant gaps seen in figure 11.12? The results show that a plate with a stiff leading edge is always preferred. In the resonant gaps, plates with a stiff leading edge produce the greatest trailing edge amplitude, leading to the greatest thrust production. This is true in the entire region of the frequency-stiffness plane dominated by Euler-Bernoulli type behaviour: the stiffness distribution that produces the greatest trailing edge amplitude also produces the greatest thrust.

The last observation we make about optimal thrust production in the region dominated by Euler-Bernoulli behaviour concerns the difference between heaving and pitching plates. For a heaving plate, the regions where a soft leading edge is preferred are more expansive than for a pitching plate. In particular, regions where a very soft leading edge is preferred for a heaving plate are replaced by a stiff leading edge for a pitching plate (these are regions where the frequency of actuation is close but not equal to a natural frequency of a plate with a soft leading edge). To understand why, consider a plate starting at rest with a soft leading edge in the limiting case $\mathrm{d}S^*/\mathrm{d}x = 1$. In this case, the stiffness at the leading edge is zero. When we pitch such a plate at the leading edge, no moment will be generated at the leading edge since the stiffness there is zero. Consequently, there will be no deflection, the plate will remain parallel to the flow, and thus no thrust will be generated. When we heave such a plate, no moment will be generated at the leading edge, but the plate still needs to satisfy the boundary condition at the leading edge. The plate will therefore take on something of a sideways L shape, so it will be at an angle to the flow near the leading edge. Because the plate is at an angle to the flow, the fluid will apply a force to the plate and cause it to deflect. Consequently, the plate is able to produce thrust. Plates with very soft leading edges are thus better suited to heaving actuation than pitching actuation.

The region dominated by flutter behaviour differs markedly from the region dominated by Euler-Bernoulli behaviour. As we see in figure 11.11, a stiff leading edge always produces the most thrust in the flutter region. As we explained in Section 11.4.1,

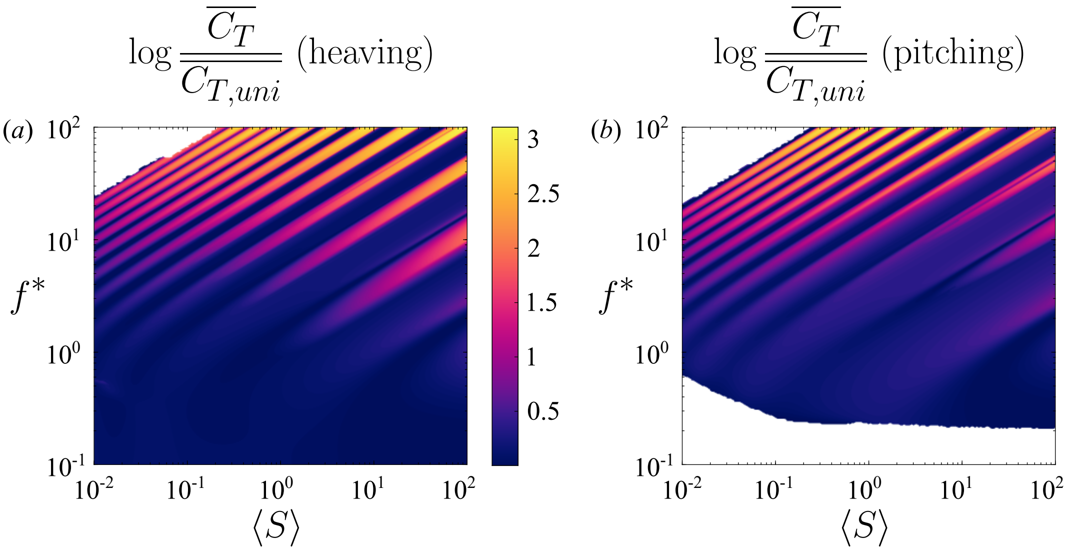

Figure 11.16: Same as figure 11.12, but compared to a plate with uniformly distributed stiffness instead of a rigid plate.

in this region the eigenvalues become more damped and move closer to each other, causing the resonant peaks to broaden and smear together. Resonant effects become weak, and the off-resonant behaviour dominates the response. Just as in the region dominated by Euler-Bernoulli behaviour, plates with a stiff leading edge produce the greatest trailing edge amplitude, leading to the greatest thrust production. That being said, the benefits over a plate with uniformly distributed stiffness are modest in this region (the same is true in the resonant gaps), whereas the benefits are quite large when the behaviour is dominated by Euler-Bernoulli modes, which we illustrate in figure 11.16.

We now shift our attention to calculating the linear stiffness distribution that minimizes power consumption. We have plotted the optimal (power-minimizing) linear stiffness distribution in figure 11.17, with the attendant optimal mean power coefficient plotted in figure 11.18. The results are essentially opposite of the results for optimal thrust. In the region where Euler-Bernoulli modes dominate the response, the optimal stiffness distribution is the one whose natural frequencies are far from the frequency of actuation. When maximizing thrust, it was desirable to actuate at

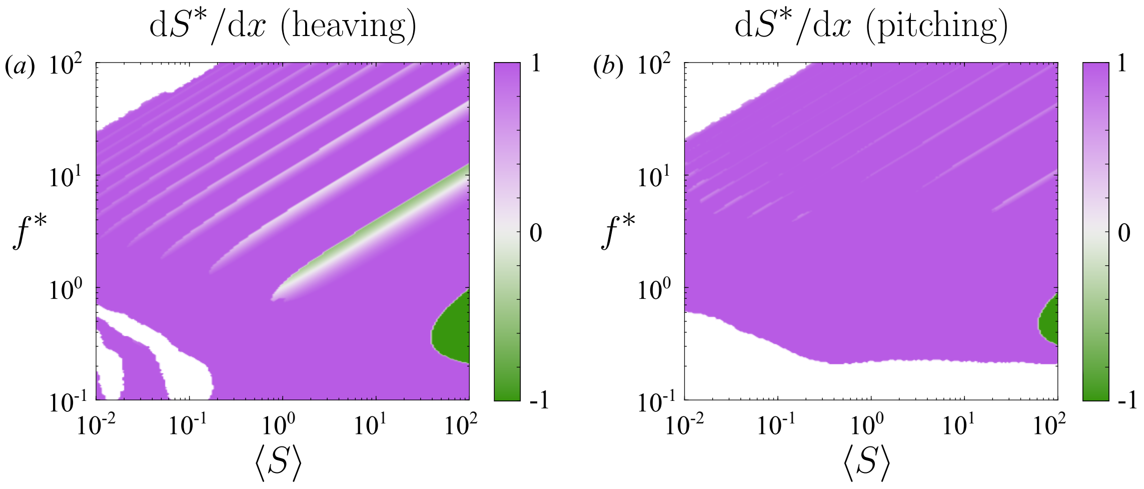

Figure 11.17: Optimal linear stiffness distribution as a function of reduced frequency f^* and mean stiffness ratio $\langle S \rangle$ for a (a) heaving and (b) pitching plate with $R \equiv 0.01$. Under-resolved areas and areas that produce negative power have been whited out. Results are for a flexible plate with linear stiffness distribution optimized for power.

resonance, whereas when minimizing power, it is undesirable to actuate at resonance. This is consistent with our understanding of uniformly flexible plates, where actuating at resonance maximizes trailing edge amplitude, thrust, and power.

In the resonant gaps, where no stiffness distribution has a natural frequency, a soft leading edge is always preferred since it produces a smaller trailing edge amplitude. As we previously explained, a plate with a soft leading edge generally produces a weaker moment at its leading edge, leading to smaller deflection and power consumption. Pitching accentuates this behaviour since the plate is entirely driven by a moment applied at the leading edge, explaining why a soft leading edge occupies a larger area of the frequency-stiffness plane when the plate is pitching than when it is heaving.

In the region dominated by flutter behaviour, a soft leading edge is also preferred. The effects of resonance are diminished in this region since the eigenvalues dampen and smear together. Just as in the resonant gaps, where resonance does not dictate the optimal stiffness distribution, plates with a soft leading edge produce the smallest trailing edge amplitude, leading to the smallest power consumption. The benefits over

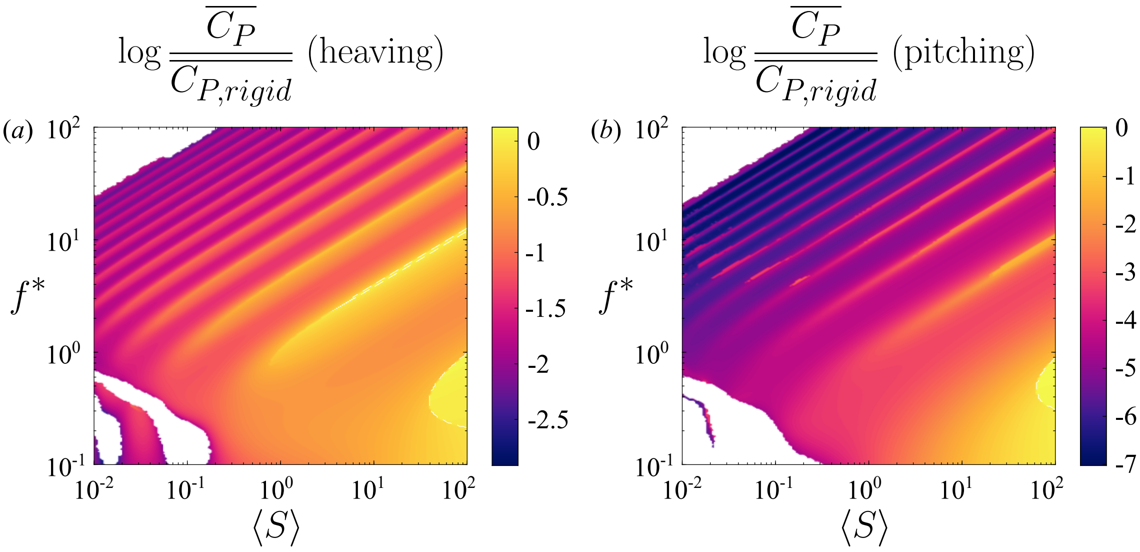

Figure 11.18: Power coefficient as a function of reduced frequency f^* and mean stiffness ratio $\langle S \rangle$ for a (a) heaving and (b) pitching plate with $R \equiv 0.01$ relative to that of an equivalent rigid plate. Dashed white lines indicate where the flexible plate has the same power coefficient as the equivalent rigid plate. Under-resolved areas and areas that produce negative power have been whited out. Results are for a flexible plate with linear stiffness distribution optimized for power.

a plate with uniformly distributed stiffness are modest when the plate is heaved, but pronounced when pitched, as we illustrate in figure 11.19. In contrast, the benefits are great in the region dominated by Euler-Bernoulli behaviour, as being able to tune the stiffness distribution (and hence natural frequencies) allows us to avoid a resonant condition.

Considering the optimal stiffness distributions for maximizing thrust and minimizing power, it is not immediately clear what stiffness distribution will maximize efficiency. In the former case, resonance is sought after as a maximizer of thrust, and a stiff leading edge is preferred when resonance is not possible. In the latter case, resonance is avoided, and a soft leading edge is preferred when resonance is not possible. We present the optimal (efficiency-maximizing) stiffness distributions in figure 11.20, with the attendant efficiency plotted in figure 11.21. When the plate is heaved, the optimizer sometimes converged to a solution with absolute efficiency

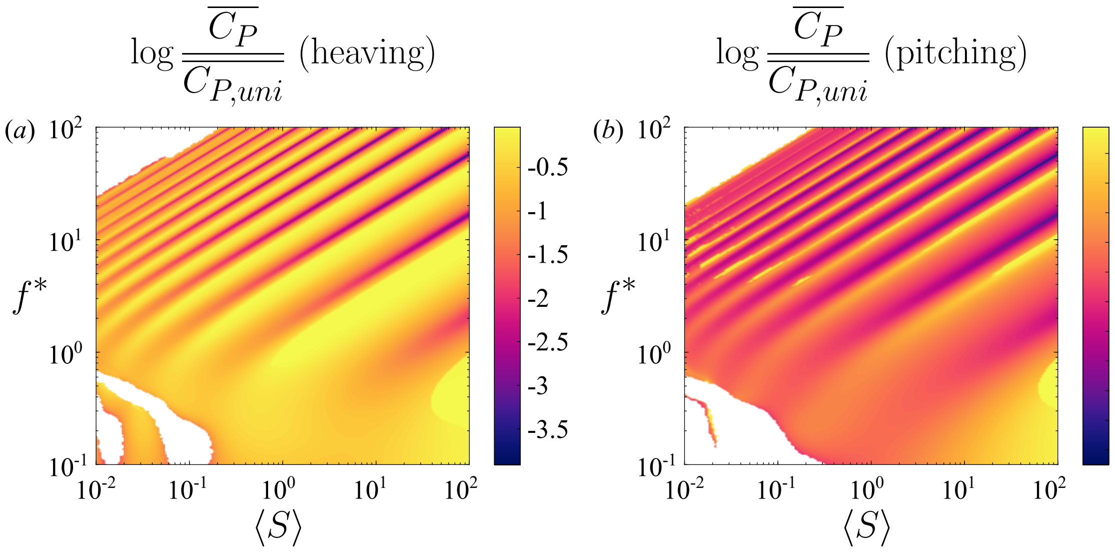

Figure 11.19: Same as figure 11.18, but compared to a plate with uniformly distributed stiffness instead of a rigid plate.

greater than unity, with both thrust and power negative; we have whited out these cases.

Unexpectedly, the frequency-stiffness plane is essentially divided into two zones: a lower zone where a plate with a soft leading edge is more efficient, and an upper zone where a plate with a stiff leading edge is more efficient. (For a pitching plate, a stiff leading edge is sometimes preferred near the zero-efficiency cutoff, where the thrust also crosses zero, since plates with a stiff leading edge produce more thrust than plates with a soft leading edge.) The boundary between the two zones changes qualitatively at $\langle S \rangle = 1$, i.e. when the behaviour changes from Euler-Bernoulli-dominated to flutter-dominated. In the Euler-Bernoulli region, the boundary is between the first and second natural frequencies, and runs parallel to them. In this region, elastic and added mass forces dominate the response, and the appropriate time scale is the bending time scale (see Section 11.B.2). We therefore expect a boundary between regions to appear when the actuation and bending time scales are nearly equal, consistent with the results. In the flutter region, on the other hand, the boundary is near $f^* = 1$. In this region, lift and added mass forces dominate the response, and the appropriate

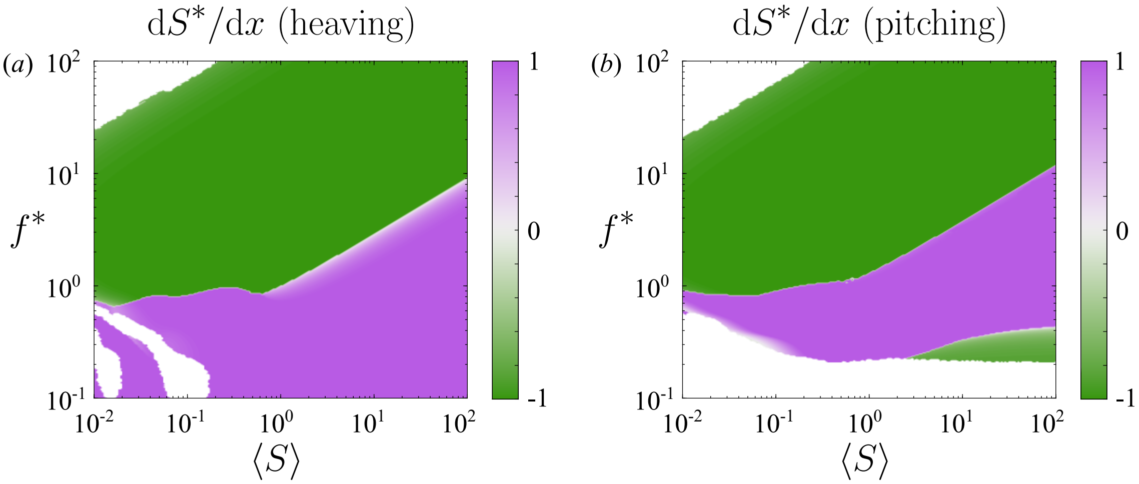

Figure 11.20: Optimal linear stiffness distribution as a function of reduced frequency f^* and mean stiffness ratio $\langle S \rangle$ for a (a) heaving and (b) pitching plate with $R \equiv 0.01$. Under-resolved areas and areas that produce negative thrust or power have been whited out. Results are for a flexible plate with linear stiffness distribution optimized for efficiency.

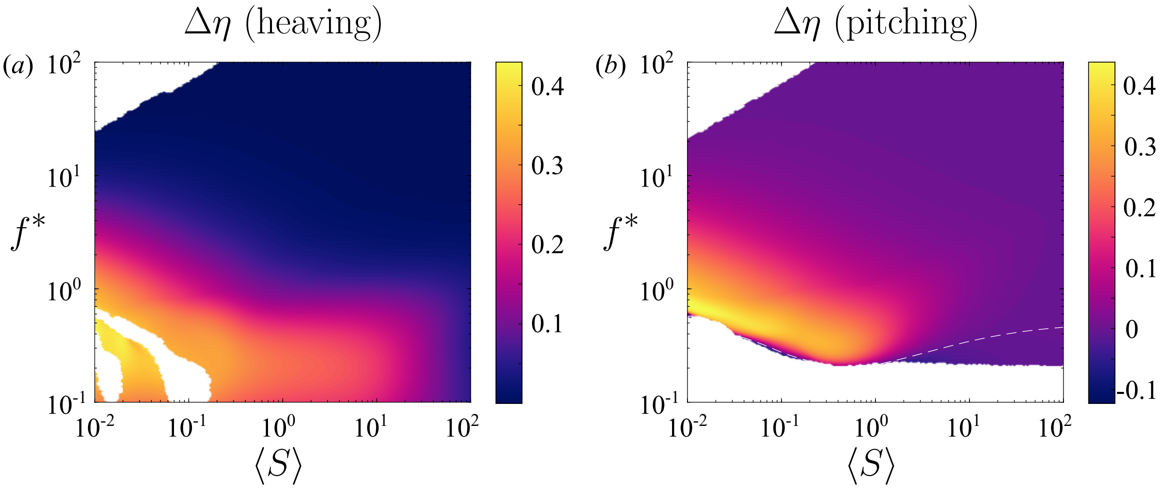

Figure 11.21: Efficiency as a function of reduced frequency f^* and mean stiffness ratio $\langle S \rangle$ for a (a) heaving and (b) pitching plate with $R \equiv 0.01$ relative to that of an equivalent rigid plate. Dashed white lines indicate where the flexible plate has the same efficiency as the equivalent rigid plate. Under-resolved areas and areas that produce negative thrust or power have been whited out. Results are for a flexible plate with linear stiffness distribution optimized for efficiency.

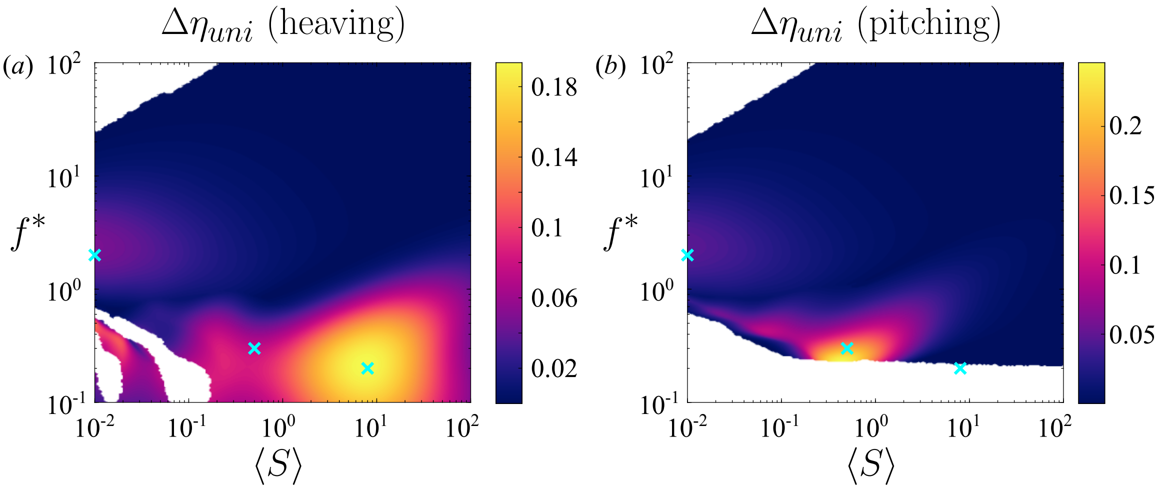

Figure 11.22: Same as figure 11.21, but compared to a plate with uniformly distributed stiffness instead of a rigid plate.

time scale is the convective time scale. Although the boundary between zones in this region corresponds to the actuation and convective time scales being nearly equal, we caution that the limit $\langle S \rangle \to 0$ is a singular one.

Why is a soft leading edge preferred in the lower zone, and a stiff leading edge preferred in the upper zone? To help answer this question, we appeal to the gains in efficiency made over a uniformly flexible plate, plotted in figure 11.22. The results show that meaningful efficiency gains are only made in the lower zone, i.e. by the plate with a flexible leading edge. We therefore focus on explaining this zone.

For uniformly flexible plates, meaningful gains in efficiency over rigid plates were made when flutter modes appeared. The flutter modes induce travelling wave kinematics in the actuated plate, which are known to be efficient (Wu, 1961). When the leading edge is soft, we saw that the natural frequencies decrease compared to a uniformly flexible plate. Moreover, flutter modes appear at higher mean stiffness ratios for plates with a soft leading edge than for uniformly flexible plates. Consequently, travelling wave kinematics can be induced in plates with a soft leading edge at higher values of the mean stiffness ratio than for uniformly flexible plates. Indeed, the area in the frequency-stiffness plane where the most significant gains in efficiency are made in going from a uniform stiffness distribution to an optimal stiffness distribution is where flutter modes are present for a plate with a soft leading edge but not present for a uniformly flexible plate (at least when the plate is heaved). When the plate is pitched, the region of greatest efficiency gains is shifted since a pitching plate produces net drag at low enough frequency. The physical reason for the efficiency gains, however, is unchanged: the plate with a soft leading edge has nice travelling wave kinematics in that region.

To verify that plates with nice travelling wave kinematics are indeed the efficient ones, we calculate the kinematics for plates with a stiff leading edge ($\mathrm{d}S^*/\mathrm{d}x = -0.99$), uniform flexibility ($\mathrm{d}S^*/\mathrm{d}x = 0$), and a soft leading edge ($\mathrm{d}S^*/\mathrm{d}x = 0.99$) for the $(\langle S \rangle, f^*)$ pairs $(8, 0.2)$, $(0.5, 0.3)$, and $(0.01, 2)$, marked by cyan crosses in figure 11.22. In all of these cases, there is a stiffness distribution that is clearly more efficient than the others. We represent the kinematics by the amplitude of the displacement along the chord, and the local dimensionless phase speed along the chord, given by

$$v_p^* = \frac{v_p}{U} = \frac{\sigma}{-\mathrm{d}(\angle Y_0)/\mathrm{d}x}, \tag{11.15}$$

where $\angle Y_0$ is the phase of the displacement along the chord. The kinematics are shown in figure 11.23 for a heaving plate and figure 11.24 for a pitching plate, with the amplitude on the left and local phase speed on the right. Note that the phase speed is always positive, indicating that waves travel from the leading edge to the trailing edge along the entire chord. In addition, we have also calculated the optimal phase speeds for each case and marked them as horizontal lines in figures 11.23 and 11.24. By optimal phase speed, we mean the constant phase speed that, given the distribution of the amplitude of deflection, produces the greatest efficiency. The point is to see how the passive kinematics determined by the fluid-structure interaction compare to the optimal travelling wave kinematics for each stiffness distribution. The results are intuitive and corroborate our previous claims: the stiffness distribution that produces nice travelling wave kinematics (closest to the optimal constant phase speed) produces the greatest efficiency in each case. One exception is for a pitching plate at $(\langle S \rangle, f^*) = (8, 0.2)$, shown in figure 11.24b, where no phase speed produces net thrust.

11.5.2 Quadratic stiffness distributions

We now add a degree of freedom, allowing the stiffness distribution to vary quadratically along the chord. As it turns out, all of the optimal distributions for the parameter values studied here lie near the boundary of the feasible set depicted in figure 11.10. (When performing the optimization, we slightly shrunk the feasible set in order to avoid problems associated with the stiffness being zero somewhere along the chord.) We may therefore represent the optimal quadratic stiffness distributions by a one-dimensional map, which is shown in figure 11.25. As before, stiffness distributions with a stiff leading edge are coded as green and those with a soft leading edge are coded as purple. In addtion, stiffness distributions that are concave up (edges stiffer than the interior) are coded as yellow and those that are concave down (edges softer than the interior) are coded as blue. Distributions on the horizontal line are linear, and distributions on the vertical line are symmetric about the mid-chord.

In figure 11.26, we have plotted the optimal (thrust-maximizing) quadratic stiffness distribution, with the attendant optimal mean thrust coefficient plotted in figure 11.27. The overall trends are comparable to those for linear stiffness distributions. In the region dominated by Euler-Bernoulli modes, the optimal stiffness distribution at a given reduced frequency and mean stiffness ratio is the one that has a natural frequency at that frequency of actuation. The additional degree of freedom in

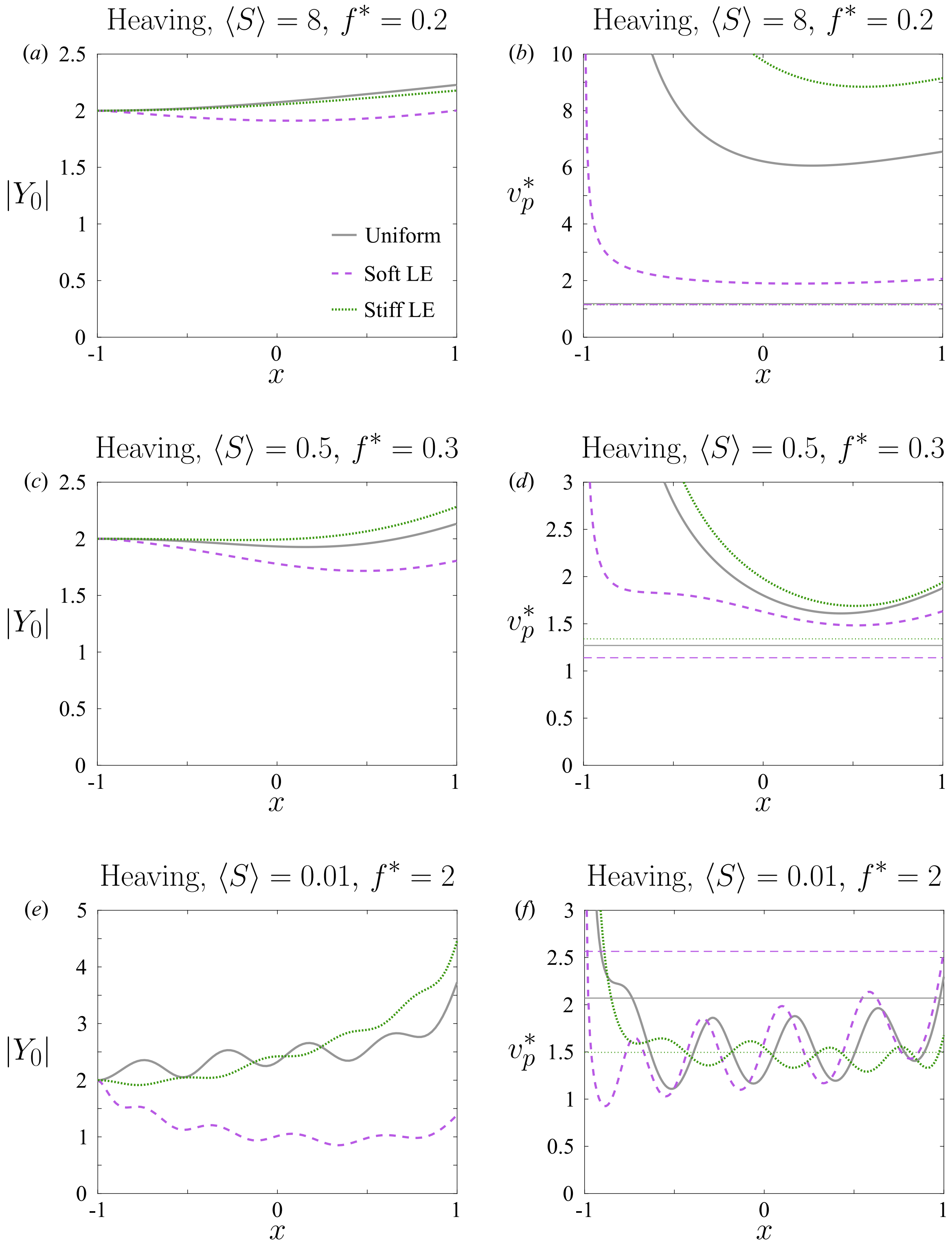

Figure 11.23: Amplitude of deflection (left column) and local phase speed (right column) along the chord for heaving plates with uniform flexibility ($\mathrm{d}S^*/\mathrm{d}x = 0$), a stiff leading edge ($\mathrm{d}S^*/\mathrm{d}x = -0.99$), and a soft leading edge ($\mathrm{d}S^*/\mathrm{d}x = 0.99$). Optimal constant phase speeds are shown as thin horizontal lines in the right column.

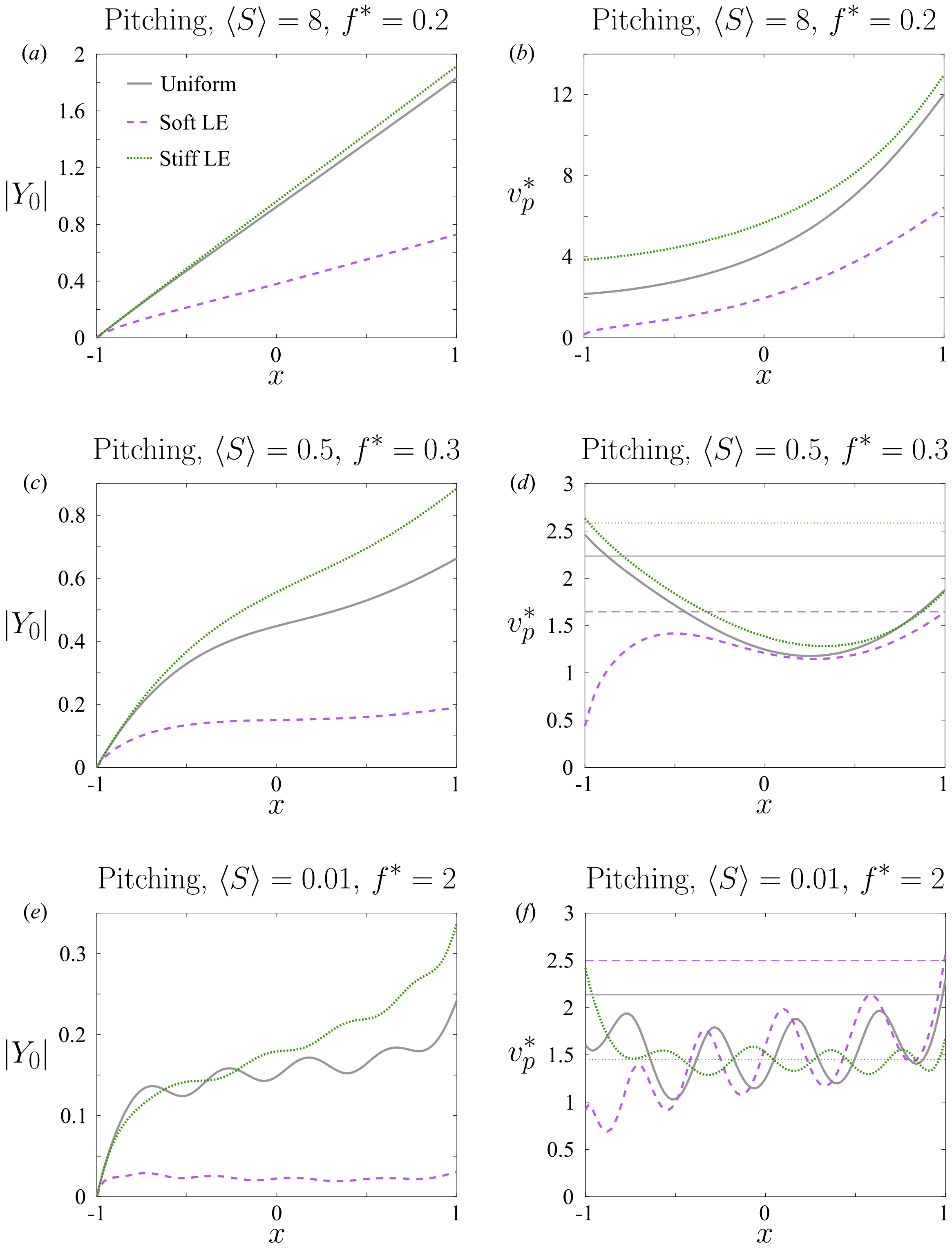

Figure 11.24: Amplitude of deflection (left column) and local phase speed (right column) along the chord for pitching plates with uniform flexibility ($\mathrm{d}S^*/\mathrm{d}x = 0$), a stiff leading edge ($\mathrm{d}S^*/\mathrm{d}x = -0.99$), and a soft leading edge ($\mathrm{d}S^*/\mathrm{d}x = 0.99$). Optimal constant phase speeds are shown as thin horizontal lines in the right column except in (b), where no phase speed produces net thrust.

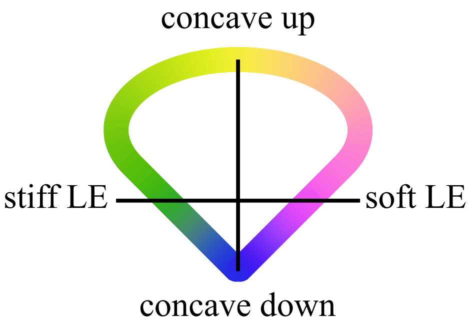

Figure 11.25: Colour coding for quadratic stiffness distributions.

the stiffness distribution gives more freedom to tune the natural frequency of the plate, thereby broadening the resonant response and narrowing the resonant gaps. As for linear distributions, a stiff leading edge is preferred when a resonant condition cannot be reached, both in the region dominated by Euler-Bernoulli modes and the region dominated by flutter modes. When distributions with a stiff or soft leading edge have the same natural frequency, a stiff leading edge is again preferred. With the additional degree of freedom in stiffness distribution, the natural frequencies of distributions with stiff leading edges are able to cover a larger portion of the frequency-stiffness plane than linear distributions. As a result, a larger portion of the frequency-stiffness plane is green in figure 11.26 (cf. figure 11.11); this is especially evident for pitching motions, where distributions with a soft leading edge have almost entirely disappeared.

We note that much of the frequency-stiffness plane has a yellow tint, reflecting that a positive quadratic component of the stiffness distribution enhances the thrust. The reason is quite simple: a positive quadratic component sacrifices the stiffness of the interior of the plate to increase the stiffness of the edges. In other words, the leading edge can be made even stiffer than with just a linear stiffness distribution while maintaining the same mean stiffness. The quadratic component of the stiffness distribution allows us to concentrate the stiffness toward the leading edge, which we have seen enhances thrust. The trends for quadratic stiffness distributions are the

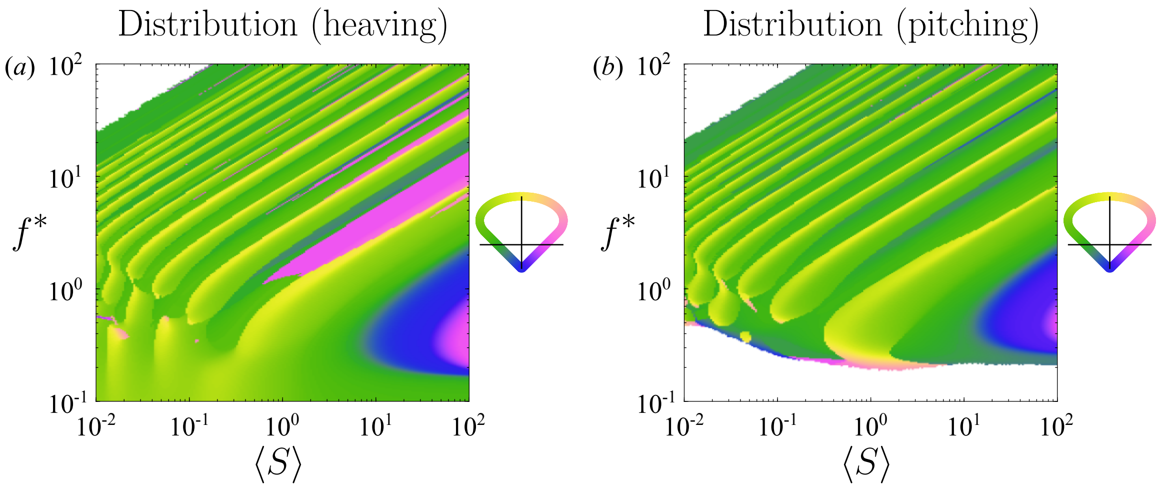

Figure 11.26: Optimal quadratic stiffness distribution as a function of reduced frequency f^* and mean stiffness ratio $\langle S \rangle$ for a (a) heaving and (b) pitching plate with $R \equiv 0.01$. Under-resolved areas and areas that produce negative thrust have been whited out. Results are for a flexible plate with quadratic stiffness distribution optimized for thrust.

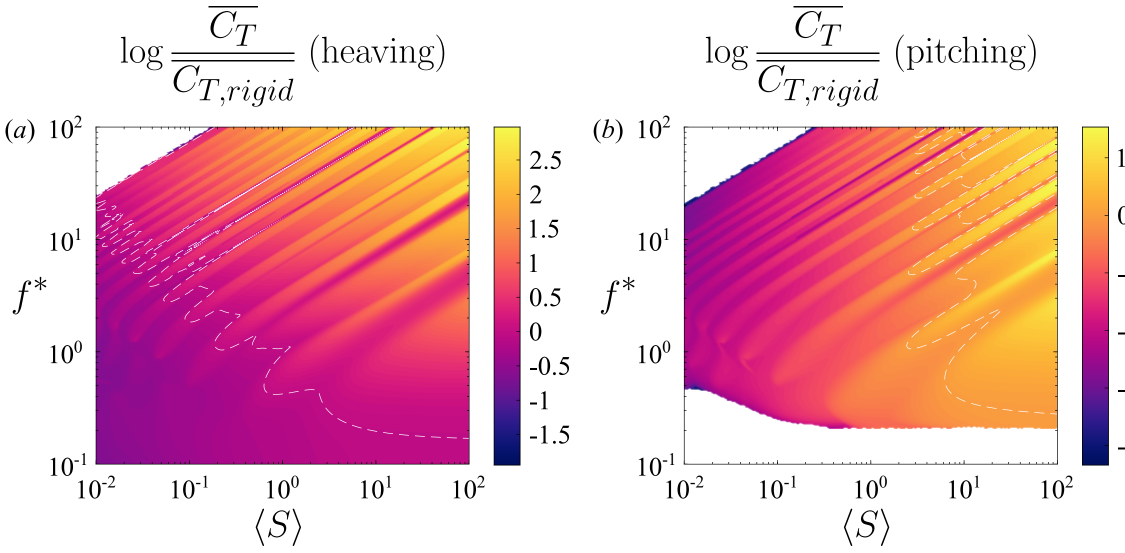

Figure 11.27: Thrust coefficient as a function of reduced frequency f^* and mean stiffness ratio $\langle S \rangle$ for a (a) heaving and (b) pitching plate with $R \equiv 0.01$ relative to that of an equivalent rigid plate. Dashed white lines indicate where the flexible plate has the same thrust coefficient as the equivalent rigid plate. Under-resolved areas and areas that produce negative thrust have been whited out. Results are for a flexible plate with quadratic stiffness distribution optimized for thrust.

same as for linear stiffness distributions. We posit that even higher-order distributions would tend to further concentrate the stiffness at the leading edge.

When minimizing the power, the results mirror those for linear stiffness distributions. The optimal quadratic stiffness distribution is plotted in figure 11.28, with the attendant optimal mean power coefficient plotted in figure 11.29. Essentially, a soft leading edge is preferred unless it creates a condition of resonance. In other words, the results are opposite of those when maximizing thrust. We note that much of the frequency-stiffness plane has a pink tint, reflecting a positive quadratic component of the stiffness distribution. The positive quadratic component allows us to concentrate the stiffness toward the trailing edge, making the leading edge softer than a linear distribution could, thereby further decreasing power consumption. There are also portions of the frequency-stiffness plane that are blue, with the stiffness being distributed symmetrically about the mid-chord and concentrated toward the interior of the plate. The blue regions largely replace regions where a uniform stiffness distribution was preferred for linear distributions, and appear in the region dominated by Euler-Bernoulli modes. In the blue regions, stiffness distributions with the stiffness concentrated away from the leading edge apparently have a natural frequency present in those regions, which would increase power consumption. The symmetric, concave-down distribution is the best option as it still softens the leading edge compared to the uniform distribution (although the leading and trailing edges are equally stiff).

Overall, the trends are the same as for linear stiffness distributions: concentrate stiffness away from the leading edge while avoiding resonance. For higher-order stiffness distributions, we posit that the preferred distribution will continue to be the one that most effectively concentrates stiffness away from the leading edge. Once the order is high enough, it may be that at each point in the frequency-stiffness plane these exists a distribution with a soft leading edge without a natural frequency at that point in the frequency-stiffness plane.

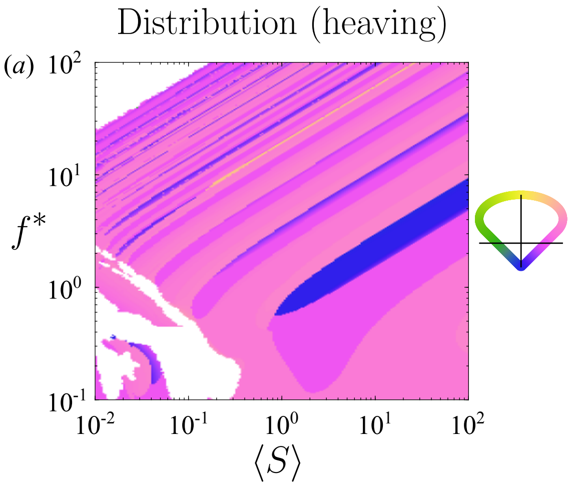
Distribution (heaving)

Distribution (pitching)

Figure 11.28: Optimal quadratic stiffness distribution as a function of reduced frequency f^* and mean stiffness ratio $\langle S \rangle$ for a (a) heaving and (b) pitching plate with $R \equiv 0.01$. Under-resolved areas and areas that produce negative power have been whited out. Results are for a flexible plate with quadratic stiffness distribution optimized for power.

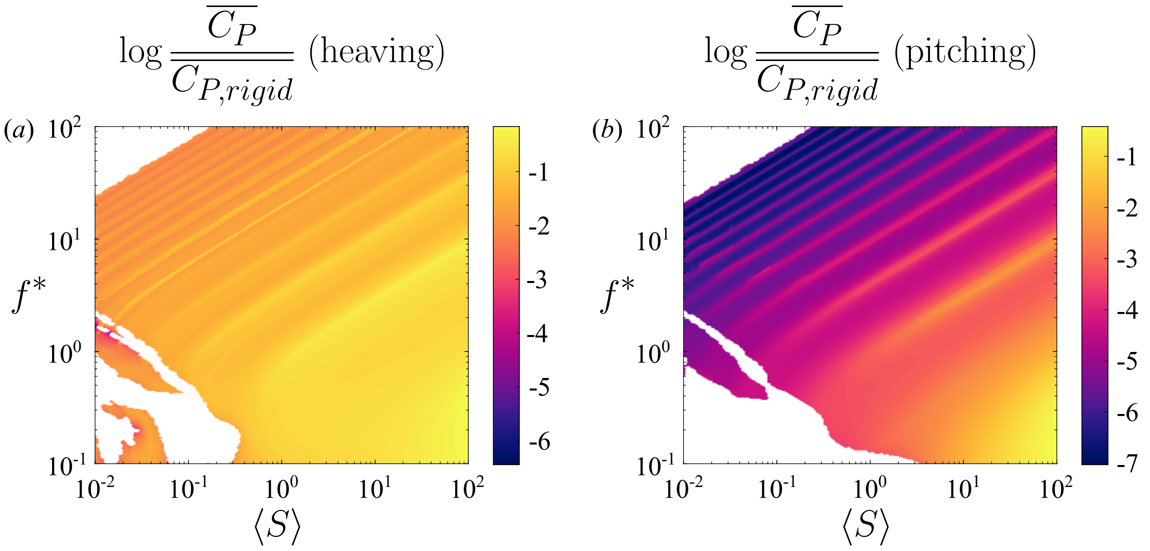
$\log \dfrac{\overline{C_P}}{\overline{C_{P,rigid}}}$ (heaving)

$\log \dfrac{\overline{C_P}}{\overline{C_{P,rigid}}}$ (pitching)

Figure 11.29: Power coefficient as a function of reduced frequency f^* and mean stiffness ratio $\langle S \rangle$ for a (a) heaving and (b) pitching plate with $R \equiv 0.01$ relative to that of an equivalent rigid plate. Dashed white lines indicate where the flexible plate has the same power coefficient as the equivalent rigid plate. Under-resolved areas and areas that produce negative power have been whited out. Results are for a flexible plate with quadratic stiffness distribution optimized for power.

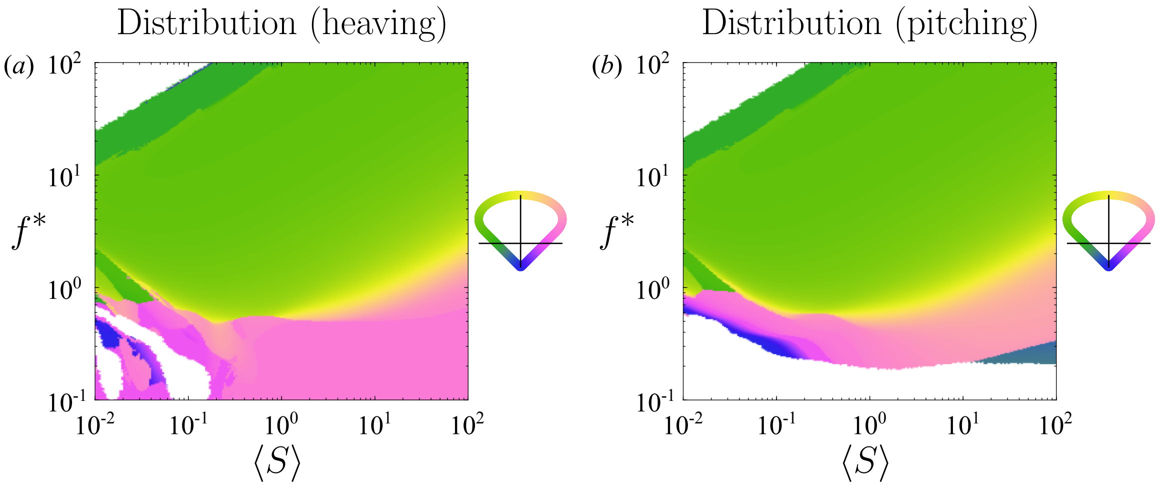

Figure 11.30: Optimal quadratic stiffness distribution as a function of reduced frequency f^* and mean stiffness ratio $\langle S \rangle$ for a (a) heaving and (b) pitching plate with $R \equiv 0.01$. Under-resolved areas and areas that produce negative thrust or power have been whited out. Results are for a flexible plate with quadratic stiffness distribution optimized for efficiency.

Since a stiff leading edge generally maximizes thrust production and a soft leading edge generally minimizes power consumption, it is not immediately clear what stiffness distribution will maximize efficiency. The efficiency-maximizing stiffness distributions are plotted in figure 11.30, with the attendant efficiency plotted in figure 11.31. When the plate is heaved, the optimizer sometimes converged to a solution with absolute efficiency greater than unity, with both thrust and power negative; we have whited out these cases.

The results mirror those for linear stiffness distributions, with the frequency-stiffness plane essentially divided into two zones: a lower zone where a plate with a soft leading edge is more efficient, and an upper zone where a plate with a stiff leading edge is more efficient. For a pitching plate, there is a small region near the zero-thrust cutoff where a plate with a stiff leading edge is more efficient. For $\langle S \rangle \gtrsim 1$, boundary between the two zones runs parallel to the natural frequencies and is quite broad compared to the same boundary for linear stiffness distributions. For $\langle S \rangle \lesssim 1$, the boundary between the two zones is irregular but still quite sharp. In most of the

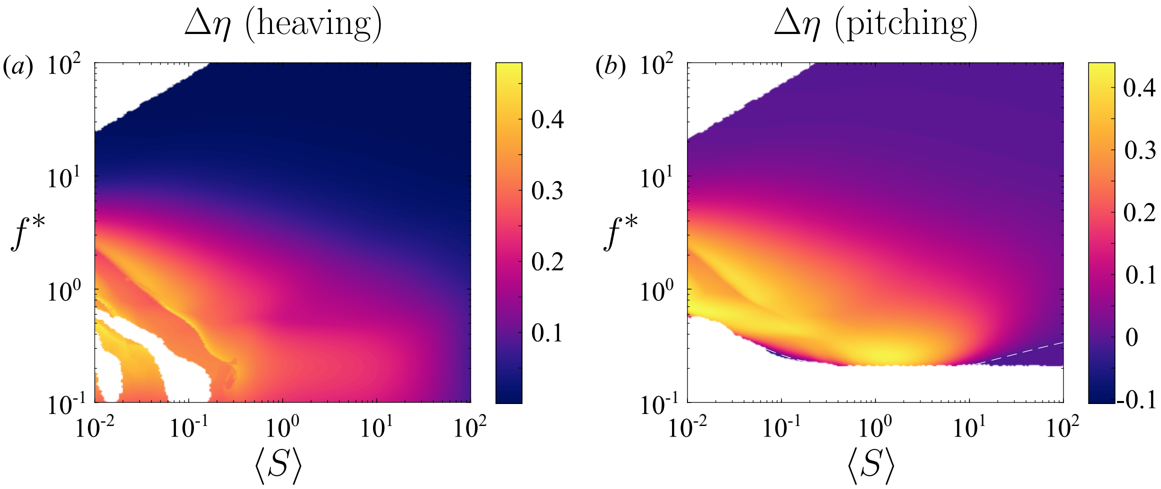

Figure 11.31: Efficiency as a function of reduced frequency f^* and mean stiffness ratio $\langle S \rangle$ for a (a) heaving and (b) pitching plate with $R \equiv 0.01$ relative to that of an equivalent rigid plate. Dashed white lines indicate where the flexible plate has the same efficiency as the equivalent rigid plate. Under-resolved areas and areas that produce negative thrust or power have been whited out. Results are for a flexible plate with quadratic stiffness distribution optimized for efficiency.

frequency-stiffness plane, the optimal stiffness distributions have a positive quadratic component, meaning that concentrating stiffness towards the edges is beneficial for efficiency. This effect was also seen when maximizing thrust and minimizing power, so we posit that it will continue to hold for higher-order stiffness distributions.

Again, only certain portions of the frequency-stiffness plane enjoy meaningful gains in efficiency over a uniformly flexible plate, shown in figure 11.32. With the addition of the quadratic component to the stiffness distribution, a significant portion of the frequency-stiffness plane where a stiff leading edge is preferred enjoys meaningful gains in efficiency over a uniformly flexible plate, whereas this was not the case for linear stiffness distributions. Although we do not show it here for brevity, the regions with meaningful gains in efficiency are those where efficient travelling wave kinematics are induced by flutter modes.

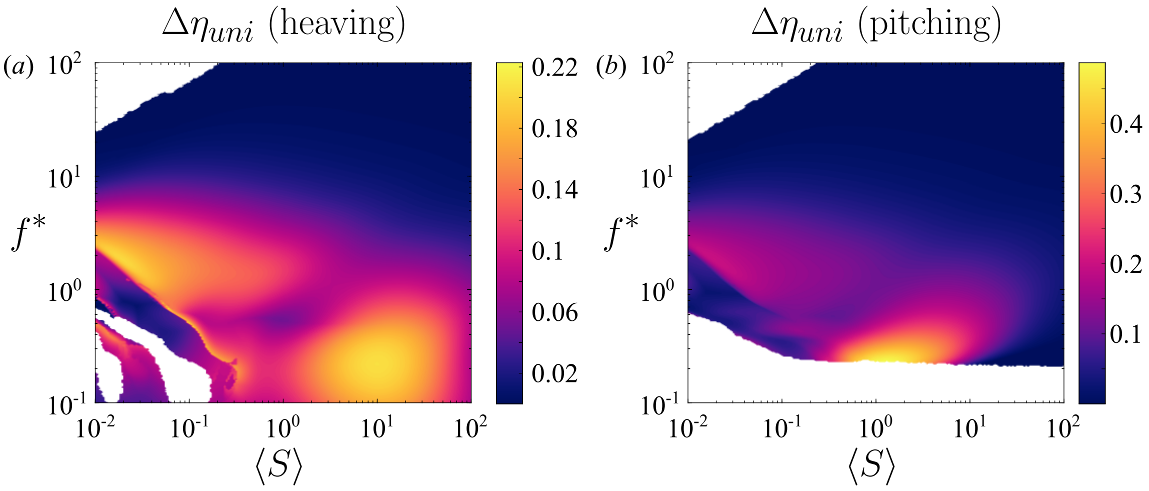

Figure 11.32: Same as figure 11.31, but compared to a plate with uniformly distributed stiffness instead of a rigid plate.

11.5.3 Finite Reynolds number effects

We take the opportunity to briefly remark on the effects of streamwise drag. Having an offset drag in the system will move where the net thrust transitions from being negative to positive to greater frequencies. Distributions with stiffness concentrated toward the leading edge will still produce the greatest thrust, and the results for power consumption will also be unaffected.

Efficiency is a different story, though. Drag can create peaks in efficiency nearby where the net thrust transitions from being negative to positive (Floryan et al., 2017a, 2018). The presence of drag also makes the efficiency quite sensitive to changes in the system. These two effects are present for both rigid and flexible plates.

For flexible plates, an additional effect emerges. As shown in figure 11.5, the efficiency of flexible plates does not have any resonant peaks in the inviscid small-amplitude regime, with the resonant peaks in thrust and power cancelling each other exactly. Upon adding drag to the system, however, resonant peaks in efficiency emerge (Floryan and Rowley, 2018). The explanation is straightforward. In moving from a non-resonant to a resonant condition in a system without drag, the mean thrust and power coefficients effectively scale up by some factor $a > 1$. Since the efficiency is the ratio of the two, the factor a appears in the numerator and denominator, cancels, and there is no resonant peak. When drag is present, it reduces the baseline non-resonant efficiency compared to the system without drag. In moving to a resonant condition, the thrust and power scale up by the factor a, but the drag does not. The net thrust therefore scales up by a factor greater than a, so the efficiency increases at resonance. This effect creates local maxima in efficiency at resonance. Since drag affects the system at first order, this effect of streamwise drag inducing resonant peaks in efficiency should be robust to nonlinearities present at finite amplitudes.

The presence of streamwise drag will therefore have two effects on the efficiency-maximizing stiffness distributions. The first is that it will wipe out the stiffness distributions with a soft leading edge at low frequencies. At low frequencies, the distributions with a soft leading edge that are highly efficient also produce very little thrust. The drag will be comparable in magnitude to the thrust produced by plates with a soft leading edge, causing the net thrust (and therefore the efficiency) to plummet. Since plates with a stiff leading edge produce greater thrust, they are more robust to the effects of drag and will be favoured in the presence of drag over plates with a soft leading edge.

The second effect occurs far from where the net thrust transitions between negative and positive. Since drag induces a resonant behaviour in efficiency, the efficiency-maximizing stiffness distribution will take advantage of this resonant effect. Consequently, the efficiency-maximizing stiffness distribution will tend towards the thrust-maximizing stiffness distribution. Altogether, the presence of drag will make the efficiency-maximizing stiffness distribution tend towards the thrust-maximizing stiffness distribution everywhere in the frequency-stiffness plane.

11.6 Conclusions

In this work, we studied a linear inviscid model of a passively flexible swimmer, valid for small-amplitude motions. We explored how distributed flexibility modifies the thrust production, power consumption, and propulsive efficiency compared to swimmers with uniform flexibility. The frequencies of actuation and mean stiffness ratios we considered spanned a large range, while the mass ratio was fixed to a low value representative of swimmers.

The distributions of flexibility were described by a set of orthogonal polynomials, making it easy to control the mean stiffness and isolate the effects of the flexibility distribution. In previous studies, the effects of distribution were never isolated from the effects of mean stiffness. We found that allowing the stiffness to vary spatially produced no qualitative changes, with the thrust, power, and efficiency all having the same dependence on frequency of actuation and mean stiffness as a uniformly flexible swimmer.

Important quantitative differences do arise, however, because changing the flexibility distribution changes the natural frequencies of the system, even though the mean stiffness is unchanged. To elucidate these differences, we calculated stiffness distributions that maximize thrust, minimize power, and maximize efficiency, and related them to the changes in the eigenvalues of the fluid-structure system. In order to maximize thrust at a given actuation frequency and mean stiffness, the flexibility should be distributed in a way that a natural frequency can be created at the frequency of actuation. If this is not possible or the mean stiffness is sufficiently low, then concentrating stiffness toward the leading edge maximizes thrust. To minimize power, the opposite conclusions hold: natural frequencies should be avoided and the stiffness should be concentrated away from the leading edge. Meaningful increases in efficiency are attained when the flexibility distribution elicits flutter behaviour, which induces efficient travelling wave kinematics. We showed that a proper distribution of flexibility leads to travelling wave kinematics with near-optimal phase speeds.

Lastly, we considered how a finite Reynolds number (in the form of streamwise drag) may change the optimal behaviour. The thrust-maximizing and power-minimizing distributions are not changed, but the presence of streamwise drag will change the efficiency-maximizing distribution to resemble the thrust-maximizing distribution.

This work was supported by ONR Grant N00014-14-1-0533 (Program Manager Robert Brizzolara).

11.A Method of solution

Consider the case where the imposed leading edge motion is sinusoidal in time with dimensionless angular frequency $\sigma = \pi L f / U$, where f is the dimensional frequency in Hz. We may then decompose the deflection into a product of temporal and spatial terms, with the temporal component being sinusoidal and the spatial component represented by a Chebyshev series:

$$\left.\begin{aligned} Y(x,t) &= \mathrm{e}^{\mathrm{j}\sigma t} Y_0(x), \\ Y_0(x) &= \frac{1}{2}\beta_0 + \sum_{k=1}^{\infty} \beta_k T_k(x), \end{aligned}\right\} \tag{11.16}$$

where $\mathrm{j} = \sqrt{-1}$, the real part in j should be taken when evaluating the deflection, and $T_k(x) = \cos(k \arccos x)$ is the Chebyshev polynomial of degree k. For a given deflection Y of this form, the solution to the flow is given in Wu (1961); we repeat the basics of that analysis in the proceeding text.

Represent two-dimensional physical space (x, y) by the complex plane $z = x + \mathrm{i}y$, where $\mathrm{i} = \sqrt{-1}$ but $\mathrm{ij} \neq -1$. There exists a complex potential $F(z,t) = \phi(z,t) +$

$\mathrm{i}\psi(z,t)$, with ϕ and ψ harmonic conjugates, that is analytic in z and related to the complex velocity $w = u - \mathrm{i}v$ through the momentum equation by

$$\frac{\partial F}{\partial z} = \frac{\partial w}{\partial t} + \frac{\partial w}{\partial z}. \tag{11.17}$$

We use the conformal transformation

$$z = \frac{1}{2}\left(\zeta + \frac{1}{\zeta}\right) \tag{11.18}$$

to map physical space in the z-plane to the exterior of the unit circle in the ζ-plane. This transformation maps the plate onto the unit circle. The complex potential can be represented by a multipole expansion

$$F(\zeta,t) = \phi(\zeta,t) + \mathrm{i}\psi(\zeta,t) = \mathrm{i}\mathrm{e}^{\mathrm{j}\sigma t}\left(\frac{a_0}{\zeta+1} + \sum_{k=1}^{\infty}\frac{a_k}{\zeta^k}\right). \tag{11.19}$$

Evaluating on the unit circle $\zeta = \mathrm{e}^{\mathrm{i}\theta}$ gives

$$\left.\begin{aligned} \phi(\zeta = \mathrm{e}^{\mathrm{i}\theta}, t) &= \mathrm{e}^{\mathrm{j}\sigma t}\left(\frac{1}{2}a_0 \tan\frac{\theta}{2} + \sum_{k=1}^{\infty} a_k \sin k\theta\right), \\ \psi(\zeta = \mathrm{e}^{\mathrm{i}\theta}, t) &= \mathrm{e}^{\mathrm{j}\sigma t}\left(\frac{1}{2}a_0 + \sum_{k=1}^{\infty} a_k \cos k\theta\right). \end{aligned}\right\} \tag{11.20}$$

In physical space, on the surface of the plate we have

$$\left.\begin{aligned} \phi(z = x \pm 0\mathrm{i}, t) &= \mathrm{e}^{\mathrm{j}\sigma t}\Phi^{\pm}(x) = \mathrm{e}^{\mathrm{j}\sigma t}\left(\pm\frac{1}{2}a_0\sqrt{\frac{1-x}{1+x}} \pm \sum_{k=1}^{\infty} a_k \sin k\theta\right), \\ \psi(z = x \pm 0\mathrm{i}, t) &= \mathrm{e}^{\mathrm{j}\sigma t}\Psi(x) = \mathrm{e}^{\mathrm{j}\sigma t}\left(\frac{1}{2}a_0 + \sum_{k=1}^{\infty} a_k T_k(x)\right), \end{aligned}\right\} \tag{11.21}$$

where we have used $x = \cos\theta$. ψ has equal values on the top and bottom since it is even in θ, whereas ϕ is odd in θ and thus has a discontinuity in physical space.

The no-penetration condition can be written as

$$\frac{\partial \psi}{\partial x}|_{y=0} = -\left(\frac{\partial}{\partial t} + \frac{\partial}{\partial x}\right)^2 Y, \tag{11.22}$$

which simplifies to

$$D\Psi = -(\mathrm{j}\sigma + D)^2 Y_0, \tag{11.23}$$

where $D = \mathrm{d}/\mathrm{d}x$. Given Y_0, this equation allows us to solve for all a_k except a_0. To solve for a_0, we begin by writing the vertical velocity on the surface of the plate as

$$v(z = x + 0\mathrm{i}, t) = \mathrm{e}^{\mathrm{j}\sigma t} V(x) = \mathrm{e}^{\mathrm{j}\sigma t}\left(\frac{1}{2}V_0 + \sum_{k=1}^{\infty} V_k T_k(x)\right). \tag{11.24}$$

The no-penetration condition can then be written as

$$V = (\mathrm{j}\sigma + D)Y_0. \tag{11.25}$$

The coefficient a_0 is given by

$$a_0 = -C(\mathrm{j}\sigma)(V_0 + V_1) + V_1, \tag{11.26}$$

where

$$C(\mathrm{j}\sigma) = \frac{K_1(\mathrm{j}\sigma)}{K_0(\mathrm{j}\sigma) + K_1(\mathrm{j}\sigma)} \tag{11.27}$$

is the Theodorsen function, and K_ν is the modified Bessel function of the second kind of order ν. The expression for a_0 is derived in Wu (1961).

With all of the a_k known, the pressure difference across the plate can be written as

$$\Delta p(x, t) = \mathrm{e}^{\mathrm{j}\sigma t} P_0(x) = \mathrm{e}^{\mathrm{j}\sigma t}\left(a_0\sqrt{\frac{1-x}{1+x}} + 2\sum_{k=1}^{\infty} a_k \sin k\theta\right). \tag{11.28}$$

We note that the pressure difference depends linearly on the deflection Y_0.

Altogether, given the deflection Y_0, we may calculate the coefficients a_k. The coefficients a_k are used to calculate the pressure difference across the plate, which alters the deflection of the plate via (11.3). The coupled fluid-structure problem must be solved numerically.

11.A.1 Numerical method

Substituting the Chebyshev series (11.16) into the Euler-Bernoulli equation (11.3) gives a fourth-order differential equation for Y_0:

$$-2\sigma^2 R Y_0 + \frac{2}{3} D^2 (S D^2 Y_0) = P_0. \tag{11.29}$$

The corresponding boundary conditions (11.6) are re-written as

$$Y_0(-1) = h_0, \quad Y_{0,x}(-1) = \theta_0, \quad Y_{0,xx}(1) = 0, \quad Y_{0,xxx}(1) = 0, \tag{11.30}$$

where h_0 and θ_0 are the heaving and pitching amplitudes at the leading edge, respectively. We re-iterate that the pressure difference across the plate P_0 is a linear function of the deflection Y_0, and so (11.29)–(11.30) give a linear, homogemeous boundary value problem for Y_0. When solving for the deflection Y_0, all infinite series are truncated to the upper limit N.

The numerical method to solve the boundary value problem is given in Moore (2017). The method is a pseudo-spectral Chebyshev scheme that uses Gauss-Chebyshev points. The method is fast ($O(N \log N)$) and accurate, avoiding errors typically encountered when using Chebyshev methods to solve high-order differential equations by pre-conditioning the system with continuous operators. Quadrature formulas for the thrust and power coefficients in (11.7) and (11.8) are also given in Moore (2017).

11.B Eigenvalues of the system

Here, we seek to determine the natural response of a flexible plate whose leading edge is held clamped in an oncoming flow (Alben, 2008a; Michelin and Llewellyn Smith, 2009; Eloy et al., 2007). This amounts to finding the eigenvalues and eigenvectors of the system (11.3) with homogeneous boundary conditions ($h(t) \equiv 0$ and $\theta(t) \equiv 0$). To do so, quantities that were previously written as Fourier-Chebyshev expansions (the deflection, complex potential, and velocity) are now written as Chebyshev series with time-varying coefficients. Following the preceding analysis, we arrive at the following equations:

$$2RY_{tt} + \frac{2}{3}(SY_{xx})_{xx} = \Delta p, \tag{11.31}$$

$$Y(x,t) = \frac{1}{2}\beta_0(t) + \sum_{k=1}^{\infty} \beta_k(t) T_k(x), \tag{11.32}$$

$$\Delta p(x,t) = a_0(t)\sqrt{\frac{1-x}{1+x}} + 2\sum_{k=1}^{\infty} a_k(t)\sin k\theta, \tag{11.33}$$

$$\sum_{k=1}^{\infty} a_k T_k' = -\frac{1}{2}\ddot{\beta}_0 - \sum_{k=1}^{\infty}\left[\ddot{\beta}_k T_k + 2\dot{\beta}_k T_k' + \beta_k T_k''\right], \tag{11.34}$$

where a dot denotes differentiation with respect to t and a prime denotes differentiation with respect to x.

As before, we need an additional equation to determine a_0. For now, we use (11.26) but treat the Theodorsen function as a constant C. The coefficient a_0 is then

$$a_0 = -C(V_0 + V_1) + V_1, \tag{11.35}$$

where V_k is the kth Chebyshev coefficient of the vertical velocity on the surface of the plate. The V_k are obtained by evaluating the no-penetration condition (11.5):

$$\frac{1}{2}V_0 + \sum_{k=1}^{\infty} V_k T_k = \frac{1}{2}\dot{\beta}_0 + \sum_{k=1}^{\infty}\left[\dot{\beta}_k T_k + \beta_k T_k'\right]. \tag{11.36}$$

Treating a_0 in this manner will yield a linear eigenvalue problem. After obtaining the eigenvalues and eigenfunctions of the linear eigenvalue problem, we will use those as initial guesses for the nonlinear eigenvalue problem, which will use the full Theodorsen function. But first, we proceed with the description of the linear eigenvalue problem.

We can write the equations more compactly as follows:

$$\begin{aligned} 2\tilde{R}\ddot{\boldsymbol{\beta}} + \frac{2}{3}D^2(\tilde{S}D^2\boldsymbol{\beta}) &= \boldsymbol{P}, && (11.37)\\ \boldsymbol{P} &= A\boldsymbol{a}, && (11.38)\\ D\boldsymbol{a} &= -\ddot{\boldsymbol{\beta}} - 2D\dot{\boldsymbol{\beta}} - D^2\boldsymbol{\beta}, && (11.39)\\ \boldsymbol{V} &= \dot{\boldsymbol{\beta}} + D\boldsymbol{\beta}, && (11.40) \end{aligned}$$

with (11.35) for a_0. In the above, $\boldsymbol{\beta}$ is a vector of the Chebyshev coefficients of the deflection Y, and similarly for $\boldsymbol{P}$ (pressure), $\boldsymbol{a}$ (potential), and $\boldsymbol{V}$ (vertical velocity). $\boldsymbol{P} = A\boldsymbol{a}$ simply states that the Chebyshev coefficients of the pressure are linear combinations of the coefficients a_k, and D is the spectral representation of the differentiation operator. Quantities with a tilde over them are spectral representations of multiplication in space, i.e. $\tilde{G} = FGF^{-1}$, where F is the linear operator that maps spatial coordinates to spectral coordinates.

Putting everything together, we get the following ordinary differential equation:

$$\begin{aligned} 2\tilde{R}\ddot{\boldsymbol{\beta}} + \frac{2}{3}D^2(\tilde{S}D^2\boldsymbol{\beta}) \;&=\; A[-D^-\ddot{\boldsymbol{\beta}} - 2D^-D\dot{\boldsymbol{\beta}} + \boldsymbol{e_1}(\boldsymbol{e_2} - C\boldsymbol{e_1} - C\boldsymbol{e_2})^T\dot{\boldsymbol{\beta}} \\ &\quad -D^-D^2\boldsymbol{\beta} + \boldsymbol{e_1}(\boldsymbol{e_2} - C\boldsymbol{e_1} - C\boldsymbol{e_2})^T D\boldsymbol{\beta}], \qquad (11.41) \end{aligned}$$

where D^- is the spectral representation of the integration operator that makes the first Chebyshev coefficient zero, and $\boldsymbol{e_k}$ is the kth Euclidean basis vector. (11.41) can be written in state-space form as

$$\left.\begin{aligned}
&\frac{\mathrm{d}}{\mathrm{d}t}\begin{bmatrix}\boldsymbol{\beta}\\ \dot{\boldsymbol{\beta}}\end{bmatrix} = \begin{bmatrix}0 & I\\ M^{-1}A_1 & M^{-1}A_2\end{bmatrix}\begin{bmatrix}\boldsymbol{\beta}\\ \dot{\boldsymbol{\beta}}\end{bmatrix},\\
&M = 2\tilde{R} + AD^{-},\\
&A_1 = -\frac{2}{3}D^2\tilde{S}D^2 - AD^{-}D^2 + A\boldsymbol{e_1}(\boldsymbol{e_2} - C\boldsymbol{e_1} - C\boldsymbol{e_2})^T D,\\
&A_2 = -2AD^{-}D + A\boldsymbol{e_1}(\boldsymbol{e_2} - C\boldsymbol{e_1} - C\boldsymbol{e_2})^T.
\end{aligned}\right\} \tag{11.42}$$

When numerically solving the system, the infinite series are truncated to finite series. In order to incorporate the four boundary conditions into (11.42), the last four rows of the differential equation for $\ddot{\boldsymbol{\beta}}$ are replaced by the boundary conditions. The system is then

$$\frac{\mathrm{d}}{\mathrm{d}t}\begin{bmatrix}I & 0\\ 0 & I_{-4}\end{bmatrix}\begin{bmatrix}\boldsymbol{\beta}\\ \dot{\boldsymbol{\beta}}\end{bmatrix} = \begin{bmatrix}0 & I\\ M^{-1}A_1 & M^{-1}A_2\end{bmatrix}\begin{bmatrix}\boldsymbol{\beta}\\ \dot{\boldsymbol{\beta}}\end{bmatrix}, \tag{11.43}$$

where I_{-4} is the identity matrix with the last four diagonal entries being zeros. The last four rows of the right-hand side are replaced by the boundary conditions. We now have a generalized eigenvalue problem to solve for the eigenvalues of the system.

11.B.1 Nonlinear eigenvalue problem

Having obtained the solution to the linear eigenvalue problem, we use it as an initial guess for the nonlinear eigenvalue problem. The nonlinear eigenvalue problem is obtained by making the ansatz

$$\left.\begin{aligned}
&Y(x,t) = \mathrm{e}^{\lambda t}Y_0(x),\\
&Y_0(x) = \tfrac{1}{2}\beta_0 + \textstyle\sum_{k=1}^{\infty}\beta_k T_k(x).
\end{aligned}\right\} \tag{11.44}$$

This is the same as in Appendix 11.A, except that we allow the exponent λ to be any complex number instead of just an imaginary number. Proceeding as in Appendix 11.B, we arrive at the following equations:

$$2\lambda^2 \tilde{R}\boldsymbol{\beta} + \frac{2}{3}D^2(\tilde{S}D^2\boldsymbol{\beta}) = \boldsymbol{P}, \tag{11.45}$$

$$\boldsymbol{P} = A\boldsymbol{a}, \tag{11.46}$$

$$D\boldsymbol{a} = -\lambda^2\boldsymbol{\beta} - 2\lambda D\boldsymbol{\beta} - D^2\boldsymbol{\beta}, \tag{11.47}$$

$$\boldsymbol{V} = \lambda\boldsymbol{\beta} + D\boldsymbol{\beta}, \tag{11.48}$$

$$a_0 = -C(\lambda)(V_0 + V_1) + V_1, \tag{11.49}$$

where the notation is as in Appendix 11.B.

Putting everything together, we get the following equation:

$$\begin{aligned} 2\lambda^2 \tilde{R}\boldsymbol{\beta} + \frac{2}{3}D^2(\tilde{S}D^2\boldsymbol{\beta}) &= A[-\lambda^2 D^- \boldsymbol{\beta} - 2\lambda D^- D\boldsymbol{\beta} + \lambda \boldsymbol{e_1}(\boldsymbol{e_2} - C(\lambda)\boldsymbol{e_1} - C(\lambda)\boldsymbol{e_2})^T\boldsymbol{\beta} \\ &\quad -D^- D^2\boldsymbol{\beta} + \boldsymbol{e_1}(\boldsymbol{e_2} - C(\lambda)\boldsymbol{e_1} - C(\lambda)\boldsymbol{e_2})^T D\boldsymbol{\beta}], \end{aligned} \tag{11.50}$$

where the notation is as in Appendix 11.B. Truncating the upper limit of the infinite series to N, (11.50) gives $N+1$ equations for $N+2$ unknowns (the $N+1$ elements of $\boldsymbol{\beta}$ and λ). We add an equation which normalizes $\boldsymbol{\beta}$ in order to make the system square. As before, the last four equations are replaced by the boundary conditions. We solve for $\boldsymbol{\beta}$ and λ using the Newton-Raphson method, using absolute and relative error tolerances 10^{-6}. For cases where the Newton-Raphson method did not converge, we calculated the solution by looking at a global picture of the determinant of the system and finding its roots.

We have previously validated our method for calculating eigenvalues of flexible plates with uniform material properties (Floryan and Rowley, 2018). To the best of our knowledge, no prior work has calculated the eigenvalues of plates with nonuniform material properties, giving us nothing to compare to. We note, however, that the same computer code calculates the eigenvalues for plates with uniform and nonuniform material properties, the former merely a special case of the latter.

11.B.2 Quiescent fluid

Consider the case where the plate is immersed in a quiescent fluid, i.e. where the bending velocity is large compared to the fluid velocity. How do the eigenvalues of the system change? To answer this question, we solve the Euler-Bernoulli and Euler equations (11.1)–(11.2) in the limit of large bending velocity. In this limit, the appropriate time scale to use is the bending time scale, which we choose to be $\sqrt{3\langle\rho_s d\rangle L^4/(4\langle Ed^3\rangle)}$. Non-dimensionalizing the solid and fluid equations using the length scale $L/2$ and the bending time scale yields

$$\left.\begin{aligned} &R^* Y_{tt} + (S^* Y_{xx})_{xx} = \frac{1}{2\langle R\rangle}\Delta p, \\ &\nabla\cdot\mathbf{u} = 0, \\ &\mathbf{u}_t + \sqrt{\frac{3\langle R\rangle}{\langle S\rangle}}\mathbf{u}_x = \nabla\phi, \end{aligned}\right\} \tag{11.51}$$

where R and S are as in (11.4), R^* is the spatial distribution (mean 1) of R, S^* is the spatial distribution (mean 1) of S, and $\phi = p_\infty - p$. In the above, x, t, Y, $\mathbf{u}$, and p are now dimensionless, with the pressure non-dimensionalized by $\rho_f\langle Ed^3\rangle/(3\langle\rho_s d\rangle L^2)$. The limit of a quiescent flow corresponds to $\langle R\rangle/\langle S\rangle \to 0$, or equivalently $\langle Ed^3\rangle/\langle\rho_s d\rangle L^2 \gg U^2$, which explicitly puts this limit in terms of velocity scales. For now, we keep all terms and discuss the limit later. Intuitively, large values of the solid-to-fluid mass ratio $\langle R\rangle$ make the fluid dynamics inconsequential to the deflection of the plate (a heavy plate will be unaffected by the surrounding fluid).

The fluid additionally satisfies the no-penetration condition, stated as

$$v|_{x\in[-1,1],y=0} = Y_t + \sqrt{\frac{3\langle R\rangle}{\langle S\rangle}}Y_x. \tag{11.52}$$

The boundary conditions on the plate are

$$Y(-1,t) = 0, \quad Y_x(-1,t) = 0, \quad Y_{xx}(1,t) = 0, \quad Y_{xxx}(1,t) = 0. \tag{11.53}$$

We solve for the fluid motion for a given deflection as in Appendix 11.A. Writing the deflection as

$$Y(x,t) = \frac{1}{2}\beta_0(t) + \sum_{k=1}^{\infty}\beta_k(t)T_k(x), \tag{11.54}$$

and the components of the complex potential evaluated on the surface of the plate as

$$\left.\begin{aligned} \phi(z = x \pm 0\mathrm{i}, t) \quad &= \pm\frac{1}{2}a_0(t)\sqrt{\frac{1-x}{1+x}} \pm \sum_{k=1}^{\infty}a_k(t)\sin k\theta, \\ \psi(z = x \pm 0\mathrm{i}, t) \quad &= \frac{1}{2}a_0(t) + \sum_{k=1}^{\infty}a_k(t)T_k(x), \end{aligned}\right\} \tag{11.55}$$

the pressure difference across the surface of the plate is

$$\Delta p(x,t) = a_0(t)\sqrt{\frac{1-x}{1+x}} + 2\sum_{k=1}^{\infty}a_k(t)\sin k\theta. \tag{11.56}$$

The coefficients a_k are obtained by applying the no-penetration condition,

$$\frac{\partial\psi}{\partial x}|_{y=0} = -\left(\frac{\partial}{\partial t} + \sqrt{\frac{3\langle R\rangle}{\langle S\rangle}}\frac{\partial}{\partial x}\right)^2 Y. \tag{11.57}$$

This does not yield a_0, which is instead given by the Laplace domain equation

$$a_0 = -\sqrt{\frac{3\langle R\rangle}{\langle S\rangle}}C(V_0 + V_1) + \sqrt{\frac{3\langle R\rangle}{\langle S\rangle}}V_1. \tag{11.58}$$

In the limit of a quiescent fluid ($\langle R\rangle/\langle S\rangle \to 0$), $a_0 \to 0$. Thus all of the coefficients a_k are determined by (11.57), which itself simplifies since the second term in the parentheses is zero in the limit $\langle R\rangle/\langle S\rangle \to 0$. We note that in this limit the only fluid force on the plate is the force due to added mass.

Putting everything together, we get the following ordinary differential equation:

$$\widetilde{R^*}\ddot{\boldsymbol{\beta}} + D^2(\widetilde{S^*}D^2\boldsymbol{\beta}) = -\frac{1}{\langle R\rangle}AD^-\ddot{\boldsymbol{\beta}}, \tag{11.59}$$

where $\boldsymbol{\beta}$ is the vector of coefficients β_k, D is the spectral representation of the differentiation operator, and D^- is the spectral representation of the integration operator that makes the first Chebyshev coefficient zero. Quantities with a tilde over them are spectral representations of multiplication in space, i.e. $\tilde{G} = FGF^{-1}$, where F is the linear operator that maps spatial coordinates to spectral coordinates. The operator A maps the coefficients a_k, which are the coefficients of a *sine* series for the pressure, into the corresponding coefficients of a *cosine* series. If T_s is an operator that takes us from the x-domain to the sine domain, and T_c is an operator that takes us from the x-domain to the cosine domain, then $A = T_cT_s^{-1}$. (11.59) can be written in state-space form as

$$\frac{\mathrm{d}}{\mathrm{d}t}\begin{bmatrix}\boldsymbol{\beta}\\ \dot{\boldsymbol{\beta}}\end{bmatrix} = \begin{bmatrix}0 & I\\ -\left(\widetilde{R^*} + \frac{1}{\langle R\rangle}AD^-\right)^{-1}D^2\widetilde{S^*}D^2 & 0\end{bmatrix}\begin{bmatrix}\boldsymbol{\beta}\\ \dot{\boldsymbol{\beta}}\end{bmatrix}. \tag{11.60}$$

When numerically solving the system, the infinite series are truncated to finite series. In order to incorporate the four boundary conditions into (11.61), the last four rows of the differential equation for $\ddot{\boldsymbol{\beta}}$ are replaced by the boundary conditions. This is fine to do since the last four rows read $\ddot{\beta}_k = 0$ due to four applications of the differentiation operator D. The system is then

$$\frac{\mathrm{d}}{\mathrm{d}t}\begin{bmatrix} I & 0 \\ 0 & I_{-4} \end{bmatrix}\begin{bmatrix} \boldsymbol{\beta} \\ \dot{\boldsymbol{\beta}} \end{bmatrix} = \begin{bmatrix} 0 & I \\ -\left(\widetilde{R^*} + \frac{1}{\langle R \rangle} A D^{-}\right)^{-1} D^2 \widetilde{S^*} D^2 & 0 \end{bmatrix}\begin{bmatrix} \boldsymbol{\beta} \\ \dot{\boldsymbol{\beta}} \end{bmatrix}, \tag{11.61}$$

where I_{-4} is the identity matrix with the last four diagonals being zeros. The last four rows of the right-hand side are replaced by the boundary conditions. We now have a generalized eigenvalue problem to solve for the eigenvalues of the system.

11.C Green's function of the system

Here, we seek to determine the response of a flexible plate to a spatially-localized, periodic-in-time fluid forcing. This amounts to finding the Green's function of the system (11.29). For this system, the Green's function is a function $G(x, \xi)$ that satisfies

$$\left.\begin{aligned} &-2\sigma^2 R G(x,\xi) + \frac{2}{3}\left(S G_{xx}(x,\xi)\right)_{xx} = \delta(x-\xi), \quad -1 < x, \xi < 1, \\ &G(-1,\xi) = 0, \quad G_x(-1,\xi) = 0, \quad G_{xx}(1,\xi) = 0, \quad G_{xxx}(1,\xi) = 0, \end{aligned}\right\} \tag{11.62}$$

where δ is the Dirac delta function. That is, $G(x, \xi)$ is the solution for a localized forcing at $x = \xi$, with homogeneous boundary conditions. Once we know $G(x, \xi)$, we can construct the solution for any forcing function by superposition. This is beyond our interests, so we refer the interested reader to any book dealing with boundary value problems.

Let G_1 be the solution of the ordinary differential equation in (11.62) for $x \in (-1, \xi)$ with boundary conditions

$$G(-1,\xi) = 0, \quad G_x(-1,\xi) = 0, \quad G_{xx}(-1,\xi) = 1, \quad G_{xxx}(-1,\xi) = 0, \tag{11.63}$$

let G_2 be the solution of the ordinary differential equation in (11.62) for $x \in (-1, \xi)$ with boundary conditions

$$G(-1,\xi) = 0, \quad G_x(-1,\xi) = 0, \quad G_{xx}(-1,\xi) = 0, \quad G_{xxx}(-1,\xi) = 1, \tag{11.64}$$

let G_3 be the solution of the ordinary differential equation in (11.62) for $x \in (\xi, 1)$ with boundary conditions

$$G(1,\xi) = 1, \quad G_x(1,\xi) = 0, \quad G_{xx}(1,\xi) = 0, \quad G_{xxx}(1,\xi) = 0, \tag{11.65}$$

and let G_4 be the solution of the ordinary differential equation in (11.62) for $x \in (\xi, 1)$ with boundary conditions

$$G(1,\xi) = 0, \quad G_x(1,\xi) = 1, \quad G_{xx}(1,\xi) = 0, \quad G_{xxx}(1,\xi) = 0. \tag{11.66}$$

The desired Green's function will have the form

$$G = \begin{cases} c_1 G_1 + c_2 G_2 & \text{for } x \leq \xi \\ c_3 G_3 + c_4 G_4 & \text{for } x \geq \xi. \end{cases} \tag{11.67}$$

The constants c_1, c_2, c_3, c_4 (which will depend on ξ) are set such that G, G_x, and G_{xx} are all continuous at $x = \xi$, and the jump condition on G_{xxx} at $x = \xi$ is met. We obtain the jump condition by integrating the ordinary differential equation in (11.62) from $x = \xi - \epsilon$ to $x = \xi + \epsilon$ for vanishingly small ϵ, giving

$$SG_{xxx}|_{\xi+\epsilon} = \frac{3}{2} + SG_{xxx}|_{\xi-\epsilon}, \tag{11.68}$$

where we have assumed that S_x is continuous.

Because the values of G and its derivatives depend linearly on c_1, c_2, c_3, c_4, we get four linear equations in four unknowns, and we just need to solve a 4×4 linear system for the unknown parameters c_1, c_2, c_3, c_4:

$$\begin{bmatrix} G_1 & G_2 & -G_3 & -G_4 \\ G_{1,x} & G_{2,x} & -G_{3,x} & -G_{4,x} \\ G_{1,xx} & G_{2,xx} & -G_{3,xx} & -G_{4,xx} \\ G_{1,xxx} & G_{2,xxx} & -G_{3,xxx} & -G_{4,xxx} \end{bmatrix} \begin{bmatrix} c_1 \\ c_2 \\ c_3 \\ c_4 \end{bmatrix} = \begin{bmatrix} 0 \\ 0 \\ 0 \\ -\dfrac{3}{2S} \end{bmatrix}. \tag{11.69}$$

In the above, all quantities are evaluated at $x = \xi$.

11.D Some useful formulas

The following is a collection of useful definitions and formulas from Moore (2017) for the Chebyshev method employed here. The (interior) Gauss-Chebyshev points are

$$x_n = \cos\theta_n, \quad \theta_n = \frac{\pi(2n+1)}{2(N+1)}, \quad \text{for } n = 0, 1, \ldots, N. \tag{11.70}$$

Consider a function $f(x)$ interpolated at these points by the polynomial $p_N(x)$ of degree N:

$$\left.\begin{aligned} f(x_n) &= p_N(x_n), \quad \text{for } n = 0, 1, \ldots, N, \\ P_N(x_n) &= \frac{1}{2}b_0 + \sum_{k=1}^{N} b_k T_k(x). \end{aligned}\right\} \tag{11.71}$$

On the θ-grid this is

$$f(x_n) = \frac{1}{2}b_0 + \sum_{k=1}^{N} b_k \cos k\theta_n, \quad \text{for } n = 0, 1, \ldots, N. \tag{11.72}$$

Thus we may use the fast discrete cosine transform to transform between a function's values on the collocation points, $f(x_n)$, and the Chebyshev coefficients b_k.

The antiderivative of $p_N(x)$ is

$$\left.\begin{aligned} D^{-1}p_N(x) &= \frac{1}{2}B_0 + \sum_{k=1}^{N+1} B_k T_k(x), \\ B_k &= \frac{1}{2k}(b_{k-1} - b_{k+1}), \quad \text{for } n = 1, 2, \ldots, N. \end{aligned}\right\} \tag{11.73}$$

B_0 is a free constant of integration.

The derivative of $p_N(x)$ is

$$\left.\begin{aligned} & Dp_N(x) = \frac{1}{2}b'_0 + \sum_{k=1}^{N} b'_k T_k(x), \\ & b'_{N+1} = b'_N = 0, \\ & b'_k = b'_{k+2} + 2(k+1)b_{k+1}, \quad \text{for } n = N-1, N-2, \ldots, 0. \end{aligned}\right\} \tag{11.74}$$

Since the endpoints $x = \pm 1$ are not part of the collocation grid, we give a formula to evaluate the function at the endpoints:

$$p_N(\pm 1) = \frac{1}{2}b_0 + \sum_{k=1}^{N} (\pm 1)^k b_k. \tag{11.75}$$

Bibliography

E. Akoz and K. W. Moored. Unsteady propulsion by an intermittent swimming gait. 2017.

S. Alben. The flapping-flag instability as a nonlinear eigenvalue problem. *Physics of Fluids*, 20(10):104106, 2008a.

S. Alben. Optimal flexibility of a flapping appendage in an inviscid fluid. *Journal of Fluid Mechanics*, 614:355–380, 2008b.

R. M. Alexander. *Principles of animal locomotion.* Princeton University Press, 2003.

A. Andersen, T. Bohr, T. Schnipper, and J. H. Walther. Wake structure and thrust generation of a flapping foil in two-dimensional flow. *Journal of Fluid Mechanics*, 812, 2017.

E. J. Anderson, W. R. Mcgillis, and M. A. Grosenbaugh. The boundary layer of swimming fish. *Journal of Experimental Biology*, 204(1):81–102, 2001.

J. M. Anderson, K. Streitlien, D. S. Barrett, and M. S. Triantafyllou. Oscillating foils of high propulsive efficiency. *Journal of Fluid Mechanics*, 360:41–72, 1998.

R. Bainbridge. The speed of swimming of fish as related to size and to the frequency and amplitude of the tail beat. *Journal of Experimental Biology*, 35(1):109–133, 1958.

R. Bainbridge. Caudal fin and body movement in the propulsion of some fish. *Journal of Experimental Biology*, 40(1):23–56, 1963.

D. S. Barrett, M. S. Triantafyllou, D. K. P. Yue, M. A. Grosenbaugh, and M. J. Wolfgang. Drag reduction in fish-like locomotion. *Journal of Fluid Mechanics*, 392: 183–212, 1999.

C. Bergmann. Über die Bewegungen von Radius und Ulna am Vogelflügel. *Arch. Anat. Physiol. wiss Med.*, 6:296–300, 1839.

A. Betz. Ein beitrag zur erklaerung des segelfluges. *Zeitschrift fuer flugtechnik und motorluftschiffahrt*, 3:269–270, 1912.

R. W. Blake. Functional design and burst-and-coast swimming in fishes. *Canadian Journal of Zoology*, 61(11):2491–2494, 1983.

J. B. Bratt. Flow patterns in the wake of an oscillating aerofoil. Technical Report 2773, ARC, 1953.

S. L. Brunton, C. W. Rowley, and D. R. Williams. Reduced-order unsteady aerodynamic models at low Reynolds numbers. *Journal of Fluid Mechanics*, 724:203–233, 2013.

S. L. Brunton, S. T. M. Dawson, and C. W. Rowley. State-space model identification and feedback control of unsteady aerodynamic forces. *Journal of Fluids and Structures*, 50:253–270, 2014.

M. G. Chopra. Large amplitude lunate-tail theory of fish locomotion. *Journal of Fluid Mechanics*, 74(1):161–182, 1976.

M. H. Chung. On burst-and-coast swimming performance in fish-like locomotion. *Bioinspiration & Biomimetics*, 4(3):036001, 2009.

S. A. Combes and T. L. Daniel. Flexural stiffness in insect wings II. Spatial distribution and dynamic wing bending. *Journal of Experimental Biology*, 206(17): 2989–2997, 2003a.

S. A. Combes and T. L. Daniel. Into thin air: contributions of aerodynamic and inertial-elastic forces to wing bending in the hawkmoth Manduca sexta. *Journal of Experimental Biology*, 206(17):2999–3006, 2003b.

S. T. M. Dawson, N. K. Schiavone, C. W. Rowley, and D. R. Williams. A data-driven modeling framework for predicting forces and pressures on a rapidly pitching airfoil. In *45th AIAA Fluid Dynamics Conference*, page 2767, 2015.

P. A. Dewey, B. M. Boschitsch, K. W. Moored, H. A. Stone, and A. J. Smits. Scaling laws for the thrust production of flexible pitching panels. *Journal of Fluid Mechanics*, 732:29–46, 2013.

J. R. Dormand and P. J. Prince. A family of embedded Runge-Kutta formulae. *Journal of Computational and Applied Mathematics*, 6(1):19–26, 1980.

C. Eloy. Optimal strouhal number for swimming animals. *Journal of Fluids and Structures*, 30:205–218, 2012.

C. Eloy, C. Souilliez, and L. Schouveiler. Flutter of a rectangular plate. *Journal of Fluids and Structures*, 23(6):904–919, 2007.

P. J. S. A. Ferreira de Sousa and J. J. Allen. Thrust efficiency of harmonically oscillating flexible flat plates. *Journal of Fluid Mechanics*, 674:43–66, 2011.

F. E. Fish and G. V. Lauder. Passive and active flow control by swimming fishes and mammals. *Annual Review of Fluid Mechanics*, 38:193–224, 2006.

F. E. Fish, J. F. Fegely, and C. J. Xanthopoulos. Burst-and-coast swimming in schooling fish (Notemigonus crysoleucas) with implications for energy economy. *Comparative Biochemistry and Physiology Part A: Physiology*, 100(3):633–637, 1991.

F. E. Fish, H. Haj-Hariri, A. J. Smits, H. Bart-Smith, and T. Iwasaki. Biomimetic swimmer inspired by the manta ray. In *Biomimetics*, pages 515–544. CRC Press, 2011.

D Floryan and C. W. Rowley. Clarifying the relationship between efficiency and resonance for flexible inertial swimmers. *Journal of Fluid Mechanics*, 853:271–300, 2018.

D. Floryan and C. W. Rowley. Distributed flexibility in inertial swimmers. Submitted, 2019.

D. Floryan, T. Van Buren, C. W. Rowley, and A. J. Smits. Scaling the propulsive performance of heaving and pitching foils. *Journal of Fluid Mechanics*, 822:386–397, 2017a.

D. Floryan, T. Van Buren, and A. J. Smits. Forces and energetics of intermittent swimming. *Acta Mechanica Sinica*, 33(4):725–732, 2017b.

D. Floryan, T. Van Buren, and A. J. Smits. Efficient cruising for swimming and flying animals is dictated by fluid drag. *Proceedings of the National Academy of Sciences*, 115(32):8116–8118, 2018.

D. Floryan, T. Van Buren, and A. J. Smits. Large-amplitude oscillations of foils for efficient propulsion. Submitted, 2019.

B. A. Free and D. A. Paley. Model-based observer and feedback control design for a rigid joukowski foil in a kármán vortex street. *Bioinspiration & Biomimetics*, 13 (3):035001, 2018.

I. E. Garrick. Propulsion of a flapping and oscillating airfoil. Technical Report 567, NACA, 1936.

M. Gazzola, M. Argentina, and L. Mahadevan. Scaling macroscopic aquatic locomotion. *Nature Physics*, 10(10):758, 2014.

H. Glauert. The force and moment on an oscillating aerofoil. In *Vorträge aus dem Gebiete der Aerodynamik und verwandter Gebiete*, pages 88–95. Springer, 1930.

A. C. Gleiss, S. J. Jorgensen, N. Liebsch, J. E. Sala, B. Norman, G. C. Hays, F. Quintana, E. Grundy, C. Campagna, A. W. Trites, B. A. Block, and R. P. Wilson. Convergent evolution in locomotory patterns of flying and swimming animals. *Nature Communications*, 2:352, 2011.

R.-N. Hua, L. Zhu, and X.-Y. Lu. Locomotion of a flapping flexible plate. *Physics of Fluids*, 25(12):121901, 2013.

K. Isogai, Y. Shinmoto, and Y. Watanabe. Effects of dynamic stall on propulsive efficiency and thrust of flapping airfoil. *AIAA journal*, 37(10):1145–1151, 1999.

A. K. Kancharala and M. K. Philen. Optimal chordwise stiffness profiles of self-propelled flapping fins. *Bioinspiration & Biomimetics*, 11(5):056016, 2016.

C.-K. Kang, H. Aono, C. E. S. Cesnik, and W. Shyy. Effects of flexibility on the aerodynamic performance of flapping wings. *Journal of Fluid Mechanics*, 689:32–74, 2011.

E. Kanso and J. E. Marsden. Optimal motion of an articulated body in a perfect fluid. In *Proceedings of the 44th IEEE Conference on Decision and Control*, pages 2511–2516. IEEE, 2005.

A. O. Kasumyan. Sounds and sound production in fishes. *Journal of Ichthyology*, 48 (11):981–1030, 2008.

J. Katz and D. Weihs. Hydrodynamic propulsion by large amplitude oscillation of an airfoil with chordwise flexibility. *Journal of Fluid Mechanics*, 88(3):485–497, 1978.

J. Katz and D. Weihs. Large amplitude unsteady motion of a flexible slender propulsor. *Journal of Fluid Mechanics*, 90(4):713–723, 1979.

R. Katzmayr. Effect of periodic changes of angle of attack on behavior of airfoils. Technical Report 147, NACA, 1922.

S. D. Kelly. *The mechanics and control of robotic locomotion with applications to aquatic vehicles*. PhD thesis, California Institute of Technology, 1998.

R. Knoller. Die gesetze des luftwiderstandes. *Flug- und Motortechnik*, 3(21):1–7, 1909.

M. M. Koochesfahani. Vortical patterns in the wake of an oscillating foil. *AIAA Journal*, 27(9):1200–1205, 1989.

D. L. Kramer and R. L. McLaughlin. The behavioral ecology of intermittent locomotion 1. *American Zoologist*, 41(2):137–153, 2001.

G. C. Lewin and H. Haj-Hariri. Modelling thrust generation of a two-dimensional heaving airfoil in a viscous flow. *Journal of Fluid Mechanics*, 492:339–362, 2003.

M. J. Lighthill. Aquatic animal propulsion of high hydromechanical efficiency. *Journal of Fluid Mechanics*, 44(02):265–301, 1970.

M. J. Lighthill. Large-amplitude elongated-body theory of fish locomotion. *Proceedings of the Royal Society of London B: Biological Sciences*, 179(1055):125–138, 1971.

T. Liu, S. Wang, X. Zhang, and G. He. Unsteady thin-airfoil theory revisited: Application of a simple lift formula. *AIAA Journal*, 53(6):1492–1502, 2014.

K. N. Lucas, P. J. M. Thornycroft, B. J. Gemmell, S. P. Colin, J. H. Costello, and G. V. Lauder. Effects of non-uniform stiffness on the swimming performance of a passively-flexing, fish-like foil model. *Bioinspiration & Biomimetics*, 10(5):056019, 2015.

A. W. Mackowski and C. H. K. Williamson. Direct measurement of thrust and efficiency of an airfoil undergoing pure pitching. *Journal of Fluid Mechanics*, 765: 524–543, 2015.

MATLAB and Optimization Toolbox Release 2016a. The Mathworks, Inc., Natick, Massachusetts, 2016.

S. Michelin and S. G. Llewellyn Smith. Resonance and propulsion performance of a heaving flexible wing. *Physics of Fluids*, 21(7):071902, 2009.

M. N. Moore. A fast Chebyshev method for simulating flexible-wing propulsion. *Journal of Computational Physics*, 345:792–817, 2017.

M. N. J. Moore. Analytical results on the role of flexibility in flapping propulsion. *Journal of Fluid Mechanics*, 757:599–612, 2014.

M. N. J. Moore. Torsional spring is the optimal flexibility arrangement for thrust production of a flapping wing. *Physics of Fluids*, 27(9):091701, 2015.

K. W. Moored, P. A. Dewey, A. J. Smits, and H. Haj-Hariri. Hydrodynamic wake resonance as an underlying principle of efficient unsteady propulsion. *Journal of Fluid Mechanics*, 708:329–348, 2012.

K. W. Moored, P. A. Dewey, B. M. Boschitsch, A. J. Smits, and H. Haj-Hariri. Linear instability mechanisms leading to optimally efficient locomotion with flexible propulsors. *Physics of Fluids*, 26(4):041905, 2014.

J. M. Moulton. Swimming sounds and the schooling of fishes. *The Biological Bulletin*, 119(2):210–223, 1960.

F. Paraz, L. Schouveiler, and C. Eloy. Thrust generation by a heaving flexible foil: Resonance, nonlinearities, and optimality. *Physics of Fluids*, 28(1):011903, 2016.

D. B. Quinn, G. V. Lauder, and A. J. Smits. Scaling the propulsive performance of heaving flexible panels. *Journal of Fluid Mechanics*, 738:250–267, 2014.

D. B. Quinn, G. V. Lauder, and A. J. Smits. Maximizing the efficiency of a flexible propulsor using experimental optimization. *Journal of Fluid Mechanics*, 767:430–448, 2015.

S. Ramananarivo, R. Godoy-Diana, and B. Thiria. Rather than resonance, flapping wing flyers may play on aerodynamics to improve performance. *Proceedings of the National Academy of Sciences*, 108(15):5964–5969, 2011.

D. A. Read, F. S. Hover, and M. S. Triantafyllou. Forces on oscillating foils for propulsion and maneuvering. *Journal of Fluids and Structures*, 17(1):163–183, 2003.

P. Riggs, A. Bowyer, and J. Vincent. Advantages of a biomimetic stiffness profile in pitching flexible fin propulsion. *Journal of Bionic Engineering*, 7(2):113–119, 2010.

J. J. Rohr and F. E. Fish. Strouhal numbers and optimization of swimming by odontocete cetaceans. *Journal of Experimental Biology*, 207(10):1633–1642, 2004. doi: 10.1242/jeb.00948.

M. Rufo and M. Smithers. GhostSwimmer^{TM} AUV: applying biomimetics to underwater robotics for achievement of tactical relevance. *Marine Technology Society Journal*, 45(4):24–29, 2011.

M. Saadat, F. E. Fish, A. G. Domel, V. Di Santo, G. V. Lauder, and H. Haj-Hariri. On the rules for aquatic locomotion. *Physical Review Fluids*, 2(8):083102, 2017.

P. G. Saffman. *Vortex dynamics*. Cambridge University Press, 1992.

J. O. Scherer. Experimental and theoretical investigation of large amplitude oscillating foil propulsion systems. Technical Report 662-1, Hydronautics, Inc., 1968.

H. Schlichting. *Boundary-layer theory*. McGraw-Hill, 7th edition, 1979.

L. Schouveiler, F. S. Hover, and M. S. Triantafyllou. Performance of flapping foil propulsion. *Journal of Fluids and Structures*, 20(7):949–959, 2005.

A. Sciacchitano, B. Wieneke, and F. Scarano. PIV uncertainty quantification by image matching. *Measurement Science and Technology*, 24(4):045302, 2013.

L. I. Sedov. On the theory of the unsteady motion of an airfoil in a fluid. Technical Report 229, CAHI, 1935.

L. I. Sedov. *Two-dimensional problems in hydrodynamics and aerodynamics*. Interscience Publishers, 1965.

L. F. Shampine and M. W. Reichelt. The MATLAB ODE suite. *SIAM Journal on Scientific Computing*, 18(1):1–22, 1997.

K. Shoele and Q. Zhu. Performance of a wing with nonuniform flexibility in hovering flight. *Physics of Fluids*, 25(4):041901, 2013.

W. N. Tavolga. Sound production and detection. In *Fish physiology*, volume 5, pages 135–205. Elsevier, 1971.

G. K. Taylor, R. L. Nudds, and A. L. R. Thomas. Flying and swimming animals cruise at a Strouhal number tuned for high power efficiency. *Nature*, 425(6959): 707, 2003.

T. Theodorsen. General theory of aerodynamic instability and the mechanism of flutter. Technical Report 496; originally published as ARR-1935, NACA, 1935.

G. S. Triantafyllou, M. S. Triantafyllou, and M. A. Grosenbaugh. Optimal thrust development in oscillating foils with application to fish propulsion. *Journal of Fluids and Structures*, 7(2):205–224, 1993.

M. S. Triantafyllou and G. S. Triantafyllou. An efficient swimming machine. *Scientific American*, 272(3):64–70, 1995.

M. S. Triantafyllou, G. S. Triantafyllou, and R. Gopalkrishnan. Wake mechanics for thrust generation in oscillating foils. *Physics of Fluids A: Fluid Dynamics*, 3(12): 2835–2837, 1991.

M. S. Triantafyllou, G. S. Triantafyllou, and D. K. P. Yue. Hydrodynamics of fishlike swimming. *Annual Review of Fluid Mechanics*, 32(1):33–53, 2000.

M. S. Triantafyllou, F. S. Hover, A. H. Techet, and D. K. Yue. Review of hydrodynamic scaling laws in aquatic locomotion and fishlike swimming. *Applied Mechanics Reviews*, 58(4):226–237, 2005.

I. H. Tuncer and M. Kaya. Optimization of flapping airfoils for maximum thrust and propulsive efficiency. *AIAA Journal*, 43(11):2329–2336, 2005.

T. Van Buren, D. Floryan, D. Quinn, and A. J. Smits. Nonsinusoidal gaits for unsteady propulsion. *Physical Review Fluids*, 2:053101, May 2017.

T. Van Buren, D. Floryan, and A. J. Smits. Scaling and performance of simultaneously heaving and pitching foils. *AIAA Journal*, pages 1–12, 2018a.

T. Van Buren, D. Floryan, N. Wei, and A. J. Smits. Flow speed has little impact on propulsive characteristics of oscillating foils. *Physical Review Fluids*, 3(1):013103, 2018b.

M. Vanella, T. Fitzgerald, S. Preidikman, E. Balaras, and B. Balachandran. Influence of flexibility on the aerodynamic performance of a hovering wing. *Journal of Experimental Biology*, 212(1):95–105, 2009.

J. J. Videler and D. Weihs. Energetic advantages of burst-and-coast swimming of fish at high speeds. *Journal of Experimental Biology*, 97(1):169–178, 1982.

Z. J. Wang. Vortex shedding and frequency selection in flapping flight. *Journal of Fluid Mechanics*, 410:323–341, 2000.

Z. J. Wang. Dissecting insect flight. *Annual Review of Fluid Mechanics*, 37:183–210, 2005.

P. W. Webb. Hydrodynamics and energetics of fish propulsion. *Bulletin of the fisheries research board of Canada*, 190:1–159, 1975.

P. W. Webb. Form and function in fish swimming. *Scientific American*, 251(1):72–83, 1984.

D. Weihs. Energetic advantages of burst swimming of fish. *Journal of Theoretical Biology*, 48(1):215–229, 1974.

F. M. White. *Fluid mechanics*. McGraw Hill, 7th edition, 2011.

G. Wu, Y. Yang, and L. Zeng. Kinematics, hydrodynamics and energetic advantages of burst-and-coast swimming of koi carps (Cyprinus carpio koi). *Journal of Experimental Biology*, 210(12):2181–2191, 2007.

T. Y. Wu. Swimming of a waving plate. *Journal of Fluid Mechanics*, 10(3):321–344, 1961.

T. Y. Wu. Hydromechanics of swimming propulsion. part 2. some optimum shape problems. *Journal of Fluid Mechanics*, 46(3):521–544, 1971.

T. Y. Wu. Fish swimming and bird/insect flight. *Annual Review of Fluid Mechanics*, 43:25–58, 2011.

P. D. Yeh, Y. Li, and A. Alexeev. Efficient swimming using flexible fins with tapered thickness. *Physical Review Fluids*, 2(10):102101, 2017.

J. Young and J. C. S. Lai. Mechanisms influencing the efficiency of oscillating airfoil propulsion. *AIAA Journal*, 45(7):1695–1702, 2007.

J. Young, J. C. S. Lai, M. Kaya, and I. H. Tuncer. Thrust and efficiency of propulsion by oscillating foils. In *Computational Fluid Dynamics 2004*, pages 313–318. Springer, 2006.

J. Zhang. Footprints of a flapping wing. *Journal of Fluid Mechanics*, 818:1–4, 2017.

X. Zhu, G. He, and X. Zhang. How flexibility affects the wake symmetry properties of a self-propelled plunging foil. *Journal of Fluid Mechanics*, 751:164–183, 2014.

Reproduced with permission of copyright owner. Further reproduction prohibited without permission.